Experimental and Computational Investigation of Spark Assisted Compression Ignition Combustion Under Boosted, Ultra EGR-Dilute Conditions

by

Vasileios Triantopoulos

A dissertation submitted in partial fulfillment
of the requirements for the degree of
Doctor of Philosophy
(Mechanical Engineering)
in The University of Michigan
2018

Doctoral Committee:

Professor André L. Boehman, Chair
President Dennis N. Assanis, University of Delaware
Dr. Stanislav V. Bohac, U.S. Environmental Protection Agency
Associate Professor Claus Borgnakke
Associate Professor Mirko Gamba
Dr. Jason B. Martz, Ford Motor Company

Vasileios Triantopoulos

vtrianto@umich.edu

ORCID iD: 0000-0002-5318-5606

To Thetis, Triantis and Lefteris

ACKNOWLEDGEMENTS

I have been extremely fortunate to work closely with many people whose support and contributions has made this work possible.

I wish to thank President Dennis Assanis for initially offering me the opportunity to join his research group at the Walter E. Lay Automotive Laboratory. While the start of my doctoral studies was marked by his departure from the University of Michigan, his continued support and advice has been invaluable and I am very lucky to be able to learn from him over the years.

I would like to thank Dr. Stanislav Bohac for his guidance and support during my doctoral studies. I am grateful for all the knowledge he has offered me on experimental engine research. I am thankful to Dr. Jason Martz, who initially helped me shape the goals of this work. His expertise on my research topic has been invaluable and his dedication to high quality research has pushed me to become a better researcher.

I am thankful to Professor André L. Boehman for his guidance and support late in my doctoral studies and for serving as chair of my dissertation committee. His knowledge, optimism and willingness to help, have been extremely important for me to reach this point.

I would also like to thank Professors Claus Borgnakke and Mirko Gamba for serving in my committee and for providing constructive feedback on my work. I wish to thank Research Scientist George Lavoie for many fruitful discussions we have had the past few years. His scientific insight has always been a source of inspiration and I greatly appreciate his genuine interest in my work. I wish to thank Dr. Robert Middleton for his assistance with the computational studies performed in this dissertation, none of which would have been possible without him. I am also grateful to

Dr. Ortiz-Soto for his valuable improvements to the heat release code used in this work.

I am thankful to all my friends from the Autolab, Dimitris Assanis, Luis Gutierrez, Ripudaman Singh, Adam Vaughan, Prasad Shingne, Josh Lacey, Stefan Klinkert, Sotiris Mamalis, Janardhan Kodavasal, Taehoon Han and Sakthish Sathasivam, who have been a source of encouragement and have made my time here more enjoyable.

This work would not have been possible without the support from the Department of Energy and Robert Bosch LLC. I would like to thank the Bosch ACCESS group who have provided unparallel support throughout my research. Particularly, I would like to thank Jeff Sterniak for his tireless support the past few years.

I wish to thank all my friends from Ann Arbor and back home, who have helped me in many ways to reach this point. Special thanks to Panos, Petros, Carolina, Emilios and Savidis for their continuous support throughout this journey.

Finally, I would like to thank my family for their unconditional love and support for as long as I can remember. Thank you for always believing in me, this work is dedicated to you.

TABLE OF CONTENTS

DEDICATION ii

ACKNOWLEDGEMENTS iii

LIST OF FIGURES viii

LIST OF TABLES xvii

LIST OF ABBREVIATIONS xix

ABSTRACT xxiii

CHAPTER

I. Introduction 1

1.1 Spark Ignition Engines 1
1.2 Homogeneous Charge Compression Ignition Combustion . . . 3
1.3 Spark Assisted Compression Ignition Combustion 6
1.3.1 Combustion Process 6
1.3.2 Multi-Mode Combustion Diagram 8
1.3.3 Benefits and Key Challenges 10
1.3.4 Charge Preparation for SACI Combustion in a Piston Engine 13
1.4 Benefits of Boosting 16
1.5 Previous Work on SACI 19
1.6 Motivation, Research Objectives and Document Organization 25

II. Experimental Setup, Methods and Analytical Models 29

2.1 Experimental Setup 29
2.1.1 Test Engine 29
2.1.2 Test Cell Systems 31
2.1.3 Engine Control and Data Acquisition 34
2.2 Analytical Models 35

2.2.1 Heat Release Analysis . . . 35
2.2.2 Cylinder Mass Estimation . . . 37
2.2.3 Heat Transfer Loss Estimation . . . 39
2.2.4 Two-Zone Thermodynamic Model . . . 41
2.2.5 End-Gas Autoignition Timing Estimation . . . 42
2.2.6 Laminar Burning Velocity Correlation . . . 44
2.3 Representative Pressure Trace . . . 47
2.4 Combustion Constraints . . . 51
2.4.1 Ringing Intensity Limit . . . 51
2.4.2 Combustion Variability Limit . . . 54
2.5 Variability in Experimental Measurements . . . 55

III. Boosted SACI Operating Limits: Load, Ringing Intensity, Efficiency and Variability . . . 58

3.1 The Maximum Pressure Rise Rate Conditions in SACI Combustion . . . 58
3.2 High Load Limits . . . 64
3.3 Combustion Phasing Effects . . . 69
3.4 Cyclic Variability in SACI . . . 73
3.5 Efficiency and Emissions . . . 83
3.5.1 Experiments at Constant Fuel Energy Input and Increasing Dilution using Boost Pressure . . . 83
3.5.2 Experiments at Constant Composition and Increasing Load using Intake Boost . . . 88
3.6 Impact of Engine Speed on SACI Combustion Rates . . . 93
3.7 Effects of Fuel Injection Timing and Fuel Pressure on SACI Heat Release . . . 96
3.8 Summary . . . 100

IV. Boost Pressure Effects on SACI Burn Rates . . . 102

4.1 Background and Experimental Objective . . . 102
4.2 Experimental Approach . . . 104
4.3 Effect of Boost Pressure on SACI Heat Release . . . 107
4.4 Spark Advance Effects on SACI Burn Rates under Boosted Conditions . . . 117
4.5 Comparison of Boost Pressure Effects on SACI Burn Rates for Varying Fuel-to-Charge Equivalence Ratios . . . 119
4.6 Effect of Charge Preheating Method on the SACI Heat Release under Boosted Conditions . . . 122
4.7 Summary . . . 128

V. Impact of Fuel-to-Charge Equivalence Ratio on SACI Burn Rates . . . 129

5.1 Background and Experimental Objective 129
5.2 EGR Dilution Effects at Constant Intake Pressure 131
5.2.1 Experiments at Constant Spark Advance and Varying Mass Fraction Burned at the Onset of Autoignition 131
5.2.2 Experiments at Constant Mass Fraction Burned at the Onset of Autoignition 139
5.2.3 Experiments at Constant End-Gas Energy and Varying Spark Timing 143
5.3 EGR Dilution Effects at Constant Load 148
5.3.1 Experiments at Constant Spark Advance and Varying Mass Fraction Burned at the Onset of Autoignition 148
5.3.2 Experiments at Constant Mass Fraction Burned at the Onset of Autoignition 152
5.4 Summary 155

VI. Understanding the End-Gas Autoignition Rates under Boosted SACI Conditions 157

6.1 KIVA-CFMZ Model for Open Cycle SACI Simulations 158
6.1.1 KIVA-CFMZ Model Description 158
6.1.2 Model Configuration 161
6.2 Comparison of Simulated and Experimental SACI trends . . . 166
6.3 Effect of Intake Boost on the End-Gas Reactivity Stratification 170
6.4 Comparison of Charge Preheating Methods on Reactivity Stratification and End-Gas Autoignition Rates under Boosted Conditions 177
6.5 Comparison of Reactivity Stratification and End-Gas Autoignition Rates under Boosted Conditions for Diabatic and Adiabatic Conditions Late in the Compression Stroke 184
6.6 Summary 189

VII. Summary, Conclusions and Recommendations for Future Work 191

7.1 Summary and Conclusions 191
7.2 Recommendations for Future Work 197

BIBLIOGRAPHY 199

LIST OF FIGURES

Figure

1.1 Estimated U.S. Energy Consumption in 2017 from Lawrence Livermore National Laboratory and the Department of Energy using data from DOE/EIA monthly energy review [9]. 3
1.2 Spark ignited combustion (left) and HCCI combustion (right) . . . 4
1.3 Typical SACI heat release rate trace highlighting the inflection point at the onset of autoignition [29]. 7
1.4 Definition of the four SACI combustion periods using the imaged flame area growth (solid line with square data points) and heat release rate (solid line) for ensemble-averaged cycles by Reuss et al. [32]. . . 8
1.5 Multi-mode combustion diagram showing SI, SACI and HCCI combustion regimes in terms of TDC unburned temperature T_U and burned gas temperature T_B for iso-octane in air. Combustion regimes are delineated based on limits for ignition, knock, flame propagation, bulk quenching and NO_x limit [34]. 9
1.6 Effect of diluent (air or EGR) as a function of fuel-to-charge ratio, ϕ' (left). Diluent effect on unburned and burned gas specific heat ratios γ_U and γ_B, Burned gas temperature T_B as a function of ϕ' (right) [39]. 11
1.7 Potential for brake efficiency gains for naturally aspirated engines depending on combustion regime: HCCI, advanced combustion and SI [39]. 13
1.8 Typical cylinder pressure trace and valve profiles for a negative valve overlap SACI engine. 14
1.9 Thermodynamic simulation results showing efficiency trends with air dilution and intake boost. At each intake boost an optimum efficiency value occurs due to the competition between dilution benefits, frictional benefits and heat transfer benefits. [39]. 17
1.10 Key efficiency losses as a function of equivalence ratio [39]. 18
1.11 Effect of earlier spark timing and lower T_U on SACI heat release rate and mass fraction burned at constant θ_{50} [42]. 23
1.12 Schematic showing the SACI conditions targeted in this work (blue circle) presented on a GMEP against ϕ' diagram. The dashed line is a best fit line from experimental data collected in this work and indicates the variation of load with ϕ' at an intake pressure of 1 bar. 26

2.1 Experimental engine setup highlighting flow paths, major components and important measurements. 33
2.2 Residual gas fraction estimations as a function of (a) negative valve overlap and (b) boost pressure from analytical models and 1-D engine simulation results [68]. 38
2.3 Example mass fraction burned curve (top), burn rate curve (middle) and second derivative of burn rate (bottom) highlighting the estimated end-gas autoignition timing at the first maxima location of the second derivative of the burn rate curve. 43
2.4 Distribution of θ_{50} (300 cycles) for a stable stoichiometric SACI operating conditions at 4.6 bar GMEP, $P_{INT} = 101$ kPa, $\phi' \approx 0.61$. Mean θ_{50}, median θ_{50} and mode θ_{50} are highlighted as well as the ensemble mean θ_{50} and ensemble median θ_{50}. 49
2.5 Distribution of maximum pressure (300 cycles) for a stable stoichiometric SACI operating conditions at 4.6 bar GMEP, $P_{INT} = 101$ kPa, $\phi' \approx 0.61$. Mean peak pressure, median peak pressure, mode peak pressure are highlighted as well as the ensemble mean trace peak pressure and ensemble median trace peak pressure. 49
2.6 Individual pressure traces for all 300 cycles highlighting the ensemble mean pressure trace and the representative pressure traces. 50
2.7 Heat release rate plot showing the effect of ensemble averaging on the heat release profile. Representative pressure traces are also shown for comparison. 50
2.8 Sample unfiltered and filtered SACI pressure traces for a low and high ringing intensity experimental condition. The arrows point to the maximum pressure rise rate of the filtered trace that is being used in the ringing intensity calculation. 52
2.9 High-pass filtered pressure trace highlighting the ΔP which is the maximum peak-to-peak pressure pulsation amplitude. 52
2.10 Relationship between the maximum peak-to-peak pressure pulsation amplitude (ΔP) and the maximum pressure rise rate of the low-pass filtered representative pressure trace ($\dot{P}_{MAX}$). 1240 experimental conditions plotted at 2000 RPM, $0.45 < \phi' < 0.75$, $5 < \theta_{50} < 15$°aTDC and $80 < P_{INT} < 150$ kPa. 53
3.1 Variation of peak gross heat release rate and maximum pressure rise rate for varying ϕ' mixtures at constant maximum pressure rise rate location using the energy conservation equations. The dashed line displays the relationship if combustion was also at constant volume and adiabatic. 61
3.2 Comparison between SACI autoignition characteristic duration ($\delta\theta_{AI}$) with (top) 25-75% burn duration and (middle) 10-90% burn duration for $\phi' = 0.45$ - 0.65 mixtures. The bottom figure shows the variation of the mass fraction burned at the onset of autoignition with $\delta\theta_{AI}$ for all experimental points. 63

3.3 Load sweeps at intake pressures ranging from 100 - 150 kPa showing the variation of GMEP (top) and NMEP (bottom) until ringing/stability limits converged. 67
3.4 Load sweeps at intake pressures ranging from 100 - 150 kPa showing the variation of PMEP (top) and EVC (bottom) until ringing/stability limits converged. 68
3.5 Effect of combustion phasing retard on coefficient of variation of NMEP (top), ringing intensity (middle) and maximum pressure rise rate (bottom) at the maximum load conditions at intake pressures 100 kPa, 130 kPa and 150 kPa. 71
3.6 Effects of combustion phasing retard described by the crank angle 50% of the representative pressure trace on peak heat release rate (top), peak end-gas burn rate (middle) and end-gas energy at autoignition onset (bottom) at the maximum load conditions at intake pressures 100 kPa, 130 kPa and 150 kPa. 72
3.7 Variation of mass fraction burned at autoignition onset (top), temperature at IVC (middle) as spark timing is advanced at constant autoignition phasing and composition. Effects of earlier spark timing and lower unburned gas temperature on standard deviation of θ_{50} (bottom). 75
3.8 Variation of COV of NMEP with standard deviation of θ_{50} for the results presented in Figure 3.7. 76
3.9 Cyclic heat release results (300 cycles) for an operating condition shown in Figure 3.7 with high variability in combustion phasing ($\mathrm{COV}_{NMEP} > 3\%$). (a) Trends in timings of end-gas autoignition (θ_{AI}) and 50% mass fraction fuel burned (θ_{50}) as a function of 2% mass fraction of fuel burned (θ_{02}). (b) Heat release profiles for 3 cycles at early, close to representative and late combustion phasing. 79
3.10 Cyclic heat release results (300 cycles) for an operating condition shown in Figure 3.7 with high variability in combustion phasing, close to the stability limit ($\mathrm{COV}_{NMEP} \approx$ 3-4%). (Top) Cyclic peak heat release and peak autoignition burn rate results, (middle) mass fraction burned at the estimated onset of autoignition and (bottom) variation of cycle estimated unburned gas temperature and pressure at the onset of autoignition as a function of end-gas autoignition phasing. 80
3.11 Variation of standard deviation of θ_{50} as a function of mass fraction burned at the onset of autoignition for the mean of the representative cycles at each operating condition. The data points correspond to 952 operating conditions at 2000 RPM, $T_{INT} = 45$°C, $\theta_{50} \approx 9$°aTDC, $\phi \approx 1$, $0.45 < \phi' < 0.81$, $51 <$ SA < 9°bTDC and $68 < P_{INT} < 150$ kPa. 82
3.12 Variation of indicated fuel conversion efficiencies (top), combustion efficiency and heat transfer loss fraction estimates during the closed portion of the cycle (middle), and pumping mean effective pressure (bottom) as a function of ϕ' at constant fuel energy input. 85

3.13 Variation of mass averaged gas temperature (top) and mean specific heat ratio of the mixture (bottom) during the close portion of the cycle as a function of ϕ' at constant fuel energy input. 86
3.14 Pumping loop comparison for the two extreme ϕ' cases shown in Figure 3.12 highlighting the pumping work penalty for the high ϕ' case due to late EVO/EVC timing and asymmetric NVO. 86
3.15 Effect of fuel to charge equivalence ratio on EGR fraction requirements (top) and emission index of NO_x (bottom). Total EGR (tEGR) in the cylinder is decomposed to internally recirculated EGR (iEGR) and externally recirculated EGR (eEGR). 87
3.16 Variation of indicated fuel conversion efficiencies (top), combustion efficiency and heat transfer loss fraction estimates during the closed portion of the cycle (middle), and hydrocarbon and carbon monoxide emission indices (bottom) as a function of GMEP at constant composition and θ_{50}. 90
3.17 Variation of total, internal and external EGR mass fractions (top) and PMEP (bottom) as a function of GMEP at constant composition and θ_{50}. 91
3.18 Pumping loop comparison for the two extreme GMEP cases shown in Figure 3.16 highlighting the pumping work penalty for the high GMEP case due to late EVO/EVC timing and asymmetric NVO. . 92
3.19 Effect of engine speed on cylinder pressure (top), unburned gas temperature evolution (middle) and gross heat release rate (bottom) at constant composition, load and end-gas autoignition timing. 95
3.20 Effect of fuel injection timing on SACI heat release at constant combustion phasing and spark timing. 98
3.21 End-gas energy and burn rate effects on maximum pressure rise rate for the $\phi' = 0.55$ intake pressure sweep. 98
3.22 Effect of fuel pressure on SACI heat release rates at stoichiometric conditions, ϕ'=0.55, constant spark advance and constant combustion phasing. 99
4.1 Schematic showing the breakdown of the cylinder mass constituents during the boost pressure experiment at $\phi' = 0.55$. Total column height represents the sum of the masses of the constituents (not to scale) 104
4.2 Experimental conditions for the $\phi' = 0.55$ boost pressure experiment shown on a load-ϕ' diagram. Constant intake pressure lines are best fit lines from SACI experimental data collected in this work. 105
4.3 Cylinder pressure traces for the boost pressure sweep at constant composition, combustion phasing, spark timing, intake temperature and engine speed. 109
4.4 Variation of (a) internal EGR and external EGR fractions and (b) ringing intensity and maximum pressure rise rates as a function of intake pressure at constant composition, combustion phasing, spark timing, intake temperature and engine speed. 109

4.5 Gross heat release rate (top), global burn rate (middle) and cumulative heat release (bottom) for the $\phi' = 0.55$ intake pressure sweep at constant engine speed, composition and combustion phasing. 110
4.6 Crank angle locations at the time of 5% mass fraction burned, 10% burned, auto-ignition, 50% burned, and 90% burned for the $\phi' = 0.55$ intake pressure sweep at constant engine speed, composition, combustion phasing. 111
4.7 Evolution of the estimated mass-averaged unburned gas temperature for the $\phi' = 0.55$ intake pressure sweep at constant engine speed, composition, combustion phasing. 111
4.8 (a) Variation of estimated end-gas energy and end-gas characteristic burn duration and (b) mass fraction burned and end-gas energy at onset of autoignition for the $\phi' = 0.55$ intake pressure sweep at constant engine speed, composition, combustion phasing. 112
4.9 Maximum pressure rise rate measurements as a function of intake pressure for the $\phi' = 0.55$ intake pressure sweep. Error bars represent minimum and maximum values of the 20 representative cycles at each operating condition. Solid markers indicate the 4 experimental conditions presented in detail in this Section. 112
4.10 Constant volume ignition delay contours (blue) as a function of pressure and temperature for a stoichiometric mixture at $\phi' = 0.55$. Grey lines indicate the trajectories of experimental pressure and estimated mass averaged-unburned gas temperature during compression up to the onset of end-gas autoignition for the boost pressure experiment at $\phi' = 0.55$ outlined in Table 4.1. The black crosses indicate the estimated autoignition timing derived from the experimental burn rate curves. 115
4.11 Trajectories of experimentally measured pressure and estimated mass-averaged unburned gas temperature from IVC to EVO for the boost pressure experiment at $\phi' = 0.55$ outlined in Table 4.1. The red markers indicate the estimated end-gas autoignition timing computed from the experimental burn rate curves. 116
4.12 Variation of peak end-gas burn rate (top) and mass fraction of fuel burned at the onset of autoignition (bottom) as a function of intake pressure at 3 spark timings. Combustion phasing ($\theta 50 = 9°$ aTDC) and composition ($\phi = 1$, $\phi' = 0.55$) are maintained constant for all experiments. 118
4.13 Effect of intake pressure on peak gross heat release rate (top) and peak end-gas burn rate (bottom) for various ϕ' mixtures at stoichiometric conditions, at constant engine speed, combustion phasing and spark advance. 120
4.14 Effect of intake pressure on mass fraction of fuel burned (top) and end-gas energy (bottom) at the estimated onset of autoignition for various ϕ' mixtures at stoichiometric conditions, constant engine speed, combustion phasing and spark advance. 121

4.15 Schematic showing the breakdown of the cylinder mass constituents during the boost pressure experiment at constant ratio of internal to external EGR and composition. Total column height represents the sum of the masses of the constituents (not to scale). 123
4.16 Cylinder pressure traces for boost pressure sweep experiments at constant internal-to-external EGR fraction and varying intake temperatures at stoichiometric conditions, constant engine speed, combustion phasing and spark advance. 124
4.17 Variation of (a) total EGR fraction displayed as a sum of internal and external EGR and (b) manifold temperatures as a function of intake pressure for experiments at constant composition, combustion phasing, spark timing, and engine speed. 125
4.18 Gross heat release rate profiles (top), global burn rate profiles (middle) and cumulative heat release (bottom) for boost pressure sweep experiments at constant internal-to-external EGR fraction and varying intake temperatures. All conditions are stoichiometric with constant composition,engine speed, combustion phasing and spark advance. 126
4.19 Comparison of peak global heat release rate (top) and peak burn rate (bottom) trends with intake pressure between residual gas heating and intake manifold heating experiments. Combustion phasing, composition, spark advance, intake valve timings and engine speed were held constant. Error bars represent minimum and maximum values from the 20 representative cycles selected at each operating condition. 127
5.1 Breakdown of the cylinder mass constituents for the fuel-to-charge equivalence ratio experiment (not to scale). Total column height represents the sum of the masses of the constituents. 135
5.2 From top to bottom: Gross heat release rate, global burn rate, end-gas burn rate and mass fraction burned as a function of ϕ' at constant end-gas autoignition timing, engine speed, intake pressure and spark timing. 136
5.3 From top to bottom: Cylinder pressure, estimated mass-averaged unburned gas temperature, estimated burned gas temperature and laminar burning velocities as a function of ϕ' at constant end-gas autoignition timing, engine speed, intake pressure and spark timing. 137
5.4 Peak gross heat release rate trends (top), peak end-gas burn rate trends (middle) and mass fraction of fuel burned at the onset of autoignition trends (bottom) as a function of ϕ' at increasing intake pressure, stoichiometric conditions, constant combustion phasing and spark timing. 138
5.5 Cylinder pressure trace (top) and unburned gas temperature evolution (bottom) for the ϕ' at constant intake pressure and mass fraction burned at the onset of autoignition. 141

5.6 From top to bottom: Effect of ϕ' on gross heat release rate, global burn rate, mass fraction burned and cumulative heat release at constant intake pressure, engine speed and mass fraction burned at the onset of end-gas autoignition. 142
5.7 (a) Estimated unburned gas temperature, (b) cylinder pressure and (c) global mass fraction of fuel burned as a function of ϕ' at similar estimated end-gas energy at the onset of autoignition. Intake pressure, engine speed, intake temperature and autoignition phasing were all held constant. 145
5.8 From top to bottom: Effect of ϕ' on gross heat release rate, global burn rate, end-gas burn rate and cumulative heat release at similar estimated end-gas energy at the onset of autoignition. Intake pressure, engine speed, intake temperature and autoignition phasing were all held constant. 146
5.9 Cylinder pressure variation (top) and unburned gas temperature (bottom) as a function of ϕ' at similar estimated end-gas energy at the onset of autoignition. Intake pressure, engine speed, intake temperature and autoignition phasing were all held constant. 150
5.10 From top to bottom: Effect of ϕ' on gross heat release rate, global burn rate, end-gas burn rate and cumulative heat release at constant load and spark timing. Engine speed, intake temperature and autoignition phasing were all held constant. 151
5.11 From top to bottom: Effect of ϕ' on gross heat release rate, global burn rate, end-gas burn rate and cumulative heat release at stiochiometric conditions and similar mass fraction burned at the onset of autoignition. Engine speed, intake temperature and autoignition phasing were held constant for all conditions. 154
6.1 Variable sizing of temperature bins with high resolution (5 K) being used for temperatures between 900 K - 1200 K (solid grey) where autoignition chemistry is sensitive to temperature changes. Reproduced from [82]. 161
6.2 Computation mesh used in this work, containing 156,000 cells, based on the FFVA engine [14, 42, 153]. Exhaust ports shown on the left, intake ports on the right. 164
6.3 Example high speed pressure measurements of cylinder 1 intake and exhaust runners for a boosted SACI operating condition. The measurements are used as boundary conditions for the KIVA simulation. The vertical lines indicate valve opening and closing times for intake valve (left) and exhaust valves (right). 165

6.4 Schematic of simulation procedure for a typical boosted SACI case highlighting cylinder pressure and valve lift traces. Simulations are initialized at 640° bTDC firing using an 8 species chemical mechanism with no reactions to capture the effects of NVO on mixture preparation. The simulation is stopped immediately after IVC at 115° bTDC firing and restarted with the 312 species chemical mechanism of Mehl et al. [128, 129]. 165
6.5 Comparison of cylinder pressure results between (a) experimental cases and (b) simulation results. 168
6.6 Comparison of mass averaged unburned gas temperature trends during compression between (a) experimental and (b) KIVA-CFMZ simulation results. 168
6.7 Comparison of heat release rate results between (a) experimental cases and (b) KIVA-CFMZ simulation results. The increasing trend in peak heat release rate is captured well in the simulation results. . 169
6.8 Comparison of burn rate between (a) experimental cases and (b) KIVA-CFMZ simulation results. 169
6.9 Ignition delay distributions at onset of autoignition (5° aTDC) for increasing intake pressure mixtures, with constant autoignition timing, composition and mass fraction burned at the onset of autoignition. . 173
6.10 Pre-ignition unburned gas temperature distribution at TDC for increasing intake pressure mixtures at constant end-gas autoignition timing, composition and mass fraction burned at the onset of autoignition. 173
6.11 Pre-ignition non-product equivalence ratio distribution at TDC for increasing intake pressure mixtures at constant end-gas autoignition timing, composition and mass fraction burned at the onset of autoignition. 174
6.12 Evolution of mass averaged unburned gas temperature (top), unburned gas thermal stratification (middle) and non-product equivalence ratio stratification (bottom) during the compression stroke up to TDC for the intake pressure sweep using residual gas heating at same composition and end-gas autoignition timing. 175
6.13 Cumulative heat loss through the cylinder walls during compression until combustion on an absolute basis (top) and mass normalized basis (bottom) for the intake pressure sweep using residual gas heating at constant composition and end-gas autoignition timing. 176
6.14 Comparison of KIVA-CFMZ heat release rate results for intake boost sweeps using (a) residual gas heating and (b) intake manifold heating at constant autoignition timing and mass fraction burned at the onset of autoignition. 179
6.15 Comparison of KIVA-CFMZ burn rate results for intake boost sweeps using (a) residual gas heating and (b) intake manifold heating at constant autoignition timing and mass fraction burned at the onset of autoignition. 180

6.16 Comparison of KIVA-CFMZ flame and autoignition burned mass fraction results for intake boost sweeps using (a) residual gas heating and (b) intake manifold heating at constant autoignition timing and mass fraction burned at the onset of autoignition. 180
6.17 Comparison of charge preheating method on the evolution of thermal stratification ($2\sigma T_U$) for the intake pressure sweep at same composition, mass fraction burned at the onset of autoignition and end-gas autoignition timing. 181
6.18 Comparison of charge preheating method on the evolution of compositional stratification ($2\sigma\varphi^*$) for the intake pressure sweep at same composition, mass fraction burned at the onset of autoignition and end-gas autoignition timing. 181
6.19 Comparison of charge preheating method on the evolution of mass averaged unburned gas temperature for the intake pressure sweep at same composition, mass fraction burned at the onset of autoignition and end-gas autoignition timing. 182
6.20 Boost pressure effect on mean unburned gas temperature (top), $2\sigma T_U$ (middle) and $2\sigma\varphi^*$ (bottom) for diabatic and adiabatic cases during the same intake boost sweep using intake manifold heating. 186
6.21 Boost pressure effect on heat release rates (top), burn rates (middle) and mass fractions burned (bottom) for diabatic and adiabatic cases using intake manifold heating. 187

LIST OF TABLES

Table

2.1 Test engine geometry and characteristics 30
2.2 Valvetrain system specifications 31
2.3 Key fuel properties of certified gasoline used in experimental studies 32
2.4 Emissions sampling specifications 32
2.5 Scatter in experimental measurements and heat release analysis results of interest over several hours of experimental testing. 22 datasets were recorded (300 cycles each) for a commonly visited SACI operating condition. The mean and standard deviation results for all cases are compared. 56
3.1 Experimental conditions for the engine speed study at $\phi' \approx 0.65$, constant intake manifold temperature, spark advance, fuel mass injected per cycle and end-gas autoignition timing. 94
4.1 Experimental conditions for the SACI boost pressure experiment at fuel-to-charge equivalence of 0.55 and constant intake temperature . 106
4.2 Experimental conditions for the SACI boost pressure experiment at fuel-to-charge equivalence of 0.55 and constant ratio of internal to external EGR 123
5.1 Experimental conditions for the ϕ' sweep at 1 bar intake pressure and constant spark advance. 135
5.2 Experimental conditions for the ϕ' sweep at constant intake pressure, mass fraction burned at the onset of autoignition and varying spark timing. 140
5.3 Experimental conditions for the ϕ' sweep at constant intake pressure and constant end-gas energy at autoignition. 147
5.4 Experimental conditions for the ϕ' sweep at constant load and constant spark advance. 149
5.5 Experimental conditions for the ϕ' sweep at constant load and constant mass fraction burned at the onset of autoignition. 153
6.1 Mesh geometry 163
6.2 Mesh thermal boundary conditions 163
6.3 Gasoline surrogate composition 163

6.4 Simulation input conditions for the boost sweep using residual gas heating at constant intake temperature, autoignition timing and composition. 182
6.5 Simulation inputs conditions for the boost sweep using intake manifold heating at similar residual gas fraction, autoignition timing and composition. 183
6.6 Simulation input conditions for the boost sweep with diabatic and adiabatic walls late in the compression stroke. 188

LIST OF ABBREVIATIONS

γ	Ratio of specific heats
$\delta\theta_{AI}$	Autoignition characteristic duration
η_{th}	Thermal efficiency
η_c	Combustion efficiency
η_f	Fuel conversion efficiency
ϕ	Fuel-to-air equivalence ratio
ϕ'	Fuel-to-charge equivalence ratio
φ^*	Non-product equivalence ratio
θ_{02}	Crank angle at 2% mass fraction burned
θ_{05}	Crank angle at 5% mass fraction burned
θ_{10}	Crank angle at 10% mass fraction burned
θ_{25}	Crank angle at 25% mass fraction burned
θ_{50}	Crank angle at 50% mass fraction burned
θ_{75}	Crank angle at 75% mass fraction burned
θ_{90}	Crank angle at 90% mass fraction burned
θ_{AI}	Crank angle at estimated end-gas autoignition timing
θ_{10-90}	Crank angle duration between 10% and 90% fuel mass fraction burned
θ_{25-75}	Crank angle duration between 25% and 75% fuel mass fraction burned
AI	Autoignition
AKI	Anti-knock index

aTDC	After top dead center of combustion
bTDC	Before top dead center of combustion
BDC	Bottom dead center
BMEP	Brake mean effective pressure
CAD	Crank angle degree
CA50	Crank angle at 50% mass fraction burned
COV	Coeffient of variation
c_p	Constant pressure specific heat capacity
c_v	Constant volume specific heat capacity
deg	Crank angle degree
DI	Direct injection
eEGR	External exhaust gas recirculated
EG	End-gas
EGR	Exhaust gas recirculation
EIVC	Early intake valve closing
EOC	End of combustion
EVC	Exhaust valve closing
EVO	Exhaust valve opening
GMEP	Gross indicated mean effective pressure
HCCI	Homegeneous charge compression ignition
HC	Hydrocarbon emissions
HRR	Heat release rate
iEGR	Internal exhaust gas recirculated
IVC	Intake valve opening
IVO	Intake valve closing
MFB	Mass fraction burned
MMCD	Multi-mode combustion diagram

MPRR	Maximum pressure rise rate of filtered pressure trace
N	Engine speed
NMEP	Net indicated mean effective pressure
NO_x	Nitrogen oxides emissions
NTC	Negative temperature coefficient
NVO	Negative valve overlap
OHC	Overhead camshaft
P	Cylinder pressure
$P_{\theta_{AI}}$	Cylinder pressure at autoignition onset
P_{FUEL}	Fuel injection pressure
P_{INT}	Intake pressure
$\dot{P}_{MAX}$	Maximum pressure rise rate of low-pass filtered pressure trace
PM	Particulate matter
PVO	Positive valve overlap
$Q_{EG,\,\theta_{AI}}$	Estimated end gas energy at onset of autoignition
Q_{HR}	Cumulative heat release rate
$\dot{Q}_{HT}$	Heat transfer rate loss
Q_{loss}	Cumulative heat transfer loss
RI	Ringing intensity
SACI	Spark assisted compression ignition
SA	Spark advance
SI	Spark ignition
S_L	Laminar burning velocity
SOC	Start of combustion
SOI	Start of injection
T_B	Burned gas temperature
TDC	Top dead center

T_{IVC}	Gas temperature at intake valve closing timing
T_U	Unburned gas temperature
$T_{U,\,\theta_{AI}}$	Estimated unburned gas temperature at autoignition onset
VVT	Variable valve timing
x_B	Mass fraction burned
x_r	Internal residual gas fraction
$x_{B,\,\theta_{AI}}$	Fuel mass fraction burned at onset of end-gas autoignition
X_{EGR}	EGR mole fraction
X_{SCP}	Mole fraction of stoichiometric combustion products
Y_{EGR}	EGR mass fraction

ABSTRACT

Low temperature combustion (LTC) engines that employ high levels of dilution have received increased research interest due to the demonstrated thermal efficiency improvements compared to the conventional Spark-Ignited (SI) engines. However, control of combustion phasing and heat release rate still remains a challenge, which limits the operating range as well as the transient operation of LTC engines. The work presented in this dissertation uses experimental and computational methods to investigate Spark Assisted Compression Ignition (SACI) combustion under boosted, stoichiometric conditions with high levels of exhaust gas recirculation in a negative valve overlap engine. Highly controlled experimental studies were performed to understand the impact of intake boosting and fuel-to-charge equivalence ratio (ϕ') on SACI burn rates, while maintaining constant combustion phasing near the optimal timing for work extraction. Previously unexplored conditions were targeted at intake pressures ranging from 80 kPa to 150 kPa and ϕ' ranging from 0.45 to 0.75, where LTC engines promise high thermodynamic efficiencies.

The use of intake boosting for load expansion and dilution extension achieved up to 10% gross thermal efficiency improvement, respectively, mainly due to reduced relative heat transfer losses and better mixture thermodynamic properties. For a given spark advance, higher pressure and/or higher ϕ' mixtures necessitated lower unburned gas temperatures (T_U) to match autoignition timing. While the overall effect of intake boost was minor on the initial flame burn rates, end-gas autoignition rates were found to approximately scale with intake pressure. Higher ϕ' mixtures exhibited faster initial flame burn rates but also led to a significant increase in end-gas autoignition rates. As a result, the high load limits shifted to lower ϕ' at higher intake pressures, creating a larger gap between the SI and SACI operating limits. Reducing the mass fraction

unburned at the onset of autoignition by advancing the spark timing and lowering T_U was, to some extent, effective at alleviating the excessive peak pressure rise rates. Under relatively high ϕ' conditions, cyclic heat release analysis results showed that the variability in autoignition timing is determined early in the cycle before any measurable pressure-based heat release. Combustion phasing retard was shown to be very effective at limiting the maximum pressure rise rates until the stability limit, primarily due to slower end-gas autoignition rates.

CFD modeling results showed good trendwise agreement with the experimental results, once autoignition timing and mass fraction burned at the onset of autoignition were matched. The pre-ignition reactivity stratification of the mixture at higher intake pressures was shown to be narrower, due to both lower thermal and compositional stratification, which explained the increase in end-gas burn rates observed experimentally. The boost pressure effect on SACI end-gas burn rates using intake manifold heating was trendwise similar to the results employing residual gas heating, albeit less pronounced. Pre-ignition thermal stratification was shown to be similar irrespective of charge preheating method, even though thermal stratification of the mixtures was very different early in the compression stroke. The effect of higher pressure on mean reactivity was offset by the lower mean temperature that was needed to match autoignition timing. Under the conditions investigated, the increase in the end-gas autoignition rates with intake boost was primarily due to the narrower thermal stratification, which was effected by reduced relative heat transfer losses late in the compression stroke.

CHAPTER I

Introduction

1.1 Spark Ignition Engines

The conventional spark ignition engine has long been the dominant engine found in light-duty powertrains in the U.S. primarily due to its high specific power, low production cost and cost effective after-treatment. In a conventional spark ignited engine, a spark initiates a flame kernel that transitions into a turbulent flame and propagates through a stoichiometric premixed charge until it extinguishes at the combustion chamber walls. Load control is achieved using a throttle valve, which regulates the air flow to the engine and ultimately the fuel flow, so that the mixture is maintained near stoichiometric conditions. The stoichiometric mixture ensures robust flame initiation and propagation and the main pollutant emissions (hydrocarbon (HC), carbon monoxide (CO) and nitrogen oxide (NO_x) emissions) are treated effectively by a three way catalyst [1]. The need to improve fuel efficiency has led to many advances in automotive technology such as variable valve timing and lift, exhaust gas recirculation (EGR) systems, more efficient turbo-machinery and direct fuel injection systems.

Recent efforts to improve the conventional SI engine efficiency has focused on downsizing, which implies that the displacement of the engine is reduced but specific power increases to maintain peak power rating. Higher specific power is achieved by increasing the intake charge density through the use of a compressor. Downsizing has demonstrated improvements in engine thermal efficiency by shifting the majority of the operating conditions to higher loads [2–4]. Thermal efficiency gains are achieved

primarily due to de-throttling, reduced relative friction and reduced relative heat loss from higher load operation. However, efficiency gains due to high load operation in downsized engines is frequently constrained by the increased propensity of the fuel to autoignite under those conditions, which leads to retarded combustion phasing and/or fuel enrichment and hence poor thermal efficiency. The peak efficiency of the spark ignition engine remains below the theoretical maximum, while engine operation is frequently away from the peak efficiency regions of the engine operating map.

Advanced combustion modes such as homogeneous charge compression ignition (HCCI) [5], spark assisted compression ignition (SACI) [6] and reactivity controlled compression ignition (RCCI) [7] have received increased research interest the past decade or two. These are dilute, low temperature combustion modes that have demonstrated high thermal efficiencies at low to medium load conditions where the efficiency of the conventional spark ignited engine suffers mostly. Figure 1.1 displays the estimated U.S. energy consumption in 2017 from Lawrence Livermore National Laboratory and the Department of Energy using data from DOE/EIA[1] monthly energy review. The total energy consumed is estimated at 97.7 quadrillion BTUs. The transportation industry uses approximately 29% of the total energy consumed and more than 90% of that energy comes from petroleum sources. On average 21% of the energy consumed becomes useful work while the remaining is rejected as heat. Improvement of the fuel conversion efficiency of the internal combustion engine can thus achieve a great impact in reduction of petroleum use and greenhouse gas (GHG) emissions.

While electrification is expected to capture approximately 40% of the powertrain market share by 2050, projections suggest that more than 80% of new vehicle market share will include an internal combustion engine ICE [8]. Improving the fuel consumption of mainstream technology vehicles is therefore considered a significant near-term opportunity for reducing fuel use and GHG emissions. Electrified powertrains also allow for synergies between advanced combustion engines due to the potential for a smaller engine operating map and reduced transient operation.

[1]DOE/EIA stands for Department of Energy/Energy Information Administration.

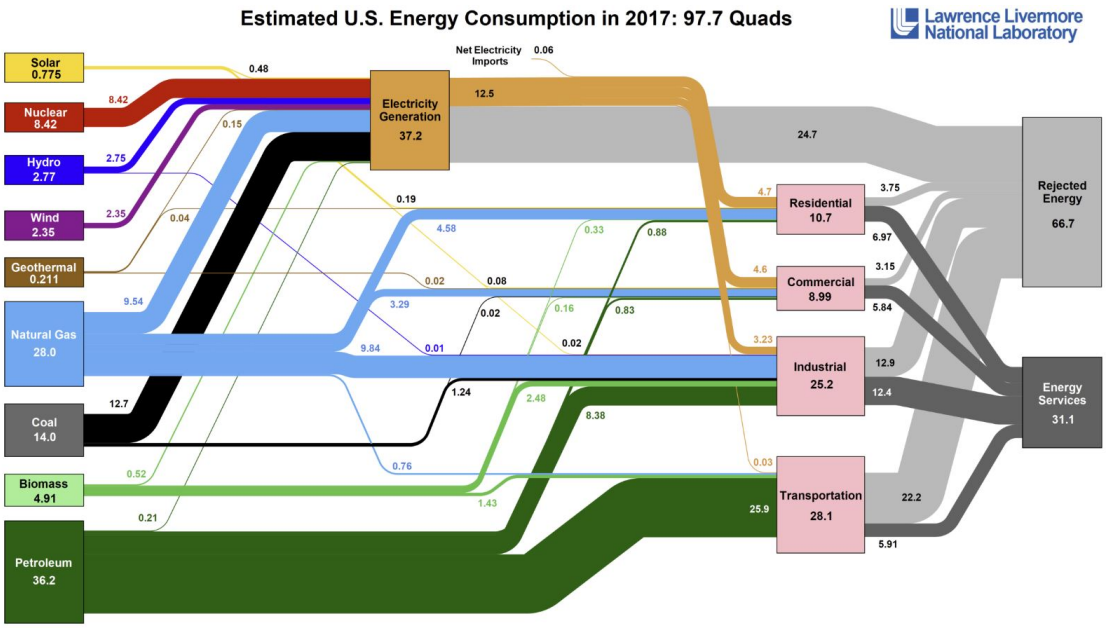

Figure 1.1: Estimated U.S. Energy Consumption in 2017 from Lawrence Livermore National Laboratory and the Department of Energy using data from DOE/EIA monthly energy review [9].

1.2 Homogeneous Charge Compression Ignition Combustion

Homogeneous charge compression ignition (HCCI) is a low temperature combustion (LTC) mode, in which an ultra dilute premixed mixture is compressed until it autoignites, resembling an idealized constant volume combustion event. Various names have been used in the literature for describing this combustion concept, such as ATAC (Active Thermo-Atmosphere Combustion) [10, 11] CIHC (Compression Ignition Homogeneous Charge combustion) [12] and CAI (Controlled Auto-Ignition) [13]. HCCI was initially experimentally studied in 2-stroke engines [10,11] due to its ability to achieve exceptionally low cycle-to-cycle variability under low load, lean conditions. Burn rates are much faster than those seen in conventional spark ignition engines, with 10 - 90% mass fraction burned durations (θ_{10-90}) often less than 10 crank angle degrees [14]. Multiple spectroscopic and imaging studies [10, 11, 15, 16] have shown that multi-point ignition occurs in HCCI and it is widely accepted that the combustion process is controlled by chemical kinetics with little effect of turbulence. The autoignition process in HCCI combustion occurs at intermediate temperatures be-

tween 850 - 1200 K and is dominated by the decomposition of H_2O_2 into OH [17]. Low temperature reactions, if any, advance the time at which H_2O_2 decomposition occurs.

A notable chemiluminescence imaging study by Dec et al. [18] showed that HCCI combustion was not really homogeneous but displayed a naturally occurring stratification due to heat transfer during compression, combined with turbulent transport. The autoignition process occurred in a staggered fashion at different sites in the combustion chamber, as illustrated schematically in Figure 1.2. This behavior was attributed to the thermal stratification throughout the bulk gas and boundary layer, which causes the combustion to occur as a sequential autoignition from the hotter to cooler regions, thus reducing the peak heat release rate.

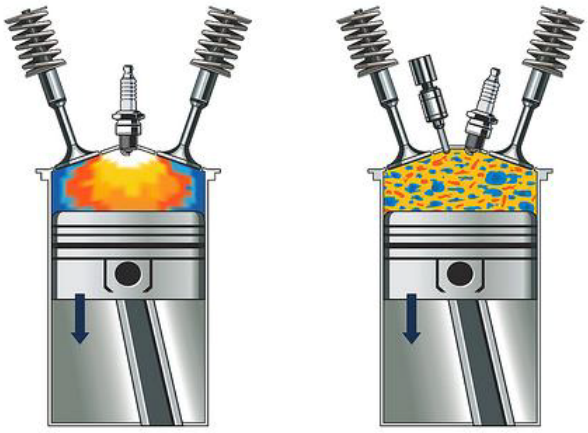

Figure 1.2: Spark ignited combustion (left) and HCCI combustion (right)

HCCI has received increased research interest because of significant efficiency and NO_x emissions improvements observed under low loads compared to conventional SI engines [19]. Benefits of HCCI combustion are realized due to several reasons. High gross thermal efficiency is achieved due to higher compression ratio, high levels of dilution and short burn durations compared to typical SI engines. High compression ratio is desired in HCCI engines to promote autoignition of the mixture. High levels of dilution lead to improved thermodynamic properties of the mixture (i.e. high ratio of specific heats) partly because of favorable compositional changes and partly because of lower expansion temperatures. Significant net efficiency improvements are

observed in HCCI engines due to unthrottled operation, which means that pumping work is reduced compared to SI engines, especially at low loads. In addition, low combustion temperatures result in ultra-low nitrogen oxide (NO_x) emissions. However, the maximum load limit of unthrottled HCCI engine operation is restricted to low load ($\approx$ 3 - 4 bar NMEP) due to the convergence of the ringing intensity and stability limits [20]. High ringing intensity is characterized by excessive pressure rise rates while unstable combustion features large variability in the work output due to partially burning cycles and/or misfires. The allowable HCCI combustion phasing range, bounded by the ringing and stability limits, is much smaller than that of conventional SI combustion. As load increases, the combustion phasing range becomes narrower primarily due to the need to retard combustion phasing to alleviate the excessive pressure rise rates [20].

Sjöberg and Dec [21,22] investigated the low load limit observed in HCCI combustion via experimental and modeling studies. It was shown that as fueling is reduced to fuel-to-air equivalence ratios (ϕ) below 0.2, CO emissions increase substantially, resulting in a significant drop in combustion efficiency from 94% to less than 55%. It was concluded that peak combustion temperatures must be at least 1500 K for the CO-to-CO_2 reactions to go to completion before the combustion is quenched by piston expansion.

HCCI combustion lacks direct control of combustion phasing as autoignition timing is dictated by chemical kinetics [18]. Autoignition phasing for HCCI is determined primarily by the temperature near top dead center TDC [23]. To ensure proper ignition, the mixture temperature has to be adjusted such that the ignition delay time at TDC conditions is equivalent to approximately 10 crank angle degrees, independent of engine speed [23]. Therefore, fine control of combustion timing necessitates fine control of temperature at TDC. In a piston engine that means that the temperature of the mixture has to be finely adjusted at the intake valve closing timing, so that by the end of compression the mixture ignition delay times are short enough to ensure complete combustion near optimal timing. Researchers have tried various strategies to address the HCCI challenges using variable compression ratio [24], fuel stratifica-

tion [25], boosting [26] and spark assistance [27]. This research study focuses on the combination of the last two strategies, namely spark assistance and boosting.

1.3 Spark Assisted Compression Ignition Combustion

1.3.1 Combustion Process

Spark assisted compression ignition (SACI) or spark assisted homogeneous charge compression ignition (SA-HCCI) combustion is a premixed, low temperature combustion (LTC) mode that can offer efficiency improvements compared to conventional SI combustion. In SACI combustion, a spark initiates a propagating flame in a premixed, high temperature, dilute mixture. As the flame front propagates and releases chemical energy, it introduces additional compression heating to the unburned portion of the charge and drives it to the point of autoignition.

Experimental investigations using optical diagnostics have supported the view that SACI combustion originates as a reaction front from the spark kernel, which propagates outwards in the combustion chamber and is followed by autoignition of the end-gas [28–32]. Average propagation rates for the reaction fronts were found to be around 2 - 10 m/s at the last 20 CAD of the compression stroke depending on dilution level and timing [29], while the autoignition event has been characterized by multiple ignition sites at the outer rim of the combustion chamber and rapid combustion rates [28, 29, 33]. A fraction of the fuel is initially consumed by the flame followed by the autoignition of the remaining charge, which is typically the major source of heat release. There is an orderly transition from deflagrative to autoignition heat release, which is depicted as a change in the slope in the heat release rate graph, as seen in Figure 1.3. Premixed laminar flame simulation studies have shown that laminar flames can exist in mixtures with high exhaust gas recirculation (EGR) dilution levels provided that unburned gas temperatures are elevated and burned gas temperatures exceed 1450 K [82]. Therefore, high unburned temperatures are essential for flame propagation in SACI combustion as well as for promoting autoignition of the end-gas. The unburned gas temperature at top dead center has to be finely adjusted to ensure

complete combustion near the optimal timing, similarly to HCCI operation.

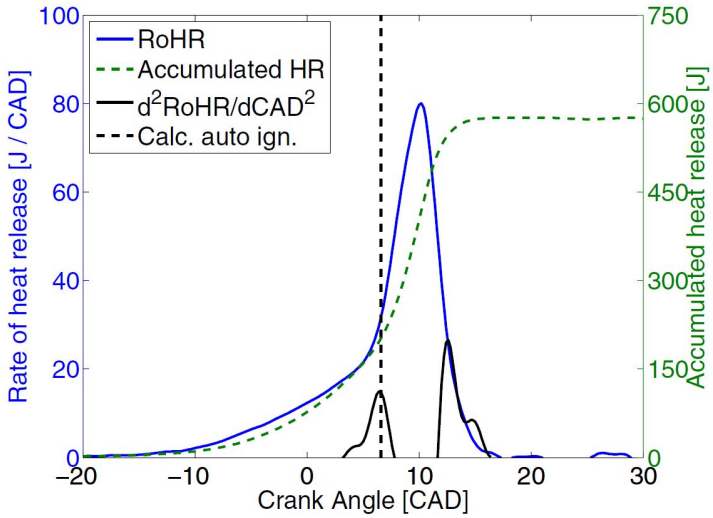

Figure 1.3: Typical SACI heat release rate trace highlighting the inflection point at the onset of autoignition [29].

Reuss et al. [32] divided the SACI combustion process into four distinct phases using cycle-resolved combustion imaging, pressure based heat release and spark voltage/current measurements for lean, premixed, stratified mixtures. The four phases of SACI included the spark discharge, the early kernel growth (EKG), the flame propagation and the compression ignition phase, as shown in Figure 1.4. The spark discharge phase was defined as the period starting from the breakdown voltage until the time where the spark discharge current returns to zero. The EKG was defined as the period between the end of spark discharge, where a small reaction kernel exists but no heat release can be detected using the cylinder pressure, until the maximum of d^2A_{flm}/dCA^2, where A_{flm} is the flame area measured through optical observations and CA is the crank angle timing. The flame propagation period was defined from the end of the EKG period until the inflection point in the pressure-based heat release curve, which was regarded as the onset of compression ignition. The reasoning behind the selection of the onset of compression ignition was that autoignition heat release rates occur over chemical reaction timescales and are faster than heat release rates of turbulent flame propagation. This metric for the onset of end-gas autoignition agreed with the work of Persson et al. [29] who used high speed chemiluminescence imaging

in a SACI optical engine. The authors noted that the actual source of heat release in the flame propagation phase may be a combination of both compression ignition and turbulent flame propagation, however it was difficult to distinguish between the two from measurements. The last period was defined as compression ignition, where the end-gas autoignites due to compression heating from the advancing flame.

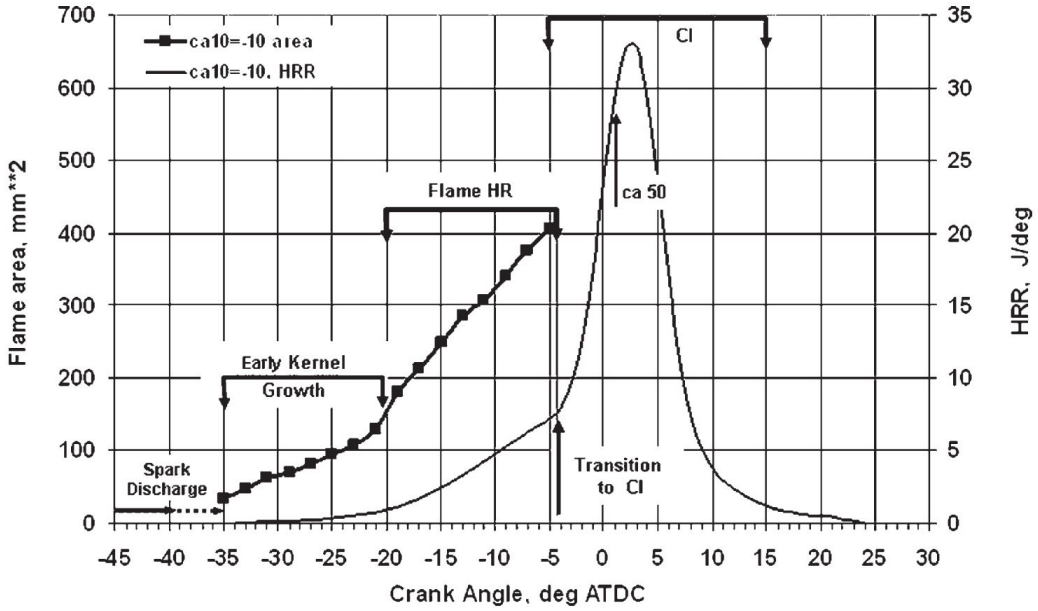

Figure 1.4: Definition of the four SACI combustion periods using the imaged flame area growth (solid line with square data points) and heat release rate (solid line) for ensemble-averaged cycles by Reuss et al. [32].

1.3.2 Multi-Mode Combustion Diagram

Lavoie et al. [34] presented SI, SACI and HCCI combustion regimes on a multi-mode combustion diagram (MMCD) in terms of unburned (T_U) and burned (T_B) gas temperatures near TDC. The burned gas temperature was calculated as the constant pressure adiabatic temperature at each condition. Figure 1.5 shows the multi-mode combustion diagram at a TDC pressure of 40 bar, which was considered representative of unthrottled, mid-load SACI combustion for a compression ratio engine around 12.4.

The combustion regimes are delineated based on the limits for ignition, flame propagation, knock and NO_x. The NO_x limits have been defined for air and residual

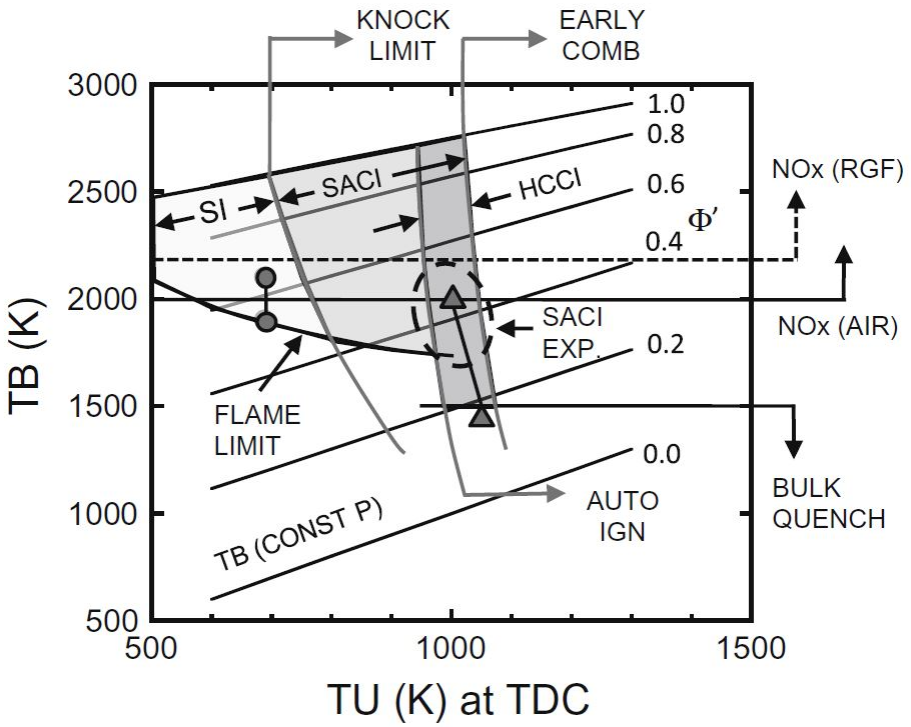

Figure 1.5: Multi-mode combustion diagram showing SI, SACI and HCCI combustion regimes in terms of TDC unburned temperature T_U and burned gas temperature T_B for iso-octane in air. Combustion regimes are delineated based on limits for ignition, knock, flame propagation, bulk quenching and NO_x limit [34].

gas dilution with an emissions index of 1 g/kg fuel. The authors make use of the fuel-to-charge equivalence ratio ϕ' term, which is defined in Equation 1.1 below.

$$\phi' = \frac{m_f/(m_a + m_{EGR})}{(m_f/m_a)_{ST}} = \frac{\phi(1 - Y_{EGR})}{1 + Y_{EGR} \cdot \phi \cdot (m_f/m_a)_{ST}} \approx \phi\,(1 - Y_{EGR}) \tag{1.1}$$

where m_f, m_a and m_{egr} are mass of fuel, air and EGR respectively, ϕ is the equivalence ratio, Y_{EGR} is the total exhaust gas recirculation mass fraction and subscript ST denotes stoichiometric conditions. The approximation holds as the stoichiometric fuel to air ratio for representative gasoline fuels is very small (≈ 0.069), so the denominator is very close to 1. Fuel-to-charge equivalence ratio, ϕ', reflects the specific energy content of the charge and thus is directly related to load and burned gas temperature, as seen from the oblique lines at constant ϕ' on the diagram. Φ'

can be used conveniently to describe engine conditions where the mixture has been diluted by a combination of air, internal EGR and external EGR. The authors [34] have tried to map points from available experimental data in the SI regime (circles), HCCI regime (triangles) and SACI (dashed oval). While the exact boundaries of the combustion regimes have not be validated extensively at different pressures, the multi-mode combustion diagram provides good insight on the potential limits for each combustion mode based on unburned and burned gas temperature at TDC. HCCI combustion requires unburned TDC temperatures in proximity of 1050 K, so that ignition delay times are short enough to ensure complete combustion near optimal combustion phasing. It is suggested that SACI would require unburned TDC temperatures slightly lower than that of HCCI as part of the temperature increase required for autoignition is achieved through compression heating from the propagating flame. However, maximum dilution levels for SACI combustion are believed to be limited to $\phi' \approx 0.3$ - 0.4 due to the inability to sustain slow and weak flames in a turbulent engine environment. The ϕ' metric used in this work is equivalent to the charge mass based equivalence ratio, ϕ_m, used by other researchers on highly dilute advanced combustion studies [35–38].

1.3.3 Benefits and Key Challenges

The engine cycle efficiency can usually be improved with increased expansion ratio and the use of a higher specific heat ratio (γ) gas mixture, however, the maximum efficiency achievable for a given working fluid may vary significantly from the ideal Otto cycle prediction due to the competing effects typically observed in an internal combustion engine [39–41]. A modeling study by Lavoie et al. [39] analytically explored the fundamental thermodynamics of operation in highly dilute and high pressure gasoline combustion regimes under realistic engine operation. A simple 1-D thermodynamic model was used in order to identify the optimal thermodynamic conditions independent of combustion constraints. Gross thermodynamic efficiency simulation results were compared with relevant experimental data and showed good agreement. It was shown in that study that increasing dilution levels using air or

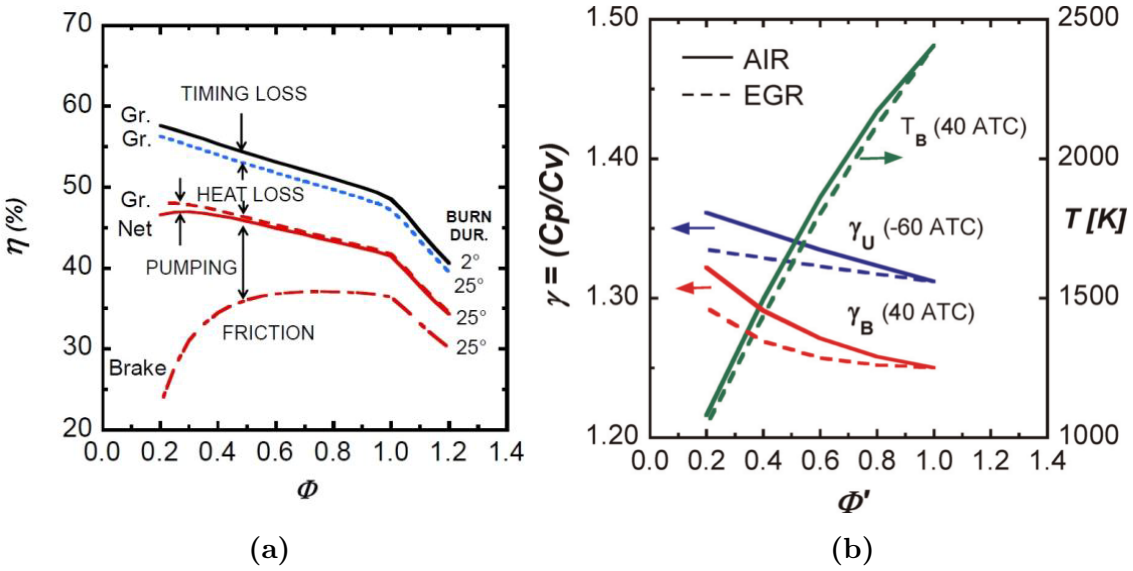

Figure 1.6: Effect of diluent (air or EGR) as a function of fuel-to-charge ratio, ϕ' (left). Diluent effect on unburned and burned gas specific heat ratios γ_U and γ_B, Burned gas temperature T_B as a function of ϕ' (right) [39].

EGR offers higher gross fuel conversion efficiency due to higher ratio of specific heats of the mixture, as seen in Figure 1.6.

The higher ratio of specific heats of the mixture comes partly from favorable compositional changes and partly from lower temperature due to dilution. Charge dilution with air was shown to be slightly more beneficial than dilution with EGR due to the higher ratio of specific heats of diatomic molecules found in air compared to triatomic molecules found in EGR. Combustion phasing, defined as the crank angle at 50% burn (θ_{50}), was found to be optimal between 5 - 10° aTDC as a result of the tradeoff between high heat transfer losses for early combustion and lower expansion work for late combustion. Deviations of more than 5 crank angle degrees (CAD) from optimal combustion phasing had detrimental effect on gross indicated efficiency for the reasons aforementioned. Burn duration, defined as the combustion duration from 10 - 90% fuel mass fraction burned (θ_{10-90}), was found to have minimal effect on efficiency up to 20 CAD.

SACI combustion has been shown to be effective at fuel-to-charge equivalence ratios between 0.4 and 0.7 [42] and therefore takes advantage of the thermal efficiency benefits due to dilution explained above. In addition, θ_{10-90} is shorter than

20 CAD and generally shorter than those seen in conventional spark ignition combustion, which can offer additional gross thermal efficiency improvements. During naturally aspirated SACI operation the engine is usually run unthrottled and load control is achieved by regulating the level of dilution. Unthrottled operation means that pumping work is reduced compared to SI combustion especially at lower loads and hence thermal efficiency is improved further. An additional benefit of SACI combustion compared to a low temperature combustion mode such as HCCI is that spark timing can be used as a means to control combustion phasing.

SACI combustion is also attractive because it can be used at mixture dilution levels where neither HCCI combustion nor SI combustion is typically effective. For dilute SI combustion at fuel-to-charge equivalence ratios below 0.65, flames are found to be too slow and weak to ensure complete combustion in a turbulent engine environment [43]. On the other hand, HCCI combustion at fuel-to-charge equivalence ratios higher than 0.4 is typically avoided because it results in excessive pressure rise rates [42]. As a result, SACI combustion can bridge the gap between the dilution level of HCCI and SI combustion which is desirable for engine efficiency and for potential multimode combustion engine operation. This potential is highlighted in Figure 1.7, which shows optimal brake thermal efficiencies for naturally aspirated engines. It can be seen that optimal brake thermal efficiencies can be achieved by employing air or EGR dilution across the load range. The authors [39] have identified a load region as advanced combustion where neither SI combustion nor HCCI combustion are currently effective. This load region corresponds to fuel-to charge equivalence ratios, ϕ' between 0.4 and 0.65. Experimental and simulation studies have shown that such dilutions levels are appropriate for SACI combustion and therefore are of great research interest.

Nevertheless, SACI combustion is challenging to control because stable combustion without excessive pressure rise rates relies on fine control of combustion phasing and heat release rate. Precise control of unburned gas temperature is needed to ensure combustion is initiated close to TDC. If the unburned temperature near TDC is too low then autoignition of the end-gas may be unsuccessful due to very long ignition delays. On the other hand, very high unburned temperatures will advance combustion

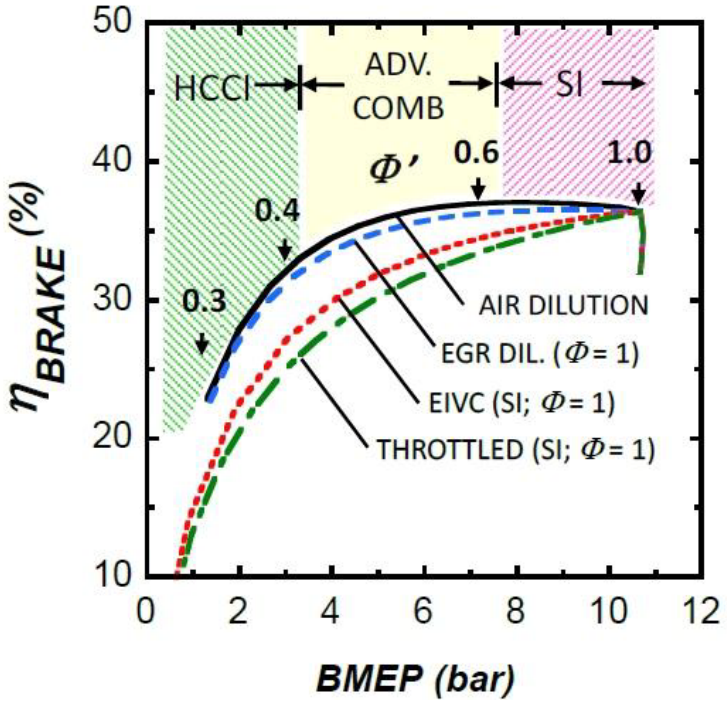

Figure 1.7: Potential for brake efficiency gains for naturally aspirated engines depending on combustion regime: HCCI, advanced combustion and SI [39].

phasing and may lead to excessive pressure rise rates. Furthermore, flame initiation and propagation is strongly influenced by the unburned temperatures and dilution levels at spark timing, which means that any changes in those parameters will also affect the compression heating effect from the flame to the end-gas and ultimately the autoignition timing.

1.3.4 Charge Preparation for SACI Combustion in a Piston Engine

SACI combustion typically requires a dilute, high temperature charge near TDC. For direct injection engines, a premixed charge is usually achieved by injecting early in the intake stroke to provide enough time for fuel, air and EGR to mix. SACI combustion at lower dilution levels results in elevated burned gas temperatures, which can lead to high NO_x formation when the engine is operated lean. For that reason researchers have usually ran SACI at stoichiometric conditions by diluting the mixture with recirculated exhaust gas [6, 42, 44].

Exhaust gas recompression through negative valve overlap (NVO) has been most

commonly used for the charge preheating needed to achieve SACI in a moderately high compression ratio (≈ 11:1). In an NVO strategy the exhaust valve closes well before gas exchange TDC, therefore trapping large amounts of residual gas. The residual is recompressed and then re-expanded during the initial portion of the intake stroke before the intake valve opens for the induction of fresh charge. An example pressure trace and valve lift profile around gas exchange TDC is shown in Figure 1.8.

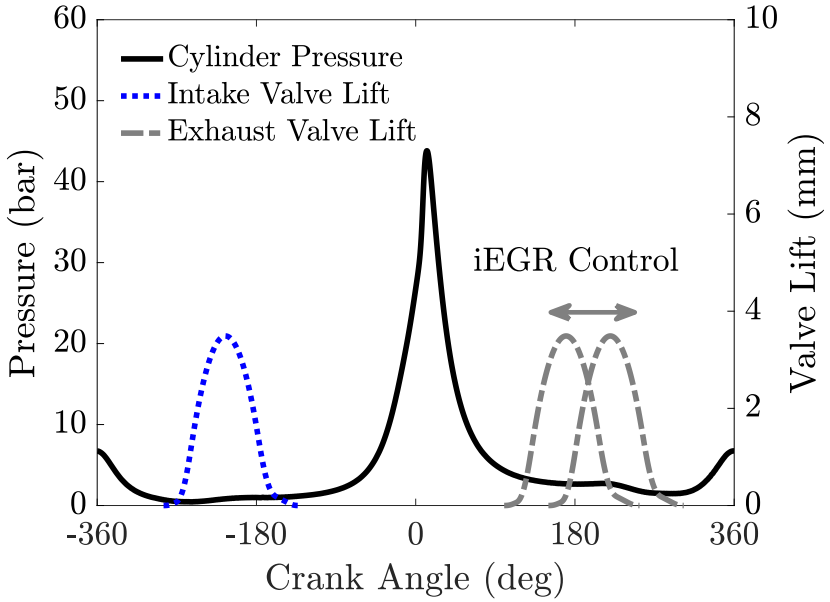

Figure 1.8: Typical cylinder pressure trace and valve profiles for a negative valve overlap SACI engine.

Exhaust gas rebreathing using positive valve overlap (PVO) is another strategy that has been recently employed by several researchers to achieve SACI combustion [45, 46]. High unburned gas temperatures at TDC are attained by rebreathing exhaust gas either through the intake port using an early intake valve opening strategy, or through the exhaust port using a late exhaust valve opening, or using a combination of the two strategies. For a naturally aspirated engine, the intake valve is typically opened before TDC during the exhaust stroke and exhaust gases are displaced into the intake manifold. These residual gases are subsequently re-inducted into the cylinder during the intake stroke. Exhaust gases from the exhaust manifold can also be re-inducted into the cylinder through late exhaust valve closing during

the intake stroke. Modern spark-ignited engines employing variable valve timing can enable unconventional valve strategies such as the ones described earlier, which are preferred over air preheating due to the improved transient control of the temperature. 1-D engine modeling studies [47,48] suggested that the use of a PVO valving strategy would be more beneficial in terms of net thermal efficiency compared to NVO, due in part to lower pumping losses. While PVO was capable of trapping adequate residual content at low-medium loads, intake manifold temperatures up to 160°C were needed to ensure end-gas autoignition near optimal timing using a 11.25:1 compression ratio engine.

End of compression temperatures near 1050 K needed for end-gas autoignition can be also achieved using a very high compression ratio (≈16 or higher) without the need for charge preheating [38]. Intake boosting can also contribute to reduced charge preheating levels but the effect of pressure on charge reactivity is typically much less pronounced compared to that of temperature under high temperature chemistry conditions [49]. The benefit of a very high compression ratio engine is that IVC temperature is lower, which enables higher volumetric efficiency and maximum load attainable at a given intake pressure. However, when the mixture becomes very reactive at high loads (i.e. high ϕ', high P_{INT}), reducing the reactivity of the charge to maintain optimal combustion phasing may be challenging due to the inability to cool the intake charge below ambient temperature. In that case, the use of EGR or lower effective compression ratio through early/late IVC timing could be effective, however, at the expense of volumetric efficiency.

1.4 Benefits of Boosting

SACI combustion can benefit from boosting through thermodynamic efficiency gains and mechanical efficiency gains. Boosting allows the dilution levels of the mixture to be maintained as fueling rate is increased and therefore maintain the thermodynamic benefits of dilute operation. In addition, boosting can increase the engine's specific power, which is commonly described by the brake mean effective pressure (BMEP). Increasing the load of an engine by increasing the mean effective pressure can also have a positive effect on both the thermal efficiency and mechanical efficiency. Everything else being equal, gross thermal efficiency gains can be achieved at higher boost and load because the relative importance of heat transfer decreases as the mean effective pressure is increased. A widely used expression for the spatially averaged heat-transfer coefficient was proposed by Woschni [50], which is based on the similarity theory for steady-state convective heat transfer. Woschni found good agreement between experimental measurements and a dimensionless equation which relates the Nusselt number to Reynolds number in the following form:

$$Nu = 0.035\ Re^{0.8} \tag{1.2}$$

If density, viscosity and conductivity are expressed as functions of pressure and temperature, as discussed by Woschni [50], the global heat transfer coefficient, h_c, takes the form shown in Equation 1.3 below.

$$h_c = 3.26\ B^{-0.2}\ P^{0.8}\ T^{-0.55}\ w^{0.8} \tag{1.3}$$

where B [m] is the cylinder bore, P [kPa] is cylinder pressure, T [K] is temperature and w [m/s] is average cylinder gas velocity. It can be seen from the Woschni heat transfer coefficient correlation that speed and load have the greatest effect on heat loss through terms P and w, and also that heat transfer increases linearly with pressure at an exponent of 0.8. Therefore, an increase in load and mean effective pressure at a given engine speed is expected to result in a reduced relative increase in heat loss,

as shown in Figure 1.9.

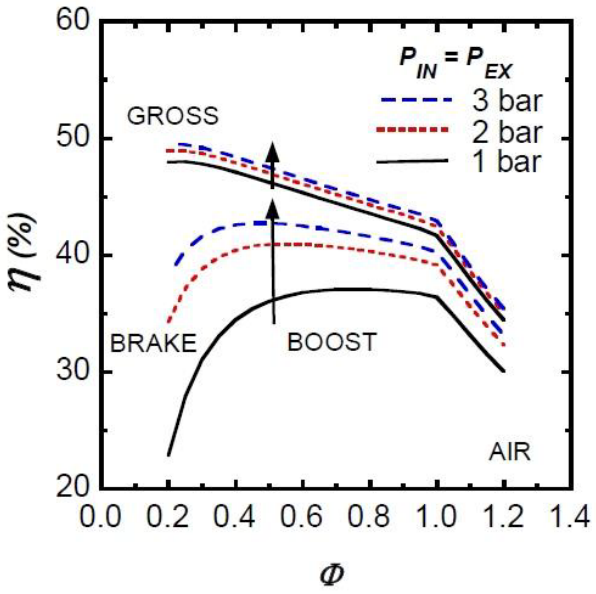

Figure 1.9: Thermodynamic simulation results showing efficiency trends with air dilution and intake boost. At each intake boost an optimum efficiency value occurs due to the competition between dilution benefits, frictional benefits and heat transfer benefits. [39].

Figure 1.10 shows key efficiency losses as a function of equivalence ratio for a naturally aspirated engine running at 2400 RPM with intake and exhaust pressures being equal. As load is decreased by decreasing the equivalence ratio, the efficiency penalty due to friction becomes relatively more important and outweighs the efficiency benefits from dilute or lean combustion on an indicated basis.

This can be explained by the fact that friction in internal combustion engines has been observed to scale primarily with mean piston speed and secondarily with peak pressure, as shown in the modified Chen-Flynn [51,52] friction correlation in Equation 1.4 below.

$$FMEP = 0.4 + 0.005\ P_{max} + 0.09\ U_P \tag{1.4}$$

where $FMEP$ is the friction mean effective pressure, P_{max} is cylinder maximum pressure and U_P is the mean piston speed. It can be seen from the Chen-Flynn correlation that as load is decreased at lower equivalence ratios friction does not

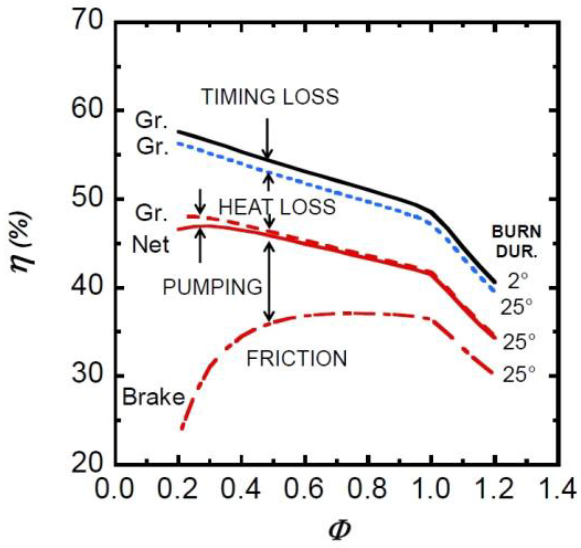

Figure 1.10: Key efficiency losses as a function of equivalence ratio [39].

decrease proportionally and introduces a larger penalty on brake thermal efficiency. Therefore, operating a downsized engine at higher load conditions using boosting can be beneficial for brake thermal efficiency. It is worth noting that the efficiency penalty due to pumping work shown in Figure 1.10 is minimal because it reflects the pumping losses of a naturally aspirated engine where intake and exhaust pressures are equal and load is controlled through equivalence ratio. However, the pumping work penalty on efficiency is significant for a conventional throttled SI engine running stoichiometric at lower loads, as shown earlier in Figure 1.7. Figure 1.7 compared brake efficiency values as a function of load for throttled stoichiometric SI operation, early intake valve closing stoichiometric operation and unthrottled diluted engine operation using air or EGR. Air or EGR dilution cases demonstrate improvements over throttled SI and EIVC partly due to lower pumping work.

1.5 Previous Work on SACI

Weinrotter et al. [53] investigated experimentally SACI combustion in an optically accessible engine using 80/20 iso-octane/n-heptane mixtures at λ values ranging between 2.8 and 3.2 using intake manifold heating with no external EGR and minimal internal residual gas. No clear difference was observed on the pressure based heat release curves between pure HCCI and spark assisted HCCI, however the optical diagnostics showed that after ignition timing, a flame structure developed and propagated similarly to conventional SI engines.

In the same year, Urushihara et al. [54] published SACI experimental studies using a combination of a uniformly distributed lean mixture and a late injection to create a stratified charge around the spark plug. Heat release analysis results showed a multimode heat release rate curve, where characteristics of SI combustion seemed to trigger HCCI combustion. The SACI combustion concept reduced the mixture temperature needed at the onset of compression, thereby expanding the HCCI low load limit. The maximum IMEP limit obtained with SACI was also improved compared to HCCI combustion due to lower pressure rise rates observed.

Persson et al. [29] investigated the early flame development in SACI combustion using high speed chemiluminescence imaging in an NVO engine. It was shown that the use of spark timing can be used to phase combustion timing, even though the majority of the heat release was observed during autoignition. Flame expansion speeds between 2 - 10 m/s were observed for cases conditions with NVO ranging between 40 and 200 CAD. However, the exact mixture composition was not reported. Under the conditions investigated, an earlier spark advance was shown to advance the autoignition timing to some extent and also to compensate for cases with slower flame propagation.

Zigler et al. [55] experimentally investigated the impact of spark assist on lean SACI combustion (ϕ = 0.38 - 0.62) using an optically-accessible research engine. It was shown that the use of spark assist (10 - 90° bTDC) led to the formation of reaction fronts at all conditions that propagated outward from the spark plug at average speeds

between 1.9 and 4.3 m/s. It was concluded that the effects of spark assist were due to the compression heating of the end-gas from the propagating reaction fronts, which led to more consistent autoignition timing under the conditions investigated.

A number of researchers have investigated SACI combustion experimentally with aim to extend the high load limit of HCCI combustion using spark assistance. Manofsky et al. [56] managed to extend the engine operating limit up to 7.5 bar NMEP using naturally aspirated SACI. A combination of internal and external EGR rate was used to achieve the required dilution level and unburned temperature of the mixture for stable SACI combustion. It was shown that as load was increased, a larger fraction of the charge was consumed by the propagating flame and less by autoignition, which satisfied the ringing limit. Their findings showed that the initial slow heat release due to the charge consumed by the flame, lengthened the total burn duration and led to lower peak heat release rates during the autoignition phase of the combustion process. These results agreed with findings from a similar study by Yun et al [46]. The high load limit was reached at $\phi' \approx 0.7$ because intense end-gas autoignition resembling SI knocking combustion was observed, even though ringing intensity value was well below the ringing limit of 5 MW/m^2 that was used. The ensemble average of the cylinder pressure data was used for performing the heat release analysis.

Szybist et al. [6] performed a similar stoichiometric SACI load expansion study using a hydraulic valve actuation system, which was used to trap significant levels of internal residual using NVO. End of compression temperatures and hence combustion phasing was controlled using a combination of residual gas fraction and IVC timing to alter the effective compression ratio. Characteristics of both spark-ignited combustion and HCCI were observed from the pressure based heat release analysis, which showed a distinctive spark ignited phase of combustion, followed by a much more rapid HCCI combustion phase. At higher loads, a larger portion of the heat release took place at the spark ignited portion of the cycle and an increase in NO_x emission was also observed compared to HCCI combustion. The increase in NO_x emission at higher load was attributed to the reduction in EGR dilution associated with higher loads and its effect on the in-cylinder temperatures. The SACI operating strategy did not

always provide an efficiency advantage compared to SI combustion; a decrease was observed at the highest speed and at loads above 500 kPa NMEP.

A later study from the same group [44] investigated experimentally the effects of fuel characteristics on stoichiometric SACI combustion for 50% volume blend of isobutanol and gasoline (IB50), and an 85% volume blend of ethanol and gasoline (E85) on a single cylinder metal engine. It was shown that the high load limit reached at unthrottled conditions was around 600 - 700 kPa. The cyclic heat release analysis RI values were much higher than the ensemble average pressure trace numbers, hence the actual load limits were found to be lower than their previous study with similar fuel. It was shown that NO_x, CO and HC emission were reduced with oxygenated fuels.

Martz [57] formulated and implemented a detailed model capable of capturing SI, SACI and HCCI combustion modes, which provided trendwise agreement with cylinder pressure and imaging data from an optical engine. The simulated reaction fronts were within the flamelet regime during the deflagration portion of SACI, even though they were ultra dilute ($\phi = 0.45$). Martz et al. [58] studied the propagation of a laminar reaction front during end-gas autoignition using transient, one dimensional premixed laminar reaction front simulations. While burning velocity increased significantly in the transition from deflagrative to chemically dominated combustion, it was shown that the reaction front contributed minimally to end-gas consumption once end-gas temperatures exceeded 1100 K.

Yun et al. [46] experimentally investigated the effects of injection timing and split injection on stoichiometric SACI combustion using an exhaust recompression strategy. As injection timing was retarded further away from recompression TDC, a delay in combustion phasing was observed, which was linked to the greater charge cooling effect and the associated increase in external EGR rates for the later injection timings. A tradeoff between ringing intensity and combustion stability was demonstrated when a split injection strategy was used. The delay of the second injection timing closer to combustion TDC led to lower ringing intensity at the expense of reduced net specific fuel consumption due to higher CO emissions.

A load extension study by the same group the following year [59] compared NVO and PVO strategies for naturally aspirated, stoichiometric SACI in an engine with a fully flexible valvetrain operating at 2000 RPM with NMEP ranging from approximately 6 to nearly 10 bar. The NVO strategy employed peak intake/exhaust valve lifts of 5/6 mm and durations of 145/160 crank angle degrees, respectively. PVO durations of approximately 60 to 100 crank angle degrees were used with peak valve lifts of 10 mm and 240 CAD durations. The amount of internal exhaust gas recirculation (iEGR) varied with load; PVO iEGR ranged from 5 to 10% while NVO iEGR varied from 5 to 25%. External EGR (eEGR) was used in conjunction with the iEGR to maintain stoichiometric equivalence ratios for all operating conditions. Because of the lower intake valve closing temperatures (T_{IVC}) associated with the reduced level of iEGR for PVO, more deflagrative heat release occurred prior to end-gas auto-ignition, which helped to limit ringing intensity. In turn, the combustion phasing (θ_{50}) could be set to a more optimal value. At high load, significantly lower pumping mean effective pressures (PMEP) resulted with the PVO valve events. The combination of lower PMEP and more optimal combustion phasing resulted in net indicated fuel consumption improvements of 3 to 7% for the PVO cases. However, details on the fuel injection strategy were not discussed in the study and EGR dilution levels at high load were in the order of 15%, where dilute SI combustion should be also effective.

Olesky et al. [42] demonstrated experimentally the ability to independently control combustion phasing and heat release rate in SACI combustion. Based on their findings, in order to control SACI combustion phasing and heat release rate, one has to control both unburned temperature and spark timing. Unburned temperature was controlled by varying the ratio of internal to external exhaust gas recirculation (EGR). Combustion phasing could be held constant by lowering the unburned temperature of the mixture at the intake valve closing (IVC) timing while advancing spark timing and vice versa. As a result, the fraction of the charge consumed by flame propagation was increased from 18% to 34% and led to an increase in burn duration and ultimately a significant decrease in peak heat release rates and ringing intensity. An inverse correlation between fraction of flame based heat release and peak heat release

rate was demonstrated, as seen in Figure 1.11. The autoignition temperatures were consistent at around 1040 K despite the changes in spark timing and heat release rates. It was concluded that for colder charges, earlier spark advance was needed to increase the fraction of flame based heat release to provide additional compression heating for promote autoignition of the end-gas. This was thought to occur because of changes in laminar flame speeds at those conditions and their assumed effect on overall turbulent burning velocity.

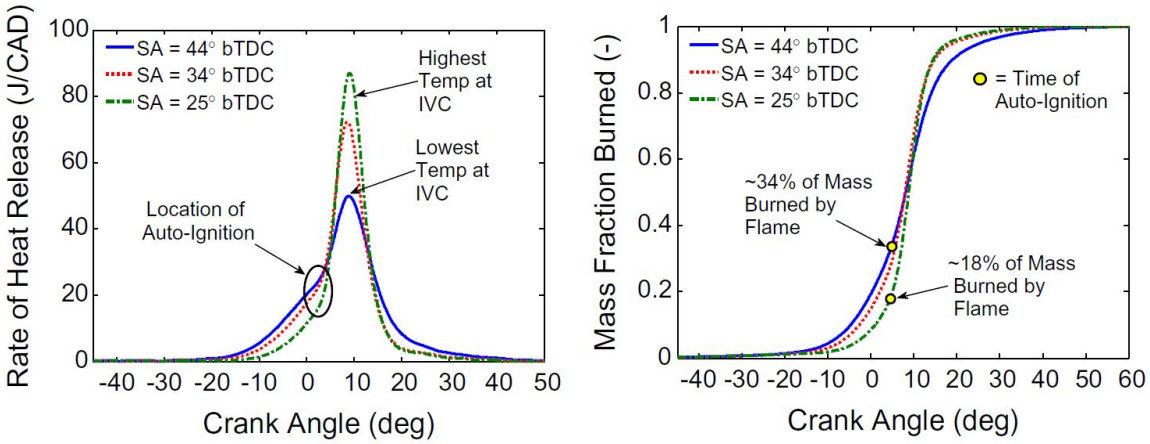

Figure 1.11: Effect of earlier spark timing and lower T_U on SACI heat release rate and mass fraction burned at constant θ_{50} [42].

A CFD based study with detailed chemistry by Middleton et al. [60] investigated the effect of spark timing and T_U on SACI heat release rate at constant autoignition timing. It was shown that for cases where flame propagation consumes a smaller fraction of the charge, the end-gas mass is greater and more reactive, namely more of its mass is at higher temperature and higher equivalence ratio. It was concluded that flame propagation in SACI can alter the end-gas thermodynamic state prior to autoignition, meaning that the end-gas thermal and compositional distributions vary with the fraction of the charge consumed by the flame. The decrease in the peak heat release rate during end-gas autoignition was shown to be a function of both the mass of the end-gas and the end-gas reactivity.

Recently, Gentz et al. [38] investigated experimentally SACI combustion under dilute, boosted conditions at $\phi' < 0.45$, where the knock/stability limit was observed.

For the conditions investigated, spark assistance at $\phi' = 0.42$ provided the greatest combustion phasing control authority under both atmospheric and boosted conditions. The lowest ϕ' for a spark-initiated flame to provide sufficient compression heating to affect the autoignition of the main portion of the charge was 0.36. In their investigation, the mixture was diluted using a combination of air and EGR, which varied depending on ϕ', so composition was not held constant.

1.6 Motivation, Research Objectives and Document Organization

The potential thermal efficiency improvements from high pressure and high dilution conditions relevant to boosted SACI combustion have been highlighted in thermodynamic modeling studies [39], but the extent to which these can be achieved in a practical combustion device is still unknown. While there have been several studies in the literature investigating SACI combustion, the benefits and limitations of this combustion mode have yet to be investigated at fuel-to-charge equivalence ratios between 0.45 and 0.75 under boosted conditions. Furthermore, within the literature there are very few highly controlled SACI experimental studies, which limits our understanding of the combustion process due to the confounding effects typically observed in metal engine experiments.

The current work investigates the impact of intake boosting on the SACI burn rates in a negative valve overlap piston engine, while maintaining constant combustion phasing near the optimal timing for work extraction. The primary mechanisms affecting end-gas autoignition rates under those conditions are explored. The relative importance of charge preheating method on SACI burn rates is investigated as well at the evolution of reactivity stratification from early in the compression stroke until the onset of autoignition. The use of intake boosting for high load expansion and dilution extension is also explored and the resulting fuel conversion efficiencies are discussed. The limits of combustion phasing and cyclic variability are investigated experimentally under those conditions. Another goal of the current work is to understand the effect of fuel-to-charge equivalence ratio on the tradeoff between deflagrative and autoignition heat release. Improved understanding of the ringing and stability limits observed SACI combustion process under those conditions can then aid both the extension of the thermal efficiency as well as the expansion of the load limit. The current work also discusses the practical engine considerations for achieving the temperature and dilution requirements for boosted SACI combustion, such as valvetrain operation, turbocharger efficiency and exhaust gas recirculation operation, which are

inherently linked to the potential thermal efficiency gains.

Figure 1.12 displays a schematic of the SACI conditions investigated in this work where there is a gap in the literature. The boundaries of HCCI, SACI and SI combustion modes have been extrapolated from experimental findings under unthrottled conditions for nearly homogeneous gasoline mixtures [56, 61]. The actual combustion mode limits as well as constant intake pressure lines are expected to vary on the GMEP - ϕ' diagram depending on several variables such as the definition of combustion constraints, the level of mixture homogeneity, compression ratio and fuel properties. The dashed black line shown is a best fit line from experimental data collected in this work for $0.45 < \phi' < 0.75$, indicating the variation of GMEP with ϕ' at constant intake pressure of 1 bar. The HCCI region has been extrapolated from the experimental data assuming similar trends in volumetric efficiency at lower GMEP-ϕ' conditions. For SI combustion charge preheating is undesirable to avoid knock, so higher loads are expected than those extrapolated from the best fit line due to higher volumetric efficiencies. On the diagram shown, boosted conditions will lie above the dashed line and vice versa for throttled conditions.

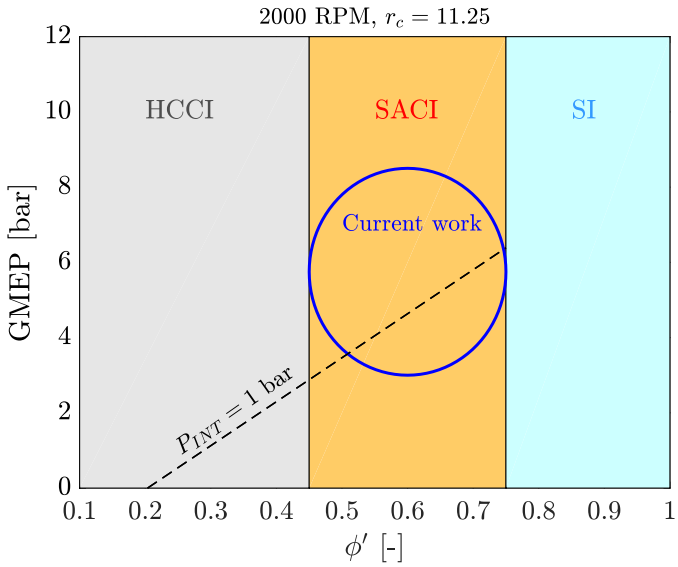

Figure 1.12: Schematic showing the SACI conditions targeted in this work (blue circle) presented on a GMEP against ϕ' diagram. The dashed line is a best fit line from experimental data collected in this work and indicates the variation of load with ϕ' at an intake pressure of 1 bar.

The work described herein is organized in the following way:

- Chapter 2 describes the experimental setup including the test engine, test cell systems and data acquisition tools are presented. The engine control techniques and data acquisition methods used to collect the experimental data are discussed. The analytical models used for the analysis of the experimental data are also discussed.

- Chapter 3 investigates the boosted SACI operating limits for the existing hardware configuration. Experimental results collected at the high load limit, combustion phasing limits and cyclic variability limits are analyzed. An analytical approach is presented to better understand the origins of the maximum pressure rise rate conditions in SACI. The trends in indicated fuel conversion efficiency and emissions are discussed as well as the effects of engine speed, fuel injection timing and fuel pressure on the heat release profiles.

- In Chapter 4, the effects of boost pressure on the SACI burn profile are studied in detail. The experiments are designed so that confounding effects on the heat release rates such as charge composition, combustion phasing and mass fraction burned at the onset of autoignition are removed. The effect of the charge preheating method on the apparent SACI heat release profile under boosted conditions is also discussed.

- Chapter 5 presents experimental studies on the impact of fuel-to-charge equivalence ratio on the balance between flame propagation and autoignition and the resulting heat release rate. The heat release trends with ϕ' are investigated both at constant intake pressure and constant load.

- In Chapter 6, the computational tools and methods are first described, then the simulation results are compared with the experimental observations. The effects of boost pressure on the thermal and compositional stratification of the end-gas are discussed. The role of the charge preheating method on the evolution of the thermal stratification and compositional stratification up to the

onset of autoignition is evaluated. The effect of heat transfer induced thermal stratification on the end-gas autoignition rate is then analyzed.

- Finally, Chapter 7 summarizes the conclusions of this work and provides recommendations for future studies.

CHAPTER II

Experimental Setup, Methods and Analytical Models

This chapter introduces the test engine and test cell systems, the engine control techniques and data acquisition systems used to collect the experimental data. Experimental methods as well as analytical models used for the analysis of the experimental data are also discussed.

2.1 Experimental Setup

2.1.1 Test Engine

The experimental data presented in this thesis was collected on a modified four cylinder turbocharged, spark-ignited GM Ecotec engine. The details of the geometry of the engine are shown in Table 2.1. The compression ratio was increased from 9.75:1 to 11.25:1 by reducing the deck height and using custom piston design to increase the end of compression pressure and temperature to promote autoignition. The engine is equipped with hydraulic variable valvetrain control on both intake and exhaust camshaft with 50 degrees of crank angle authority on each camshaft. Details on the valvetrain system can be found in Table 2.2. The pistons and connecting rods were upgraded to tolerate higher pressure rise rates and peak cylinder pressures up to 120 bar. The piston features valve cutouts and an dome and bowl design to enhance the fuel-air mixing process. The spark plug is centrally mounted in the combustion

chamber and the stock J-type spark plugs were used for all experimental studies. The ignition power supplied was approximately 70 mJ, which was measured using a Tektronix A622 current probe and a Tektronix P6015A voltage probe.

The stock turbocharger was sized for high enthalpy, high flow conditions characteristic of high load stoichiometric SI combustion and therefore was not well suited for high dilution, low exhaust temperatures characteristic of SACI combustion. An Eaton R410 roots-type supercharger with associated bypass valve was installed to the engine to achieve the target boosted conditions with better controllability.

Table 2.1: Test engine geometry and characteristics

Parameter	*Value*
Compression ratio	11.25
Bore	86 mm
Stroke	86 mm
Cylinders	4
Valves per Cylinder	4
Displacement	2.0 L
Piston pin offset	0.8 mm
Connecting rod length	145.5 mm
Turbocharger	Borg-Warner K04
Supercharger	Eaton R410
Fuel Injection	Side mounted DI
Spark plug location	Centrally mounted
Head design	Pent roof

A water-to-air heat exchanger was used to control the temperature of the compressed charge out of the turbocharger and supercharger. The water-to-air heat exchanger as well as the intake path were insulated to better control the intake temperature. Heating tapes were installed in the intake path close to intake manifold to enable intake charge heating up to 85°C. An external high pressure EGR loop, with associated cooler and EGR valve, was installed to regulate the flow of external EGR to the engine. The EGR loop was connected upstream of the throttle body and the throttle body was moved further upstream in the air path to allow for better mixing of EGR with the air stream before entering the intake manifold. EGR was introduced to the fresh air stream using four inlets spaced out radially along the intake

duct to improve its mixing with the fresh incoming air. A wire mesh was added to the intake path to enhance turbulent mixing and ensure the EGR is well mixed by the time it enters the intake manifold. A valvetrain kinematic model was built in commercial software VT-Design for the design and manufacture of a custom negative valve overlap cam profile. The details of the cam profile can be found in Table 2.2. Air flow to the engine was passed through the stock air filter and the production hot film anemometer was used for the total airflow measurement to the engine.

Table 2.2: Valvetrain system specifications

Parameter	*Value*
Intake Valve Diameter	35.0 mm
Exhaust Valve Diameter	30.1 mm
Intake/Exhaust Valve Peak Lift	3.5 mm
Intake/Exhaust Valve Duration[1]	104 CAD
Intake/Exhaust Phasing Control Authority	50 CAD
Valve Actuation	Dual OHC
Phasing Control Method	Dual Hydraulic VVT

2.1.2 Test Cell Systems

A Westinghouse 200hp DC dynamometer combined with a DyneSystems DynLoc IV controller was used to control the engine speed during experiments. UTG-96 gasoline certification fuel was used for all experiments presented in this work. Key fuel properties are displayed in Table 2.3. The fuel conditioning system supplied fuel at 5 bar and maintained fuel temperature at 32° C. The cam driven fuel pump was then used to increase the fuel rail pressure up to 150 bar. The total fuel flow into the engine was measured by a Pierburg PLU 103A positive displacement flow meter. External liquid-to-liquid heat exchangers were also installed for conditioning the oil and coolant temperatures at 90° C. An exhaust backpressure valve was installed to control the backpressure to the engine, in order to drive the external EGR and to maintain realistic turbocharger efficiency values.

[1]Valve opening and closing timings are defined at 0.2 mm opening.

Exhaust gas was sampled from cylinder 1 exhaust runner near the exhaust port and transferred via a heated line to a Horiba MEXA7500 D-EGR bench for measurement of exhaust constituents. Total hydrocarbons (THC), carbon monoxide and carbon dioxide (CO/CO_2), oxygen (O_2) and nitrogen oxides (NO_x) were measured by individual emissions analyzers using the measurement principles outlined in Table 2.4. CO_2 was sampled both at the exhaust runner of cylinder 1 as well as the intake manifold for the measurement of the external EGR rate to the engine. The experimental setup highlighting flow paths, major components and important measurements is shown in Figure 2.1.

Table 2.3: Key fuel properties of certified gasoline used in experimental studies

Fuel Property	*Test Method*	*Value*
Research Octane Number [-]	ASTM D-2699	96.7
Motor Octane Number [-]	ASTM D-2700	88.8
Antiknock Index (R+M)/2 [-]	N/A	92.8
Carbon [wt%]	ASTM D-5291	86.4
Hydrogen [wt%]	ASTM D-5291	13.6
Stoichiometric Air-Fuel Ratio [-]	N/A	14.55
Specific Gravity [-]	ASTM D-4052	0.7402
Lower Heating Value [MJ/kg]	ASTM D-240	42.901
Reid Vapor Pressure [psia]	ASTM D-5191	9

Table 2.4: Emissions sampling specifications

Exhaust species	*Analyzer measurement principle*
CO/CO_2	Non-dispersive infrared (NDIR)
THC	Flame ionization detector (FID)
O_2	Paramagnetic
NO_x	Chemiluminescense detector (CLD)

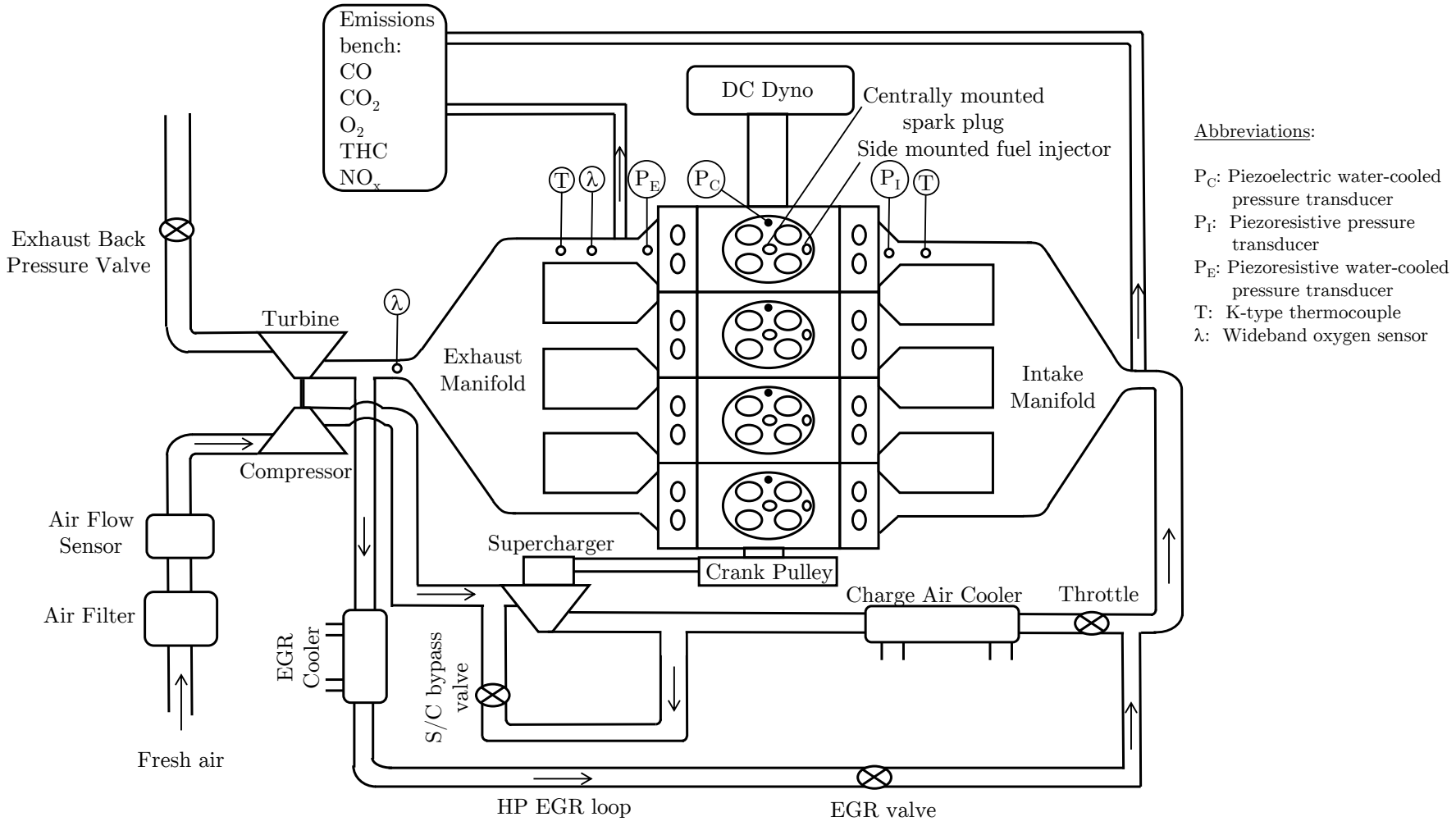

Figure 2.1: Experimental engine setup highlighting flow paths, major components and important measurements.

2.1.3 Engine Control and Data Acquisition

The engine controller hardware included an open Bosch Motronic MED17 ECU interfaced with ETAS INCA software. ETAS measurement modules were used for recording low speed data. The engine controller software (INCA) was used to monitor the engine and experimental facility sensors and modulate engine actuators such as spark timing, fuel injector pulse width, throttle angle, valvetrain phasing and external EGR valve angle. Cylinder pressure data was sampled at a 0.1 crank ankle resolution using Kistler 6041A water cooled piezoresistive pressure transducers in each cylinder. The amplification and conditioning of the cylinder pressure signal was done on Kistler 5010A units. Cylinder 1 was instrumented with dynamic piezoresistive sensors (Kistler model 4045A) positioned in the intake and exhaust runners to capture the pressure waves oscillations during valve events. The high response pressure measurements in the intake and exhaust manifold were used for pegging the cylinder pressure measurement at BDC timing and calculating the cyclic residual gas fraction, respectively. High speed data was recorded in an AVL combustion analysis system, which included Indiset 643 hardware and Indicom v2.3 software. An AVL 365C encoder was used to allow synchronization of the high-speed data acquisition system with the engine crank position. TDC was determined using a thermodynamic loss angle of 0.7 CAD at unthrottled motoring conditions at the engine speed of interest, while the engine had reached operating temperature. Each experimental condition was recorded at 300 continuous cycles to include enough cycles for statistical significance. A wideband Bosch LSU 4.9 oxygen sensor was installed pre-turbine to record lambda of the recirculating EGR with an ETAS LA4 unit. An additional LSU 4.9 wideband oxygen sensor was installed at the exhaust runner of cylinder 1 to record cylinder 1 lambda. Fuel-to-air equivalence ratio was also calculated from emissions as well as using Brettschneiders equation [62] for redundancy.

2.2 Analytical Models

2.2.1 Heat Release Analysis

A First Law of Thermodynamics approach was used to estimate the global heat release derived from the cylinder pressure data. Assuming an ideal gas and neglecting any mass lost through the crevices, the gross chemical heat release rate is given by Equation 2.1:

$$\frac{dQ_{HR}}{dt} = mc_v\frac{dT}{dt} + P\frac{dV}{dt} + \frac{dQ_{HT}}{dt} \tag{2.1}$$

where P is the measured cylinder pressure, V is the total cylinder volume and m, c_v and T are the estimated mass, constant volume specific heat capacity and mean gas temperature of the mixture, respectively. The model for the estimation of the heat transfer loss rate (dQ_{HT}/dt) model is discussed in Section 2.2.3. The cylinder volume is calculated using crank-slider kinematic equations given the engine geometry and the crank angle encoder signal. The heat release analysis was performed for the closed portion of the cycle, that is from IVC to EVO timing. The burned mass fraction, x_b, is the fraction of heat release relative to the total cumulative gross chemical heat release ($Q_{hr,ch}$) between the start of combustion (SOC) and end of combustion (EOC). Start of combustion and end of combustion are assumed to be the minimum and maximum points of the cumulative heat release curve. The global burn rate, $\dot{x}_B$, can then be calculated by numerically differentiating the mass fraction burned curve. The mean (mass averaged) gas temperature of the mixture was estimated using the ideal gas equation of state shown in Equation 2.2 below.

$$T_{mean} = \frac{PV}{mR} \tag{2.2}$$

where m is the total trapped mass, R is the specific gas constant and P and V are the instantaneous cylinder pressure and volume, respectively. The estimation of the mass trapped in the cylinder for the closed portion of the cycle is discussed in Section 2.2.2. The thermodynamic state of the gas varies as the piston moves, which will affect the

heat release rate and temperature estimates through the c_v and R terms. A variable properties routine was employed to take those effects into account, as described in Ortiz-Soto et al. [63]. The mean composition of the mixture was calculated as a mixture of burned and unburned gases, weighted by the burned mass fraction, x_B. The mass fraction of the kth species, Y^k, is given by Equation 2.3. The composition of the burned gas, Y_B^k, was modeled as complete combustion products at the measured equivalence ratio. The unburned composition, Y_U^k, was modeled as a mixture of fresh reactants, Y_{reac}^k, based on the measured equivalence ratio and the EGR composition, weighted by the EGR mass fraction (Y_{EGR}). The EGR composition (Y_{EGR}^k) was approximated as a mixture of fresh reactants and complete combustion products for the given equivalence ratio, ϕ, weighted by the combustion efficiency (η_c). The engine-out combustion efficiency was calculated from exhaust emission measurements using the equations presented in Stivender [64]. The thermodynamic gas properties were calculated using standard reference databases [65, 66].

$$Y^k = (1 - x_B) \cdot Y_U^k + x_B \cdot Y_B^k \tag{2.3}$$

$$Y_U^k = (1 - Y_{EGR}) \cdot Y_{reac}^k + Y_{EGR} \cdot Y_{EGR}^k \tag{2.4}$$

$$Y_{EGR}^k = (1 - \eta_c) \cdot Y_{reac}^k + \eta_c \cdot Y_{prod}^k \tag{2.5}$$

An energy balance was used to assess the lumped error in the heat release analysis by comparing the estimated cumulative heat release at the end of combustion to the expected heat release from the fuel energy burned. The energy balance expression is shown in Equation 2.6, where $Q_{HR}(EOC)$ is the estimated cumulative heat release at the end of combustion and η_c, m_f and Q_{LHV} are the combustion efficiency, fuel mass trapped in the cylinder and the lower heating value of the fuel, respectively. Deviations from unity in the energy balance expression can be observed due to measurements errors as well as uncertainties linked to the analytical models described in this section, in particular the heat transfer model. The energy balance calculation

can however be used as an indirect way to check for considerable errors in the measurements and/or assumptions into the analytical models. The vast majority of the data presented in this thesis had an energy balance error below 3%.

$$\text{Energy Balance} = \frac{Q_{HR}(EOC)}{\eta_c \, m_f \, Q_{LHV}} \tag{2.6}$$

2.2.2 Cylinder Mass Estimation

The cylinder mass (m_{tot}) during the closed portion of the cycle is determined by Equation 2.7, where m_f, m_a, m_{eEGR}, m_{iEGR} are the masses of injected fuel, inducted air, external EGR and internal EGR, respectively. External EGR is the exhaust gas mass that mixes with the fresh air upstream in the intake path, while internal EGR is retained in the cylinder from the previous cycles, also known as residual gas.

$$m_{tot} = m_f + m_a + m_{eEGR} + m_{iEGR} \tag{2.7}$$

The injected fuel mass in the cylinder was directly measured while the air mass in cylinder was indirectly calculated using the fuel and exhaust lambda measurements. Cylinder 1 exhaust lambda was determined from a carbon balance using the measured exhaust constituents [64] as well as from a standard wideband oxygen sensor. The two measurements showed very good agreement. The uncertainty in both the hot film anemometer measurement and the distribution of air into the cylinders was too large, so the air flow measurement was not used for the calculation of the trapped air in cylinder 1. External EGR mass was calculated by taking the ratio of volumetric CO_2 measurements in the intake and exhaust after correcting for background CO_2.

Significant amounts of residual gas were used in the negative valve overlap test engine, which have a direct impact on the mass-averaged temperature estimation and the fuel-to-charge equivalence ratio estimates. The residual gas mass was modeled due to the complexity and practical issues linked to the direct measurement of the residual gas [67]. Ortiz-Soto et al. [68] performed an assessment of 3 residual mass estimation methods commonly used in HCCI studies against simulations from a validated 1-D

engine model using experimental data. It was shown that for a negative valve overlap configuration operating under boosted conditions, the model presented by Yun and Mirsky [69] was the most robust, even though it always underpredicted the residual gas fraction by approximately 1% on an absolute basis, as seen in Figure 2.2. Such a small systematic error is expected to have a minor impact on the trend-wise behavior of the heat release analysis results. The model proposed by Fitzgerald et al. [70] for HCCI combustion showed better agreement under naturally aspirated conditions but overpredicted the residual fraction under boosted conditions. The sensitivity analysis results from that same study showed that the Yun and Mirsky model is insensitive to potential errors in the cylinder pressure or exhaust temperature measurements, as those errors cancel out in the formulation of the model described below. For the above reasons, the Yun and Mirsky model was selected as the most appropriate for use under the engine operating conditions investigated in this work.

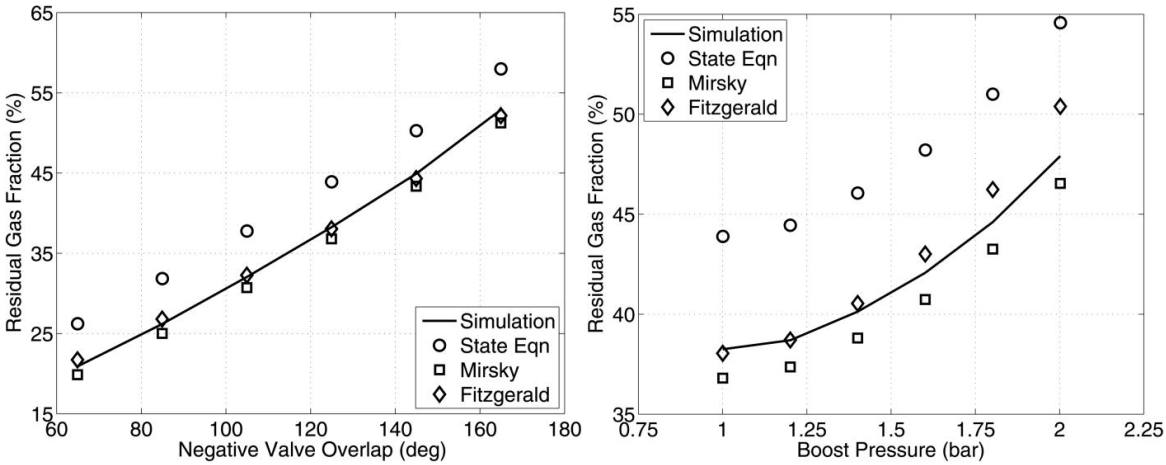

Figure 2.2: Residual gas fraction estimations as a function of (a) negative valve overlap and (b) boost pressure from analytical models and 1-D engine simulation results [68].

The Yun and Mirsky model assumes that the combustion products undergo an isentropic process during the exhaust blowdown, as shown in Equation 2.8. Assuming no leakage in the cylinder, the mass at EVO (m_{EVO}) corresponds to the total mass (m_{tot}), while the mass at EVC is equal to the internal residual mass (m_{iEGR}). The average specific heat ratio ($\bar{\gamma}$) is calculated using the mean temperature at EVO

(T_{EVO}) and EVC (T_{EVC}), given by Equations 2.9 and 2.10, respectively. An iterative approach was used to solve equations 2.7 - 2.10, as the temperatures (T_{EVO}, T_{EVC}), the masses (m_{iEGR}, m_{tot}) and the specific gas constant (R) are interrelated.

$$m_{iEGR} = m_{EVC} = m_{EVO} \left(\frac{V_{EVC}}{V_{EVO}}\right) \left(\frac{P_{EVC}}{P_{EVO}}\right)^{\frac{1}{\gamma}} \tag{2.8}$$

$$T_{EVO} = \frac{P_{EVO} V_{EVO}}{m_{EVO} R} \tag{2.9}$$

$$T_{EVC} = \frac{P_{EVC} V_{EVC}}{m_{EVC} R} \tag{2.10}$$

2.2.3 Heat Transfer Loss Estimation

The instantaneous heat transfer loss rate ($\dot{Q}_{HT}$) during the closed portion of the cycle was modeled using the form shown in Eq. 2.11, where h is a spatially averaged heat transfer coefficient, T is the mass-averaged gas temperature, A_i are the surface areas (head, piston and liner) participating in the heat transfer and T_{w_i} are the relevant mean surface temperatures. The piston and head area are constant, while the cylinder liner area varies as a function of crank angle.

$$\dot{Q}_{HT} = \sum_i h A_i (T - T_{w_i}) \tag{2.11}$$

In the absence of a global heat transfer coefficient validated experimentally for SACI conditions, a number of relevant expressions available in the literature were tested [50, 63, 71, 72]. The widely used expression proposed by Woschni [50] was selected as its predictions did not deviate from the expected heat transfer loss (using energy closure calculations) with changes in boost, load or dilution, under the conditions investigated. However, a low energy balance error does not necessarily imply that the heat transfer modeling is precise, since possible errors in the apparent heat release are lumped in the cumulative gross heat release estimate. The heat transfer model estimates were therefore used with caution, primarily to understand trendwise

behaviors in the experimental results. It should be also noted that errors in the heat transfer model have negligible impact on the heat release profiles typically up to 90% mass fraction burned (θ_{90}) for optimal combustion phasing. Due to the lack of a direct measurement, the temperature of the wall was set to 450 K for all three regions, which is in proximity to the 1-D full engine model predictions under the conditions investigated.

The spatially averaged heat transfer coefficient, h ($\mathrm{W{\cdot}m^{-2}{\cdot}K^{-1}}$), proposed by Woschni is shown in Equation 2.12, where T (K) is the gas mean temperature, P (kPa) is the cylinder pressure, B (m) is the engine bore used as a characteristic length, $\bar{S_p}$ (m/s) is the mean piston speed and w (m/s) is the characteristic gas velocity term.

$$h = 3.26 \cdot B^{-0.2} \cdot P^{0.8} \cdot T^{-0.53} \cdot w^{0.8} \tag{2.12}$$

$$w = C_1 \bar{S_p} + C_2 \left(\frac{V_d T_r}{P_r V_r} \right) (P - P_{mot}) \tag{2.13}$$

The gas velocity, w, given by Equation 2.13, is effected by the piston motion and by combustion itself. The second term in Eq. 2.13 is an empirical expression describing the intensity of the combustion, where V_d ($\mathrm{m^3}$) is the displaced volume and T_r (K), P_r (kPa), V_r ($\mathrm{m^3}$) are temperature, pressure and volume at a reference state (IVC in this work) and P, P_{mot} are the instantaneous cylinder pressure and motoring pressure, respectively. P_r, P and P_{mot} should have the same units to ensure dimensional consistency of Eq. 2.13. For an unfired engine, the instantaneous pressure, P, would be equal to the instantaneous motoring pressure, P_{mot}, so the combustion induced gas velocity would be zero, as expected. The empirical coefficients $C_1 = 2.28$ and $C_2 = 3.24$ x 10^{-3} m/(s·K) were used in this work, as suggested by Woschni [50].

2.2.4 Two-Zone Thermodynamic Model

A two-zone thermodynamic model was used to estimate the state of the end-gas (unburned gas) during the closed portion of the cycle. The model is described in detail in the work of Ortiz-Soto et al. [63], which is based on typical two-zone assumptions for flame propagation [73–76] with autoignition in the end-gas. At spark timing, the charge in the cylinder is divided into two zones: the post-flame zone and the end-gas (unburned) zone. The model assumes that the two zones are separated by a null thickness flame front and the pressure for both zones is equal to the measured cylinder pressure. The end-gas zone contains the mass of the unreacted mixture (fuel, air, EGR) and the post-flame zone contains the mass that has been consumed by the flame. The cylinder mass is assumed to be constant (no blow-by) and the contents in each zone are assumed to be fully mixed in terms of composition and properties. The end-gas species are converted into constant pressure and enthalpy complete combustion products at a rate determined from flame propagation ($\dot{m}^k_{u,FL}$). The First Law in terms of enthalpy for an open system was used to estimate the end-gas state, shown in Equation 2.14 below.

$$\frac{dH_u}{dt} = V_u \frac{dP}{dt} - \dot{Q}^{HT}_u + \sum \dot{m}^k_{u,FL} h^k_u \tag{2.14}$$

where V_u is the unburned gas volume, $\dot{Q}^{HT}_u$ is the volume scaled heat transfer loss to the walls and $\dot{m}^k_{u,FL} h^k_u$ is the enthalpy outflow due to the mass consumed by the flame. At each time step, the enthalpy of the end-gas changes due to the contributions from the piston compression/expansion, the compression from the expanding burned gases, the heat transfer lost to the walls and the mass transferred from the end-gas to the post flame zone. The end-gas state is estimated at each time step using the measured pressure and the integrated enthalpy value. Once the end-gas and global state (see Section 2.2.1) and composition are known, the post-flame state and composition are then computed algebraically by balancing mass and energy. The model calculates the relative burn fractions in SACI by employing a series of semi-empirical assumptions. An exponential function is used to fit the autoignition burn rate between the 1%

burn fraction and autoignition timing (θ_{AI}). The autoignition burn fraction at θ_{AI} is assumed to be 5%, while an exponential decay is imposed on the flame burn rate after autoignition timing. These assumptions were validated against high fidelity KIVA simulations and showed good agreement. A full sensitivity analysis and further details on the model can be found in the original work of Ortiz-Soto et al. [63].

2.2.5 End-Gas Autoignition Timing Estimation

The end-gas autoignition timing (θ_{AI}) was estimated from the pressure based heat release information using the first maxima of the second derivative of the burn rate curve, as shown in Figure 2.3. An empirical minimum threshold of 0.005 [1/cad^3] was applied on the second derivative of the burn rate curve to differentiate between cycles with and without end-gas autoignition.

Previous cycle resolved combustion imaging studies [32, 77] have shown that this metric corroborates with the visual transition from flame propagation to end-gas autoignition. Optical images of SACI combustion by Zigler et al. [55] have shown concurrent heat release between flame propagation and auto-ignition, indicating that the two modes can exist simultaneously. Reuss et al. [32] reported that the inflection point on the pressure based heat release rate curve occurred at the same time where chemiluminescence filled the field of view and had an intensity that began to exceed that of the flame. Computational work by Martz [58, 78] on laminar flames propagating into autoigniting end-gases, showed that at the transition to the spontaneous ignition front regime, the ignition wave travels only one front thickness within the remaining chemical lifetime of the end-gas. As a result, the contribution of the spontaneous ignition front to the overall energy release was relatively insignificant. These findings support the assumption made in this work that there is a bimodal switch from flame propagation to chemically controlled autoignition. While the pressure based heat release can be used to get a reasonable estimate of the autoignition timing, the exact amount of flame based heat release is difficult to determine and can often be overestimated since pure HCCI combustion without spark will also result in a few percent ($\approx$ 5-10%) of mass fraction burned using this autoignition estimation

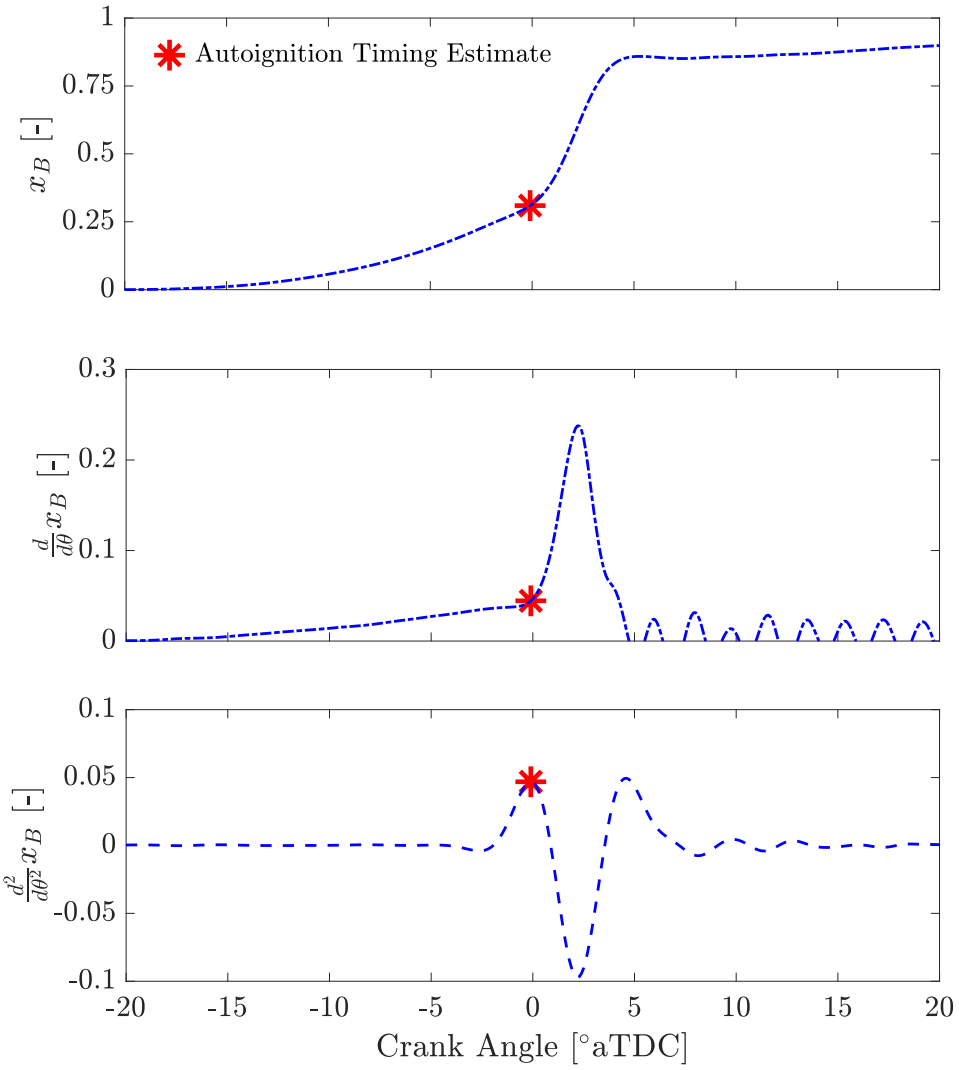

Figure 2.3: Example mass fraction burned curve (top), burn rate curve (middle) and second derivative of burn rate (bottom) highlighting the estimated end-gas autoignition timing at the first maxima location of the second derivative of the burn rate curve.

method. Nevertheless, the above analysis should still provide valuable information on the trendwise behavior of the initial flame based heat release in SACI combustion under the conditions investigated.

2.2.6 Laminar Burning Velocity Correlation

A correlation published by Middleton et al. [79] was used to estimate laminar burning velocities (S_L) near the time of spark to draw additional insight from the early flame based heat release trends observed from the experimental data. The correlation was developed using planar laminar isooctane-air-EGR reaction front simulations performed at constant pressure with HCT [80], which solves the one dimensional momentum, species and energy transport equations. This correlation was used due to the lack of experimentally developed correlations in the literature of premixed iso-octane-air-EGR laminar reaction front data under the highly dilute, high preheat temperatures relevant to SACI combustion. The simulation was exercised over fuel-air equivalence ratios, unburned gas temperatures, pressures and EGR levels ranging from 0.1 to 1.0, 298 to 1000 K, 1 to 250 bar, and 0% to 60% (by mass), respectively, thus covering the range of conditions visited in this work. The expressions for the laminar burning velocity (S_L), the inner layer temperature (T^0) and the burned gas temperature (T_B) are shown in Equations 2.15 - 2.17, respectively. Inputs to the S_L correlation include the unburned gas temperature (T_u), pressure (P) and mixture composition at the crank angle of interest. Cylinder pressure and unburned gas temperature were determined from the two-zone thermodynamic model described in Section 2.2.4, while composition was computed using the fuel-air equivalence ratio (ϕ) and total EGR mole fraction (X_{EGR}). The best fit parameters for Equations 2.15 - 2.17 can be found in the original work by Middleton et al. [79].

$$S_L = F\varphi^m \exp(-G/T^0)\left(\frac{T_u}{T^0}\right)\left(\frac{T_b - T^0}{T_b - T_u}\right)^n (1 - X_{SCP})^{D_1} \tag{2.15}$$

$$T^0 = \left(\frac{-E}{ln(P/B)}\right)[\varphi(1 - X_{SCP}) + C_7]^{C_8} + C_9 T_u + a_1 P^{a_2}[[\varphi(1 - X_{SCP})]^{a_3} - 1] \tag{2.16}$$

$$T_b = T_u + \varphi(c + d\varphi + e\varphi^2 + fT_u + gP)(1 - X_{SCP})^h \tag{2.17}$$

The S_L expression uses the non-product equivalence ratio, φ, and the mole fraction of stoichiometric combustion products (X_{SCP}) to completely define a gas mixture, while accounting for charge stratification, which is typically present in advanced combustion modes with direct fuel injection. The variables ϕ and X_{EGR} were related to φ and X_{SCP} using Equations 2.18 and 2.19 below, where x and y represent the atomic numbers for carbon and hydrogen, respectively, of the chemical formula of a hydrocarbon fuel in the form C_xH_y.

$$\varphi = \frac{(1 - X_{EGR})\phi}{1 - X_{EGR}\phi} \tag{2.18}$$

$$X_{\mathrm{CO_2}} = \frac{X_{EGR}\ \phi\ x}{X_{EGR}\ \phi\ (y/4 - 1) + \phi + 4.76(x + y/4)} \tag{2.19}$$

The mole fraction of the stoichiometric combustion products, X_{SCP} is defined in Eq. 2.20 below. The mole fraction of N_2 is divided into two parts, $X_{N_2,Reac}$ and $X_{\mathrm{N_2},st}$, where the subscript *Reac* refers to the N_2 associated with the molecular O_2, and the subscript *st* refers to the N_2 associated with the O_2 required to produce the CO_2 and H_2O present.

$$X_{SCP} = X_{\mathrm{CO_2}} + X_{\mathrm{H_2O}} + X_{\mathrm{N_2},st} = \left[1 + \frac{y}{2x} + (x + \frac{y}{4})\frac{3.76}{x}\right] X_{\mathrm{CO_2}} \tag{2.20}$$

The remaining species mole fractions are determined from the following expressions 2.21 - 2.25, which are derived from stoichiometry for the complete combustion of a hydrocarbon fuel at a given global equivalence ratio (ϕ). Further details on the development of the correlation can be found in the work of Middleton et al. [79].

$$1 = X_{\mathrm{C}_x\mathrm{H}_y} + X_{\mathrm{O_2}} + X_{\mathrm{H_2O}} + X_{\mathrm{N_2},Reac} + X_{\mathrm{N_2},st} + X_{\mathrm{CO_2}} \tag{2.21}$$

$$X_{\mathrm{C}_x\mathrm{H}_y} = \frac{\varphi(1 - X_{SCP})}{\varphi + 4.76(x + y/4)} \tag{2.22}$$

$$\frac{X_{\mathrm{N_2},Reac}}{X_{\mathrm{O_2}}} = 3.76 \tag{2.23}$$

$$\frac{X_{\mathrm{N_2},st}}{X_{\mathrm{CO_2}}} = \frac{3.76(x + y/4)}{x} \tag{2.24}$$

$$\frac{X_{\mathrm{H_2O}}}{X_{\mathrm{CO_2}}} = \frac{y/2}{x} \tag{2.25}$$

2.3 Representative Pressure Trace

In experimental metal engine studies, heat release analysis has been typically performed on the ensemble average pressure trace of several hundred cycles recorded. This post-processing method can be problematic in the analysis of SACI experimental pressure traces, which has been also discussed in previous work [44,81,82]. Cyclic heat release analysis has been used instead by some researchers of LTC combustion modes [83,84] to better understand the heat release process. If the calculated variables from the cyclic heat release analysis display a gaussian distribution, then averaging cyclic heat release calculated variables should describe well a SACI operating condition. However, ensemble averaging cyclic heat release results to create a curve, such as a heat release curve or a temperature curve, will have the same effect as using the ensemble average pressure trace for the heat release analysis.

Temel et al. [81] performed a statistical analysis to identify a single pressure trace that would best describe the average cyclic heat release results for several combustion parameters such as maximum pressure rise rate, θ_{50} and RI under several fairly high COV_{NMEP} SACI conditions at a range of speed and loads. It was shown that no particular pressure trace was best at representing the average cyclic heat release values. However, the distribution of the combustion parameters from the cyclic heat release analysis wasn't assessed to verify whether averaged cyclic heat release results would be the most appropriate to describe the operating conditions studied. Nevertheless, it was shown that the ensemble average pressure trace correlated poorly with the average cyclic heat release data while the cycles closest to the ensemble mean and ensemble median best described the maximum pressure rise rate, ringing intensity and peak pressure.

The use of representative pressure traces and ultimately heat release profiles is very important in this work to ensure good estimation of end-gas autoignition timing, mass fraction burned at the onset of autoignition as well as peak heat release rates and ringing intensity estimates. For that reason, the distributions of θ_{50} and peak pressure for a representative operating condition were analyzed, to understand why the SACI

pressure trace selection can lead to very different heat release analysis results and what cycles should be considered representative in this work.

The mean, median and mode values of θ_{50} and peak pressure from cyclic heat release analysis were used in this analysis as well as the ensemble average and ensemble median pressure traces. Both θ_{50} and peak pressure distributions, shown in Figures 2.4 and 2.5 respectively, are Gaussian and θ_{50} results matched for all traces investigated. However, the ensemble mean peak pressure was found to be lower than all other reference peak pressure values, as shown in Figure 2.5.

Looking at the pressure traces and heat release rate curves in Figures 2.6 and 2.7 it is apparent that the ensemble averaging process leads to filtering of the pressure traces, which results in approximately half peak heat release rate values compared to the representative cases. In addition, the estimated location of autoignition for the ensemble average trace is several crank angle degrees earlier compared to the representative cycles. The filtering observed in the ensemble averaging process is due to the fact that the spread in peak heat release rate phasing is close to the main combustion duration (θ_{25-75}), therefore peaks in individual cycle heat release curves average out with troughs of other cycles. The magnitude of the filtering due to ensemble averaging increased as $\sigma_{\theta_{50}}$ increased, while COV_{NMEP} was well below the cyclic variability limit, like in this example.

In this work, representative pressure traces were selected by considering the 20 actual pressure traces closest to the ensemble median trace. The representative cycles matched important combustion parameters such as the cyclic average θ_{50}, the cyclic average $x_{B,\,\theta_{AI}}$ and the cyclic average $\dot{P}_{MAX}$ at each operating condition. The vast majority of the data presented in this thesis was collected under stable operating conditions which displayed very close to gaussian distributions in the aforementioned combustion parameters. The ensemble mean from those 20 representative cycles is used in the plots presented in the main chapters of this work.

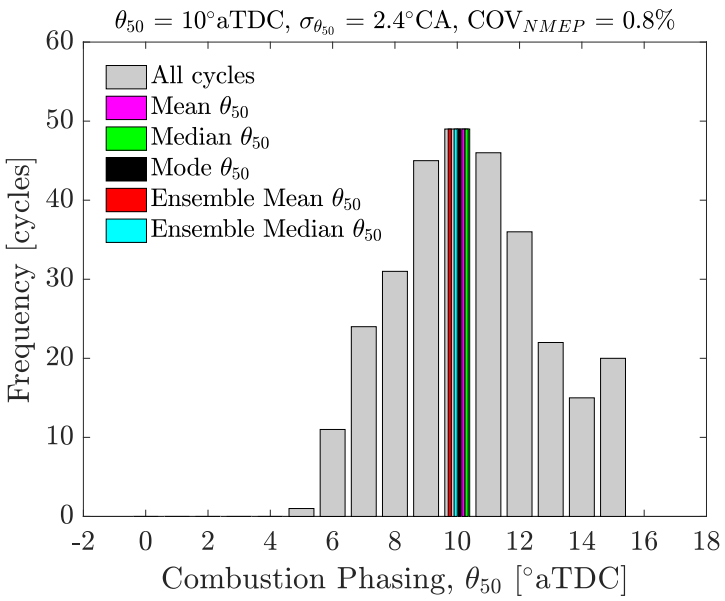

Figure 2.4: Distribution of θ_{50} (300 cycles) for a stable stoichiometric SACI operating conditions at 4.6 bar GMEP, P_{INT} = 101 kPa, $\phi' \approx 0.61$. Mean θ_{50}, median θ_{50} and mode θ_{50} are highlighted as well as the ensemble mean θ_{50} and ensemble median θ_{50}.

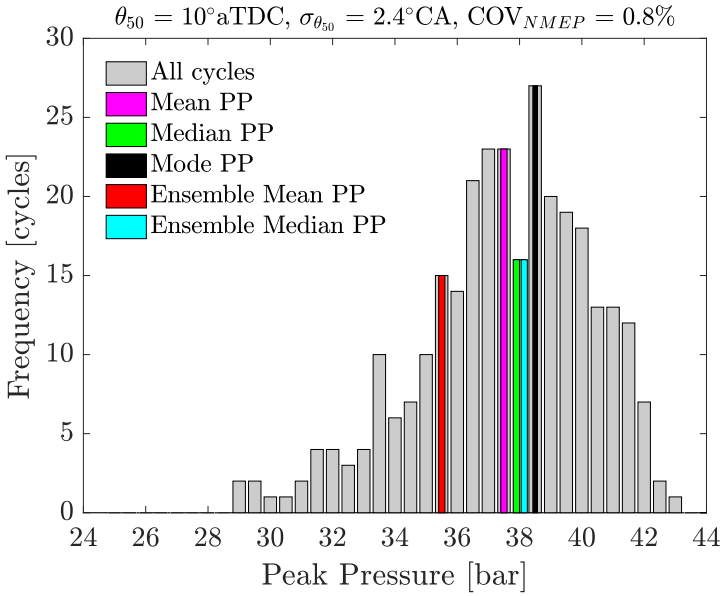

Figure 2.5: Distribution of maximum pressure (300 cycles) for a stable stoichiometric SACI operating conditions at 4.6 bar GMEP, P_{INT} = 101 kPa, $\phi' \approx 0.61$. Mean peak pressure, median peak pressure, mode peak pressure are highlighted as well as the ensemble mean trace peak pressure and ensemble median trace peak pressure.

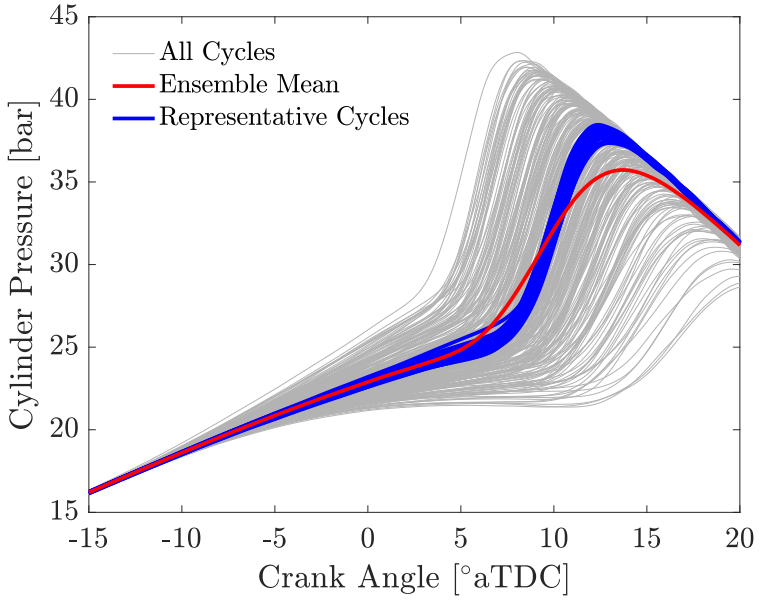

Figure 2.6: Individual pressure traces for all 300 cycles highlighting the ensemble mean pressure trace and the representative pressure traces.

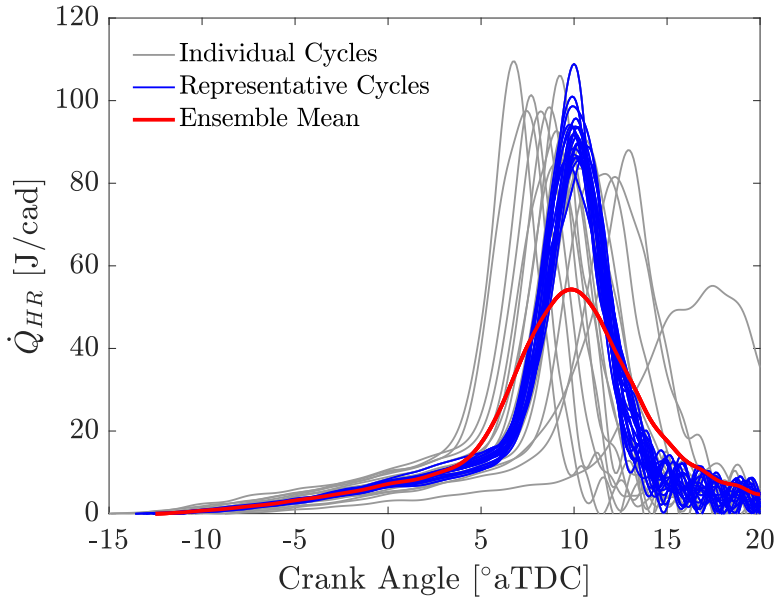

Figure 2.7: Heat release rate plot showing the effect of ensemble averaging on the heat release profile. Representative pressure traces are also shown for comparison.

2.4 Combustion Constraints

2.4.1 Ringing Intensity Limit

SACI combustion is frequently limited by high maximum pressure rise rates due to the rapid energy release during the end-gas autoignition phase. High pressure rise rates cause acoustic oscillations in the charge gas, which result in audible engine knock [85]. If uncontrolled this can result in excessive noise levels and potentially engine damage. The ringing intensity (RI) constraint proposed by Eng [86] for LTC modes is used in this work as a measure of the propensity for engine knock. Figure 2.8 displays the unfiltered and filtered pressure traces for a low and a high ringing intensity operating condition, highlighting the maximum pressure rise rate ($\dot{P}_{MAX}$) for each trace. Figure 2.9 shows an example high pass filtered pressure trace, highlighting the maximum peak-to-peak pressure pulsation amplitude (ΔP).

As derived by Eng [86], RI is correlated to the cylinder pressure wave intensity (I) or power flux in [W/m^2] generated by the rate of pressure rise, as shown in Equations 2.28 - 2.27 below.

$$I = \frac{1}{2\gamma}\frac{\Delta P^2}{P_{max}}\sqrt{\gamma R T_{max}} \tag{2.26}$$

$$\Delta P = \beta \cdot \dot{P}_{MAX} \tag{2.27}$$

$$RI \approx \frac{1}{2\gamma}\frac{\left[\beta \cdot \dot{P}_{MAX}\right]^2}{P_{max}}\sqrt{\gamma R T_{max}} \tag{2.28}$$

where ΔP is the maximum peak-to-peak pressure pulsation amplitude, $\dot{P}_{MAX}$ [kPa/ms] is the low-pass filtered maximum pressure rise rate, P_{max} [kPa] is the peak cylinder pressure, T_{max} [K] is the peak burned gas temperature, γ is the mixture's ratio of specific heats, R [J/kg/K] is the gas constant and β [ms] is a scale factor determined from experimental data. β is derived using Equation 2.27, which relates the pressure pulsation amplitude to the low-pass filtered maximum pressure rise rate. For the

representive pressure traces, the maximum pressure rise rate values $\dot{P}_{MAX}$ approximately scale with the maximum peak-to-peak pressure pulsation amplitude (ΔP), as shown in Figure 2.10. In this work, β was set to 0.05 ms, which was determined approximately using the experimental data shown in Figure 2.10.

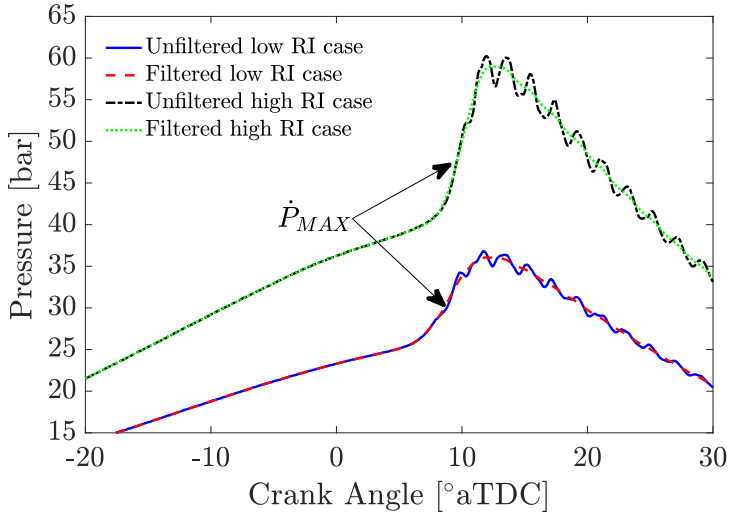

Figure 2.8: Sample unfiltered and filtered SACI pressure traces for a low and high ringing intensity experimental condition. The arrows point to the maximum pressure rise rate of the filtered trace that is being used in the ringing intensity calculation.

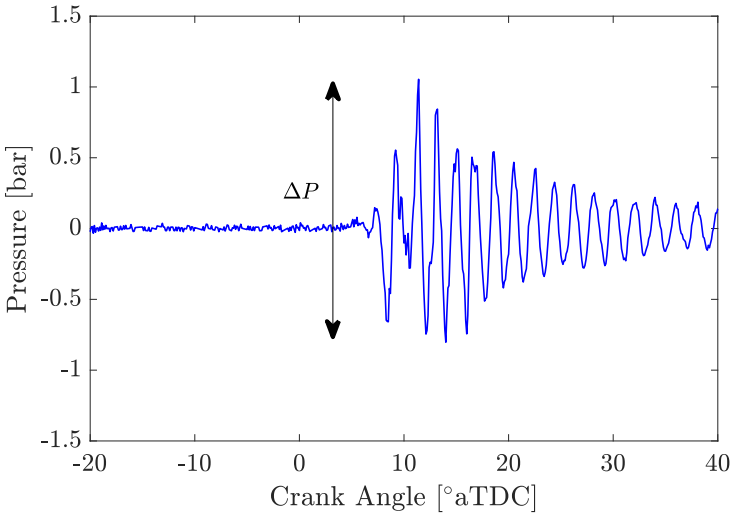

Figure 2.9: High-pass filtered pressure trace highlighting the ΔP which is the maximum peak-to-peak pressure pulsation amplitude.

Ringing intensity was calculated for all 300 cycles after filtering the individual raw pressure traces using a 2nd order low-pass Butterworth digital filter with a prescribed cutoff at 3.5 kHz. A ringing intensity limit of 5 MW/m^2 was used in this work consistent with previous LTC studies [26,35,87] that used that limit as a reliable indicator for avoiding the onset of significant ringing. At 2000 RPM and $\phi' = 0.64$, ringing intensity of 5 MW/m^2 corresponds to a maximum pressure rise rate of approximately 5 MPa/ms, which was also found to be a good indicator of the onset of knock in the work on HCCI engine knock by Andreae et al. [85]. The ringing intensity values reported in this work were calculated using the average of the 20 representative cycles, as described in Section 2.3 earlier. Early autoigniting cycles compared to the representative pressure traces depicted much higher ringing intensities and vice versa for late autoigniting cycles.

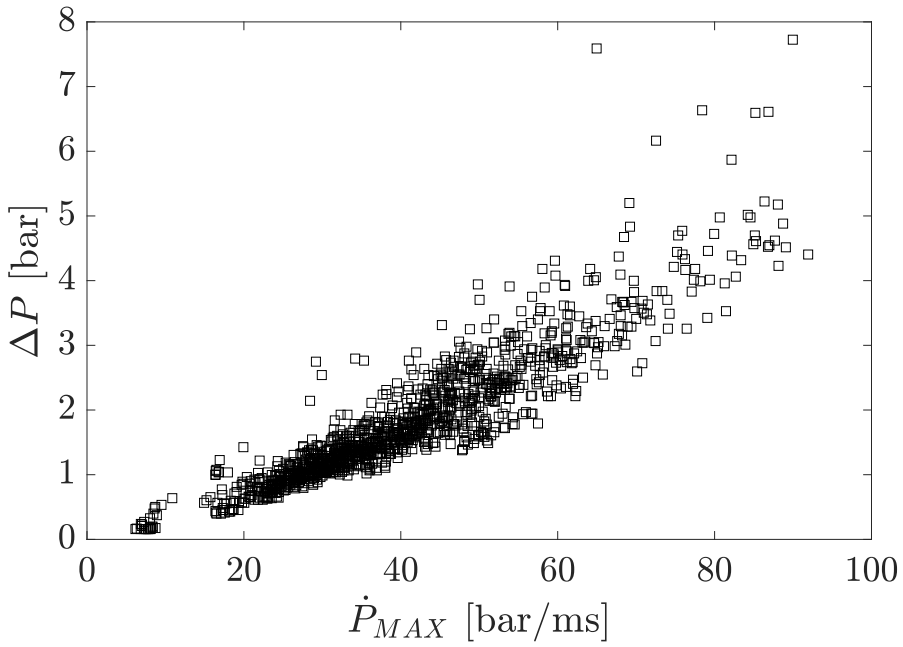

Figure 2.10: Relationship between the maximum peak-to-peak pressure pulsation amplitude (ΔP) and the maximum pressure rise rate of the low-pass filtered representative pressure trace ($\dot{P}_{MAX}$). 1240 experimental conditions plotted at 2000 RPM, $0.45 < \phi' < 0.75$, $5 < \theta_{50} < 15$°aTDC and $80 < P_{INT} < 150$ kPa.

2.4.2 Combustion Variability Limit

When TDC mixture state is not properly adjusted in SACI, combustion efficiency may be poor due to partial burning cycles and/or misfires. This can lead to elevated pollutant emissions levels, reduced thermal efficiency and driveability concerns due to variable torque output, which is undesirable. In this work, the combustion stability limit was set to a coefficient of variation of NMEP (COV_{NMEP}) approximately 4% for at least one of the cylinders. COV_{NMEP} is defined as the ratio of the standard deviation of NMEP to the mean of NMEP for the 300 cycles recorded. When end-gas autoignition was unsuccessful in SACI, a significant decrease in work output was observed during that cycle, which had a large impact on COV_{NMEP}, even for a single cycle. As a result, COV_{NMEP} would increase sharply from an initially stable operating condition depending on the frequency of partial burning cycles and/or misfires. For that reason, the standard deviation in combustion phasing ($\sigma_{\theta_{50}}$) was also used as an additional indicator of combustion variability in combination with COV_{NMEP} values.

2.5 Variability in Experimental Measurements

At the start of every experimental study, the baseline motoring and firing conditions were met to verify that the engine structure and main engine actuators did not show any damage or malfunction. Additionally, the energy closure calculation described in Section 2.2.1 was performed on every experimental dataset as a consistency check, to verify that the expected heat release and computed heat release closely match. However, in experimental studies, variability in data collection is unavoidable and hence it is an important aspect in the interpretation of the results.

To assess the variability in experimental measurements, a commonly visited stable operating condition was recorded 22 times throughout the duration of few hours. The experimental measurements were then used in the heat relase analysis routine, which incorporates a number of analytical models presented earlier in this Chapter. Table 2.5 compares the mean and standard deviation of important experimental measurements and heat release analysis outputs that were used to investigate SACI combustion in the main chapters of this thesis. It can be seen in Table 2.5 that the variability in the results is rather small for all parameters. Combustion parameters that are very sensitive to autoignition timing, such as peak pressure rise rate, peak heat release rate and peak end-gas burn rate, display a slightly larger variability compared to the rest of parameters investigated. This is understandable given the inherent variability in the initial flame development process in SACI, which ultimately affects the timing of autoignition. However, it also highlights the importance of maintaining an approximately constant autoignition timing when analyzing those parameters, which was one of the main focus areas of this research work.

Other potential sources of experimental error that were identified in this work are linked to the use of a multi-cylinder engine for the experimental studies. Sufficient mixing of fresh air and external EGR, precise measurement of cylinder 1 exhaust equivalence ratio as well as precise measurement of external EGR equivalence ratio were extremely important to reduce uncertainty in the mixture composition, combustion efficiency calculations and all other combustion parameters affected by those.

Table 2.5: Scatter in experimental measurements and heat release analysis results of interest over several hours of experimental testing. 22 datasets were recorded (300 cycles each) for a commonly visited SACI operating condition. The mean and standard deviation results for all cases are compared.

Parameter	*Mean*	*Error (1σ)*
Fueling rate [mg/cyc/cyl]	13.04	±0.08%
GMEP [kPa]	433	±0.2%
Autoignition timing, θ_{AI} [°aTDC]	6.5	±5.7%
Combustion timing, θ_{25} [°aTDC]	7.1	±3.4%
Combustion phasing, θ_{50} [°aTDC]	9.7	±3.2%
Combustion timing, θ_{75} [°aTDC]	12.4	±3.0%
Peak pressure rise rate [bar/cad]	2.80	±5.7%
Peak end-gas burn rate [1/cad]	0.16	±3.2%
Peak gross heat release rate [J/cad]	72.5	±3.7%
Mass fraction burned at autoignition [-]	0.21	±5.9%
Peak cylinder pressure [bar]	37.3	±1.3%
Internal EGR fraction [-]	0.35	±1.0%
External EGR fraction [-]	0.09	±2.2%
Total EGR mass fraction [-]	0.44	±1.0%
Exhaust temperature [°C]	500.2	±0.3%
Intake temperature [°C]	45.6	±1.0%
Fuel-to-air equivalence ratio, ϕ [-]	1.01	±0.5%
Fuel-to-charge equivalence ratio, ϕ' [-]	0.55	±1.0%
IVC temperature [°C]	562	±0.5%
T_U at autoignition timing [K]	1148	±0.25%

The actions that were taken to provide sufficient time and mixing of external EGR with fresh air were to introduce external EGR very early in the intake stream and to enhance the mixing process as described in Section 2.1.1. To achieve precise measurement of cylinder 1 exhaust equivalence ratio, a lambda sensor as well as emission sampling were installed as close as possible to cylinder 1 runner. To measure the equivalence ratio of the externally recirculated EGR, an additional lambda sensor was installed at the entry of the external EGR loop.

Another source of uncertainty comes from the estimation of the residual gas described in Section 2.2.5, which primarily affects the fuel-to-charge equivalence estimation and the cylinder temperature estimates. Given the internal residual estimation error of the Yun and Mirsky model [69] discussed in Section 2.2.2, a sensitivity anal-

ysis of the internal residual fraction was performed at a commonly visited SACI operating condition. For an operating condition with 27% internal EGR, a 4% uncertainty on the residual gas fraction leads to an uncertainty of approximately 1.5% at IVC temperature. This corresponded to an uncertainty of approximately 15 K on T_U at autoignition timing. For that reason, trends in temperature estimates that were reported in this work were at least 15 K. The effect of the change in residual gas fraction on other important parameters, such as the peak heat release rate and peak end-gas burn rate, was negligible. However, while the Yun and Mirsky estimation method may lead to an absolute error of the internal residual mass, it primarily relies on cylinder volume and pressure measurements. As a result, the directional trend, if any, is expected to be captured even if the temperature change is lower than 15 K. The estimation method is also insensitive to potential errors in pressure and/or volume measurements as the errors cancel out in the model formulation, as shown in Ortiz-Soto et al. [68].

CHAPTER III

Boosted SACI Operating Limits: Load, Ringing Intensity, Efficiency and Variability

3.1 The Maximum Pressure Rise Rate Conditions in SACI Combustion

Low temperature combustions like SACI can feature high ringing intensities levels at high loads due to excessive pressure rise rates, which limit the load expansion and could potentially cause damage to the engine structure. To get a better understanding of the contributions at the maximum pressure rise conditions, an analytical approach is employed starting from the conservation of energy. Assuming an ideal gas and neglecting any mass lost through the crevices, the energy conservation equation for a closed system has the form shown Equation 3.1. The change in the mixture gas constant from reactants to products during combustion is very small ($\approx 3\%$) so that term has also been neglected in this analysis which focuses at a small crank angle window around the location of maximum pressure rise rate.

$$\frac{dQ_{HR}}{dt} = \frac{\gamma}{\gamma - 1} P \frac{dV}{dt} + \frac{1}{\gamma - 1} V \frac{dP}{dt} + \frac{dQ_{loss}}{dt} \tag{3.1}$$

Rearranging Eq. 3.1, we can get an expression for pressure rise rate, as shown in Eq. 3.2.

$$\frac{dP}{dt} = \frac{\gamma - 1}{V} \frac{dQ_{HR}}{dt} - \frac{\gamma}{V} P \frac{dV}{dt} - \frac{\gamma - 1}{V} \frac{dQ_{loss}}{dt} \tag{3.2}$$

The three terms on the right hand side of the equation represent the pressure rise rate contributions of the fuel chemical energy released, the volumetric change due to the piston movement and the heat lost to the walls, respectively. The total heat transfer loss in the cycle typically accounts for around 10 - 20% of the total fuel chemical energy depending on the operating condition and engine design. However, the heat loss term becomes important in Equation 3.2 late in the combustion process, where cylinder temperatures are elevated and there is no heat release term. At the maximum pressure rise rate timing ($\theta_{\dot{P}_{MAX}}$), which is near TDC under the conditions investigated, the heat loss term is more than an order of magnitude smaller than the heat release term. The heat loss term can thus be ignored, leading to the simplified $\dot{P}_{MAX}$ expression shown in Equation 3.3. The fuel chemical energy release term dominates in Equation 3.3, being several times larger than the volumetric expansion term. For a given heat release rate, retarding the combustion phasing would lead to reduced $\dot{P}_{MAX}$ due to larger volume and higher volume expansion rate, however it may be associated with lower peak pressure, lower expansion work and thus lower thermal efficiency which is undesirable.

$$\dot{P}_{MAX} \approx \left(\frac{\gamma - 1}{V} \dot{Q}_{HR} - \frac{\gamma}{V} P \dot{V} \right)_{MAX} \tag{3.3}$$

Since combustion phasing has to be maintained at a narrow crank angle range for maximum fuel conversion efficiency, the analysis here assumes a constant combustion phasing near optimal timing for work extraction ($\theta_{50} \approx 9°$aTDC). Under the conditions investigated, $\theta_{\dot{P}_{MAX}}$ was found to be very close to θ_{50}. For a constant $\theta_{\dot{P}_{MAX}}$, both the heat release term and volumetric expansion term approximately scale with each other due to the positive relationship between pressure and energy content, which results in an approximately proportional relationship between the maximum pressure rise rate in the cycle and peak heat release rate, as shown in Figure 3.1 and described in Equation 3.4.

$$\dot{P}_{MAX} \propto \dot{Q}_{HR_{MAX}} \ , \quad \text{if } \theta_{\dot{P}_{MAX}} = \text{constant} \tag{3.4}$$

Figure 3.1 shows the approximately proportional relationship between the maximum pressure rise rate and peak heat release rate for 451 experimental conditions at 3 fuel-to-charge equivalence ratios and approximately constant maximum pressure rise rate location of 9°aTDC. This is not an experimental finding, but a consistency check since both variables are related through the energy balance equations described earlier. Intake pressure for these conditions vary between 80 - 150 kPa and spark timing varies between 10 - 40° bTDC. The results are shown on a crank angle basis instead of a time basis, which should not affect the relationship since engine speed was held constant at 2000 RPM. The dashed blue line shows the relationship if combustion was adiabatic at constant volume, in which case the slope of the curve is equal to $[(\gamma - 1)/V]$ evaluated at 9° aTDC. The gap between the dashed blue line and the best fit line of the experimental data depicts primarily the magnitude of the effect of volume expansion on pressure rise rate under the conditions investigated. Changes in ϕ' from 0.45 to 0.65 have negligible impact on the relationship between peak heat release rate and peak pressure rise rate due to the minimal change in γ.

In SACI combustion, a fraction of the mixture is consumed by the propagating flame while the end-gas is burned through a cascade of autoignition events. Assuming an orderly transition from flame propagation to autoignition, the maximum global heat release rate can be related to the autoignition process using Equation 3.5, where $Q_{EG,\,\theta_{AI}}$ is the end-gas energy released during autoignition and $\delta\theta_{AI}$ is the end-gas autoignition characteristic duration. The SACI autoignition characteristic duration can be computed by rearranging terms, as shown in Equation 3.5.

$$\left(\frac{dQ}{d\theta}\right)_{MAX} = \frac{Q_{EG,\,\theta_{AI}}}{\delta\theta_{AI}} \Rightarrow \delta\theta_{AI} = Q_{EG,\,\theta_{AI}} \Big/ \left(\frac{dQ}{d\theta}\right)_{MAX} \tag{3.5}$$

The end-gas energy released during autoignition $Q_{EG,\,\theta_{AI}}$ can be estimated using equation 3.6, where $x_{B,\,\theta_{AI}}$ is the mass fraction of fuel burned at the estimated autoignition timing, m_f is the total fuel mass injected in the cycle and Q_{LHV} is the lower heating value of the fuel. The mass fraction of fuel burned at autoignition can be estimated using the estimated location of autoignition from the normalized heat

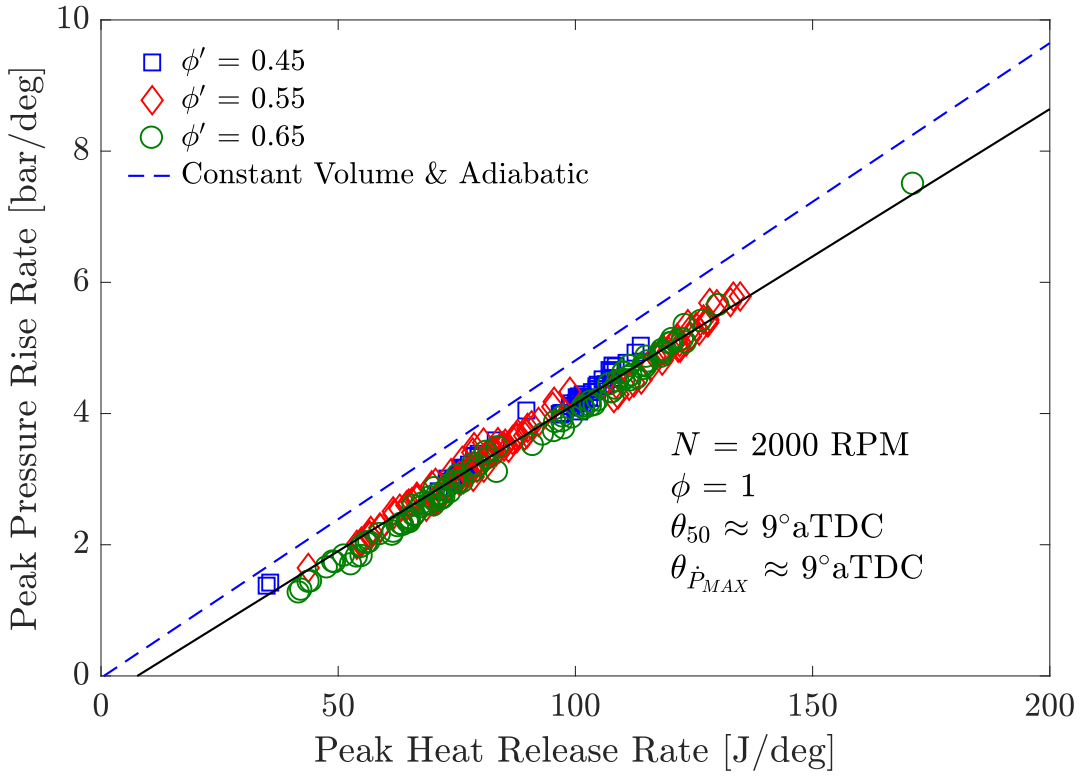

Figure 3.1: Variation of peak gross heat release rate and maximum pressure rise rate for varying ϕ' mixtures at constant maximum pressure rise rate location using the energy conservation equations. The dashed line displays the relationship if combustion was also at constant volume and adiabatic.

release rate curve. For stable engine operation, combustion efficiency measurements were consistently high ($\approx 98\%$) and showed negligible difference between experimental conditions, so combustion efficiency was neglected in the end-gas energy estimation.

$$Q_{EG,\,\theta_{AI}} = (1 - x_{B,\,\theta_{AI}}) \cdot \; m_f \cdot \; Q_{LHV} \tag{3.6}$$

Combining Equations 3.4 and 3.5, the maximum pressure rise rate should be approximately proportional to the end-gas chemical energy during autoignition ($Q_{EG,\,\theta_{AI}}$) and inversely proportional to the autoignition characteristic duration $\delta\theta_{AI}$, as shown in Equation 3.7.

$$\dot{P}_{MAX} \propto Q_{EG,\,\theta_{AI}} \cdot \delta\theta_{AI}^{-1}, \quad \text{if } \theta_{\dot{P}_{MAX}} = \text{constant} \tag{3.7}$$

The 25 - 75% and 10 - 90% burn durations have been typically used to describe the

HCCI or SACI combustion duration [6,41,88]. Figure 3.2 compares $\delta\theta_{AI}$ with 25-75% (top) and 10-90% burn duration (middle), while the bottom figure shows the variation in the mass fraction burned at the onset of autoignition between the experiments. It can be seen that the 25 - 75% and 10 - 90% durations do not always scale with $\delta\theta_{AI}$. For experiments at $\phi' = 0.45$, 10-90% durations vary less than changes in $\delta\theta_{AI}$, while the opposite is true for the cases at $\phi' = 0.65$. The 25-75% durations seem to scale with $\delta\theta_{AI}$ for $\phi' = 0.45$ and $\phi' = 0.55$ experimental points, but still show high sensitivity for experiments at $\phi' = 0.65$. The discrepancies in the slopes at each ϕ' are mostly due to the variation of the mass fraction burned at the onset of autoignition between the experiments. Differences in the relative burn fractions between flame propagation and autoignition will cause discrepancies between the autoignition characteristic duration and the global burn durations (e.g. θ_{10-90}, θ_{25-75}).

The 25 - 75% and 10 - 90% burn durations may therefore not be appropriate to describe SACI duration in the context of the maximum pressure rise rate conditions, due to the large difference observed between flame propagation and autoignition burn rates. In other words, a decrease in the autoignition burn duration by 2 crank angle degrees would have a much more pronounced effect on the maximum pressure rise rate compared to a similar decrease in burn duration during initial flame propagation. The maximum pressure rise rates originate due to rapid autoignition burn rates, hence $\delta\theta_{AI}$ reflects the combustion rate after the onset of autoignition and around the maximum pressure rise rate timing.

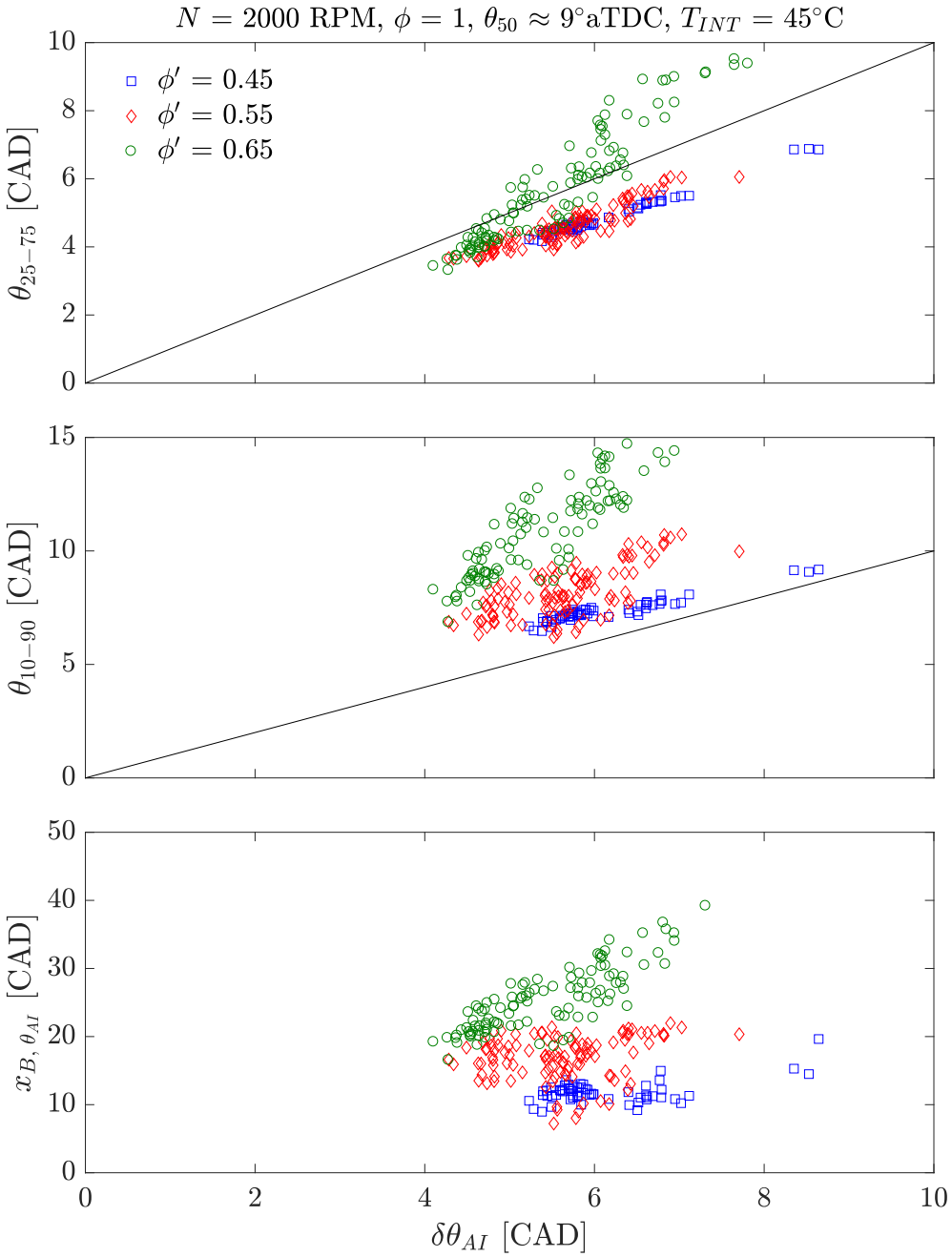

Figure 3.2: Comparison between SACI autoignition characteristic duration ($\delta\theta_{AI}$) with (top) 25-75% burn duration and (middle) 10-90% burn duration for $\phi' = 0.45$ - 0.65 mixtures. The bottom figure shows the variation of the mass fraction burned at the onset of autoignition with $\delta\theta_{AI}$ for all experimental points.

3.2 High Load Limits

The maximum load limits were investigated up to a intake pressure of 150 kPa, which was the practical boost limit imposed by the hardware configuration. Load sweeps at constant intake pressures of 100 kPa, 130 kPa and 150 kPa were performed by trading recirculated exhaust gas (EGR) with fresh air and fuel mass, thereby increasing the fuel-to-charge equivalence ratio (ϕ'). The mixture was maintained at stoichiometry and the temperature at IVC was controlled by varying the ratio of internal to external EGR. EVC timing was used to vary the internal residual amount while the external EGR valve was used to regulate eEGR rates. IVO/IVC timings were held constant at 265/161° bTDC, which maximized volumetric efficiency under the conditions investigated. Spark timing was initially set at 30°bTDC and T_{IVC} was modulated so that combustion phasing was targeted at MBT timing, which was approximately 8 - 12° aTDC under the conditions investigated. Intake temperature was held constant around 45° C and engine speed was fixed at 2000 RPM.

As load was increased at every intake pressure higher pressure rise rates were observed. To alleviate the high pressure rise rates, the charge was cooled by reducing the internal-to-external EGR ratio and spark timing was advanced. As a result, the initial flame based heat release increased and the peak heat release rates decreased while maintaining similar combustion phasing, as described in the studies of Olesky et al. [89] and Middleton et al. [60]. As spark timing was advanced and the mixture was cooled down further, higher cycle-to-cycle variability in combustion phasing was observed. At that point, T_{IVC} was increased marginally and combustion phasing was retarded by retarding the spark timing until the ringing and stability limits converged. The stability limit was defined by a coefficient of variation COV_{NMEP} of 4-5% and the ringing intensity limit used was 5 MW/m^2, which corresponded to a maximum pressure rise rate of approximately 5 MPa/ms under the conditions investigated.

Figure 3.3 show the variation of GMEP and NMEP with ϕ' for the 3 load sweeps at constant intake pressure. The maximum GMEP reached was 615 kPa, 685 kPa and 705 kPa at intake pressures of 100 kPa, 130 kPa and 150 kPa, respectively. Pumping

mean effective pressure (PMEP), shown in Figure 3.4, increased with higher intake pressure and ϕ'. PMEP at the maximum load conditions reached values between 80 - 100 kPa for all intake pressures leading to a significant drop in NMEP values. The PMEP trends are primarily caused by the phasing of the intake and exhaust valves and the cam profiles used rather than differences between the intake and exhaust manifold pressures. The exhaust pressure was maintained at approximately 25 kPa higher than the intake pressure, which led to an overall turbocharger efficiency of around 25% and 30% for the load sweeps at 1.3 bar and 1.5 bar intake pressure, respectively. Previous low temperature combustion studies on negative valve overlap (NVO) engines [90–92] have used symmetric NVO to control the mass of internal residual trapped from the previous cycle. Symmetric NVO means that the recompression work is gained back during expansion, except for heat transfer losses during the NVO period. This leads to minimal pumping losses compared to an asymmetric NVO strategy and thus improved net thermal efficiency [93, 94]. However, for a fixed cam profile, a symmetric NVO duration implies that at higher NVO conditions the intake valve closing (IVC) timing has to be retarded and exhaust valve opening (EVO) timing has to be advanced. Changes in IVC timing will alter the effective compression ratio and hence the end of compression temperature and pressure of the charge. Additionally, the mixture's temperature and/or compositional stratification at top dead center may be also altered, which can impact the autoignition rates [20, 95]. In this study, IVO/IVC timings were held constant in all load sweeps to maintain the effective compression ratio constant and remove potential effects on the combustion process, which was the main focus of the current work.

The initial increase in the pumping work with load is observed due to the NVO duration becoming more and more asymmetric, while the steep increase in pumping work at the highest ϕ' cases for each intake pressure is primarily caused by the extremely late EVO timing. As load and ϕ' increase exhaust temperatures increase and less internal residual mass is required, which is achieved with a later EVC timing, as seen in Figure 3.4. This can lead to extremely late EVO timing which causes recompression of the gases during the initial part of the exhaust stroke, thus elevating

the pumping work. More details on the changes in pumping work in the load - ϕ' space and its effect on fuel conversion efficiency can be found in Section 3.5. It is worth noting that the net IMEP results were not optimized in this work. They are shown here to highlight possible inefficiencies during the breathing process for a fixed cam profile NVO engine, operating under boosted SACI conditions. Symmetric NVO, optimal EVO timing across the load range and higher turbocharger efficiencies could offer significant improvements on a net indicated basis.

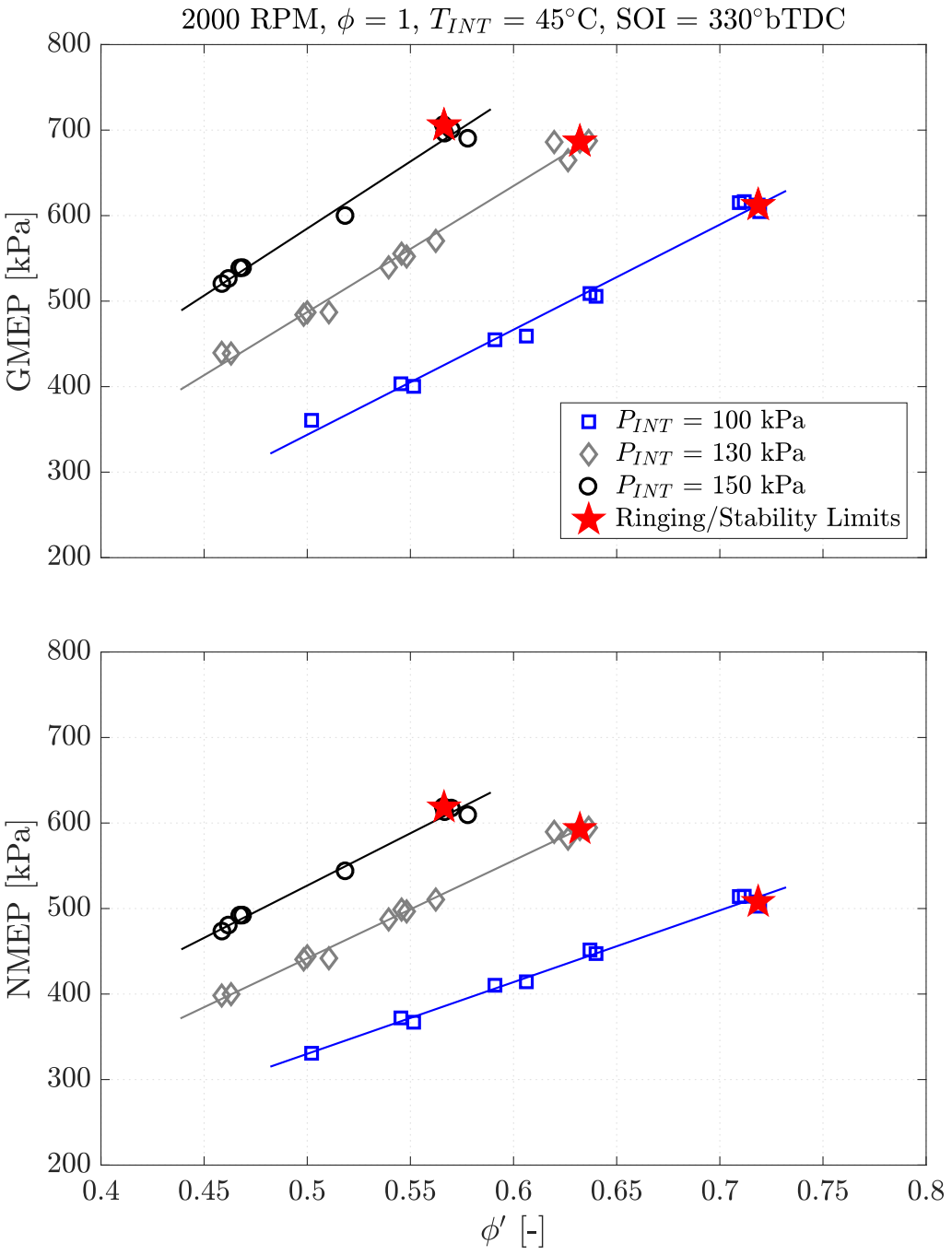

Figure 3.3: Load sweeps at intake pressures ranging from 100 - 150 kPa showing the variation of GMEP (top) and NMEP (bottom) until ringing/stability limits converged.

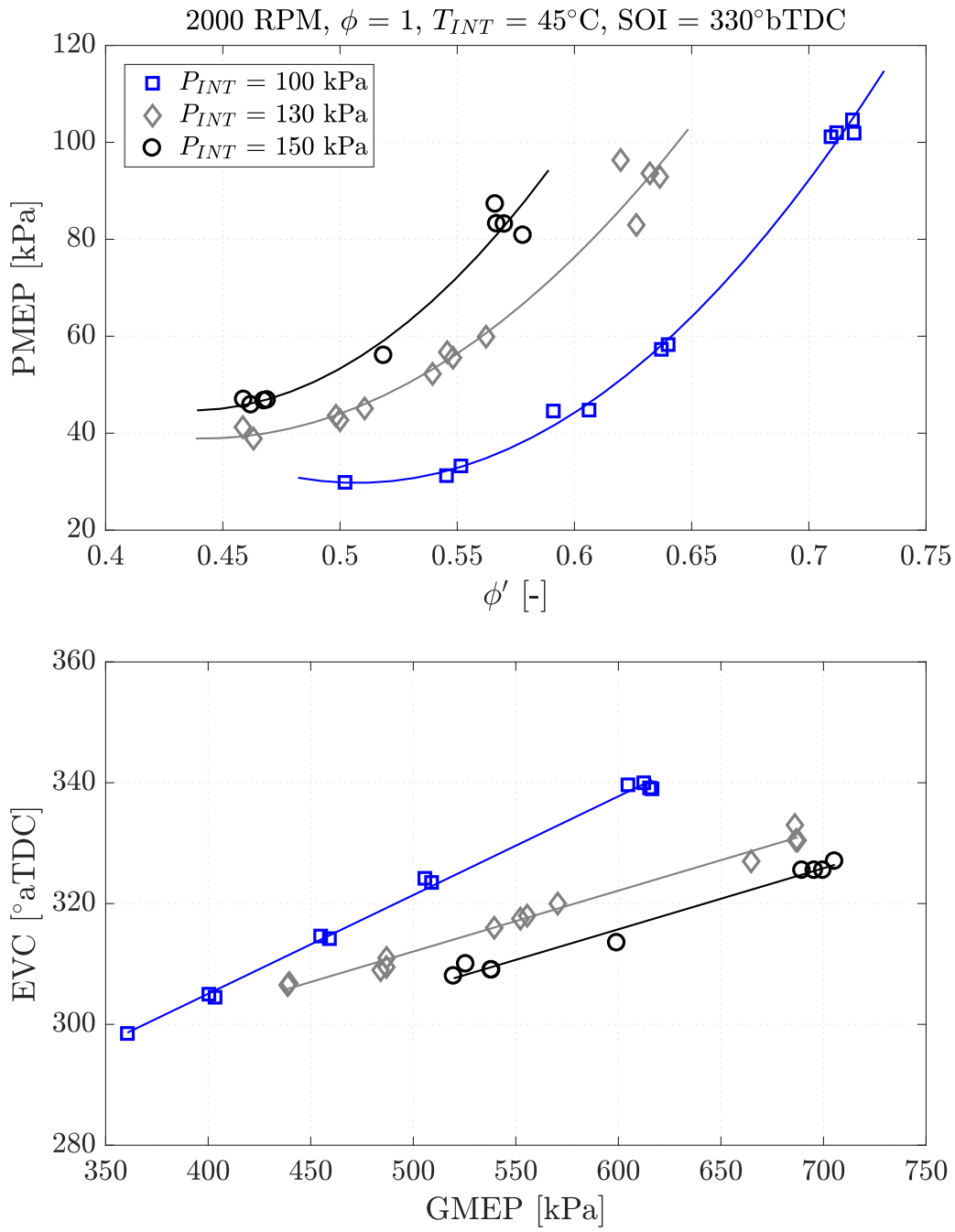

Figure 3.4: Load sweeps at intake pressures ranging from 100 - 150 kPa showing the variation of PMEP (top) and EVC (bottom) until ringing/stability limits converged.

3.3 Combustion Phasing Effects

At the maximum load conditions shown in Figure 3.3, the mixture ϕ' reached was 0.57, 0.63 and 0.72 at intake pressures of 100 kPa, 130 kPa and 150 kPa, respectively. At each condition spark timing was advanced and T_{IVC} was decreased in order to maximize the mass fraction burned at the onset of autoignition and thus minimize the maximum pressure rise rates. Spark advance was limited due to the cyclic variability approching 4 - 5% COV_{NMEP}. However, excessive pressure rise rates were still observed so combustion phasing was retarded primarily by retarding the spark timing since cooling down the mixture further would lead to excessive cycle-to-cycle variability. An analysis of cyclic variability effects under SACI conditions where θ_{50} is much earlier than the late stability limit, can be found in Section 3.4.

Figure 3.5 shows the effect of combustion phasing on the ringing intensity and maximum pressure rise rate for the maximum load conditions at the three intake pressures used. As θ_{50} is retarded, both ringing intensities and pressure rise rates decrease linearly. In particular, when retarding θ_{50} from 10 to 13°aTDC, ringing intensity levels exhibit a decrease of 50%, from approximately 10 to 5 MW/m^2. The drop in ringing intensity is primarily due to the decrease in the maximum pressure rise rate. The combined effect of the drop in maximum cylinder pressure and peak burned gas temperature also contribute to the rather than changes in P_{max} and T_{max} that are used in the ringing intensity calculation. Taking a closer look at the θ_{50} sweeps at ϕ' = 0.57 and $\phi' = 0.63$, the mass fraction burned at the onset of autoignition remained approximately constant, which resulted in a similar estimated end-gas energy at the onset of autoignition, as shown in Figure 3.6. The drop in peak heat release rate seen in Figure 3.6, is therefore primarily attributed to the decrease in the autoignition rate. The peak end-gas burn rate, shown in Figure 3.6, drops by approximately 25% from θ_{50} = 10°aTDC to θ_{50} = 13° aTDC. Several possible reasons could be causing the slower end-gas burn rate observed. As θ_{50} is retarded, the volume expansion rate at 13°aTDC is approximately 30% higher than that at 10°aTDC. The expansion cooling rate further away from TDC is therefore faster, which should counteract

the compression heating of the unburned zones post autoignition, thus slowing down the autoignition cascade. Additionally, as θ_{50} becomes later, the combustion chamber volume increases which tends to reduce the temperature and pressure of the unburned gas, resulting in an overall less reactive mixture. The higher expansion rate and the larger volume at later θ_{50} are also expected to contribute to the decrease in the maximum pressure rise rate observed, based on Equation 3.3.

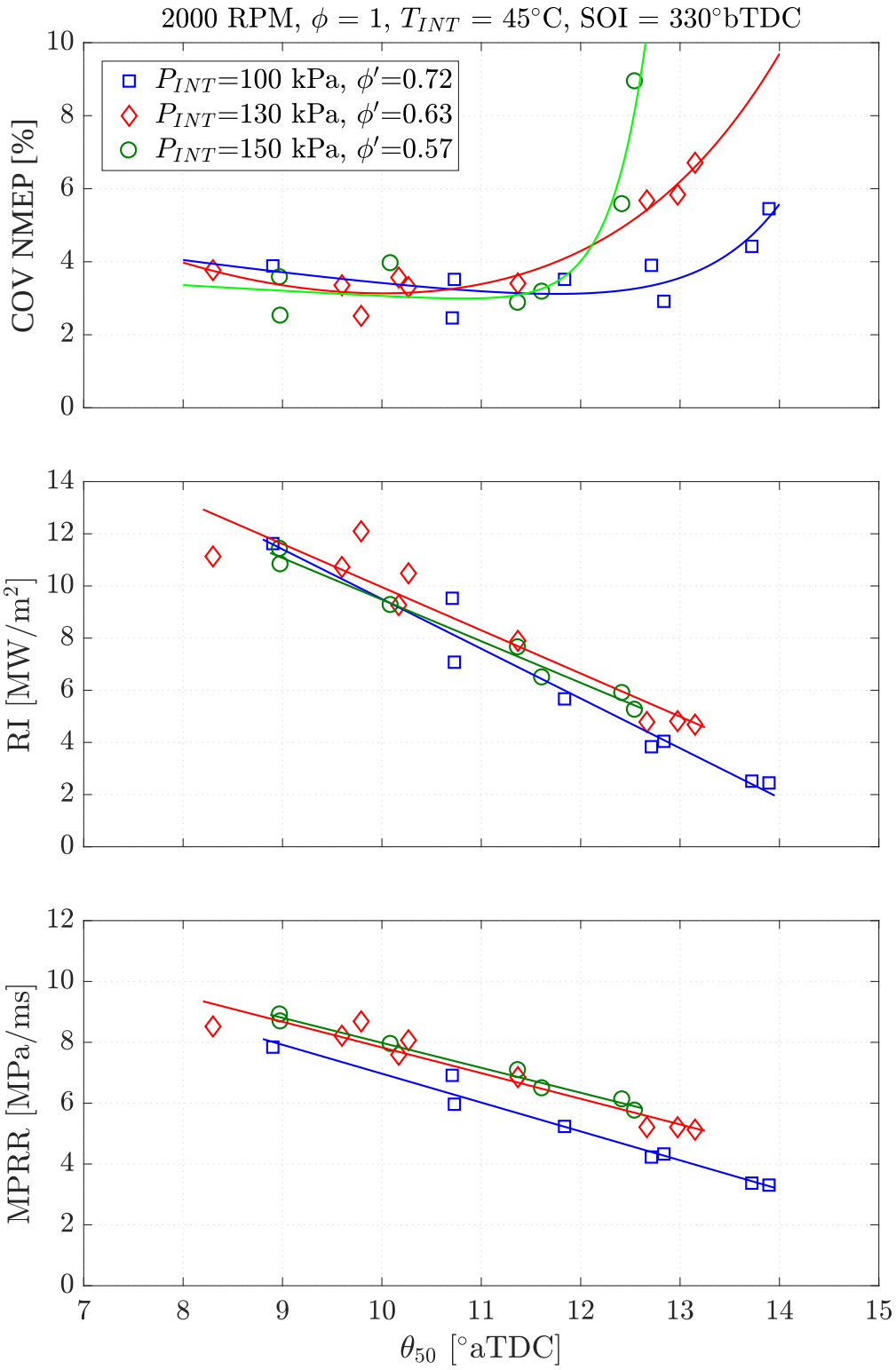

Figure 3.5: Effect of combustion phasing retard on coefficient of variation of NMEP (top), ringing intensity (middle) and maximum pressure rise rate (bottom) at the maximum load conditions at intake pressures 100 kPa, 130 kPa and 150 kPa.

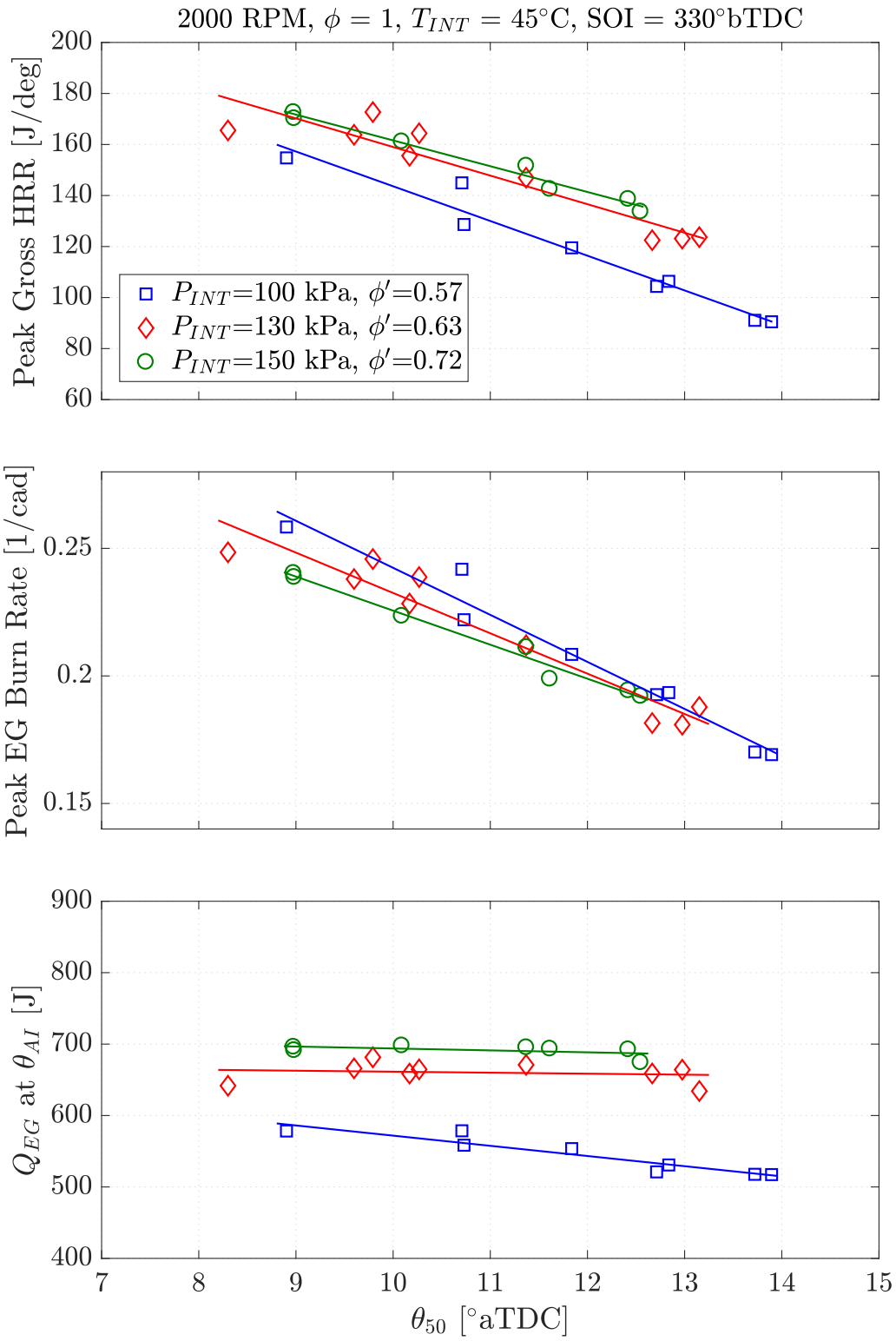

Figure 3.6: Effects of combustion phasing retard described by the crank angle 50% of the representative pressure trace on peak heat release rate (top), peak end-gas burn rate (middle) and end-gas energy at autoignition onset (bottom) at the maximum load conditions at intake pressures 100 kPa, 130 kPa and 150 kPa.

3.4 Cyclic Variability in SACI

One mode of combustion instability in SACI is linked to late mean combustion phasing, as shown in Figure 3.5 earlier. Retarding combustion phasing to approximately 13°aTDC at the maximum load conditions was effective at limiting ringing intensity to 5 MW/m^2 but combustion stability deteriorated, resulting in high COV_{NMEP} values. The convergence of the pressure rise rate and stability limits at the highest load condition is commonly seen in low temperature combustion studies [20, 96]. At higher loads, the energy released during autoignition typically increases leading to higher pressure rise rates, which are usually alleviated by retarding autoignition phasing. However, the cylinder volume expansion rate increases during the first half of the expansion stroke due to crank-slider kinematics. The expansion cooling rate of the unburned gas thus increases as the piston moves down from TDC, so the propensity for autoignition drops rapidly for a fuel that exhibits Arrhenius ignition delay behavior. The late autoignition phasing limit could be extended for a faster burning mixture or if there is intermediate temperature heat release that would counteract the temperature decrease from expansion cooling [97–99]. In SACI, higher heat release rates from the initial flame propagation can also help extend the late autoignition phasing due to compression heating of the unburned mixture. On the contrary, turbulent stoichiometric flames in modern SI engines with low dilution levels can propagate late into the power stroke, so much later mean combustion phasing ($\theta_{50} \approx 29$°aTDC) can be achieved without torque output variability problems [100].

Under relatively high ϕ' conditions (e.g. $\phi' \approx 0.6$ - 0.7), SACI combustion can exhibit high cyclic variability even though mean autoignition phasing is close or even earlier than the optimal timing for maximum work extraction (e.g. $\theta_{AI} \approx 7$°aTDC). Experiments were performed to investigate the effect of advancing the spark timing and reducing the mixture temperature on cyclic variability, while maintaining approximately constant θ_{50}. The autoignition timing was held constant near 7°aTDC while composition was fixed (ϕ =1, $\phi' = 0.63$), engine speed and intake pressure was fixed. Similar observations to the ones discussed in this section were observed for a range

of intake pressure conditions primarily at high ϕ' mixtures. The temperature at IVC was controlled by making small adjustments to the fraction of internal to external EGR rates. Cyclic variability is described using both the standard deviation of θ_{50} and COV_{NMEP}. It can be seen in Figure 3.7 that advancing spark timing and reducing the mixture temperature leads to increased mass fraction burned at the onset of autoignition, while autoignition timing remains constant. This behavior is consistent with previous work [60, 89] which showed that the higher flame based heat release provided the additional compression heating for the cooler mixture to autoignite at constant timing. However, as spark timing is advanced the standard deviation in θ_{50} increases linearly, nearly doubling from SA = 27 - 40°bTDC. The increase in $\sigma_{\theta_{50}}$ has no effect on COV_{NMEP} initially, which remains low around 1%. As $\sigma_{\theta_{50}}$ increases above 3 CAD, COV_{NMEP} increases rapidly exceeding 3%, as shown in Figure 3.8. The rapid increase in COV_{NMEP} close to the stability limit was commonly observed during the experiments conducted. In a multi-cylinder engine configuration, fine control of θ_{AI} across all cylinders is challenging, so combustion can become uncontrollable even faster near the stability limit.

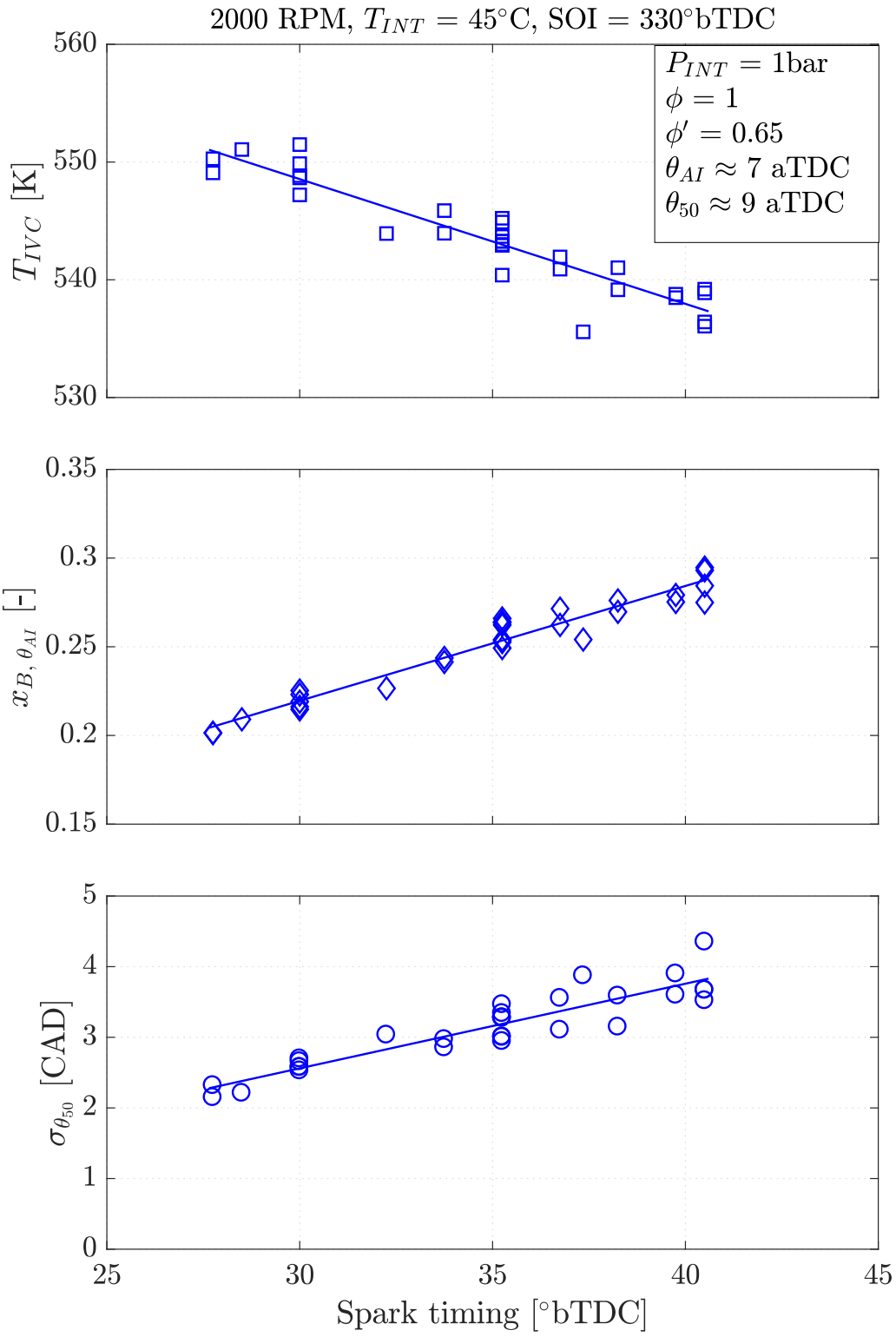

Figure 3.7: Variation of mass fraction burned at autoignition onset (top), temperature at IVC (middle) as spark timing is advanced at constant autoignition phasing and composition. Effects of earlier spark timing and lower unburned gas temperature on standard deviation of θ_{50} (bottom).

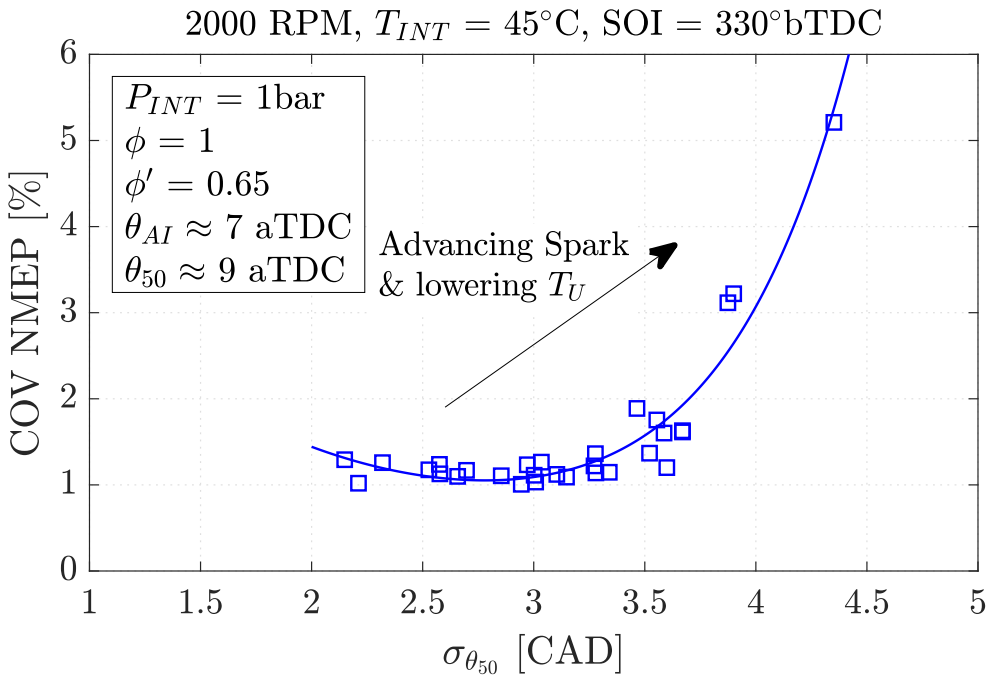

Figure 3.8: Variation of COV of NMEP with standard deviation of θ_{50} for the results presented in Figure 3.7.

A closer look at individual cycles of unstable operating conditions revealed that high COV NMEP occurs due to very few cycles exhibiting very low gross cyclic work rather than a larger spread in work output between the cycles. Very late autoignition cycles ($\theta_{AI} > 15$ °aTDC) or non autoigniting cycles resulted in reduced cycle work output by 50% or more at times. As the count of those cycles increases, the impact on gross IMEP reduction is significant, which explains the rapid increase in COV IMEP observed.

All 300 cycles were analyzed to investigate the causes of the large variability in combustion phasing that eventually leads to high COV IMEP. Figure 3.9 shows cyclic heat release results for an operating condition close to the stability limit (COV IMEP $> 3\%$) with high variability in combustion phasing ($\sigma_{\theta_{50}} \approx 4$ CAD). A clear correlation can be seen between θ_{02} and θ_{AI}, where a delay in θ_{02} leads to an almost equivalent delay in θ_{AI}. The 50% mass fraction burned timing (θ_{50}) closely follows θ_{AI} due to the rapid autoignition rates unless autoignition phasing is very late, as seen for 2 very late cycles in Figure 3.9a. Figure 3.9b shows net heat release profiles for 3 representative cycles at early, normal and late combustion phasing. The timings of 2% mass fraction burned, autoignition and 50% burned are highlighted for each cycle. It is apparent that variability in autoignition timing is already determined by θ_{02}, suggesting that variability is introduced in processes prior to θ_{02}. Experiments with a dual coil offset ignition system [101] providing up to 1 J of ignition energy on the secondary coil under those conditions had negligible effect on the cyclic variability in combustion phasing. The variability is likely introduced due to flow-flame interactions in the early kernel growth period as discussed in the work by Reuss et al. [32], even though their work focused on stratified mixtures. Cycles that exhibit faster transition from the spark discharge time to θ_{02}, exhibit higher flame heat release rates leading to an earlier autoignition timing and vice versa. As a result, the mass fraction burned at the onset of autoignition is fairly constant for the 300 cycles even though θ_{AI} spans from 0 - 10° aTDC, as shown in the middle of Figure 3.10.

Figure 3.10 shows the peak heat release results (top), peak autoignition burn rate results (middle) and P, T_U values at the onset of autoignition (bottom) for all 300

cycles as a function θ_{AI}. The peak heat release rate is negatively correlated to θ_{AI}, similarly to results presented in Section 3.3. Since the end-gas energy is approximately constant, the drop in peak heat release rate with later θ_{AI} is due to an equivalent drop in autoignition burn rate. The slower end-gas autoignition rate observed with later θ_{AI} is likely due to several reasons. At later θ_{AI}, the mean mixture reactivity is expected to be lower due to lower unburned temperature and pressure, as seen in Figure 3.10. Later autoignition cycles are also likely to have developed greater thermal stratification as demonstrated in the planar imaging thermometry studies by Dronniou and Dec [102]. Additionally, the faster expansion cooling rate at retarded θ_{AI} is expected to slow down the autoignition cascade as discussed in Section 3.3.

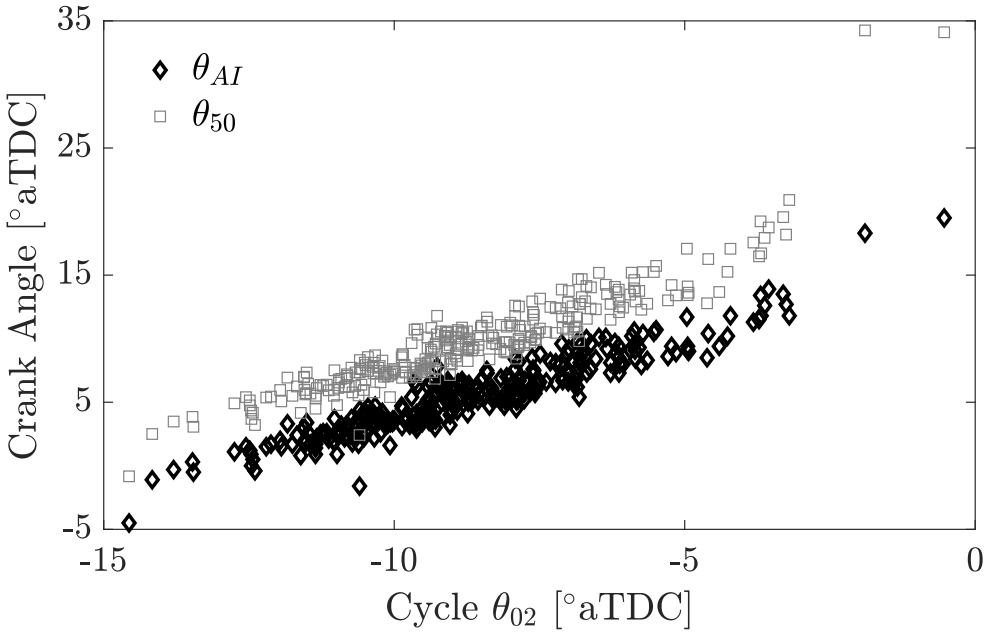

(a)

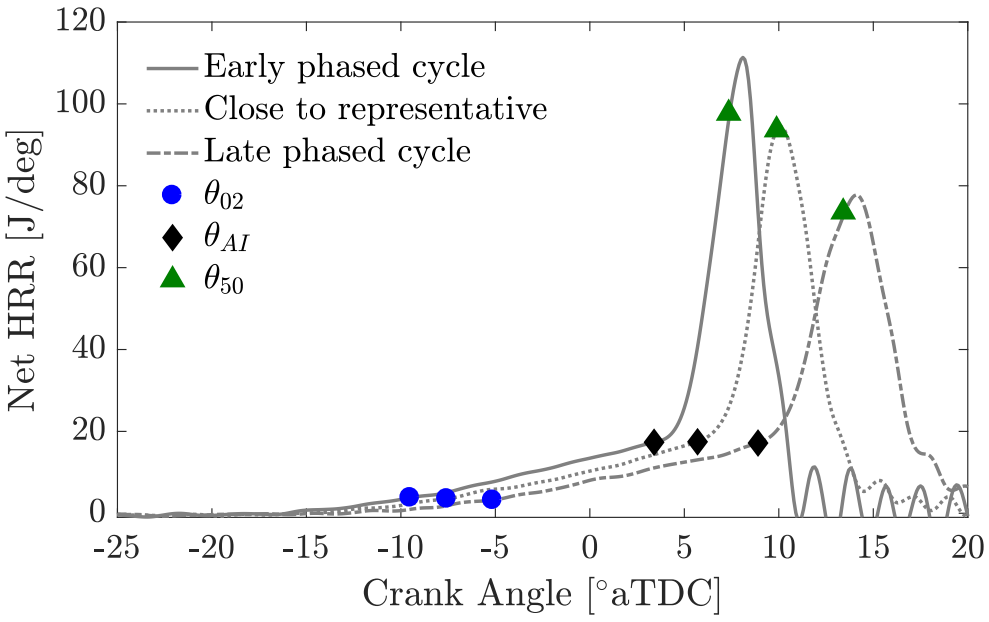

(b)

Figure 3.9: Cyclic heat release results (300 cycles) for an operating condition shown in Figure 3.7 with high variability in combustion phasing ($\text{COV}_{NMEP} > 3\%$). (a) Trends in timings of end-gas autoignition (θ_{AI}) and 50% mass fraction fuel burned (θ_{50}) as a function of 2% mass fraction of fuel burned (θ_{02}). (b) Heat release profiles for 3 cycles at early, close to representative and late combustion phasing.

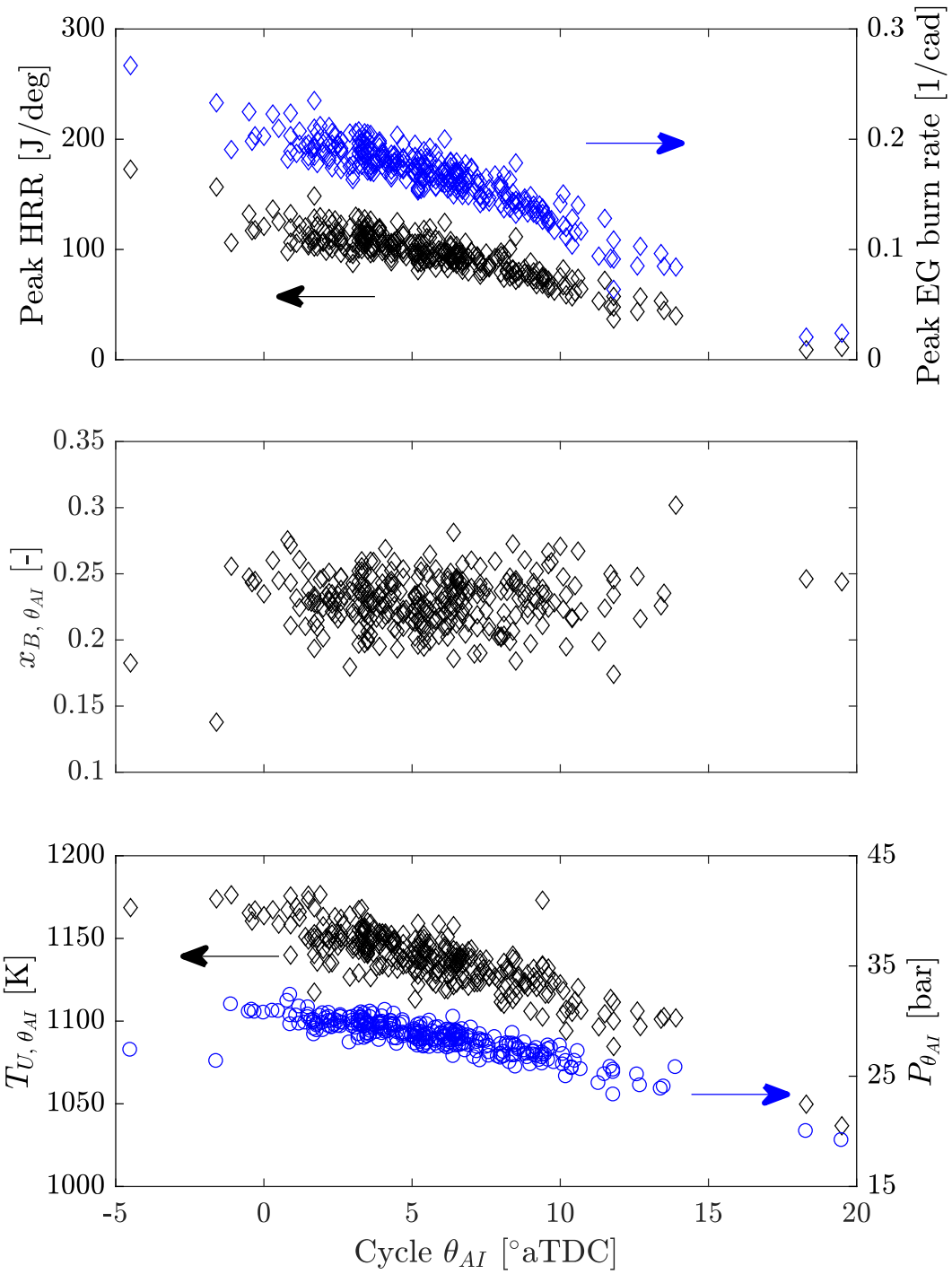

Figure 3.10: Cyclic heat release results (300 cycles) for an operating condition shown in Figure 3.7 with high variability in combustion phasing, close to the stability limit ($COV_{NMEP} \approx$ 3-4%). (Top) Cyclic peak heat release and peak autoignition burn rate results, (middle) mass fraction burned at the estimated onset of autoignition and (bottom) variation of cycle estimated unburned gas temperature and pressure at the onset of autoignition as a function of end-gas autoignition phasing.

When the cyclic variability analysis was extended to other operating conditions, a correlation was observed between the mass fraction burned at the onset of autoignition for the representative cycles ($x_{B,\,\theta_{AI}}$) and $\sigma_{\theta_{50}}$ at each operating condition, as shown Figure 3.11. The experimental data points plotted in Figure 3.11 correspond to 952 operating conditions at approximately constant combustion phasing ($\theta_{50} \approx 9°$aTDC), while intake pressure varies from 68 - 150 kPa, ϕ' varies from 0.45 - 0.81 and spark advance varies from 51 - 9° bTDC. The almost proportional relationship between $x_{B,\,\theta_{AI}}$ and $\sigma_{\theta_{50}}$ suggests that, while combustion phasing is near optimum for work extraction, variability in θ_{50} is a function of the mass fraction burned at the onset of autoignition.

A possible explanation for this behavior, is that the initial variability in flame development gets amplified when the representative mass fraction burned at the onset of autoignition increases. For low $x_{B,\,\theta_{AI}}$ cases, the compression heating effect of the initial flame development on the autoignition timing is minimal, and autoignition timing is primarily determined by the compression heating due to the piston movement. On the other hand, for high $x_{B,\,\theta_{AI}}$ cases the additional compression heating from the advancing flame is needed to trigger end-gas autoignition. Any variability in the initial flame development will thus have a greater impact for high $x_{B,\,\theta_{AI}}$ cases, where the role of the flame compression heating to trigger end-gas autoignition is more important. While there are limited experimental data at $x_{B,\,\theta_{AI}} > 0.4$, a decrease in $\sigma_{\theta_{50}}$ can be observed for 4 operating conditions. These cases correspond to the lowest EGR dilute mixtures at $\phi' \approx 0.80$. It is likely that, under those very low EGR dilution conditions, the initial flame burn rates are high enough that the variability in the initial flame development is greatly reduced, thereby leading to a more repeatable onset of end-gas autoignition.

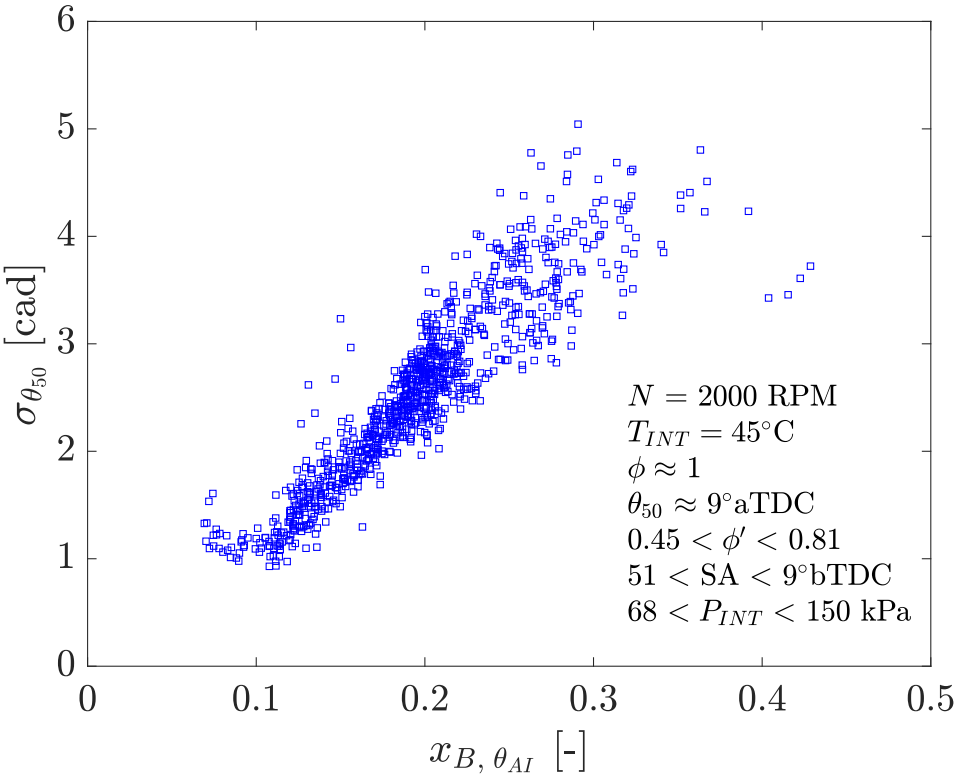

Figure 3.11: Variation of standard deviation of θ_{50} as a function of mass fraction burned at the onset of autoignition for the mean of the representative cycles at each operating condition. The data points correspond to 952 operating conditions at 2000 RPM, $T_{INT} = 45$°C, $\theta_{50} \approx 9$°aTDC, $\phi \approx 1$, $0.45 < \phi' < 0.81$, $51 <$ SA < 9°bTDC and $68 < P_{INT} < 150$ kPa.

3.5 Efficiency and Emissions

In boosted SACI combustion, a specific load condition can achieved by different combinations of intake pressure and ϕ'. To demonstrate the trends in indicated efficiencies and emissions in the load-ϕ' operating map, results from two experimental approaches are presented in this section, First, ϕ' was varied at constant fuel energy input which resulted in approximately constant load, and second, load was increased at constant composition. Engine speed was kept constant at 2000 RPM and combustion phasing was maintained near the optimal timing for work extraction ($\theta_{50} \approx 9^\circ$ aTDC) unless excessive ringing was observed where combustion was retarded until the ringing/stability limits converged.

3.5.1 Experiments at Constant Fuel Energy Input and Increasing Dilution using Boost Pressure

Figure 3.12 shows the variation of fuel indicated conversion efficiencies with respect to fuel-to-charge equivance ratio (ϕ') at constant fuel energy input of 15 mg per cycle per cylinder, which resulted in a load of approximately 5.2 bar GMEP. Fuel conversion efficiency is computed by the product of combustion efficiency and thermal efficiency. Efficiency results are shown in both gross (compression and power strokes) and net (compression, power and gas exchange strokes) bases. A decrease in ϕ' from 0.75 to 0.45 resulted in a gross fuel conversion efficiency improvement from around 38% to 41%, namely an increase of 3 absolute efficiency points or an 8% increase on a relative basis. The improvement in gross fuel conversion efficiency can be attributed to the increase in the specific heat ratio during expansion for the lower ϕ' mixtures, as seen in Figure 3.13. Favorable mixture properties and lower burned gas tempeartures led to better specific heat ratio of the mixture during expansion. Emissions indices for hydrocarbon and carbon monoxide were calculated at around 15 g/kg-fuel and 23 g/kg-fuel, respectively, for all cases. As a result, combustion efficiencies were fairly constant and consistently high for all experiments at around 98%, as seen in Figure 3.12. The estimated heat transfer loss fraction during the closed

portion of the cycle remained approximately constant during the ϕ' sweep, although combustion temperatures were significantly lower as ϕ' decreased. Since load was maintained constant, the increased EGR dilution of lower ϕ' mixtures was associated with higher intake pressures and higher charge mass. Looking at the terms of the Woschni expression for heat transfer, the higher charge mass of lower ϕ' mixtures is likely offsetting the effect of reduced expansion temperature on heat transfer losses to the cylinder walls, keeping the total heat transfer loss approximately constant.

Figure 3.12 shows the variation of pumping mean effective pressure with changes in ϕ'. While PMEP is constant at low ϕ' mixtures, it starts increasing exponentially at ϕ' of 0.65 and above, even though the manifold pressure differential between intake and exhaust was kept approximately constant at 25 kPa. Taking a closer look at the pumping loop of the two extreme ϕ' conditions in Figure 3.14, it can be seen that the EVO timing for the high ϕ' case is after BDC of expansion. The extremely late EVO timing is initially restricting the exhaust flow leading to higher pressure during the exhaust stroke and therefore elevated pumping work. The late EVO timing of the high ϕ' is a result of the late EVC timing due to the lower internal EGR requirement under that operating condition. Figure 3.15 shows the variation of internal, external and total EGR fraction for the experiments in this study. Note that intake temperature is maintained constant for all results shown at approximately 45° C. Higher ϕ' mixtures require less internal residual compared to lower ϕ' mixtures, as the exhaust temperatures are higher and the IVC temperatures needed to match combustion phasing are lower. The resulting ratio of internal (iEGR) to total EGR (tEGR) remains approximately constant around 0.75 for all experiments. More details on the unburned gas temperature requirements as a function of ϕ' can be also found in Section 5.3. Figure 3.15 shows the NO_x emission index results for this set of experiments, which follow an exponential trend as ϕ' increases. The increase in NO_x emissions is most likely observed due to the increase in burned gas temperatures associated with higher ϕ' mixtures. As the mixture is kept at stoichiometry, the NO_x emissions could be treated using a three-way catalyst even at low exhaust temperatures relevant to SACI conditions [103].

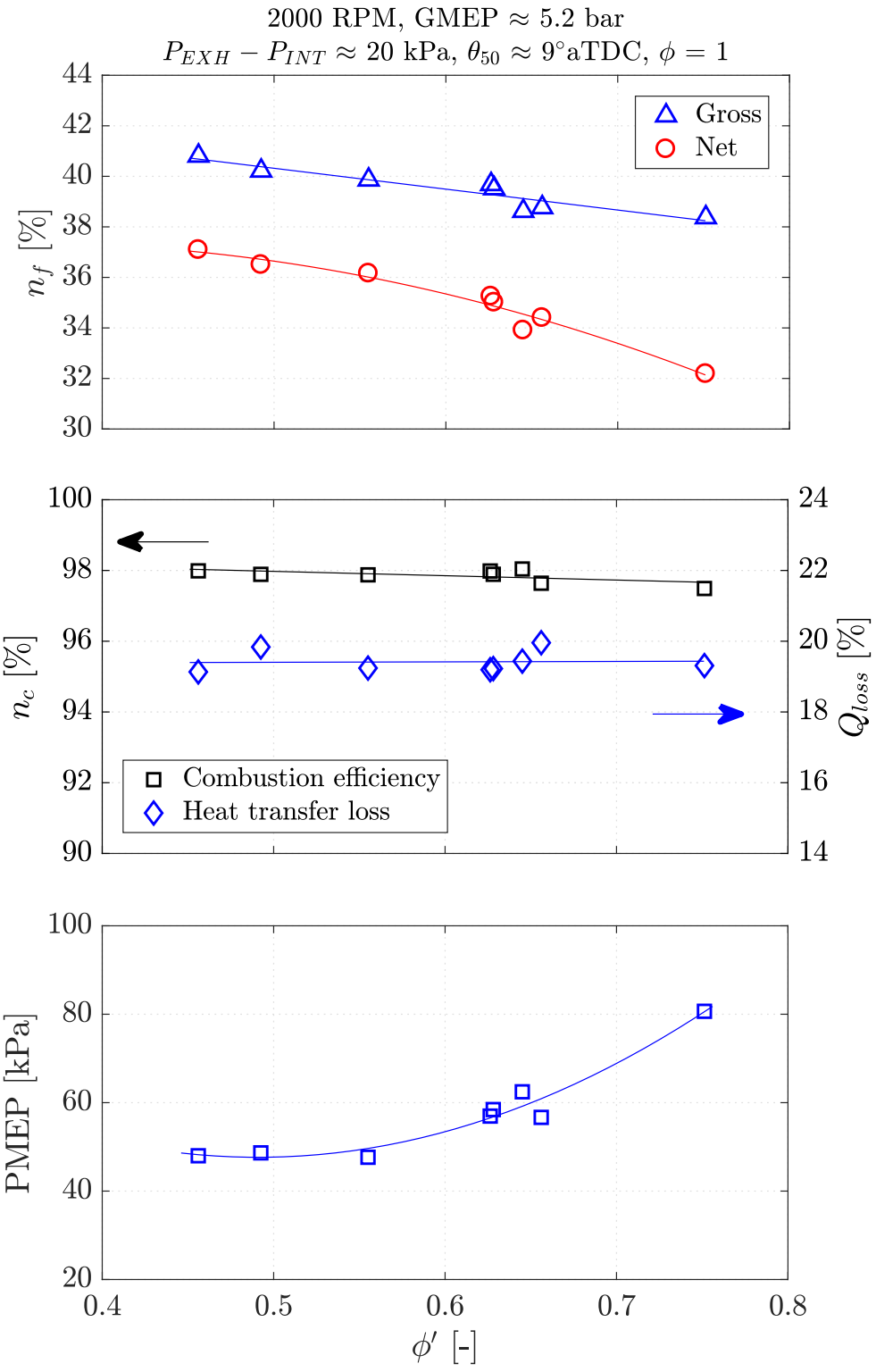

Figure 3.12: Variation of indicated fuel conversion efficiencies (top), combustion efficiency and heat transfer loss fraction estimates during the closed portion of the cycle (middle), and pumping mean effective pressure (bottom) as a function of ϕ' at constant fuel energy input.

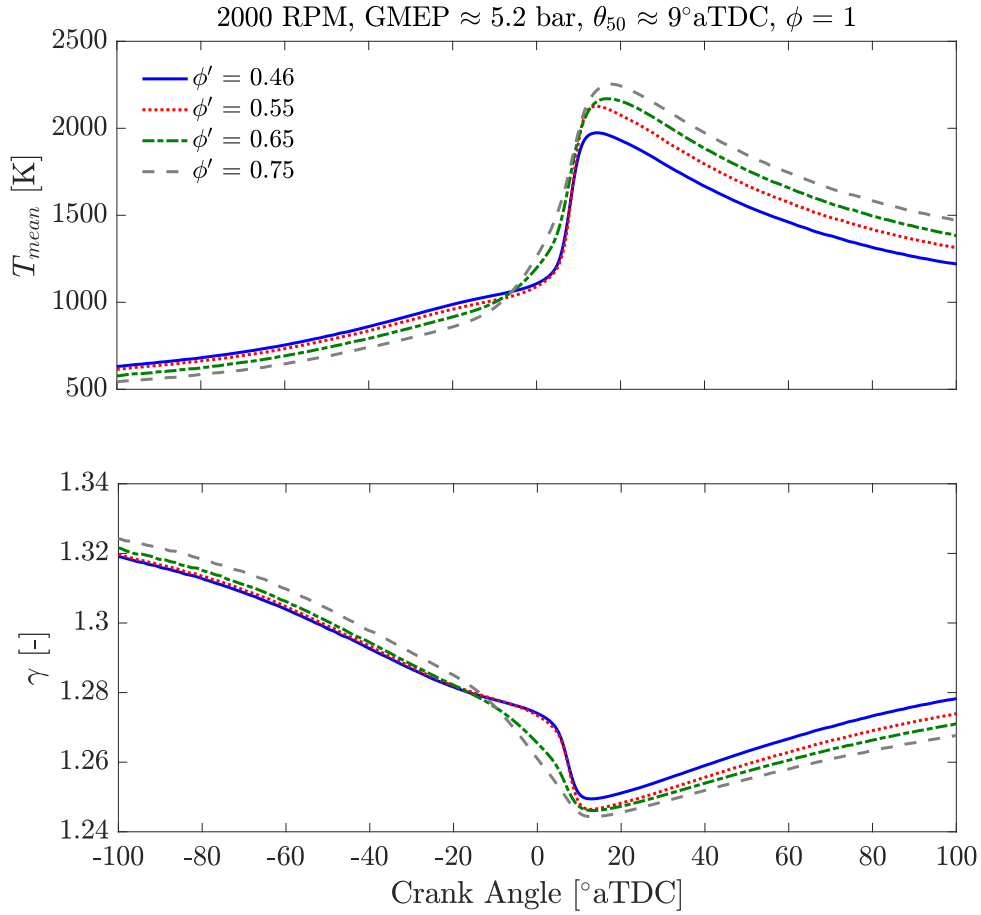

Figure 3.13: Variation of mass averaged gas temperature (top) and mean specific heat ratio of the mixture (bottom) during the close portion of the cycle as a function of ϕ' at constant fuel energy input.

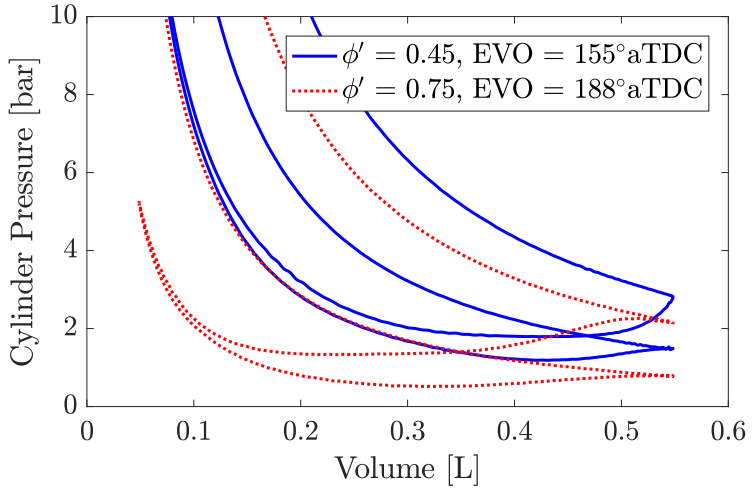

Figure 3.14: Pumping loop comparison for the two extreme ϕ' cases shown in Figure 3.12 highlighting the pumping work penalty for the high ϕ' case due to late EVO/EVC timing and asymmetric NVO.

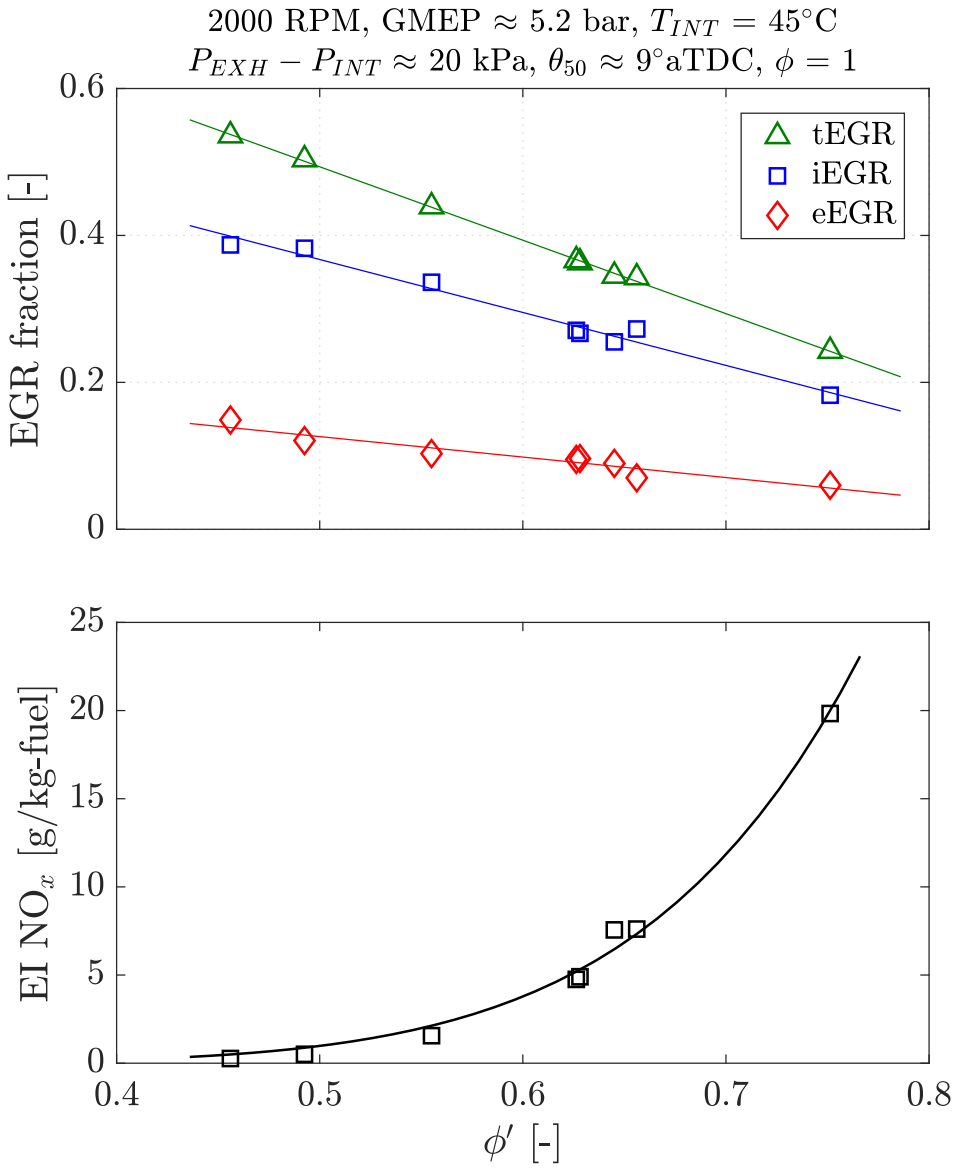

Figure 3.15: Effect of fuel to charge equivalence ratio on EGR fraction requirements (top) and emission index of NO_x (bottom). Total EGR (tEGR) in the cylinder is decomposed to internally recirculated EGR (iEGR) and externally recirculated EGR (eEGR).

3.5.2 Experiments at Constant Composition and Increasing Load using Intake Boost

In the second set of experiments ϕ' was fixed at approximately 0.55 and load was increased at constant engine speed of 2000 RPM by increasing the intake pressure. Combustion phasing was maintained at MBT timing until the ringing limit was reached, at which point combustion phasing was retarded until ringing and stability limits converged. Figure 3.16 shows the variation of indicated fuel conversion efficiencies as a function of load. Increasing the load from 300 kPa to 700 kPa resulted in a gross fuel conversion efficiency improvement of 4 absolute percentage points or an 11% increase on a relative basis. The efficiency improvements on a gross basis arise primarily from the reduced relative heat transfer loss at increased charge density, as suggested by the heat transfer loss estimates shown in Figure 3.16. A decrease in both carbon monoxide and hydrocarbon emissions was also observed as load was increased. The improvement in combustion efficiency from 96.5% to 98.5%, shown in Figure 3.16, also contributed to the overall gains in fuel conversion efficiency. Nitrogen oxide emissions were approximately constant at around 1.4 g/kg-fuel likely due to the similar maximum cylinder temperatures as composition and combustion phasing were kept approximately constant.

The ringing limit was reached at around 600 kPa GMEP, so combustion phasing was retarded until around 700 kPa load where ringing and stability limits converged. A detailed analysis of the causes leading to the excessive ringing under boosted conditions is presented in Chapter IV. The gross fuel conversion efficiency curve flattens at 700 kPa due to lower expansion work associated with late, non-optimal combustion phasing. The net fuel conversion efficiency curve follows a similar increasing trend initially but flattens earlier at around 600 kPa, beyond which it starts decreasing. The net fuel conversion efficiency gains initially are not as pronounced as those observed on a gross indicated basis due to changes in pumping work. While the pressure differential between the intake and exhaust manifolds was kept approximately constant around 25 kPa, the pumping work increases with increasing load. It can be seen in

Figure 3.17 that the pumping mean effective pressure is initially constant at low loads but increases almost exponentially as load increases. This trend in PMEP is caused by the reduced internal EGR mass requirement at higher load conditions. As the load increases at fixed composition, intake pressure increases almost proportionally which increases the reactivity of the mixture. The temperature of the charge at intake valve timing has to therefore decrease to maintain combustion phasing constant. Figure 3.17 shows how internal EGR is being traded for cooled external EGR as load is increased and intake temperature is held constant at 45°C.

A closer look at the pumping loop for the two extreme cases, shown in Figure 3.18, depicts an inefficient blowdown process for the high load case due to late EVO timing. Higher than expected cylinder pressure is observed during the start of the exhaust stroke, resulting in elevated pumping work. A similar trend in PMEP was observed for the high ϕ' cases presented in the previous section. The need to control combustion phasing using the residual gas fraction means that the EVC/EVO timing may not be ideal for a single cam profile if the load range is sufficiently large. Longer duration exhaust valve profiles would improve the blowdown process for low NVO conditions but may lead to reduced expansion work for high NVO conditions due to very early EVO timing. A tradeoff between low expansion work and poor exhaust blowdown is expected for a fixed cam profile SACI engine which only uses NVO duration to control the charge temperature at start of compression and ultimately combustion phasing.

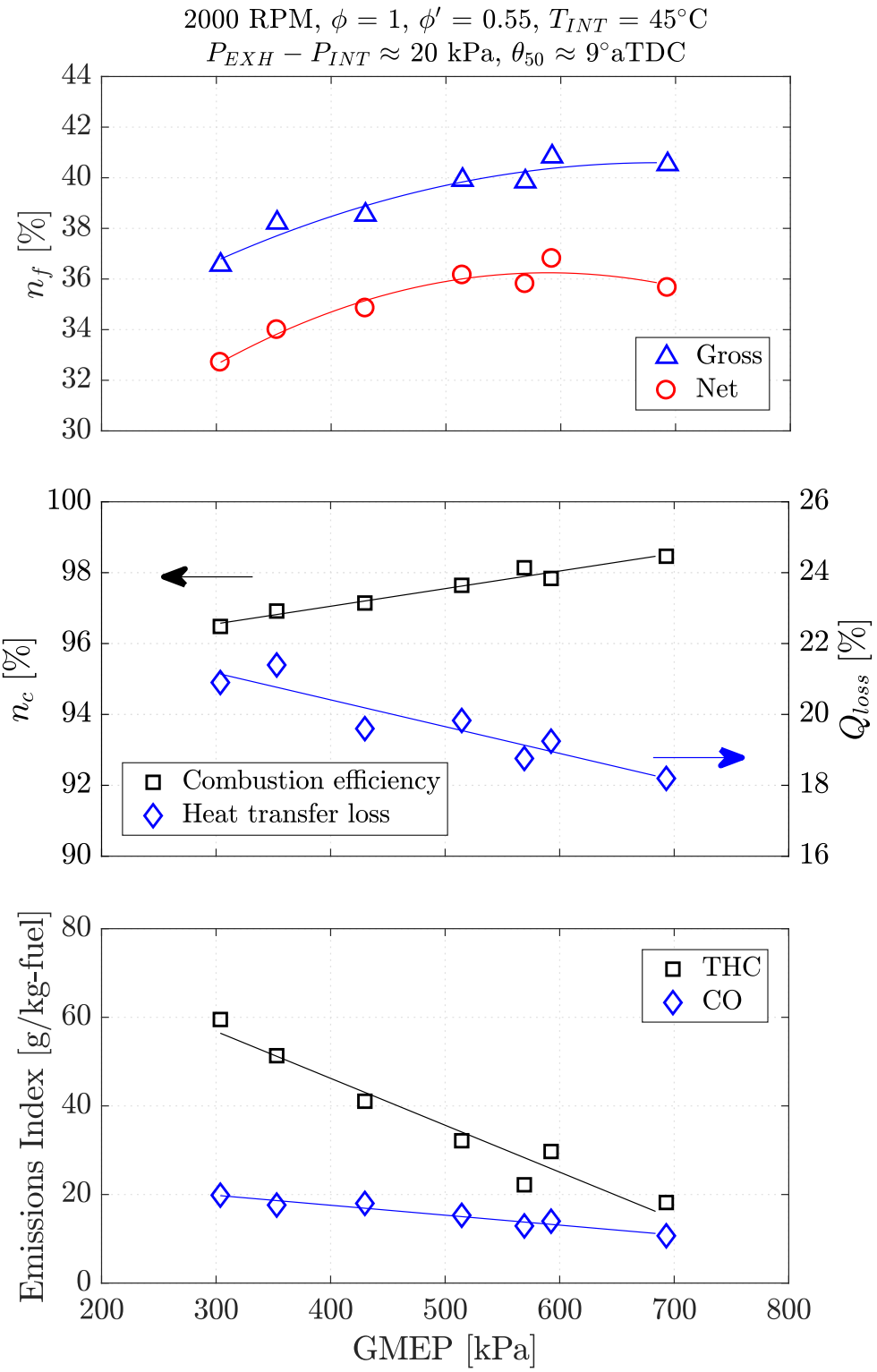

Figure 3.16: Variation of indicated fuel conversion efficiencies (top), combustion efficiency and heat transfer loss fraction estimates during the closed portion of the cycle (middle), and hydrocarbon and carbon monoxide emission indices (bottom) as a function of GMEP at constant composition and θ_{50}.

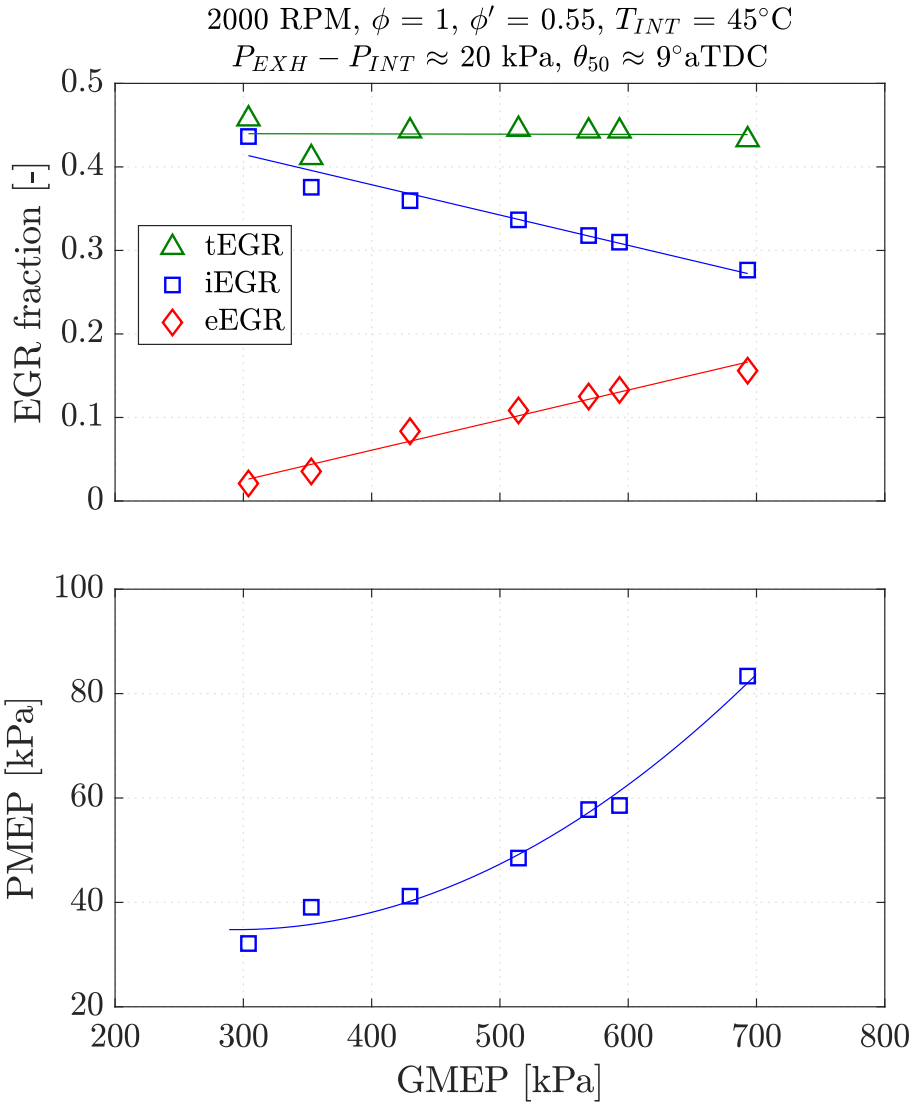

Figure 3.17: Variation of total, internal and external EGR mass fractions (top) and PMEP (bottom) as a function of GMEP at constant composition and θ_{50}.

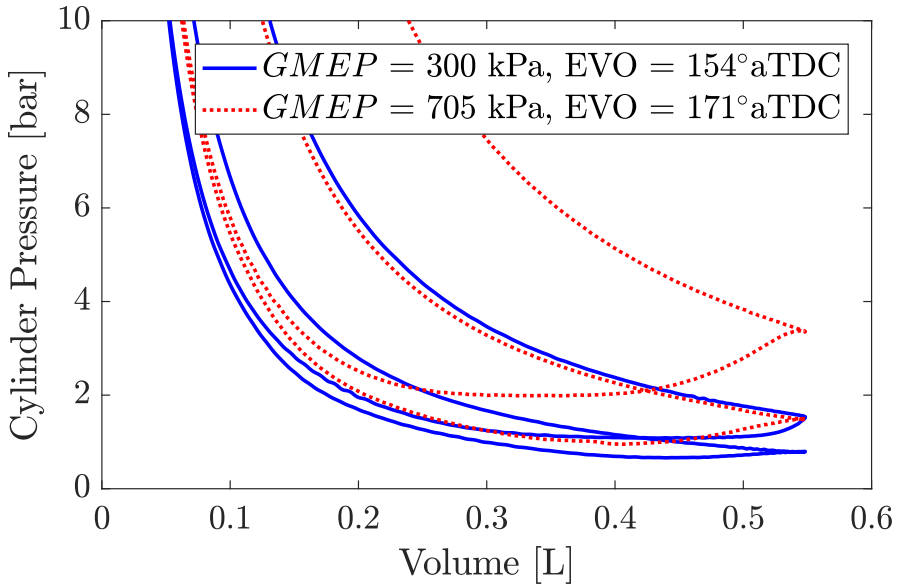

Figure 3.18: Pumping loop comparison for the two extreme GMEP cases shown in Figure 3.16 highlighting the pumping work penalty for the high GMEP case due to late EVO/EVC timing and asymmetric NVO.

3.6 Impact of Engine Speed on SACI Combustion Rates

The role of turbulence on premixed combustion rates has been well documented in the literature. The in-cylinder flow in internal combustion engines is highly turbulent and turbulence wrinkles the flame front, thereby increasing its surface-to-volume ratio [104]. A larger flame surface area in turn leads to higher burning velocities. The TDC turbulent intensity has been shown to approximately scale with mean piston speed [105], which scales with engine speed for a constant stroke length. Persson et al. [106] demonstrated faster early flame expansion speeds in SACI by increasing turbulence levels through higher swirling motion using inlet valve deactivation. However, a careful investigation of the effect of engine speed on SACI heat release rates and the tradeoff between flame propagation and autoignition is still missing in the literature. Controlled experiments were designed to investigate the effect of engine speed on SACI combustion rates at high EGR dilution levels. The fueling rate per cycle, mixture composition, intake temperature, autoignition timing and spark timing were maintained constant. As engine speed was increased from 1500 to 2500 RPM, intake pressure was slightly increased (≈4 kPa) to maintain stoichiometry and $\phi' = 0.64$ partly due to higher flow frictional losses. Since spark timing was held constant, small adjustments to the ratio of internal to external EGR were made to adjust the temperature of the charge at IVC, in order to target autoignition at 7°aTDC. Spark timing was fixed at 35.5°bTDC and intake valve timings were constant. The details of the experimental conditions can be seen in Table 3.1.

Figure 3.19 shows the effect of engine speed on cylinder pressure, unburned gas temperature and heat release rate. Higher engine speed cases exhibit higher temperature at IVC by approximately 60K, a difference which continues until the onset of autoignition. The unburned gas temperature increase can be explained by the fact that shorter ignition delay are needed at higher engine speeds to maintain autoignition timing constant. Since temperature at IVC is higher and fuel energy per cycle is constant, a small increase in intake pressure ($\approx$ 4%) is needed at higher engine speeds to match the volumetric efficiency and thus composition at IVC among all

cases. This small change in intake pressure is depicted in the cylinder pressure traces. The overall effect of engine speed on the heat release profiles is minor on a crank angle basis. The initial flame based heat release rates are similar between the cases and peak heat release rates vary by less than 4%. However, on a time basis the peak heat release rates and maximum pressure rise rates scale with engine speed, as shown in Table 3.1. As a result, ringing intensity increases from 2.6 to 6.5 MW/m^2, exceeding the ringing limit. Under the conditions investigated, RI scales with the time based maximum pressure rise rate to the power of 2, so the increase in RI is much more pronounced. A similar experiment was performed at $\phi' = 0.55$, which agreed with the behavior discussed above and has not been included here for clarity. The maximum GMEP at 1500 RPM, was therefore expanded to approximately 780 kPa at P_{INT} = 150 kPa and $\phi' = 0.61$, where maximum pressure rise rate and ringing intensity and COV_{NMEP} were 7.1 bar/cad, 5.8 MW/m^2 and 2.5%, respectively.

Parameter	*Case1*	*Case 2*	*Case 3*
Fuel mass injected [mg/cycle/cyl]		15.2	
Intake temperature [°C]		45	
Start of injection [°aTDC]		-330	
Intake valve opening/closing timing [°aTDC]		-265 / -161	
Spark timing [°aTDC]		-35.5	
Autoignition timing [°aTDC]		7	
Fuel injection pressure [MPa]		7	
Engine speed [RPM]	1500	2000	2500
Intake pressure [bar]	0.98	1.01	1.02
Fuel-to-air equivalence ratio, ϕ [-]	1.00	0.99	0.99
Fuel-to-charge equivalence ratio, ϕ' [-]	0.65	0.64	0.64
Combustion phasing, θ_{50} [°aTDC]	9.8	9.2	8.9
Internal EGR mass fraction [-]	0.27	0.26	0.25
External EGR mass fraction [-]	0.08	0.10	0.11
Maximum pressure rise rate [bar/deg]	3.8	3.9	3.7
Maximum pressure rise rate, [MPa/ms]	3.5	4.7	5.5
Ringing intensity, [MW/m^2]	2.6	4.7	6.5

Table 3.1: Experimental conditions for the engine speed study at $\phi' \approx 0.65$, constant intake manifold temperature, spark advance, fuel mass injected per cycle and end-gas autoignition timing.

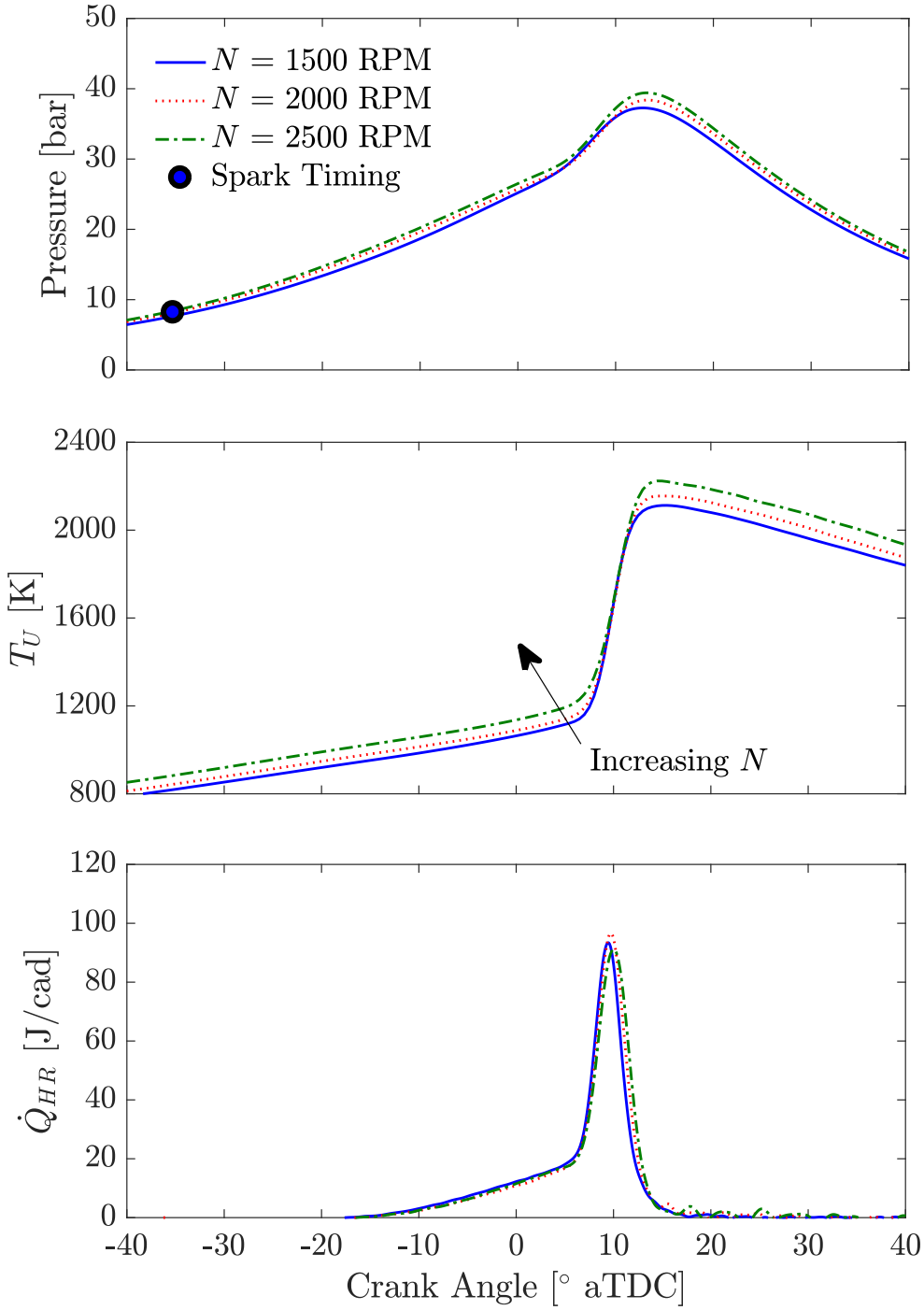

Figure 3.19: Effect of engine speed on cylinder pressure (top), unburned gas temperature evolution (middle) and gross heat release rate (bottom) at constant composition, load and end-gas autoignition timing.

3.7 Effects of Fuel Injection Timing and Fuel Pressure on SACI Heat Release

Fuel injection during the negative valve overlap period under high temperature, low oxygen conditions has been shown to produce considerable concentrations of fuel reformed species (H_2, CO, CH_4) under stoichiometric conditions with 20% EGR dilution [107]. The concentration of the reformed H_2 was observed to correlate with the time-temperature integral, meaning that higher temperatures and earlier injection timings (i.e. longer residence time) both promoted the reforming reactions. In SI combustion, hydrogen and CO reformates have been successfully used to increase the EGR dilution tolerance [108–110]. One of the reasons for the benefits observed is related to the higher flame front propagation rates linked to the use of hydrogen. In SACI, faster initial flame burn rates driven by sufficient concentrations of hydrogen reformate could extend high load limit by reducing the end-gas absolute energy content as well as end-gas burn rates. To test this hypothesis, start of injection timing was varied from 420°bTDC to 270°bTDC while fixing fueling rate, intake temperature, intake valve timing and spark timing. As SOI was varied, small variations in combustion phasing were observed, even though all other actuators were held constant. This observation is consistent with previous work, where SOI timing has been used as a fine control knob for HCCI combustion phasing [111, 112]. Even if there is no heat released/absorbed due to chemical reactions during NVO, the fuel injection event will reduce the specific heat ratio of the mixture, which will affect the temperature change during the re-compression event and eventually the mixture temperature at IVC timing. Changes in EVC timing up to 4 CAD were required to match combustion phasing for all cases when SOI was changed from 420°bTDC to 270°bTDC. The earliest injection timing in this study was limited by the EVC timing. Any further advancement in SOI timing than 420°bTDC was avoided to ensure that no fuel escapes the combustion chamber through the exhaust valves prior to the main combustion event.

Figure 3.20 displays the heat release rate curves for all experimental conditions at

similar combustion phasing. It can be seen that varying the start of injection timing has minimal impact on the heat release profile, once combustion phasing is matched. The initial slow heat release curves overlap with each other resulting in a similar mass fraction burned at the onset of autoignition. The autoignition heat release profiles are also very similar as a function of SOI. Peak heat release rates from two experimental sets at $\phi' = 0.55$ and $\phi' = 0.65$ are plotted as a function of SOI in Figure 3.21, which displays minimal changes in peak heat release rate for both ϕ' due to changes in SOI timing. Under the conditions investigated, the variation of injection timing and in-cylinder fuel reforming, if any, during NVO has negligible impact on the SACI heat release rates.

Direct injection (DI) of fuel into the cylinder early into the intake stroke was used for all the results presented in this work, with aim to achieve a nearly homogeneous mixture. Fuel stratification of the mixture near the spark plug or during autoignition has been observed to influence the heat release rate in low temperature combustion [113–115]. To investigate the effect of fuel pressure on heat release profile and assess the homogeneity of the mixture for early DI experiments, fuel injection pressure was varied from 70 bar to 150 bar at a commonly visited operating condition. Spark timing was set at 40° bTDC which was used for many of the data presented in this thesis. The mixture was kept at stoichiometry and ϕ' was fixed at 0.55. Figure 3.22 displays the heat release rate curves for three cases at 70 bar, 110 bar and 150 bar injection pressure. It can be observed that minimal changes in the SACI heat release rate were observed by doubling the fuel injection pressure, suggesting that, under the conditions investigated, fuel stratification, if any, due to the direct injection of fuel early in the intake stroke has negligible impart on the SACI heat release rates.

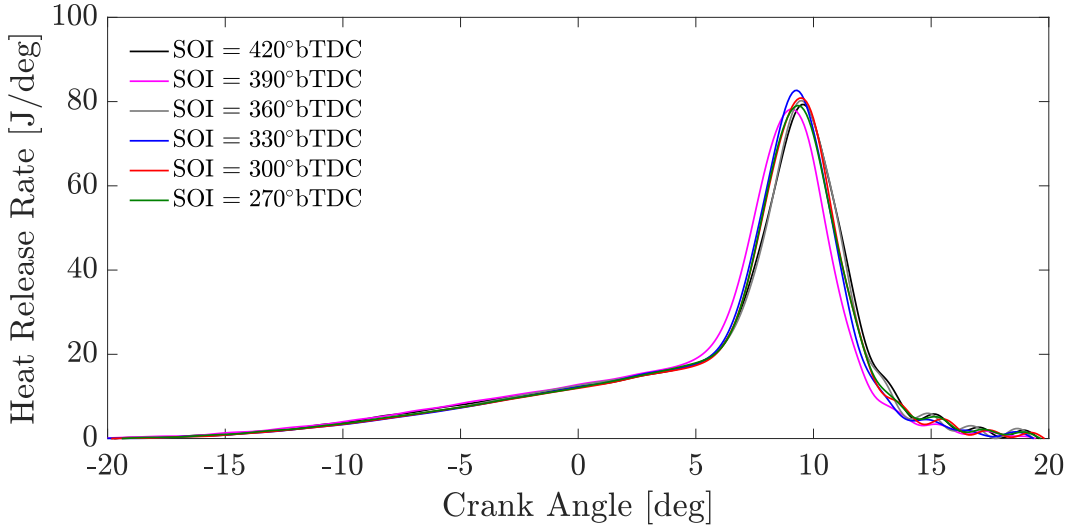

Figure 3.20: Effect of fuel injection timing on SACI heat release at constant combustion phasing and spark timing.

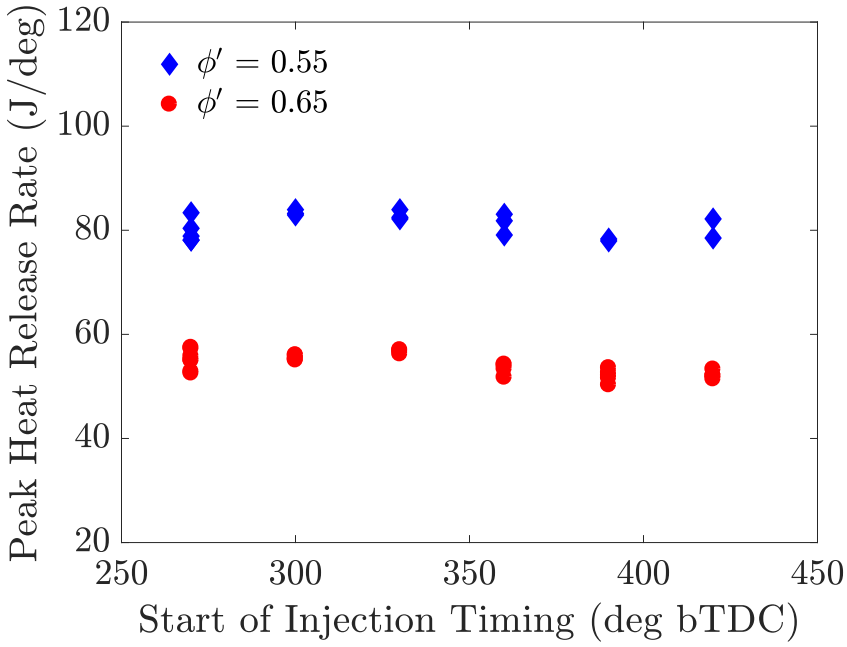

Figure 3.21: End-gas energy and burn rate effects on maximum pressure rise rate for the $\phi' = 0.55$ intake pressure sweep.

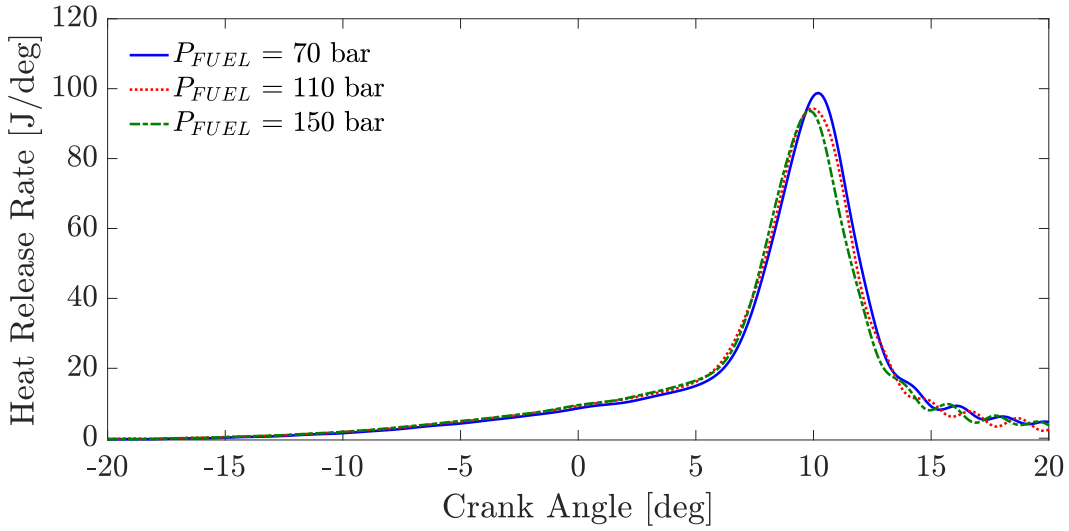

Figure 3.22: Effect of fuel pressure on SACI heat release rates at stoichiometric conditions, ϕ'=0.55, constant spark advance and constant combustion phasing.

3.8 Summary

An analytical approach starting from the conservation of energy for a closed system was used to better understand the maximum pressure rise rate conditions in SACI. It was shown that the maximum pressure rise rate should be approximately proportional to the end-gas energy at the onset of autoignition and inversely proportional to an autoignition characteristic duration ($\delta\theta_{AI}$), assuming that there is an orderly transition from flame propagation to autoignition and maximum pressure rise rate phasing is constant. The autoignition characteristic duration was defined as the ratio of the estimated end-gas energy released during autoignition to the peak gross heat release rate, which were derived from the pressure-based heat release analysis. The typical 10 - 90% and 25 - 75% global burn durations did not always scale with $\delta\theta_{AI}$ due to variations in the flame and autoignition burn fractions. The global burn durations were thus not appropriate to describe the SACI autoignition rate, which causes the excessive pressure rise rates observed at high loads.

Load sweeps were performed at 2000 RPM and constant intake pressures up to 150 kPa by increasing ϕ' while maintaining stoichiometric conditions. The maximum intake pressure was limited to 150 kPa due to the hardware configuration. At 2000 RPM, the maximum GMEP of 705 kPa was reached at an intake pressure of 150 kPa and a $\phi' = 0.57$, where the ringing and stability limits converged. At the maximum load condition, a combustion phasing (θ_{50}) retard from 10°aTDC to 13°aTDC resulted in a 50% decrease in ringing intensity, which was primarily due to a decrease in the maximum pressure rise rate in the cycle. The significant decrease in the maximum pressure rise rate was observed primarily due to a slower autoignition burn rate but also due to the higher volume expansion rate at later θ_{50}.

A gross fuel conversion efficiency improvement of approximately 3% absolute (8% relative) was demonstrated for an approximately constant load condition by reducing ϕ' from 0.75 to 0.45 at optimal combustion phasing. The gross efficiency benefits were primarily attributed to better thermodynamic properties of the diluted mixture. An increase in load from 300 kPa to 700 kPa GMEP at constant composition ($\phi = 1$, ϕ'

= 0.55) and θ_{50} led to an efficiency improvement of approximately 4% absolute (10% relative), which was explained by an equivalent drop in the estimated heat transfer losses. For the given valvetrain design and operation used in work, high pumping work was observed under high ϕ' and/or high load conditions primarily due to late EVO timing but also due to asymmetric NVO. Lower internal EGR requirements under those conditions led to later EVO/EVC timing, which caused an inefficient blowdown process. While these trends are dependent on valvetrain design and charge preheating method, they highlight potential inefficiencies in the breathing process for a fixed cam profile NVO engine operating under a large load range within SACI.

Higher cyclic variability in combustion phasing ($\sigma_{\theta_{50}}$) was observed when the mixture was ignited earlier in the compression stroke and the IVC temperatures were decreased, even though mean combustion phasing was near optimal timing (θ_{50} = 9.7° aTDC). The increase in $\sigma_{\theta_{50}}$ eventually led to a rapid increase in COV_{NMEP} values due to very few cycles exhibiting very late/slow autoignition or no autoignition at all. The variability in θ_{50} was driven by the variability in autoignition timing, which in turn correlated well with θ_{02}. Under the conditions investigated, the cyclic variability was attributed to variability in the time between the spark discharge and measureable heat release from the pressure trace. It was shown that high cyclic variability in autoignition timing can also lead to excessive peak heat release rate cycles due to faster end-gas autoignition close to TDC, where cylinder volume is smaller, volume expansion rates are lower and the mixture pressure and temperature are higher.

The effect of engine speed on SACI heat release was investigated at constant composition, fueling rate per cycle, autoignition timing and spark timing. Increasing engine speed from 1500 RPM to 2500 RPM necessitated higher unburned gas temperature by approximately 60K to match autoignition timing. The overall effect of engine speed on the heat release rate was negligible on a crank angle basis. However, maximum pressure rise rates scaled with engine speed on a time basis leading to excessive ringing intensity at 2500 RPM under the conditions investigated. This allowed an increase in the high load limit to approximately 780 kPa GMEP at 1500 RPM, P_{INT} = 150 kPa and ϕ' = 0.61.

CHAPTER IV

Boost Pressure Effects on SACI Burn Rates

4.1 Background and Experimental Objective

A number of reasons motivate the need to investigate the effect of boosting on SACI combustion. In the context of efficient combustion, boosting has been commonly used in the past decade to increase the specific power output of the conventional spark ignition engine in order to leverage the thermal efficiency benefits from downsizing and downspeeding [3, 116, 117]. These efficiency benefits arise primarily from de-throttling, reduced relative heat transfer and increased mechanical efficiency. In naturally-aspirated SACI combustion, the engine can be operated unthrottled and load control can be achieved by modulating the levels of dilution [6, 56, 118], hence efficiency benefits due to de-throttling would not be applicable under the boosted SACI regime. However, the effects of reduced relative heat transfer losses and improved mechanical efficiency could still offer potential efficiency gains. Boosted SACI operation can also work synergistically with boosted SI in a multi-mode combustion engine, which is very relevant due to the recent trend with downsized-boosted spark ignition engines [8, 119, 120]. Furthermore, previous experimental studies on naturally aspirated SACI have shown that EGR dilution levels between of 30 - 60% can be used effectively, offering gross thermal efficiency improvements from dilution, as described in detail in section 1.3.3. However, increasing the engine load at unthrottled conditions implies that EGR mass has to be displaced by fuel and air masses, thus limiting EGR dilution levels. As a result, the efficiency gains from low temperature

combustion diminish and fuel-to-charge equivalence ratios reach values where EGR dilute SI combustion could be employed without the combustion control complexities associated with SACI [46]. Boosting can thus be used to maintain the high EGR dilution levels and the associated thermodynamic benefits, while increasing the load.

In section 3.2, it was shown that the maximum load under boosted SACI combustion is limited due to excessive pressure rise rates. There is a need to get a better understanding of the effect of pressure on the SACI combustion process, particularly the underlying processes that lead to excessive pressure rise rates. The effect of intake pressure on the hybrid combustion mode of SACI has yet to be investigated experimentally. The complex nature of SACI combustion coupled with the complexity of the mutually dependent influences of the large number of different operation parameters in a real engine makes this a challenging task. The objective of the experiments in this study is to isolate the effect of pressure on the SACI combustion process from other effects such as combustion phasing, EGR dilution, fuel-to-air equivalence ratio, mass fraction burned at the onset of autoigntion and effective compression ratio. A detailed analysis of the experimental data is conducted to understand the effect of pressure on the resulting onset of autoignition, the tradeoff between the deflagrative and auto-ignition heat release rates, the peak heat release rate that ultimately determine the peak pressure rise rates in every cycle. A better understanding of the effect of pressure on SACI can then navigate the efforts for extension of the load limit and hence the potential for further thermal efficiency gains.

4.2 Experimental Approach

In this study SACI experiments were performed at increasing intake pressure, while maintaining a fixed mixture composition. As intake pressure was increased, the masses of fuel, air and EGR were increased at the same rate, therofore increasing the charge density but maintaining a constant composition. The fuel-to-air equivalence ratio, ϕ, of the mixture was maintained at stoichiometry and dilution was achieved by a mixture of internal and external EGR. The composition of EGR was fixed as fuel-to-air equivalence ratio was maintained constant. Fuel-to-charge equivalence ratio, ϕ', was fixed at 0.55, where SACI has been shown to be effective under naturally aspirated conditions [56]. A schematic showing the cylinder constituents at increasing intake pressure is shown in Figure 4.1.

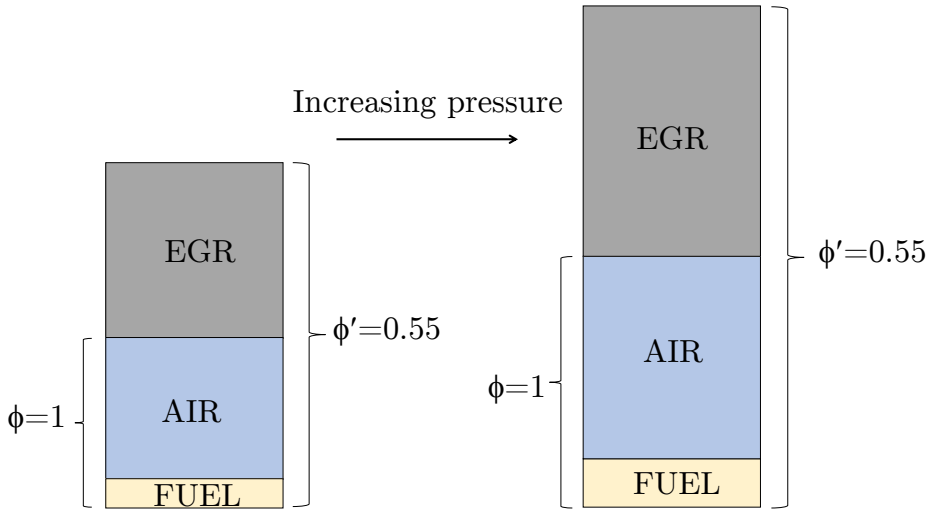

Figure 4.1: Schematic showing the breakdown of the cylinder mass constituents during the boost pressure experiment at $\phi' = 0.55$. Total column height represents the sum of the masses of the constituents (not to scale)

To remove the effect of effective compression ratio and since the burn rates during the main combustion event are of interest in this study, intake valve opening/closing (IVO/IVC) timings were fixed at 265/161°bTDC, respectively. Spark advance was fixed at 40.5°bTDC. Exhaust valve closing (EVC) timing was adjusted to vary the mass of internal EGR trapped from the previous cycle. As a result, the mean tem-

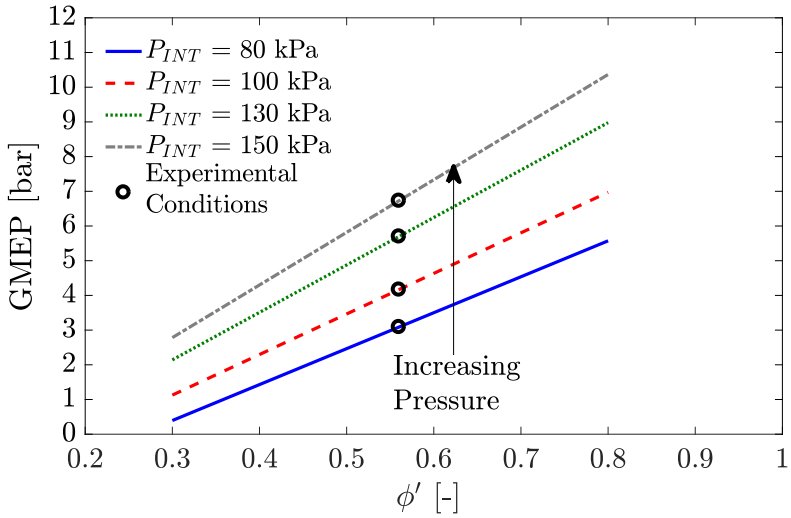

Figure 4.2: Experimental conditions for the $\phi' = 0.55$ boost pressure experiment shown on a load-ϕ' diagram. Constant intake pressure lines are best fit lines from SACI experimental data collected in this work.

perature of the mixture at intake valve closing (IVC) was adjusted to maintain the crank angle at 50% fuel mass burned (θ_{50}) at around 9°aTDC, which is at the optimal efficiency for the particular engine under the conditions investigated. The backpressure valve was adjusted to maintain an exhaust pressure close to 0.2 bar higher than intake pressure to drive the required external EGR rates. This resulted in a modest but realistic overall turbocharger efficiency around 25 - 30%. The detailed values of the experimental conditions for this study are listed in Table 4.1.

Figure 4.2 shows the experimental conditions on a load (i.e. GMEP) against EGR dilution (i.e. ϕ') diagram to demonstrate the experimental approach. Constant intake pressure lines for ϕ' ranging from 0.3 to 0.8 are overlaid on the GMEP-ϕ' graph by fitting experimental results at similar combustion phasing ($\theta_{50} \approx 9$°aTDC). The exact GMEP at each ϕ' is primarily determined by the volumetric efficiency at each operating condition which will be primarily a function of the gas temperature at IVC. At each intake pressure level, the temperature at IVC will in turn be determined by the parameters that will ensure that autoignition of the mixture will occur near TDC such as effective compression and fuel properties. The use of a higher compression ratio engine or a more reactive fuel is expected to shift the constant intake pressure lines upwards as the IVC temperature would decrease and hence volumetric efficiency

would increase.

Table 4.1: Experimental conditions for the SACI boost pressure experiment at fuel-to-charge equivalence of 0.55 and constant intake temperature[1].

Parameter	*Case1*	*Case 2*	*Case 3*	*Case 4*
Engine speed [RPM]		2000		
Spark timing [°aTDC]		-40.5		
Start of injection [°aTDC]		-330		
Intake valve opening/closing Timing [°aTDC]		-265 / -161		
Fuel injection pressure [bar]		70		
Fuel flow rate [mg/cycle/cylinder]	9.4	12.3	16.0	19.9
Combustion phasing, θ_{50} [°aTDC]	9.6	9.5	9.3	9.8
Fuel-to-air equivalence ratio, ϕ [-]	0.99	0.99	1.00	0.99
Fuel-to-charge equivalence ratio, ϕ' [-]	0.55	0.56	0.55	0.56
Intake pressure [bar]	0.80	1.00	1.30	1.51
Exhaust pressure [bar]	1.05	1.15	1.51	1.75
Internal EGR mass fraction [-]	0.43	0.36	0.32	0.27
External EGR mass fraction [-]	0.02	0.08	0.13	0.17
Exhaust valve opening timing [°aTDC]	174	177	183	193
Exhaust valve closing timing [°aTDC]	278	281	287	297

[1]All timings are referenced to combustion TDC. Valve timings are defined at 0.2 mm opening.

4.3 Effect of Boost Pressure on SACI Heat Release

Figure 4.3 displays the cylinder pressure curves for all 4 experimental cases. During the intake boost sweep from 80 - 150 kPa, GMEP increases from 299 kPa to 700 kPa, while cylinder pressure close to autoignition increases from approximately 20 bar to 40 bar. Figure 4.4a shows the variation of internal and external EGR during the intake pressure sweep. As intake pressure is increased at constant composition and intake temperature, high temperature internally recirculated EGR (iEGR) is being traded for low temperature externally recirculated EGR (eEGR) to maintain the total EGR fraction constant. The reactivity of the mixture increases with higher pressure and therefore less high temperature internal residual is required to maintain a constant θ_{50}. As seen in Figure 4.4b, at the maximum intake pressure of 150 kPa excessive pressure rise rates were observed reaching 6 bar/cad, which corresponded to a ringing intensity of approximately 8 MW/m^2.

Figure 4.5 displays from top to bottom global heat release rate curves, burn rate curves and cumulative heat release curves. Rate of heat release plots depict a significant increase in peak rate of heat release with increasing intake pressure. As the intake pressure increases from 80 kPa to 150 kPa, peak heat release rate increases from approximately 39 J/cad to 154 J/cad. Looking at the initial slow heat release phase, there is a higher amount of energy being release by the propagating flame at increasing intake pressure. The total mass and, hence, total energy of the mixture increases with higher intake pressure, so the increase in absolute energy release is expected due to a higher mass burning flux. When normalizing the heat release rate by the total heat released for each case, the initial burn rates collapse with each other indicating a similar burn rate until autoignition. However, the peak burn rate during the end-gas autoignition phase increases almost proportionally with intake pressure.

The locations of 5% mass fraction burned, 10% burned, auto-ignition, 25% burned, 50% burned, 75% burned and 90% burned are plotted in Figure 4.6. As intake pressure is increased from 0.8 bar to 1.5 bar, the location of 5% burned (θ_{05}) is later by approximately 1.5 CAD, which leads to a similar retard in the burn rate until

the onset of autoignition. While the onset of autoignition is retarded by 1.5 CAD, θ_{50} is matched between the cases due to faster autoignition burn rates with higher pressure. It is worth noting that the 10% - 90% burn duration (θ_{10-90}) decreases by approximately 20% from 24.5 CAD to 20 CAD, which does not reflect the increase in peak autoignition burn rate by a factor of 2.

Figure 4.7 shows the evolution of the estimated unburned gas temperature during the intake boost sweep. Higher boost mixtures required lower gas temperature at IVC by approximately 35 K. This offset remained approximately constant at spark timing as well as the estimated autoignition timing.

The mass fraction of fuel burned at the onset of autoignition is maintained constant around 20%, as seen in Figure 4.8b. However, the end-gas energy during autoignition increases linearly with pressure, since the total energy of the mixture increases. Figure 4.8a shows the variation of the characteristic autoignition duration ($\delta\theta_{AI}$) and the estimated end-gas energy at the start of autoignition with increasing intake pressure. With higher intake boost, the estimated end-gas energy approximately doubles while the autoignition charasteristic duration approximately halves. Using the relationship between the peak heat release rate and maximum pressure rise rate (see Figure 3.1), we can demonstrate the effects of end-gas energy during autoignition and end-gas autoignition rate on the maximum pressure rise rate, as shown in Figure 4.9.

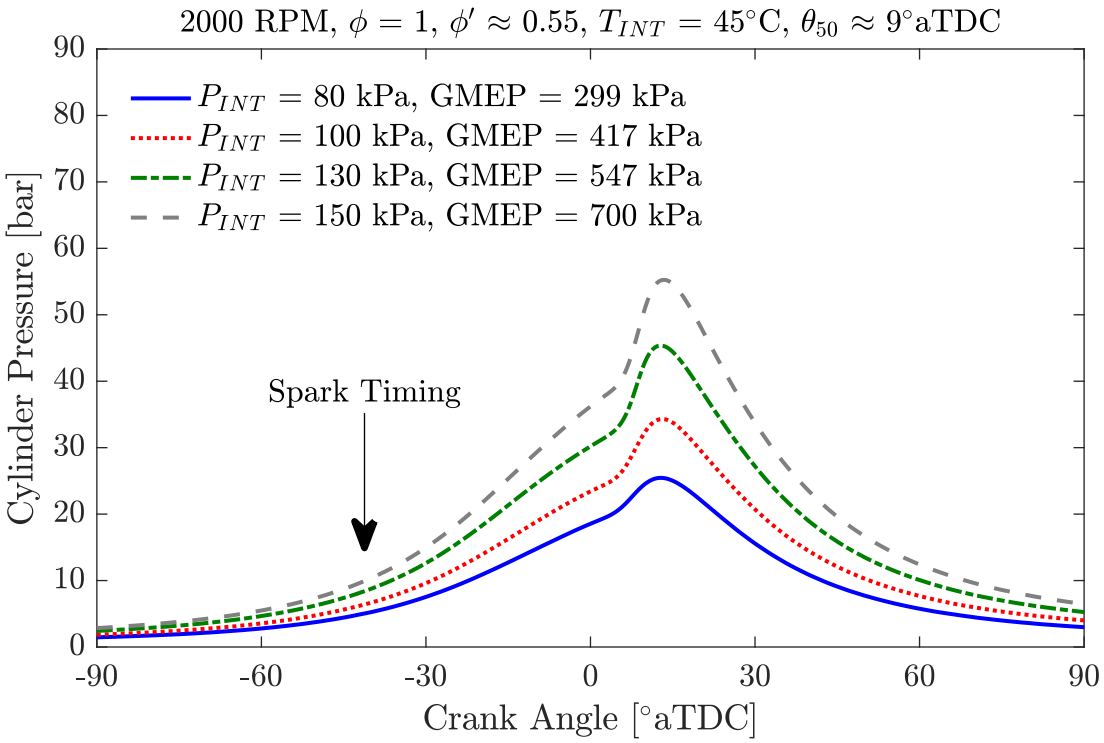

Figure 4.3: Cylinder pressure traces for the boost pressure sweep at constant composition, combustion phasing, spark timing, intake temperature and engine speed.

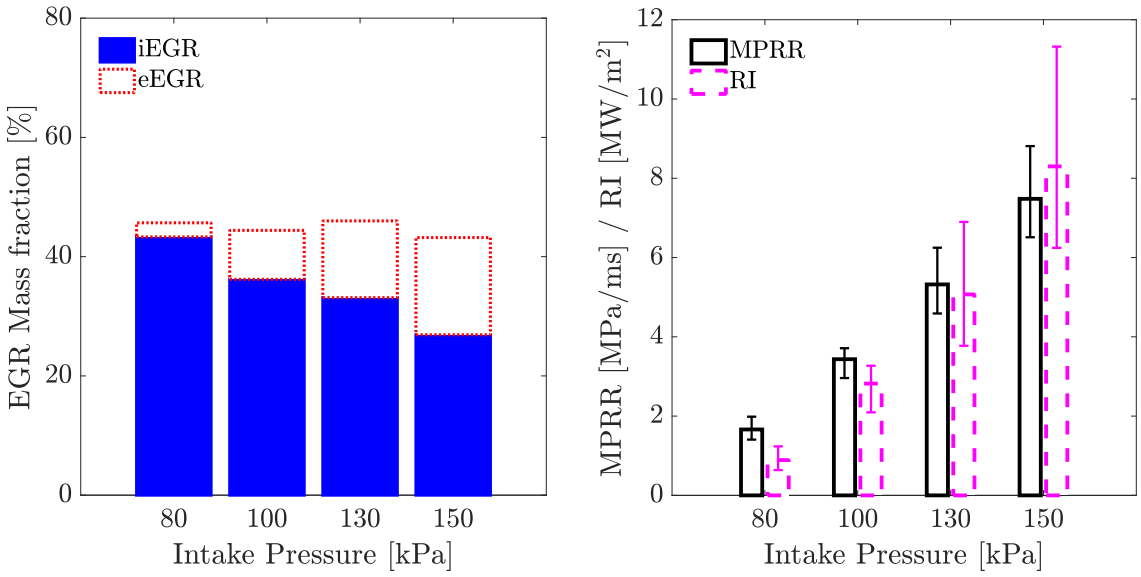

Figure 4.4: Variation of (a) internal EGR and external EGR fractions and (b) ringing intensity and maximum pressure rise rates as a function of intake pressure at constant composition, combustion phasing, spark timing, intake temperature and engine speed.

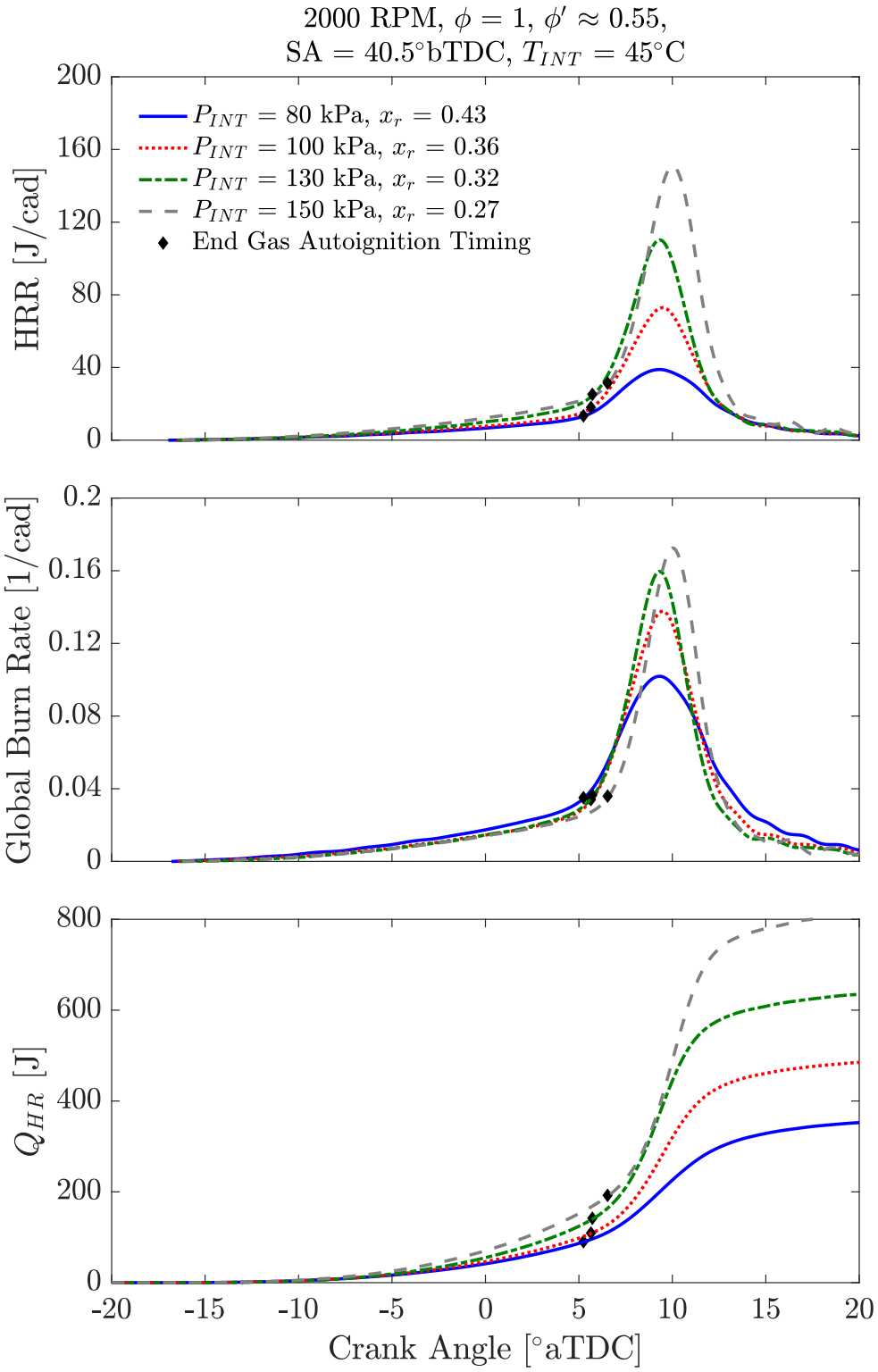

Figure 4.5: Gross heat release rate (top), global burn rate (middle) and cumulative heat release (bottom) for the $\phi' = 0.55$ intake pressure sweep at constant engine speed, composition and combustion phasing.

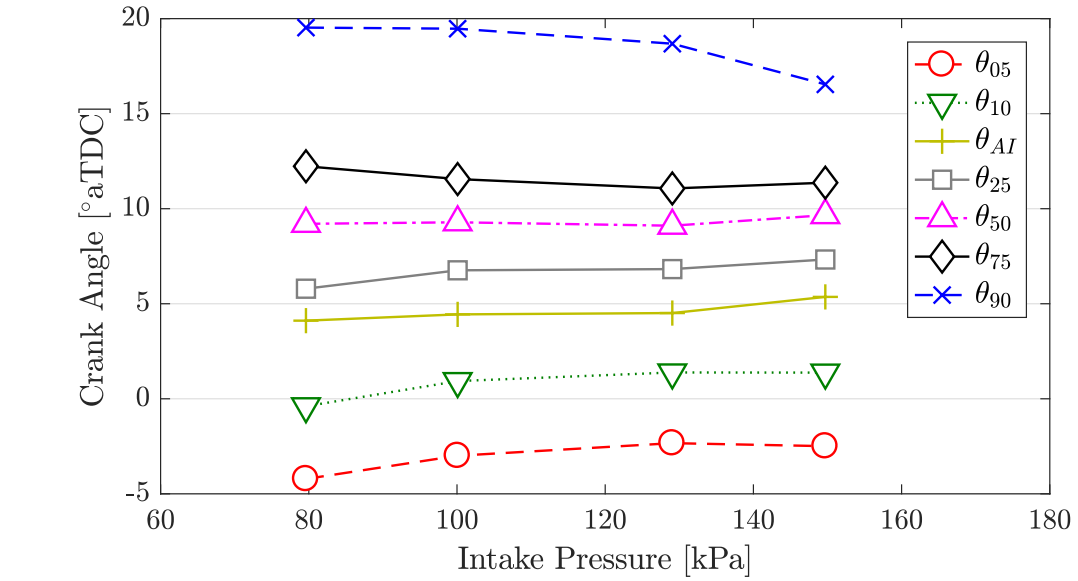

Figure 4.6: Crank angle locations at the time of 5% mass fraction burned, 10% burned, auto-ignition, 50% burned, and 90% burned for the $\phi' = 0.55$ intake pressure sweep at constant engine speed, composition, combustion phasing.

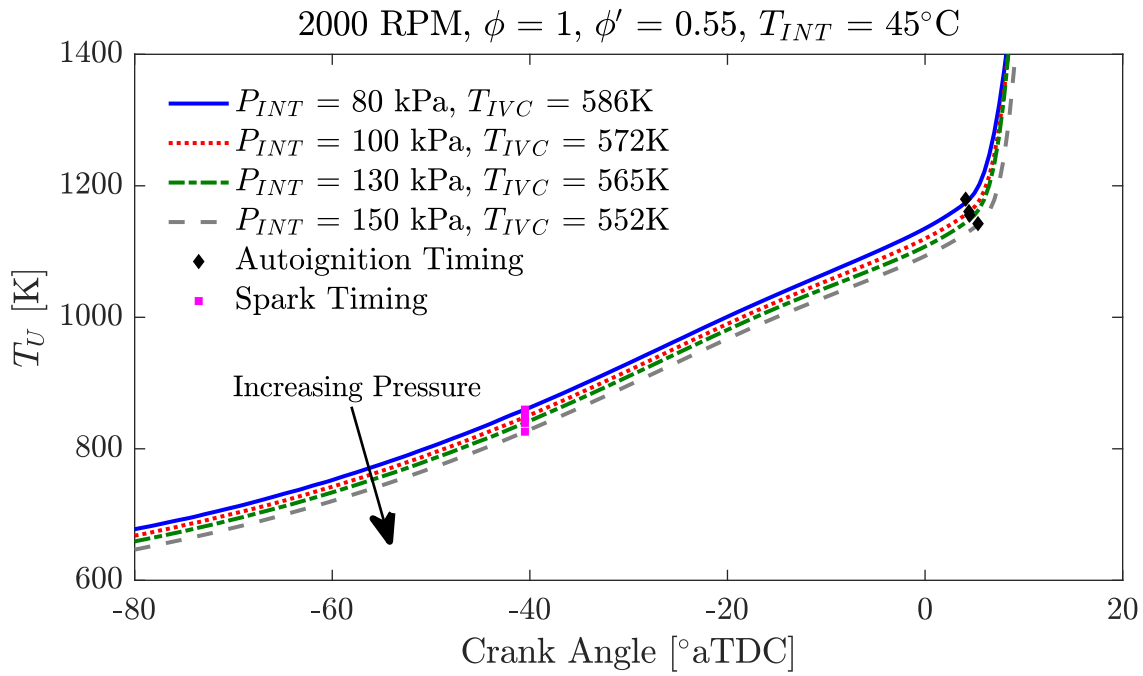

Figure 4.7: Evolution of the estimated mass-averaged unburned gas temperature for the $\phi' = 0.55$ intake pressure sweep at constant engine speed, composition, combustion phasing.

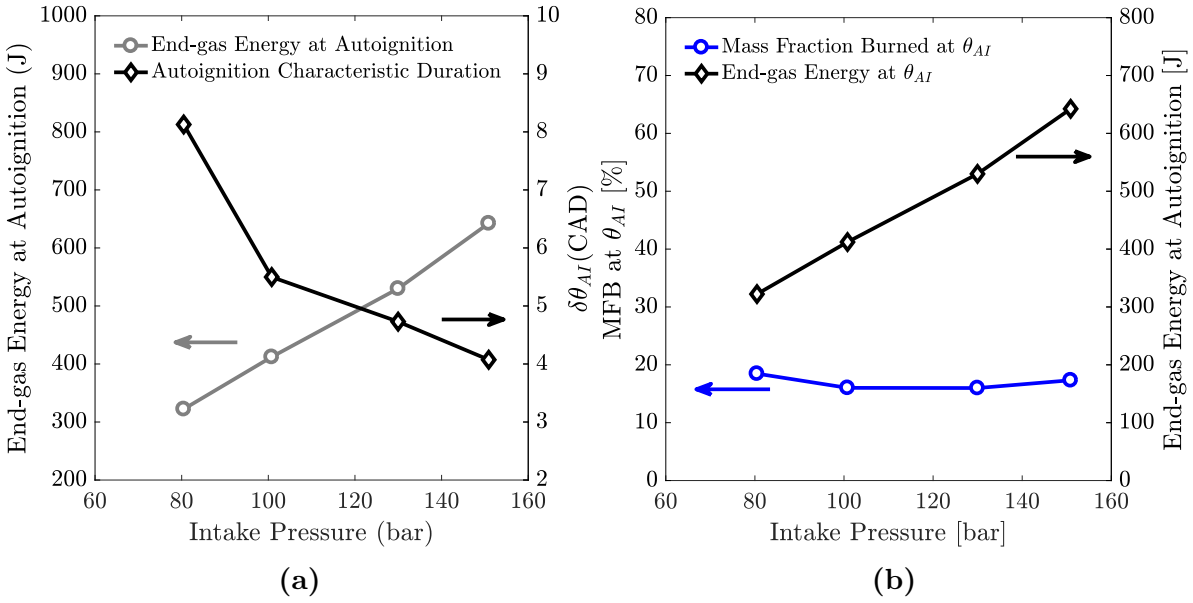

Figure 4.8: (a) Variation of estimated end-gas energy and end-gas characteristic burn duration and (b) mass fraction burned and end-gas energy at onset of autoignition for the $\phi' = 0.55$ intake pressure sweep at constant engine speed, composition, combustion phasing.

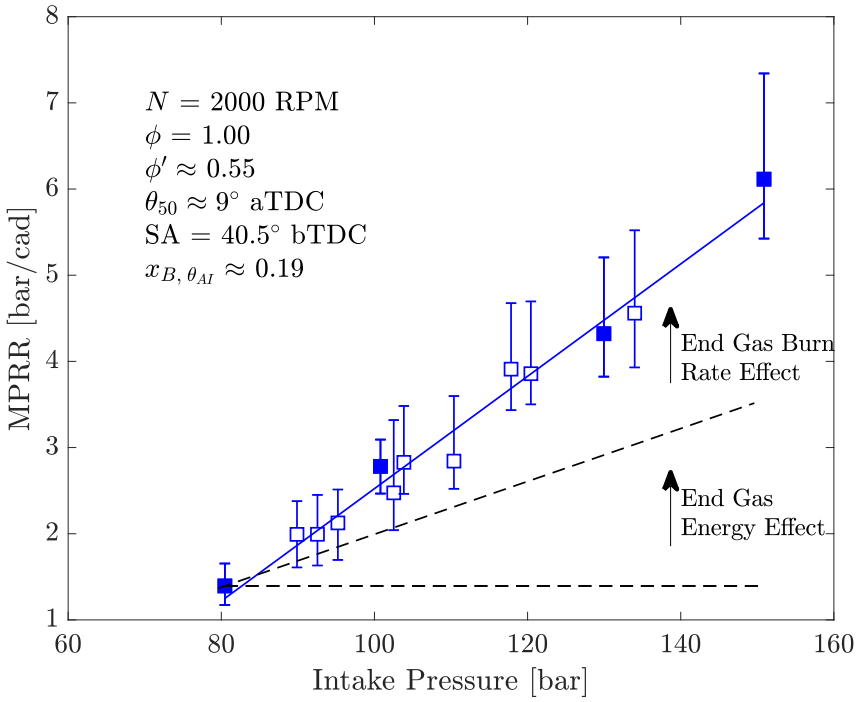

Figure 4.9: Maximum pressure rise rate measurements as a function of intake pressure for the $\phi' = 0.55$ intake pressure sweep. Error bars represent minimum and maximum values of the 20 representative cycles at each operating condition. Solid markers indicate the 4 experimental conditions presented in detail in this Section.

Previous investigations of the autoignition behavior of hydrocarbon fuels have shown that representative gasoline fuels exhibit negative temperature coefficient (NTC) behavior, in which the ignition delay time becomes longer as the temperature increases [121–125]. Fieweger et al. [124] showed that at a pressure of 40 bar, stoichiometric iso-octane mixtures exhibit NTC behavior in the range of 770 - 910 K. At higher pressures this behavior has been shown to be more pronounced and shifted to higher temperatures [100,126]. Details on the differences in the high and low temperature reaction mechanisms in the oxidation of iso-octane that lead to a lower reactivity in the NTC region, can be found in the modeling work of Curran et al. [127]. For the intake pressure sweep results at ϕ'=0.55 presented in Figure 4.5, no measurable heat release was observed at timings earlier than 20°bTDC, which corresponded to temperatures lower than 950 K. Furthermore, when the spark timing was retarded from 40° bTDC to TDC, the heat release prior to TDC disappeared suggesting that the initial slow heat release observed is due to the propagating reaction front initiated from the spark discharge. In SACI metal engine experimental data, it is difficult to distinguish between intermediate temperature heat release and flame based heat release, if observed after the spark discharge and prior to the onset of autoignition.

To further investigate the boosted SACI results presented earlier in relation to the autoignition behavior, the mass averaged unburned gas temperature and pressure trajectories were overlaid on ignition delay predictions under the conditions investigated, as shown in Figure 4.10. Constant volume ignition delays were computed for homogeneous conditions with a detailed kinetic mechanism with 312 species representing an RD-387 gasoline surrogate with an AKI of 87 [128,129], at ϕ=1 and ϕ'=0.55. Ignition delay was defined as the time of 50% mass fraction burned for each computation. It can be seen in Figure 4.10 that the pressure-temperature trajectories for all cases cross below the NTC region, where ignition delay is sensitive to both temperature and pressure. The black crosses on the plot indicate the estimated autoignition timing for each experimental case, as defined in Section 2.2.5. Interestingly, the ignition delay prediction at the estimated onset of autoignition is close to the 0.8 ms isoline for all cases, which would be equivalent to 9.6 CAD at the engine speed used. This

could suggest that the effect of the higher pressure on the mean reactivity of the unburned gas is likely being offset by the reduction in the temperature at the onset of autoignition.

Figure 4.11 shows the pressure and temperature trajectories of the four cases investigated during the closed portion of the cycle, with markers highlighting autoignition, IVC and EVO timings. The temperature rise during combustion is similar for all cases starting from around 1150 K and ending around 2100 K. Given the controlled variables in this experiment, such as θ_{50} and mass fraction burned at the onset of autoignition, the temperature increase is expected to be primarily a function of the specific heat capacity of the mixtures, which is similar for all mixtures as composition is held approximately constant. Higher boost mixtures have slightly higher maximum temperatures likely due to the faster end-gas autoignition rate. However, the pressure increase from the onset of autoignition until peak pressure is expected to scale with the end-gas energy even if the burn rate is identical, as described in Section 3.1. In the current experiment, the cylinder pressure rise due to combustion increases from approximately 6 bar for the lowest intake pressure case (i.e. 80 kPa) to 20 bar for the highest intake pressure case (i.e. 150 kPa). This is partly due to the increase in end-gas energy and partly due to the faster end-gas burn rate. It is unclear whether the pre-ignition reactivity stratification or the change in the evolution of the pressure post-ignition is responsible for the increase in end-gas burn rate observed. The above questions are addressed in the computational investigation presented in Chapter VI.

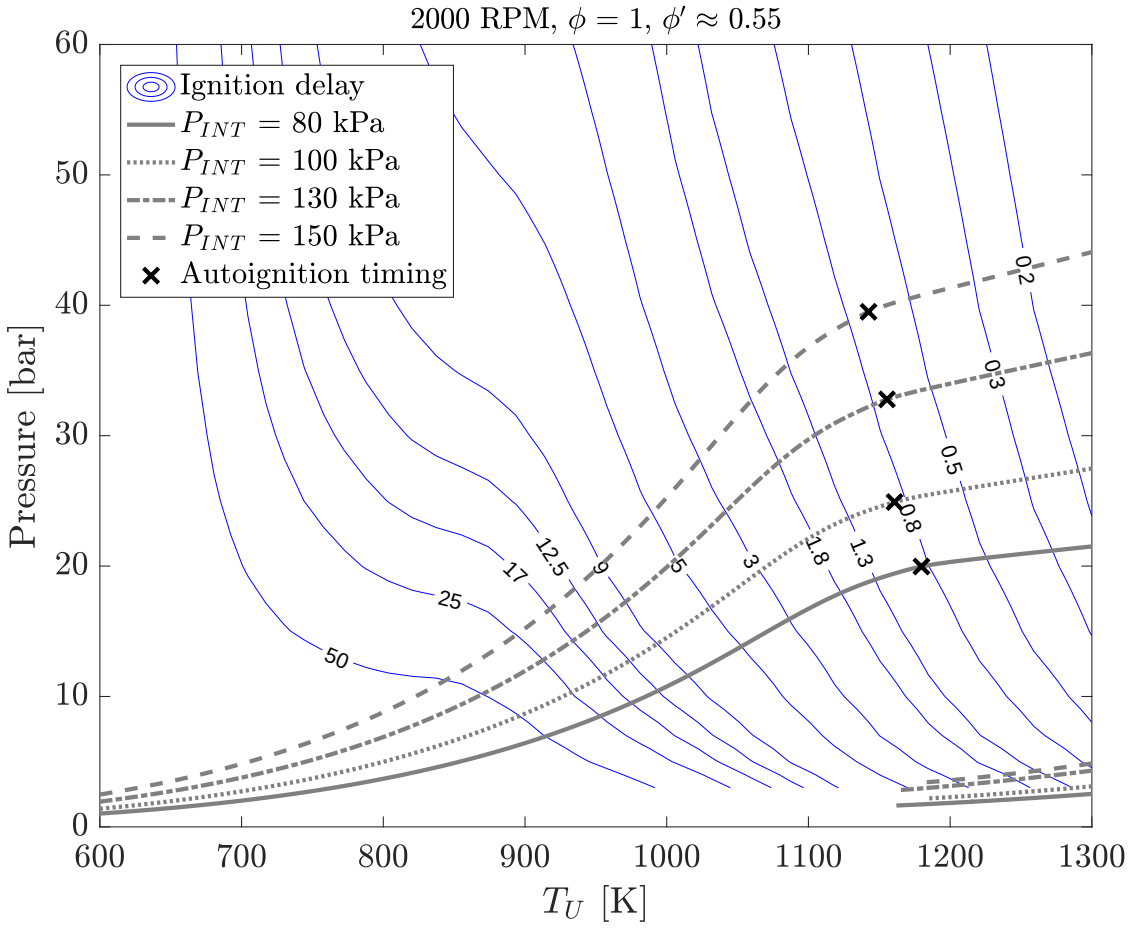

Figure 4.10: Constant volume ignition delay contours (blue) as a function of pressure and temperature for a stoichiometric mixture at $\phi' = 0.55$. Grey lines indicate the trajectories of experimental pressure and estimated mass averaged-unburned gas temperature during compression up to the onset of end-gas autoignition for the boost pressure experiment at $\phi' = 0.55$ outlined in Table 4.1. The black crosses indicate the estimated autoignition timing derived from the experimental burn rate curves.

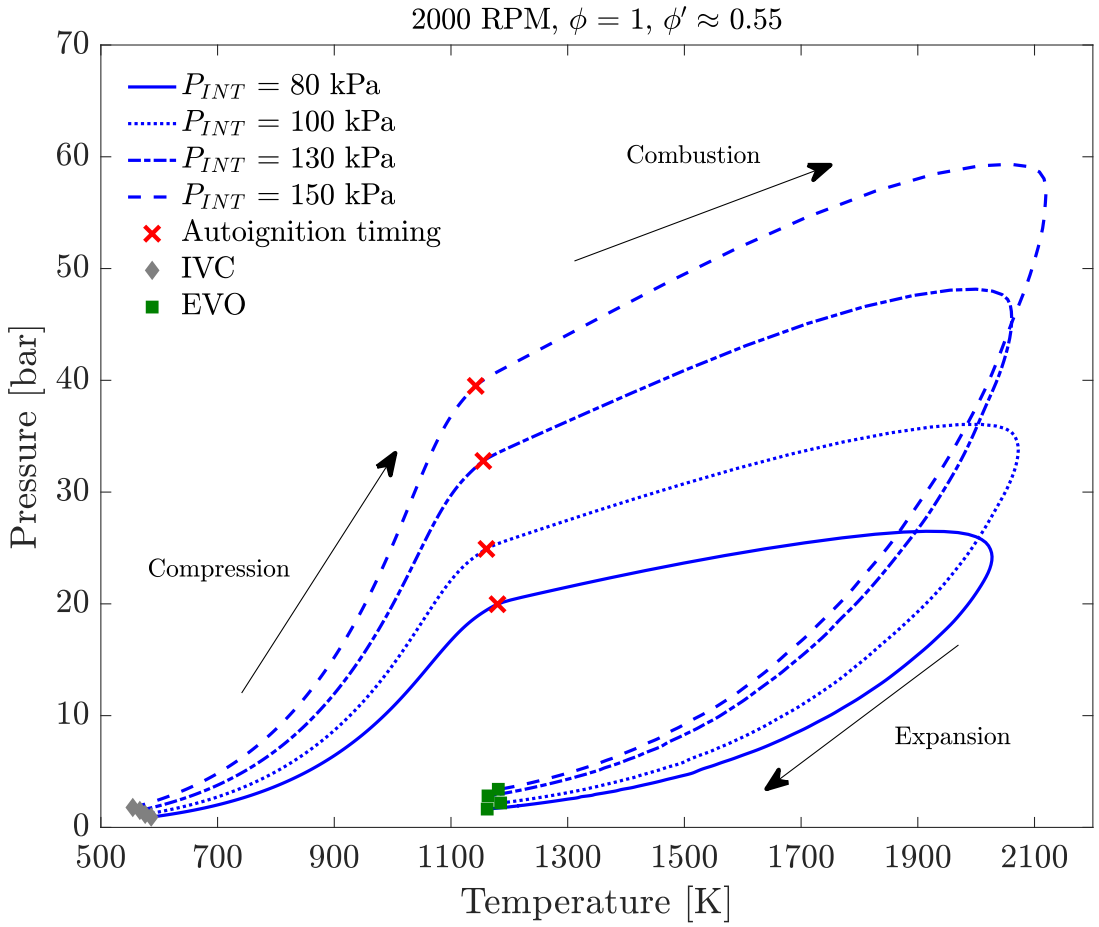

Figure 4.11: Trajectories of experimentally measured pressure and estimated mass-averaged unburned gas temperature from IVC to EVO for the boost pressure experiment at $\phi' = 0.55$ outlined in Table 4.1. The red markers indicate the estimated end-gas autoignition timing computed from the experimental burn rate curves.

4.4 Spark Advance Effects on SACI Burn Rates under Boosted Conditions

The effect of pressure on the SACI burn rates was investigated in detail in Section 4.3 above at a fixed spark timing of 40° bTDC. However, a SACI experimental and computation study by Olesky et al. [113] using a similar engine configuration showed that the in-cylinder mixture became increasingly stratified at more advanced crank angle and in-cylinder stratification significantly affected the behavior and effectiveness of SACI. To test whether the boosted pressure effects are affected by the timing of spark and potential mixture inhomogeneity around the spark plug, a similar experimental approach to that outlined in Section 4.2 was employed for later spark timings at 35.5 and 30° bTDC where the mixture is expected to be more homogeneous due to longer residence time.

Figure 4.12 depicts the variation of peak end-gas burn rate at constant composition and combustion phasing but varying spark timings. It is clear that as pressure is increased, peak end-gas burn rates increase linearly with intake pressure, irrespective of the mass fraction burned at the onset of autoignition. Additionally, the mass fraction of fuel burned by the flame remains fairly constant with pressure irrespective of spark timing, as seen in Figure 4.12. It can be also seen in Figure 4.12 that at a given intake pressure, the peak end-gas burn rate and mass fraction burned by the flame both decrease with earlier spark timings. These trends at a fixed intake pressure agree well with the findings from studies by Olesky et al. [89] and Middleton et al. [60]. It was shown in [89] that to maintain combustion phasing, a colder charge with an earlier spark timing can be used to increase the fraction of flame based heat release to provide the additional compression heating needed for autoignition. It was also shown in [60] that for cases where flame propagation consumes a larger fraction of the charge, the end-gas state becomes less reactive, which explains the decrease in peak end-gas burn rates observed in Figure 4.12. These findings suggest that potential inhomogeneity due to the timing of spark is not responsible for the boost pressure effects on SACI burn rates that are observed.

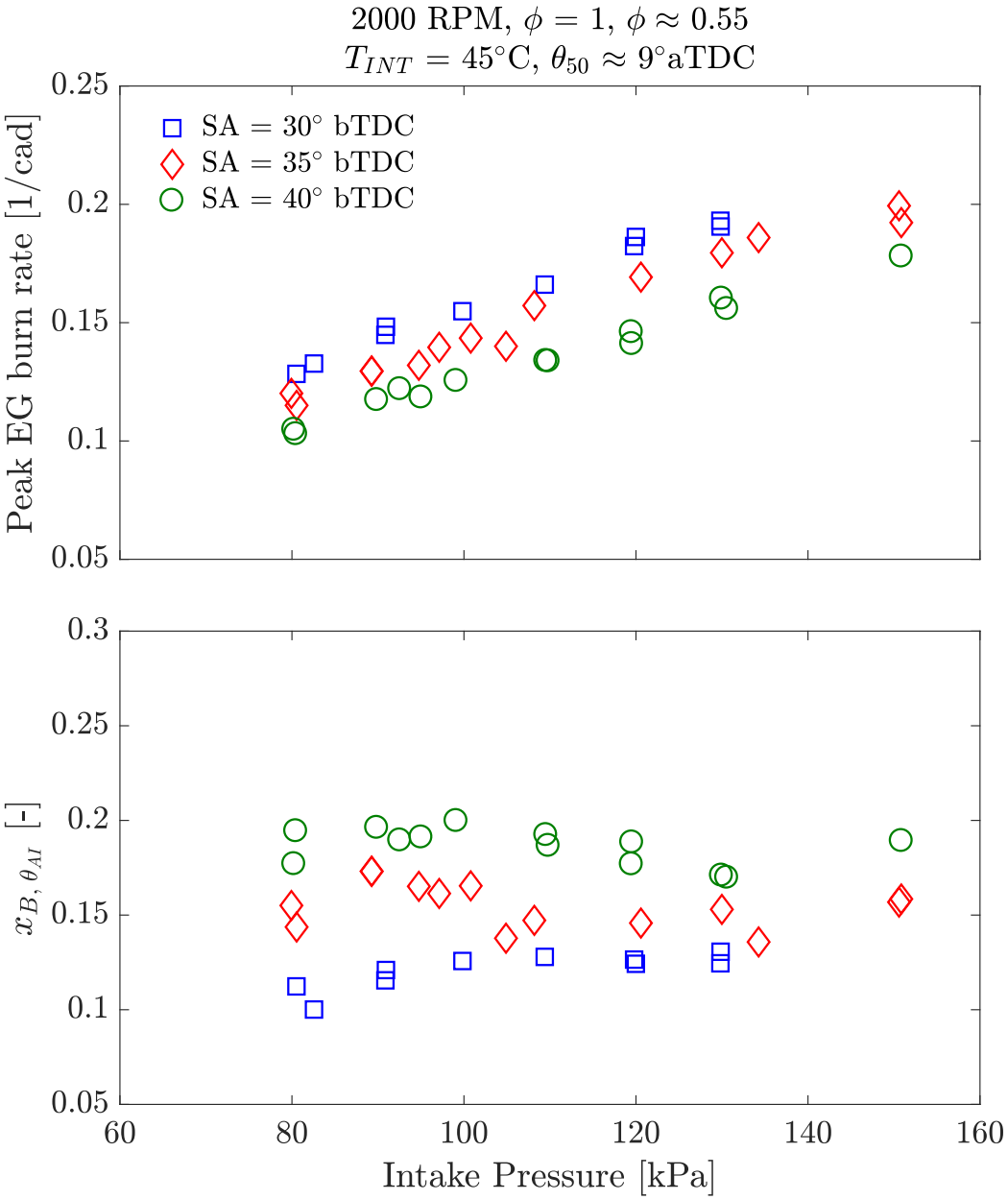

Figure 4.12: Variation of peak end-gas burn rate (top) and mass fraction of fuel burned at the onset of autoignition (bottom) as a function of intake pressure at 3 spark timings. Combustion phasing ($\theta 50 = 9°$ aTDC) and composition ($\phi = 1$, $\phi' = 0.55$) are maintained constant for all experiments.

4.5 Comparison of Boost Pressure Effects on SACI Burn Rates for Varying Fuel-to-Charge Equivalence Ratios

The analysis of the results in Section 4.3 showed that increasing intake pressure/charge density at $\phi' = 0.55$ leads to similar burn rates up to onset of autoignition but faster autoignition rates. SACI combustion has been shown to be effective at fuel-to-charge equivalence ratios ranging between 0.45 - 0.75. It is expected that the SACI burn profile would be altered at different ϕ' mixtures. It is, however, unclear whether the boost pressure effects on SACI burn rates vary at different fuel-to-charge equivalence ratios. To investigate this, a similar experimental approach to Section 4.3 was employed for mixtures varying from $\phi' = 0.45$ - 0.63. At each ϕ', intake pressure was increased while maintaining constant fuel-to-air equivalence ratio (ϕ=1), intake valve timings (IVO/IVC), combustion phasing ($\theta_{50} \approx 9°$aTDC), spark advance (SA = 40.5°bTDC and start of injection timing (SOI = 330°bTDC). Intake temperature was fixed at 45°C and the unburned gas temperature was controlled by modulating the internal to external EGR ratio.

Figures 4.13 and 4.14 show experimental results of the effect of intake pressure on peak gross heat release rate, peak end-gas burn rate, mass fraction of fuel burned at the onset of autoignition and end-gas energy at the onset of autoignition (bottom right) for ϕ' mixtures ranging from 0.45 - 0.63. Linear least square fit lines were added to the experimental points at each ϕ'. It is apparent that the heat release analysis trends are similar as a function of intake pressure, irrespective of ϕ'. Specifically, as intake pressure increases from 0.8 to 1.5 bar, peak heat release rates rise by approximately a factor of 3.5 for all ϕ'. Mass fraction burned at the estimated onset of autoignition was approximately constant as a function of pressure for all cases. As a result, the end-gas energy at the estimated onset of autoignition increased at similar rates as a function of intake pressure for all mixtures. For the intake pressure range investigated the peak end-gas burn rate increased by approximately a factor of 1.8. Similarly to the analysis for the mixtures at 0.55, it can be seen that the increase in end-gas energy and faster autoignition rate both contribute to the increase in peak

heat release rates observed. For the experiments shown in Figures 4.13 and 4.14, significant changes can be observed between ϕ' mixtures at a given intake pressure, which motivated the work presented in the following chapter. A detail analysis of the effects of fuel-to-charge equivalence ratio on SACI heat release rates is shown in Chapter V.

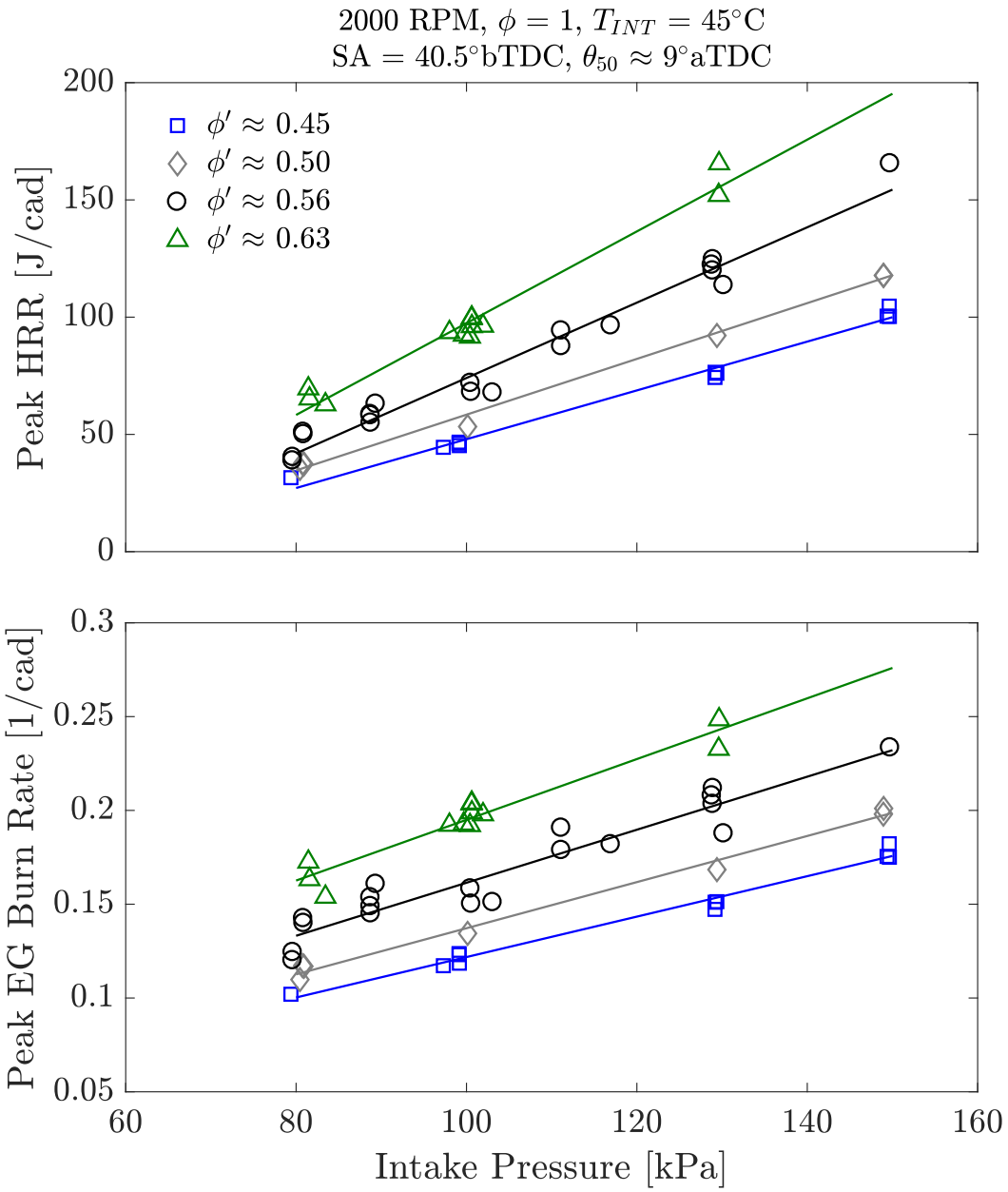

Figure 4.13: Effect of intake pressure on peak gross heat release rate (top) and peak end-gas burn rate (bottom) for various ϕ' mixtures at stoichiometric conditions, at constant engine speed, combustion phasing and spark advance.

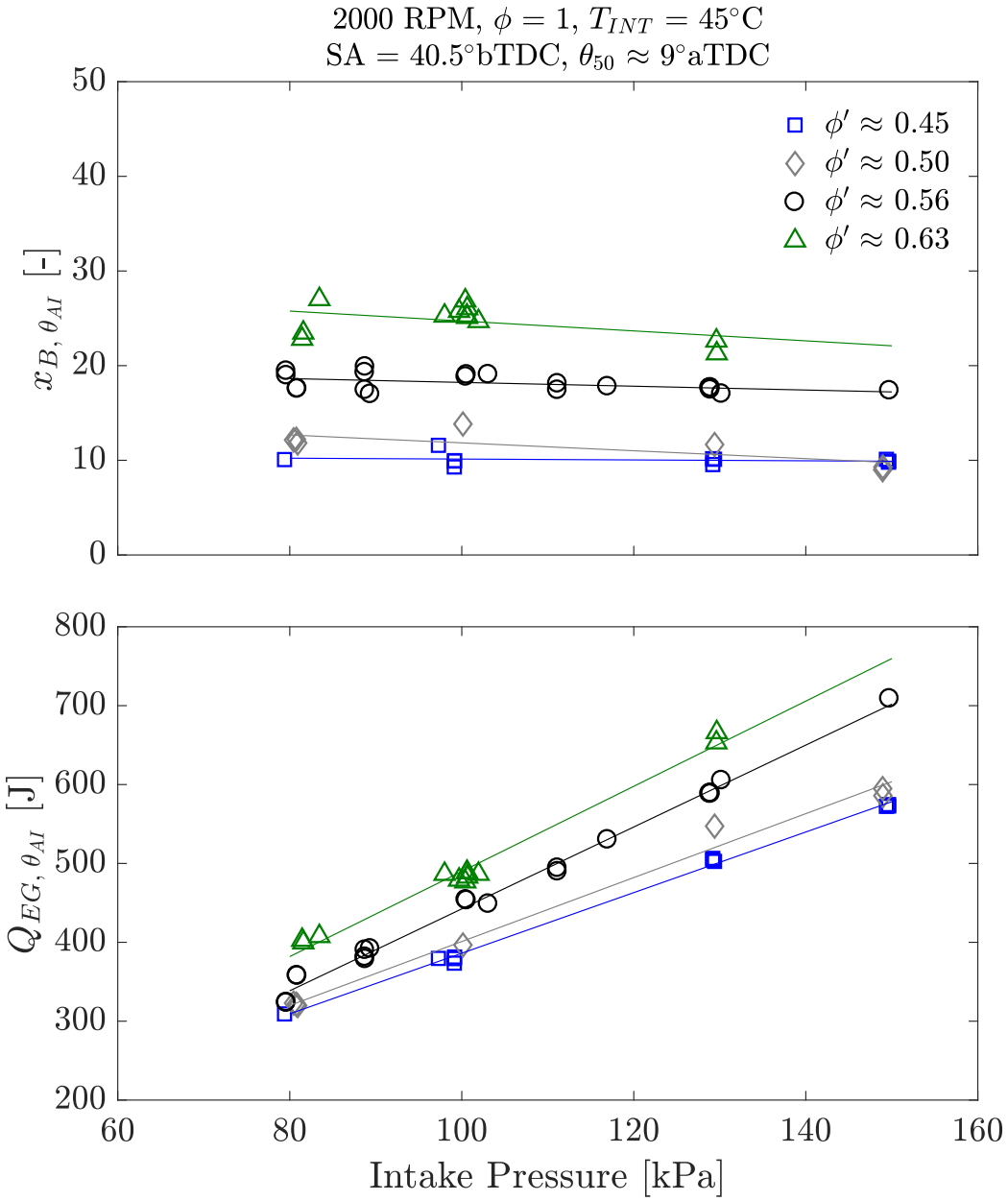

Figure 4.14: Effect of intake pressure on mass fraction of fuel burned (top) and end-gas energy (bottom) at the estimated onset of autoignition for various ϕ' mixtures at stoichiometric conditions, constant engine speed, combustion phasing and spark advance.

4.6 Effect of Charge Preheating Method on the SACI Heat Release under Boosted Conditions

In Section 4.3, the effects of boost pressure on SACI burn rates were investigated at constant composition and intake temperature. It was shown that as intake pressure is increased at constant spark timing, a lower IVC temperature is required to maintain constant θ_{50}. This was achieved by reducing the ratio of internal to external EGR while maintaining a constant intake temperature. The findings from those experiments would certainly be valuable from a practical engine operation point of view, as large changes in intake temperature would be difficult to achieve in few engine cycles. However, those experiments did not decouple the potential thermal and compositional stratification associated with variations in the ratio internal to external EGR from the effects of pressure on the burn rates. Previous studies [95, 130–134] have shown that increasing the internal EGR mass fraction of the mixture can lead to a greater temperature stratification during combustion, resulting in slower autoignition burn rates. On the other hand, other studies [89, 135, 136, 138] showed that changes in the internal EGR fraction of the mixture had no impact in the overall burn rates. It is hence unknown whether the boost pressure effects shown in Section 4.3 were affected by the varying amounts of internal EGR, which motivated the experimental studies shown in this section.

As intake pressure was increased, ϕ' was fixed at approximately 0.55, fuel-to-air equivalence was fixed around stoichiometry and θ_{50} was fixed at approximately 9.8°aTDC. Since spark timing and the ratio of internal to external EGR was maintained constant, the intake manifold temperature was varied to ensure combustion phasing is matched. The detailed experimental conditions are listed in Table 4.2. Figure 4.15 shows the breakdown of the cylinder constituents in this study.

Figure 4.16 displays the cylinder pressure traces during compression and expansion. Higher intake boost pressures lead to proportionally higher pressures near autoignition timing. Since combustion phasing is matched between the cases, locations of peak pressure rise rate and peak pressure are also closely matched.

Table 4.2: Experimental conditions for the SACI boost pressure experiment at fuel-to-charge equivalence of 0.55 and constant ratio of internal to external EGR [2]

Parameter	*Case1*	*Case 2*	*Case 3*	*Case 4*
Engine speed [rpm]		2000		
Spark timing [°aTDC]		-40.5		
Start of injection [°aTDC]		-330		
Intake valve opening/Closing [°aTDC]		-265/-161		
Fuel flow rate [mg/cycle/cylinder]	11.1	12.9	13.9	15.0
Combustion phasing, θ_{50} [aTDC]	9.8	9.7	9.8	9.8
Fuel-to-air equivalence ratio, ϕ [-]	1.00	0.99	0.99	0.99
Fuel-to-charge equivalence ratio, ϕ' [-]	0.55	0.55	0.55	0.56
Intake pressure [bar]	0.94	1.04	1.12	1.20
Exhaust pressure [bar]	1.37	1.31	1.24	1.38
Intake temperature [°C]	83	71	52	32
Internal EGR mass fraction [-]	0.34	0.33	0.33	0.32
External EGR mass fraction [-]	0.10	0.11	0.11	0.11
Exhaust valve opening [°aTDC]	190	186	180	183
Exhaust valve closing [°aTDC]	294	290	284	287

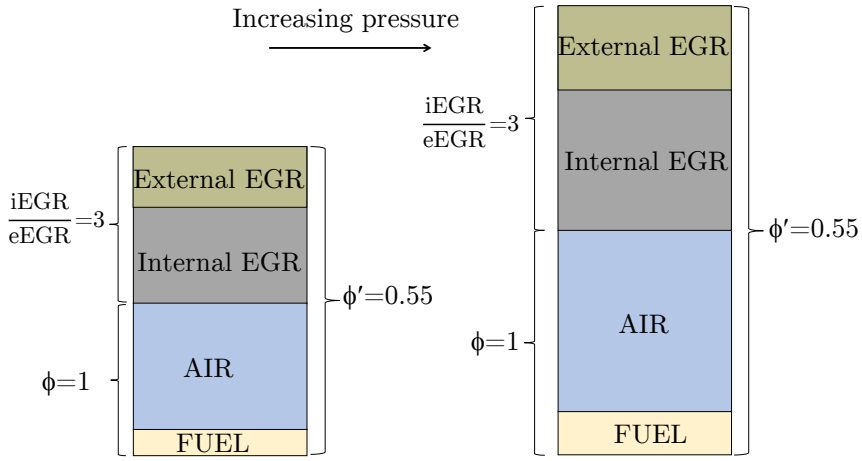

Figure 4.15: Schematic showing the breakdown of the cylinder mass constituents during the boost pressure experiment at constant ratio of internal to external EGR and composition. Total column height represents the sum of the masses of the constituents (not to scale).

[2] All timings are referenced to combustion TDC. Valve timings are defined at 0.2 mm opening.

Internal and external EGR mass fractions, shown in Figure 4.17a, were maintained constant with increasing intake pressure. As a result, as intake pressure was increased from 94 kPa to 120 kPa, intake temperature had to be reduced from 83°C to 32°C to maintain constant combustion phasing, as seen in Figure 4.17b. The boost pressure range was limited due to intake temperature range limitations of the hardware. However, the variation in intake pressure allowed for a 36% increase in fuel energy input and was deemed sufficient for the objective of this study.

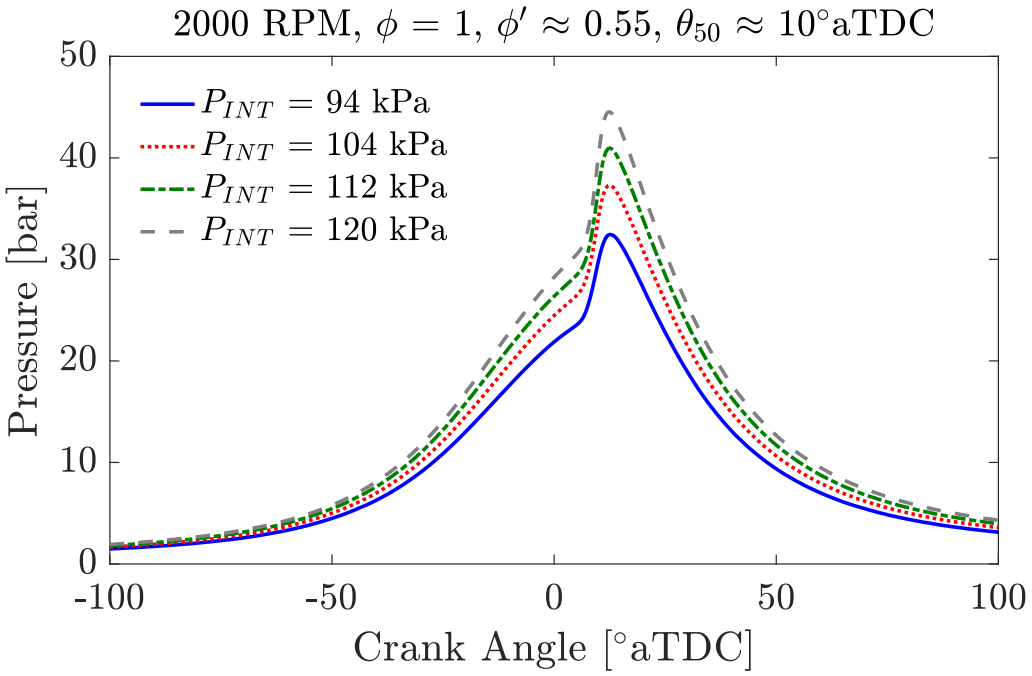

Figure 4.16: Cylinder pressure traces for boost pressure sweep experiments at constant internal-to-external EGR fraction and varying intake temperatures at stoichiometric conditions, constant engine speed, combustion phasing and spark advance.

Heat release rates curves, shown in Figure 4.18, display a similar trend to the results of the intake pressure sweep using residual gas heating. As intake pressure is increased, more energy is being released during both flame propagation and autoignition. When normalizing the heat release rate by the total heat released for each case, the initial burn rates collapse with each other but autoignition burn rates are still faster. The increase in global burn rate is smaller that what was observed in Figure 4.5 for the residual gas heating cases, however the change in intake pressure in this experiment is also smaller.

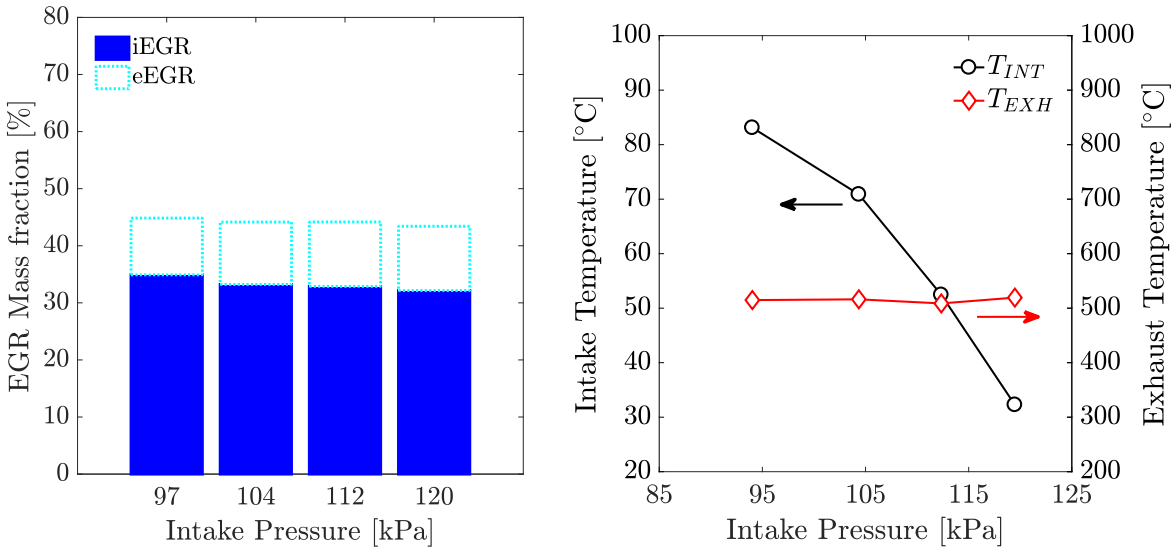

Figure 4.17: Variation of (a) total EGR fraction displayed as a sum of internal and external EGR and (b) manifold temperatures as a function of intake pressure for experiments at constant composition, combustion phasing, spark timing, and engine speed.

Similarly to the intake pressure sweep results at constant intake temperature, mass fraction burned at autoignition was constant at around 18%. To quantitatively compare the effect of pressure on the peak heat release rate between residual gas heating and intake manifold heating, peak heat release rate and peak burn rate values were plotted against intake pressure for both sets of experiments, as shown in Figure 4.19. It is clear that that the rate of increase of the peak heat release rate is approximately the same with increasing boost pressure, irrespective of charge preheating method. Very similar increase in peak burn rate was also observed between the two charge preheating methods. These findings suggest that changes in residual gas fraction have negligible effect on the peak end-gas burn rate trend observed with intake boost.

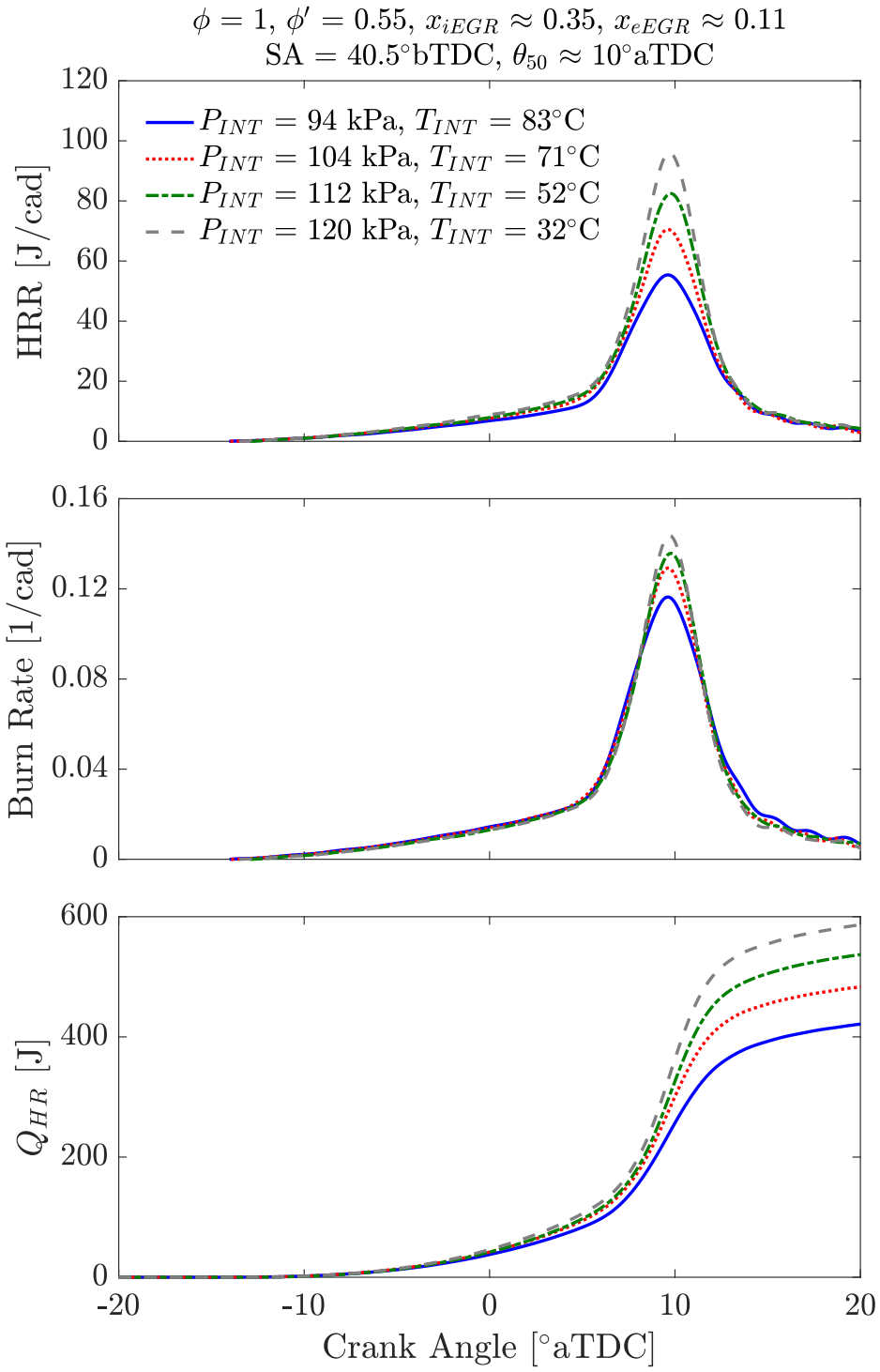

Figure 4.18: Gross heat release rate profiles (top), global burn rate profiles (middle) and cumulative heat release (bottom) for boost pressure sweep experiments at constant internal-to-external EGR fraction and varying intake temperatures. All conditions are stoichiometric with constant composition,engine speed, combustion phasing and spark advance.

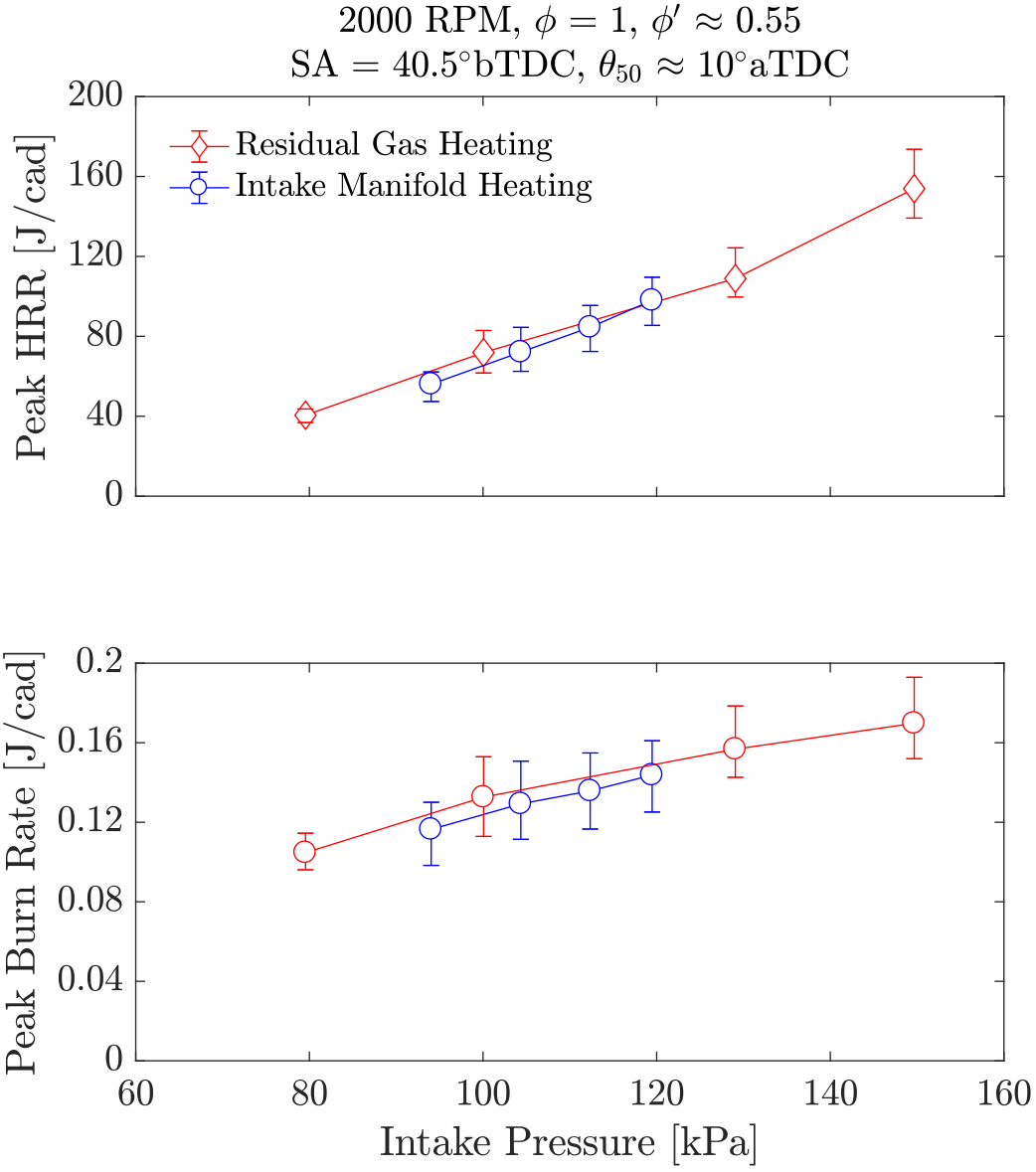

Figure 4.19: Comparison of peak global heat release rate (top) and peak burn rate (bottom) trends with intake pressure between residual gas heating and intake manifold heating experiments. Combustion phasing, composition, spark advance, intake valve timings and engine speed were held constant. Error bars represent minimum and maximum values from the 20 representative cycles selected at each operating condition.

4.7 Summary

Experiments were conducted at typical SACI fuel-to-charge equivalence ratios between 0.45 and 0.63 to understand the effect of intake pressure on the burn rates of stoichiometric SACI combustion. The effect of pressure on the combustion process was isolated from other confounding variables such as combustion phasing, mixture composition, mass fraction of fuel burned at the onset of end-gas autoignition and effective compression ratio. Experiments at 2000 RPM, $\phi' = 0.55$ and SA = 40°bTDC showed that as intake pressure is increased from 80 kPa to 150 kPa, bulk gas temperature has to be decreased by approximately 40 K to match combustion phasing. While extensive flame-based heat release rates were higher with increasing pressure due to higher energy content, the mass fraction of the fuel burned at the onset of autoignition was found to be approximately constant for a constant θ_{50} timing. The overall effect of pressure on SACI initial flame burn rates was thus minor, but led to an almost proportional increase in end-gas autoignition rates. An increase in intake pressure by a factor of 2 led to an increase in the peak heat release rates by approximately a factor of 4. Approximately half of this increase was attributed to the increase in the end-gas energy at the onset of autoignition and the other half was attributed to the increase in the end-gas burn rate.

Varying the fuel-to-charge equivalence ratio of the mixture between 0.45 to 0.63 caused no difference on the effect of pressure on the SACI burn rates, even though the burn profile was altered. Any temperature or compositional stratification associated with the variation in the ratio of internal to external EGR with increasing pressure, was found to have a negligible effect on the burn rates. Low temperature heat release in the NTC region was not observed under the boosted conditions investigated. Ignition delay calculations at the estimated onset of end-gas autoignition were found to be very similar ($\approx$ 0.8 ms) for all intake pressure cases due to the competing effects of higher pressure and lower temperature on the mean mixture reactivity.

CHAPTER V

Impact of Fuel-to-Charge Equivalence Ratio on SACI Burn Rates

5.1 Background and Experimental Objective

In conventional SI combustion EGR dilution leads to slower burn rates due to lower flame propagation speeds associated with lower burned gas temperatures [139]. In low temperature combustion modes, such as HCCI combustion, EGR dilution has been used to alleviate the high pressure rise rates by slowing down the autoignition rate [140]. In the hybrid combustion mode of SACI, the effect of EGR dilution on the tradeoff between deflagrative and autoignition heat release is not fully understood. The analysis in Chapter IV showed that, for a given composition and combustion phasing, higher boost pressures led to higher pressure rise rates due to higher end-gas energy content at the onset of autoignition as well as faster autoignition burn rates. It remains unclear how different fuel-to-charge equivalence ratios could be employed to reduce the peak heat release rates in SACI combustion and thus extend the high load operation limits. Several experimental studies in the literature have attempted to expand the SACI load limit by decreasing the EGR dilution at stoichiometric, unthrottled conditions [6,33,46]. While their work has provided good insights into the SACI combustion process, an analysis and understanding of the effect of fuel-to-charge equivalence ratio on the tradeoff between deflagrative and autoignition heat release is still missing. Furthermore, there is no work currently in the literature using boost

pressure to vary the EGR dilution of the charge at a fixed load or fuel energy input. A boosted engine configuration can enable higher EGR rates at a fixed load condition, which may be beneficial for SACI load expansion. The experimental approach and analysis in this chapter attempts to address these shortcomings by isolating the effect of EGR dilution on SACI burn rates, while maintaining constant autoignition timing. Two experimental approaches were employed; first EGR dilution was varied at a fixed intake pressure, hence changing the total fuel energy input; second EGR dilution was varied at a fixed fuel energy input by varying the intake pressure. It is impossible to isolate the effect of dilution from both pressure and total energy content at the same time, so both approaches were used to understand the effect of EGR dilution on SACI burn profile and the trade-off between flame propagation and autoignition heat release rates. The findings of the first experimental approach would be useful as a load expansion method at a given intake pressure while the second approach tries to understand what dilution level would be most appropriate to alleviate excessive pressure rise rates at a given load condition in SACI. Similarly to experiments in Chapter IV, variables such as autoignition phasing, fuel-to-air equivalence ratio and effective compression ratio were kept constant to remove their effect on the combustion process.

5.2 EGR Dilution Effects at Constant Intake Pressure

5.2.1 Experiments at Constant Spark Advance and Varying Mass Fraction Burned at the Onset of Autoignition

In this study SACI experiments were performed at increasing fuel-to-charge equivalence ratio (ϕ'), while maintaining a fixed intake pressure. As fuel mass injected was increased, EGR dilution was traded for air to maintain a stoichiometric mixture, thus reducing the EGR dilution levels. The fuel-to-air equivalence ratio (ϕ) of the mixture was maintained at stoichiometry and dilution was achieved by a mixture of internal and external EGR. The composition of EGR was constant since fuel-to-air equivalence ratio was held constant. Φ' was varied from 0.55 to 0.72 and intake pressure was fixed at 1 bar. Spark timing was fixed at 30° bTDC, intake temperature was maintained at approximately 45°C and intake valve closing timing was fixed at 161° bTDC. In order to match autoignition timing at around 7° bTDC, EVC timing was varied to modulate the amount of internal residual (iEGR) and ultimately the mean temperaure of the mixture at inlet valve closing timing. External EGR was controlled to maintain the fuel-to-air equivalence ratio at stoichiometry. Details of the experimental conditions can be found at Table 5.1 and a schematic showing the breakdown of the cylinder constituents during the experiment can be seen in Figure 5.1.

At higher fuel-to-charge equivalence ratios, absolute heat release rates increased during both the flame and autoignition phases of the combustion process, as shown in Figure 5.2. Peak heat release rates increased from approximately 69 J/deg to 150 J/deg, as ϕ' increased from 0.55 to 0.72. The increase in peak heat release corresponded to an increase in peak pressure rise rate from 2.6 bar/cad to 6.5 bar/cad. As mentioned earlier, in this experiment higher ϕ' mixtures were achieved by increasing the fuel energy input at a constant intake pressure of 1 bar. Therefore, the increasing trend observed in absolute heat release rates with ϕ' was somewhat expected due to the increasing energy content of the mixture. It is of greater interest to understand the changes in the burn rates during flame propagation and autoignition and the resulting tradeoff between the two combustion modes. When normalizing the heat

release rate with the total energy content of each mixture, higher ϕ' mixtures exhibit faster global burn rates up to the onset of autoignition and higher peak global burn rates during autoignition, as seen in Figure 5.2. Specifically, the mass fraction of the fuel burned at the onset of autoignition increases from 15% to 26%.

Laminar flame speed estimates from spark timing up to TDC, shown in Figure 5.3, increase by approximately 50% with higher ϕ' under the conditions investigated, which explains the higher mass fraction burned at the onset of autoignition. Since intake pressure, intake valve timing, spark timing and engine speed are constant during this experiment, variations in the turbulent flow conditions between the cases are expected to be minor immediately after the spark event. The laminar flame speed estimates follow the increasing trend in burned gas temperature (T_b) with higher ϕ' (i.e. lower EGR dilution), even though the unburned gas temperatures decrease with higher ϕ'.

Figure 5.3 shows the evolution of the estimated unburned gas temperature during the ϕ' sweep at constant intake pressure and spark timing. As ϕ' increases, the unburned gas temperature of the mixture is seen to decrease by approximately 60 K at spark timing, while at the onset of autoignition it is lower by approximately 25 K. The observed trend in the mean unburned gas temperature can be attributed to the following underlying effects. At higher ϕ' conditions, the mixture is expected to be more reactive exhibiting shorter ignition delays. Therefore, the unburned gas temperature at autoignition timing would have to decrease in order to match autoignition timing. Additionally, the higher ϕ' mixtures exhibit higher flame-based heat release rates up to the point of autoignition, which leads to an increase in-cylinder pressure at the location of autoignition from 24 bar to 34 bar, further increasing the reactivity of the end-gas. The higher flame burn rates observed with higher ϕ' mixtures cause a larger compression effect on the unburned mass, resulting in a larger temperature rise from spark timing up to the onset of autoignition. As a result, at higher ϕ' and constant spark timing, the temperature at spark has to be reduced even further compared to the temperature drop at autoignition timing, as seen in Figure 5.3.

Global burn rates, shown in Figure 5.2, depict an increase in peak global burn

rate during autoignition from 0.13 1/deg to 0.19 1/deg, an approximately 50% rise. However, since the mass fraction burned by the flame varies in this experiment, peak global burn rates do not reflect peak autoignition burn rates. When normalizing the end-gas heat release rates by the end-gas energy at autoignition, we get the end-gas burn rate profiles, shown in Figure 5.2. As a result, the increasing trend in peak end-gas burn rate with ϕ' becomes even more pronounced than that observed for the global burn rate curves due to the decrease in mass fraction burned at the onset of autoignition. Specifically, as ϕ' is increased from 0.55 to 0.72 at constant intake pressure, spark timing and autoignition timing, the peak end-gas burn rate increases from approximately 0.14 1/deg to 0.22 1/deg ($\approx$ 60% increase), while the mass fraction burned by the flame increases from 15% to 26%. A significant decrease in the end-gas burn rate is therefore observed for the lower ϕ' mixture, which should be desirable for alleviating the excessive pressure rise rates observed in SACI combustion. However, for a given spark timing and autoignition timing, lower ϕ' mixtures depict slower burn rates during flame propagation which implies that there is a higher fraction of the energy content released during autoignition. This in turn leads to higher absolute heat release rates and ultimately higher maximum pressure rise rates. The increase in absolute heat release rate by approximately a factor of 2.2 can be attributed to the increase in the end-gas energy as well as the increase in the end-gas burn rates, as shown in Figure 5.2. The rate at which the end-gas burn rate increases during this ϕ' sweep is double that of the end-gas energy increase, which highlights the importance of dilution on the autoignition rate and ultimately its impact on the global heat release rate.

The above study of the behavior of ϕ' was extended at different intake pressures, while maintaining constant spark timing and autoignition timing. The effect of ϕ' on the SACI combustion process was found to be consistent across the different intake pressures investigated, as shown in Figure 5.4. When ignited at the same timing, higher ϕ' mixtures resulted in higher peak heat release rates for all intake pressure cases. This trend was observed due to the increase in the end-gas energy at autoignition and the faster end-gas burn rates. The mass fraction burned at autoignition

increased as ϕ' increased for all intake pressures. However, the mass fraction burned at autoignition collapse onto each other for all intake pressures suggesting that, for a given spark and autoignition timing, pressure has a minor effect on the SACI initial burn rates, as discussed in Chapter IV. Lastly, it is clear that for a given fuel-to-charge equivalence increasing the intake pressure results in faster end-gas burn rates, consistent again with the analysis in Chapter IV.

Table 5.1: Experimental conditions for the ϕ' sweep at 1 bar intake pressure and constant spark advance.

Parameter	*Case1*	*Case 2*	*Case 3*	*Case 4*
Engine speed [RPM]	2000			
Intake temperature [°C]	45			
Start of injection [°aTDC]	-330			
Spark timing [°aTDC]	-30			
Intake valve opening/closing timing [°aTDC]	-265 / -161			
Intake pressure [kPa]	101			
Fuel-to-air equivalence ratio, ϕ [-]	1.00			
Fuel injected [mg/cycle/cyl]	12.3	13.6	15.1	17.9
Fuel-to-charge equivalence ratio, ϕ' [-]	0.55	0.61	0.65	0.72
Autoignition timing [°aTDC]	6.0	7.1	6.9	6.7
Combustion phasing, θ_{50} [°aTDC]	10.2	10.1	9.5	8.9
Exhaust valve opening [°aTDC]	170	182	189	203
Exhaust valve closing [°aTDC]	274	286	293	307
Internal EGR mass fraction [-]	0.39	0.30	0.26	0.19
External EGR mass fraction [-]	0.06	0.08	0.09	0.10

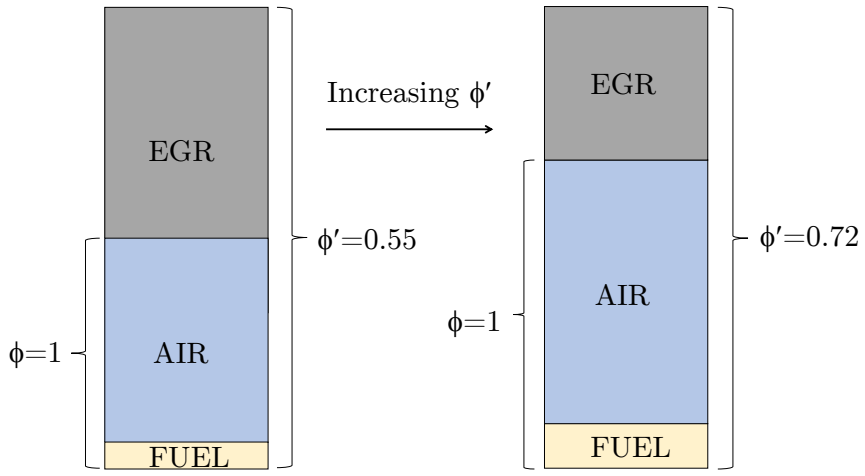

Figure 5.1: Breakdown of the cylinder mass constituents for the fuel-to-charge equivalence ratio experiment (not to scale). Total column height represents the sum of the masses of the constituents.

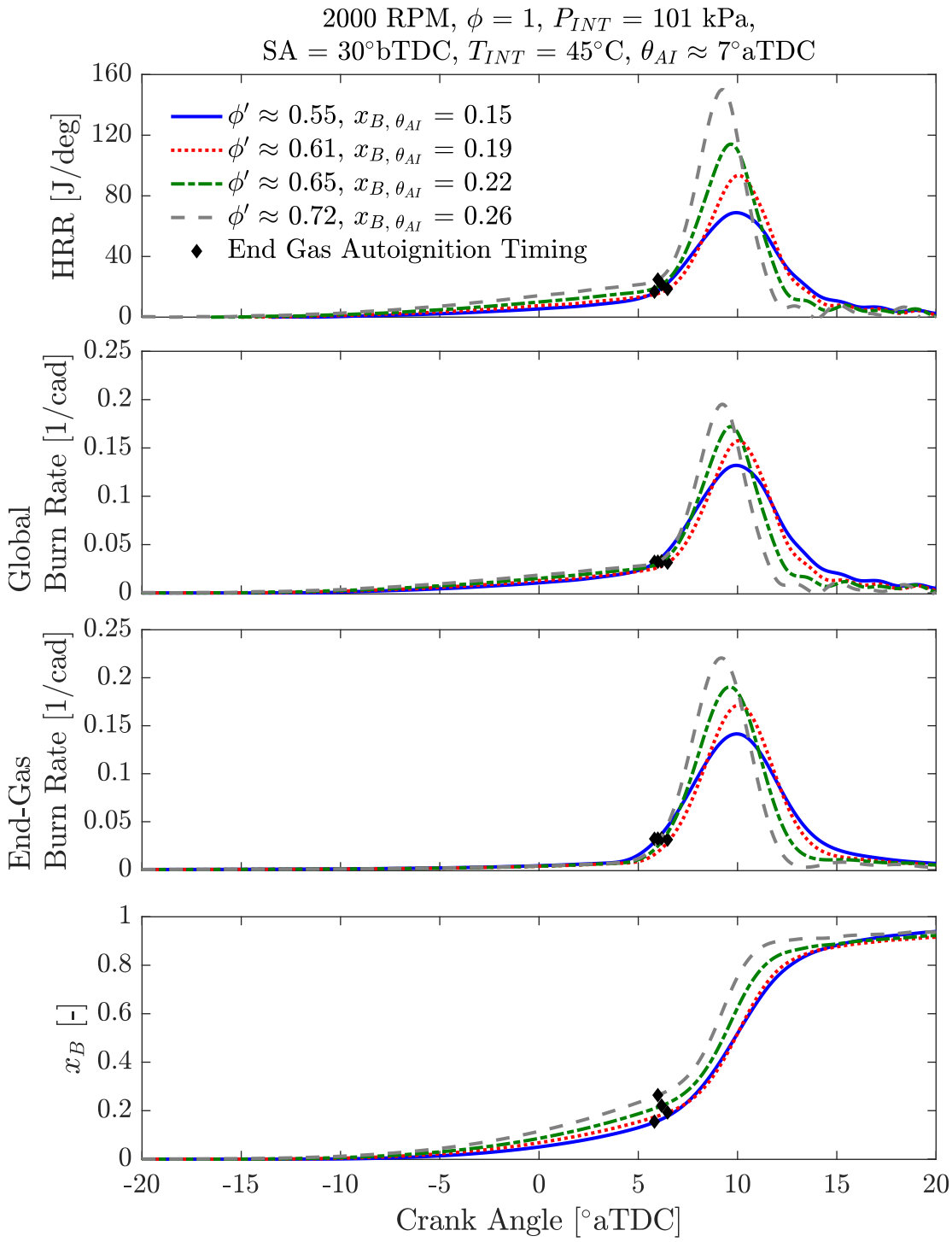

Figure 5.2: From top to bottom: Gross heat release rate, global burn rate, end-gas burn rate and mass fraction burned as a function of ϕ' at constant end-gas autoignition timing, engine speed, intake pressure and spark timing.

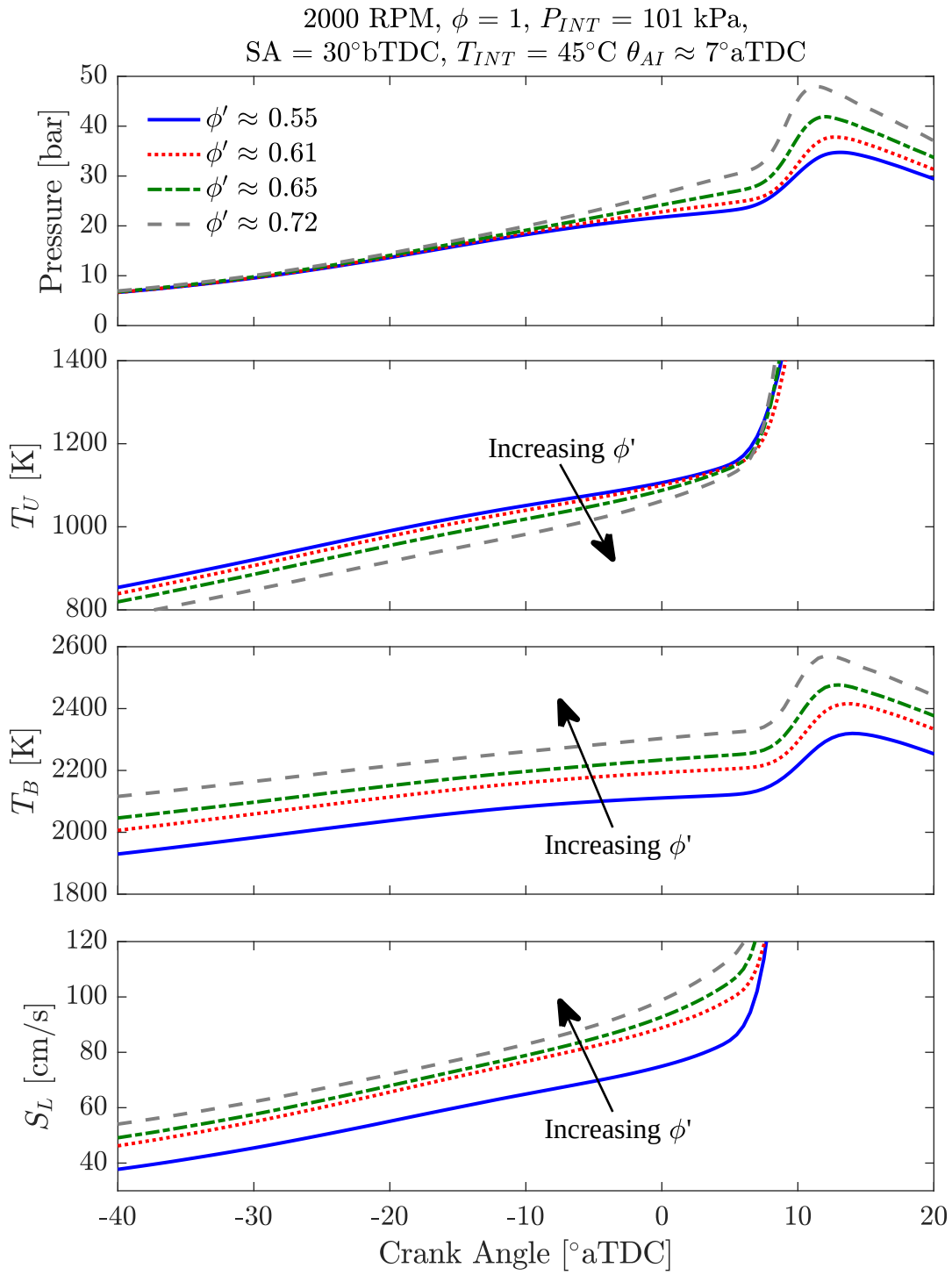

Figure 5.3: From top to bottom: Cylinder pressure, estimated mass-averaged unburned gas temperature, estimated burned gas temperature and laminar burning velocities as a function of ϕ' at constant end-gas autoignition timing, engine speed, intake pressure and spark timing.

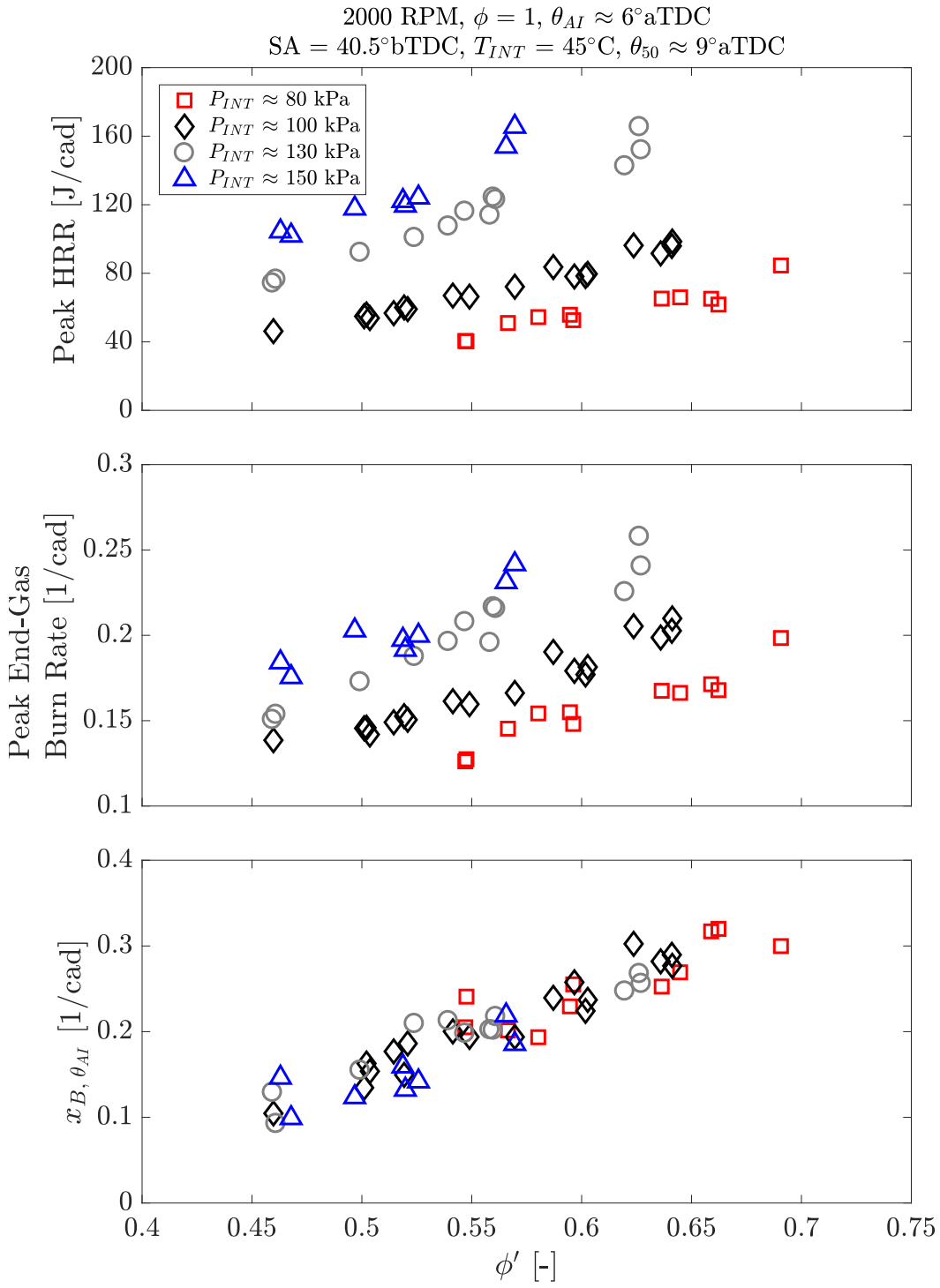

Figure 5.4: Peak gross heat release rate trends (top), peak end-gas burn rate trends (middle) and mass fraction of fuel burned at the onset of autoignition trends (bottom) as a function of ϕ' at increasing intake pressure, stoichiometric conditions, constant combustion phasing and spark timing.

5.2.2 Experiments at Constant Mass Fraction Burned at the Onset of Autoignition

Previous modeling work by Middleton et al. [60] has shown that changes in mass fraction burned at the onset of autoignition in SACI can affect the autoignition burn rate due to changes in end-gas reactivity. To remove that effect from the analysis additional experiments were performed where spark timing and temperature at IVC were varied in order to match the mass fraction burned at the onset of autoignition. Since intake temperature was maintained constant at 45°C, changes in the charge temperature at IVC timing were achieved by altering the ratio of internal to external EGR. Details of the experimental conditions can be found in Table 5.2.

Figure 5.5 displays the cylinder pressure and unburned gas temperature for the three cases. Similar trends to the constant spark advance can be observed, albeit less pronounced. Figure 5.6 shows the effect of ϕ' on the heat release rate, global burn rate, mass fraction burned curves and comulative heat release at constant intake pressure and mass fraction burned at the onset of autoignition. As ϕ' increased, flame burn rates increased based on the analysis and findings in Section 5.2.1. Spark timing had to be retarded from 41° bTDC to 30° bTDC for the higher ϕ' cases, in order to match the mass fraction burned at the autoignition timing of 6.7° aTDC. This resulted in a mass fraction of fuel burned at autoignition of approximately 25% under the conditions investigated.

Peak heat release rates increase by a factor of 3 when ϕ' is increased from 0.58 to 0.71 partly due to increased end-gas energy and partly due to faster end-gas burn rates. The increase in ϕ' from 0.58 to 0.71, which corresponded to an approximately 50% increase in gross IMEP, resulted in a 200% increase in autoignition burn rates. It becomes clear that, everything else being equal, increasing the load in SACI by increasing ϕ' can quickly hit the pressure rise rate limit. The trends from the heat release analysis results are similar to those of the constant spark timing experiments except for the variation of the peak end-gas burn rate with ϕ'. Comparing Figures 5.6 and 5.2 one can observe that the rate at which the end-gas burn rate increases

is higher when the mass fraction burned by the flame is fixed compared to the cases when ignition timing is maintained constant. Again this behavior is attributed to the changes in mass fraction burned at the onset of autoignition and the associated effect on the autoignition burn rates.

Table 5.2: Experimental conditions for the ϕ' sweep at constant intake pressure, mass fraction burned at the onset of autoignition and varying spark timing.

Parameter	*Case1*	*Case 2*	*Case 3*
Engine speed [rpm]		2000	
Intake temperature [°C]		45	
Start of injection [°aTDC]		-330	
Intake valve opening/closing timing [°aTDC]		-265 / -161	
Fuel-to-air equivalence ratio, ϕ [-]		1.00	
Intake pressure [kPa]	98	100	100
Fuel injected [mg/cycle/cyl]	13.0	15.4	17.9
Spark timing [°aTDC]	-41	-35	-30
Fuel-to-charge equivalence ratio, ϕ' [-]	0.58	0.64	0.72
Autoignition timing [°aTDC]	6.7	6.7	6.7
Combustion phasing, θ_{50} [°aTDC]	9.8	9.2	8.9
Exhaust valve opening [°aTDC]	180	191	204
Exhaust valve closing [°aTDC]	284	296	308
Internal EGR mass fraction [-]	0.33	0.26	0.19
External EGR mass fraction [-]	0.09	0.10	0.10

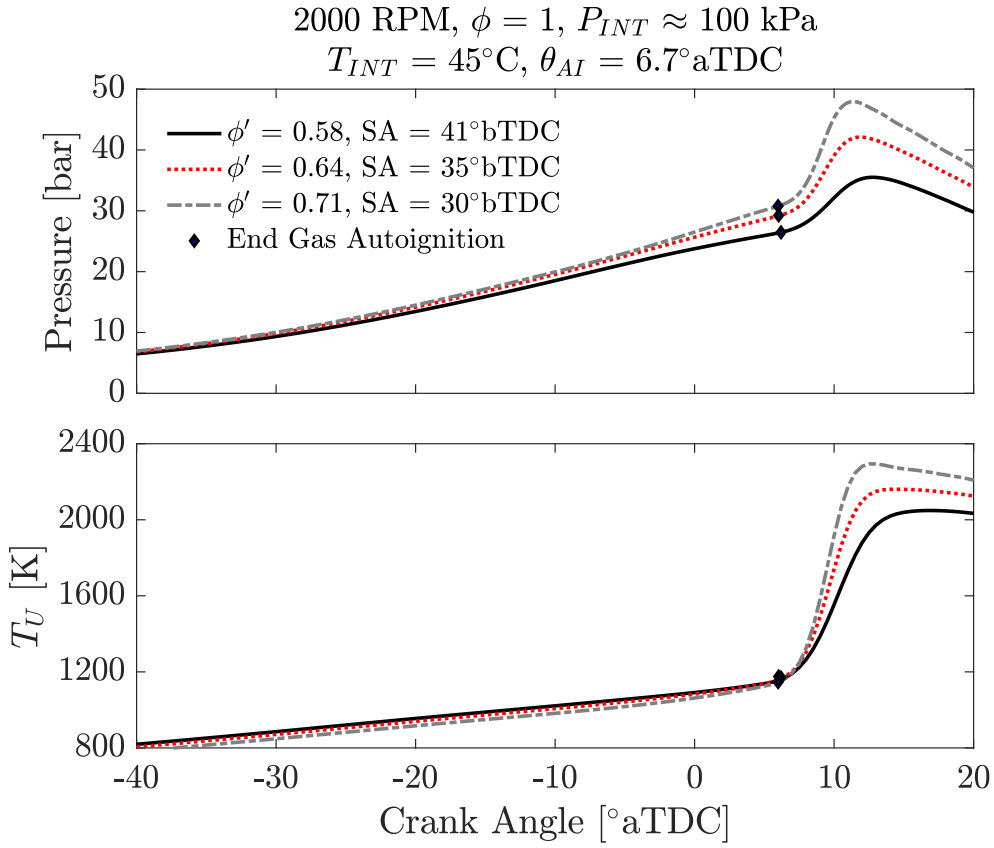

Figure 5.5: Cylinder pressure trace (top) and unburned gas temperature evolution (bottom) for the ϕ' at constant intake pressure and mass fraction burned at the onset of autoignition.

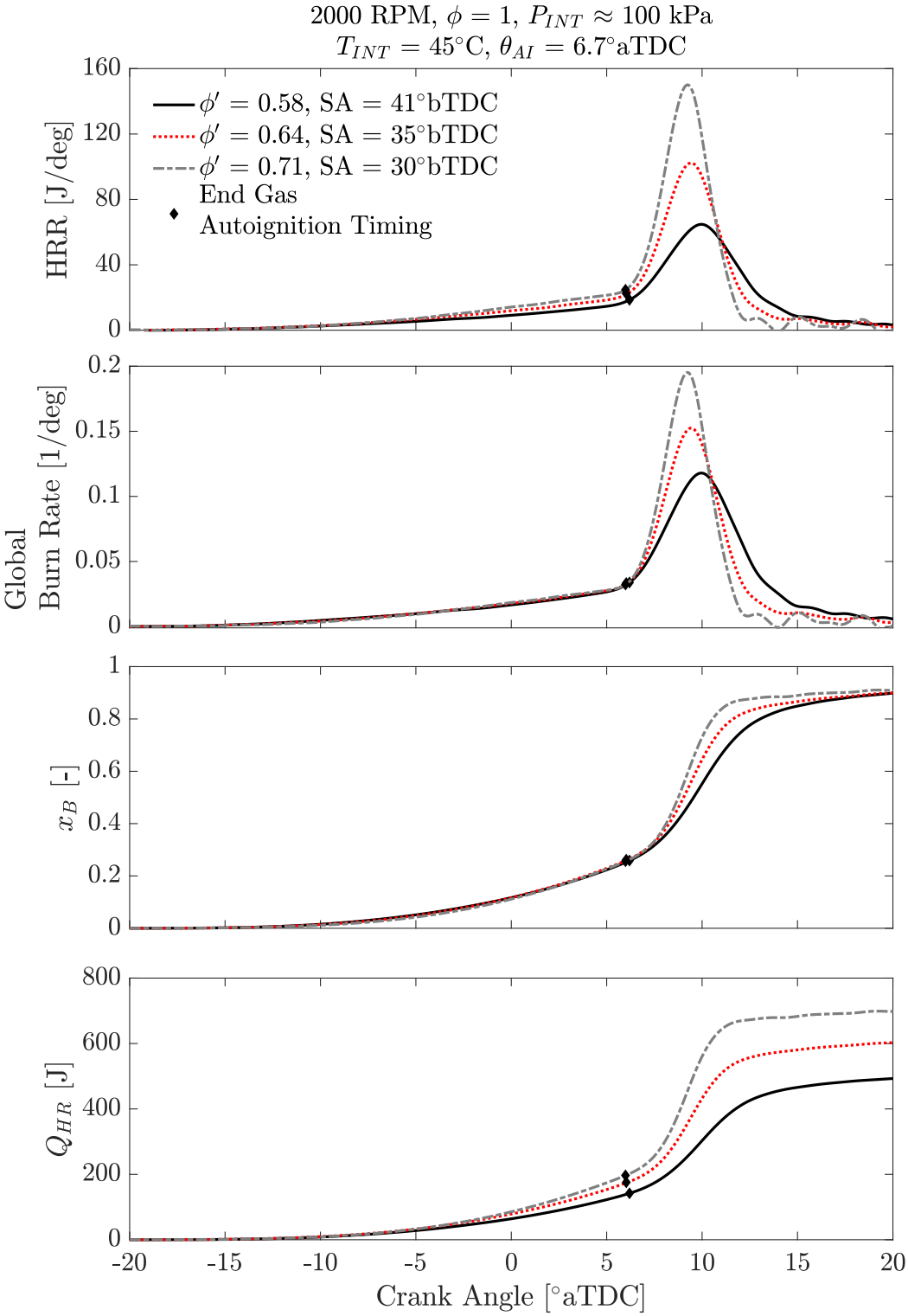

Figure 5.6: From top to bottom: Effect of ϕ' on gross heat release rate, global burn rate, mass fraction burned and cumulative heat release at constant intake pressure, engine speed and mass fraction burned at the onset of end-gas autoignition.

5.2.3 Experiments at Constant End-Gas Energy and Varying Spark Timing

The analysis in Section 5.2.1 showed that for a given intake pressure and spark timing, an increase in fuel-to-charge equivalence ratio at constant intake pressure leads to faster flame burn rates and higher mass fraction burned at the onset of autoignition when autoignition timing is fixed. However, the end-gas energy content still increased and more importantly the end-gas burn rate increased significantly with higher ϕ'. This led to excessive pressure rise rates, which limited the load expansion.

It has been shown in previous work of Olesky et al. [89] and Middleton et al. [60] that the heat release profile can be modified by varying both the temperature of the charge and the timing of the spark event, while maintaining constant combustion phasing. Additional experiments were conducted in this study to explore the potential of using the higher flame burn rate of higher ϕ' mixtures to maintain a constant pressure rise rate while increasing load. As ϕ' increased from 0.55 to 0.65, spark timing was advanced from 30° to 45° bTDC to match the end-gas energy at the onset of autoigntion. The higher ϕ' cases exhibit faster flame burn rates as shown in the previous section but also contain more fuel energy, so spark timing had to be further advanced to match the absolute end-gas energy at the onset of autoignition. The ratio of internal to external EGR was varied to modulate the temperature at IVC and target an autoignition timing around 7°aTDC for all cases. The details about the experimental conditions can be found in Table 5.3.

Figure 5.7 displays the estimated unburned gas temperatures, cylinder pressures and mass fraction burned curves for the 3 cases investigates. As expected higher ϕ' require lower temperatures at spark timing to match autoignition phasing. The higher ϕ' case that is ignited earlier leads to a slightly higher pressure at autoignition timing. The mass fraction burned at autoignition increases from 0.15 to 0.26, which results in an estimated end-gas energy of 480 J for all cases.

Heat release rate plots, shown in Figure 5.8, depict that the higher ϕ' cases exhibit higher heat release rates up to autoignition, as the mixture is more reactive, contains

more chemical energy and is ignited earlier in the cycle. However, during autoignition peak heat release rates are similar for all three cases, unlike the behavior observed in Section 5.2.1. The global burn rates, which can be seen in Figure 5.8 show an increase in the combustion rate during flame propagation and a decrease in the peak autoignition burn rate. The decrease in the peak global burn rate is observed due to the higher mass fraction burned at autoignition rather than a decrease in the end-gas combustion rate. When looking at the end-gas burn rates in Figure 5.8, the peak values are similar between all cases even though the EGR dilution level of the autoigniting mixture is different. This behavior agrees with the computational study by Middleton et al. [60], which showed that an increase in the burned gas mass at the onset of autoignition results in a decrease in the end-gas burn rate due to changes in reactivity stratification. That study was performed at a fixed fuel-to-charge equivalence ratio but the findings are expected to apply trendwise in this study.

The results suggest that load can be increased by increasing ϕ' at constant intake pressure while maintaining constant peak heat release rate and optimum combustion phasing as long as the mass fraction burned at the onset of autoignition increases sufficiently. Higher ϕ' mixtures ignite faster and exhibit higher flame burn rates, however, to match the end-gas energy, spark timing had to be significantly advanced to allow enough time for the flame to propagate in the combustion chamber. This technique was employed further but was found to be limited due to high cyclic variability in combustion phasing and ultimately high COV_{NMEP} due to partial burning cycles. More details on the causes of cyclic variability in SACI under similar conditions can be found in Section 3.4.

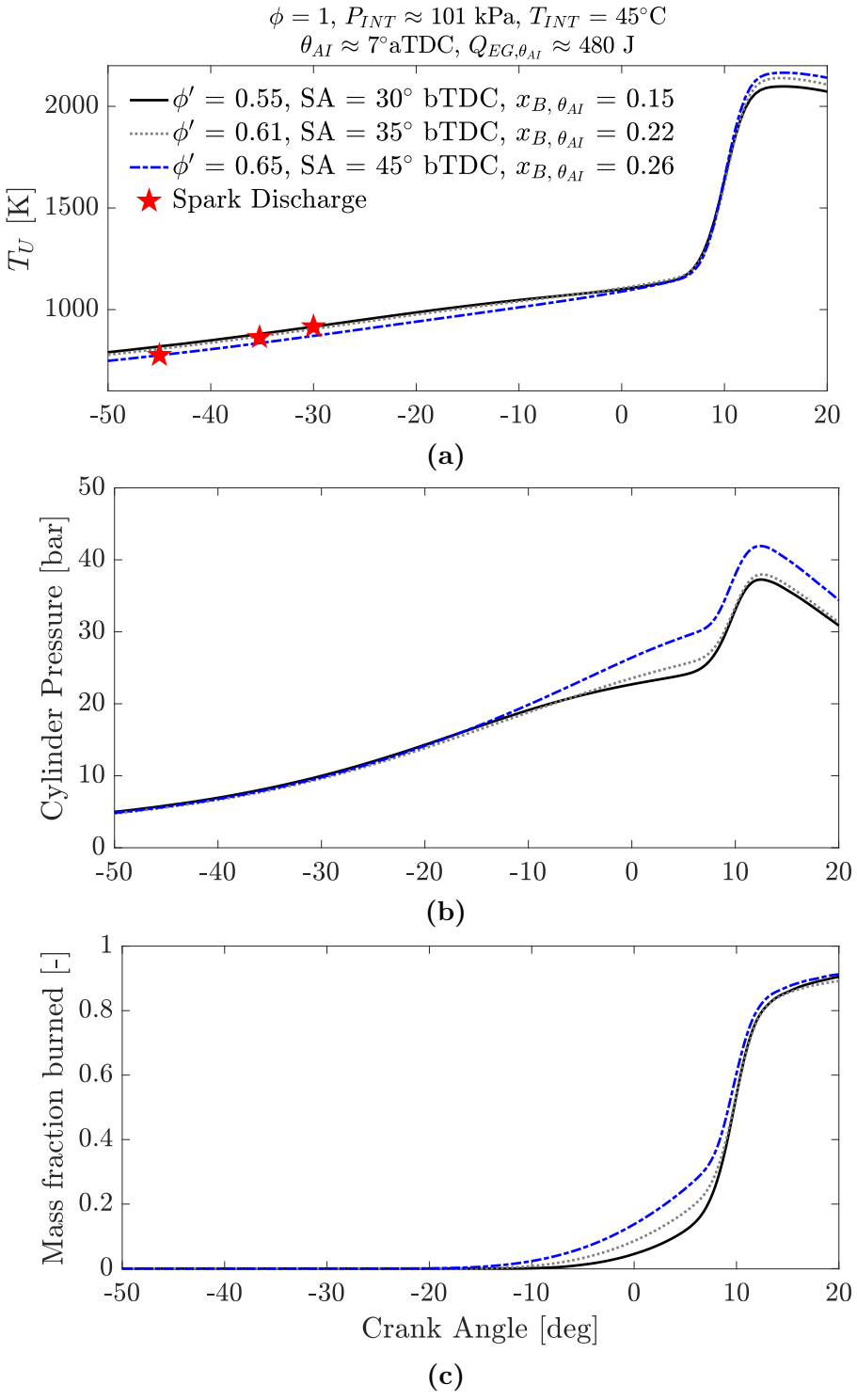

Figure 5.7: (a) Estimated unburned gas temperature, (b) cylinder pressure and (c) global mass fraction of fuel burned as a function of ϕ' at similar estimated end-gas energy at the onset of autoignition. Intake pressure, engine speed, intake temperature and autoignition phasing were all held constant.

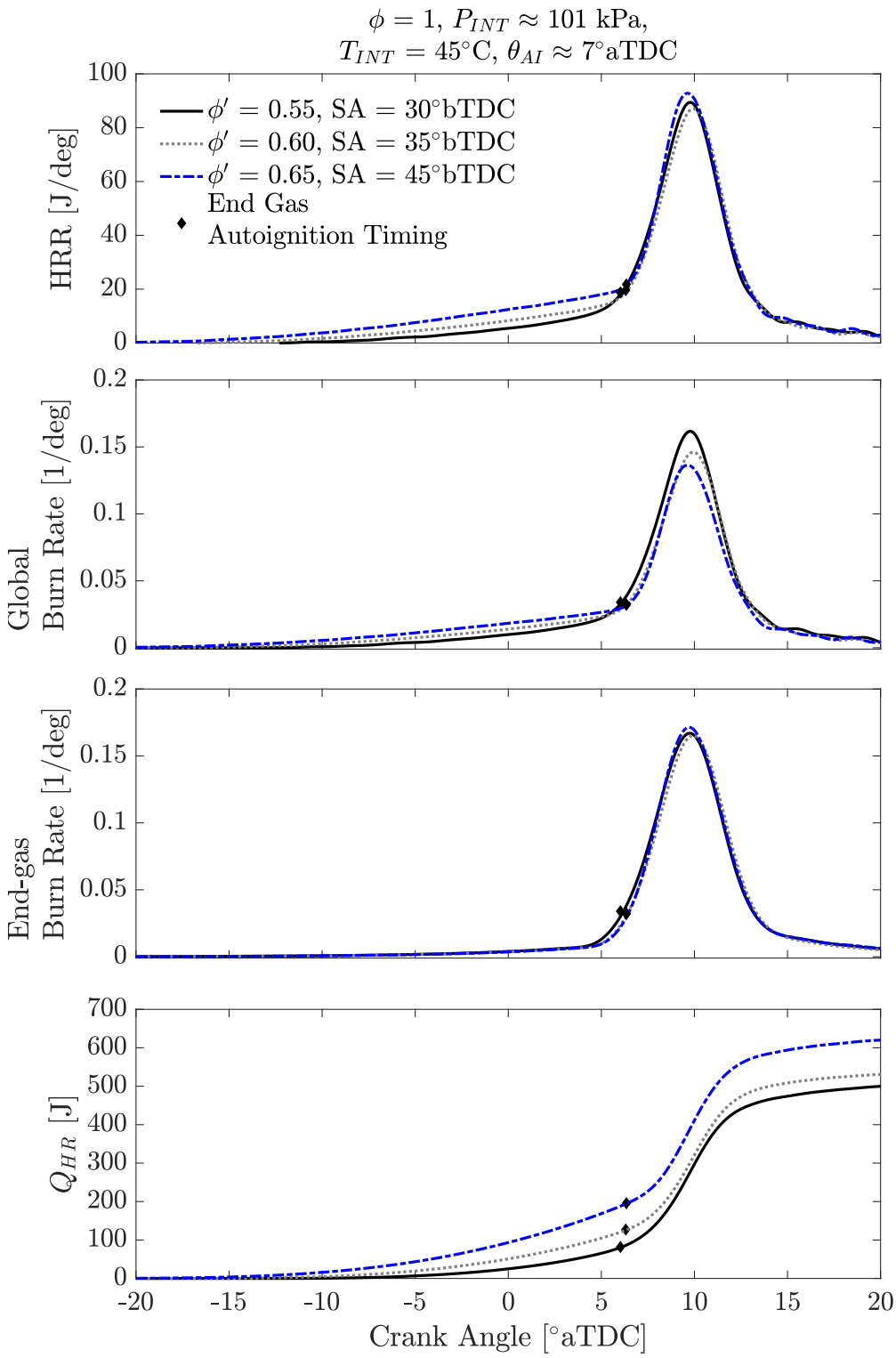

Figure 5.8: From top to bottom: Effect of ϕ' on gross heat release rate, global burn rate, end-gas burn rate and cumulative heat release at similar estimated end-gas energy at the onset of autoignition. Intake pressure, engine speed, intake temperature and autoignition phasing were all held constant.

Table 5.3: Experimental conditions for the ϕ' sweep at constant intake pressure and constant end-gas energy at autoignition.

Parameter	*Case1*	*Case 2*	*Case 3*
Engine speed [RPM]		2000	
Intake temperature [°C]		45	
Start of injection [°aTDC]		-330	
Intake valve opening / closing [°aTDC]		-265 / -161	
Fuel-to-air equivalence ratio, ϕ [-]		1.00	
Intake pressure [bar]	1.04	1.01	1.00
Fuel injected [mg/cycle/cyl]	13.0	13.6	15.4
Spark timing [°aTDC]	-30	-35	-45
Fuel-to-charge equivalence ratio, ϕ' [-]	0.55	0.60	0.65
Autoignition phasing, θ_{AI} [°aTDC]	6.6	6.8	7.0
Combustion phasing, θ_{50} [°aTDC]	10.0	10.0	9.5
Exhaust valve opening [°aTDC]	177	184	192
Exhaust valve closing [°aTDC]	281	288	296
Internal EGR mass fraction [-]	0.36	0.30	0.25
External EGR mass fraction [-]	0.09	0.08	0.09

5.3 EGR Dilution Effects at Constant Load

5.3.1 Experiments at Constant Spark Advance and Varying Mass Fraction Burned at the Onset of Autoignition

In a boosted SACI engine a given load condition can be achieved at different EGR dilution levels as the boost pressure is varied. It remains unclear how changes in fuel-to-charge equivalence ratio at a fixed load influence the tradeoff between between flame propagation and autoignition and the resulting peak heat release rate. Understanding the combined effects of intake pressure and ϕ' on the SACI burn profile would help access the high thermal efficiency regions demonstrated by thermodynamic simulations in the literature [39] and hence aid the practical implementation of this combustion mode.

In this set of experiments, the fuel mass injected was fixed at 15 mg per cycle per cylinder, corresponding to a GMEP of approximately 5.2 bar. Spark timing was fixed at 40° bTDC and intake pressure was decreased from 120 bar to 84 kPa, which led to a ϕ' increase from 0.55 to 0.70. The internal and external EGR rates were adjusted to maintain stoichiometry and target autoignition timing at around 7° aTDC. Details of the experimental conditions can be seen in Table 5.4.

Figure 5.9 shows the evolution of cylinder pressure and unburned gas temperature for all cases. Since the fuel mass injected is held constant, low ϕ' cases are achieved by using higher intake pressures and vice versa. The mean unburned gas temperature is lower for the high ϕ' cases up to the onset of autoignition. The difference in unburned gas temperature between the highest and lowest ϕ' case is approximately 75 K at spark timing and approximately 20 K at autoignition timing. Similarly to the results at constant intake pressure, these temperature trends offset the increased reactivity of the higher ϕ' so that autoignition timing is matched at around 7°aTDC.

Figure 5.10 shows the heat release analysis results for the ϕ' sweep at constant fuel energy input. While spark timing is held constant at 40°bTDC, higher ϕ' cases burn faster during the initial flame propagation phase resulting in higher heat release rates. As a result, mass fraction burned at the onset of autoignition increases from

22% to 39%. However, unlike the results shown in Section 5.2.1, peak heat release rate decreases at higher ϕ' conditions. This trend is observed due to changes in the end-gas energy at the onset of autoignition, since the peak end-gas burn rates are similar between the cases, as seen in Figure 5.10. The fact that the end-gas burn rates are similar even though the fuel-to-charge equivalence ratio increases is likely due to the changes in mass fraction burned at autoignition timing, as discussed in the computational studies by Middleton et al. [60] and Martz et al. [141]. In those studies, as the burned gas mass at autoignition timing increased, the end-gas reactivity was shown to decrease as the unburned mixture mass near the cylinder wall was less reactive [60]. Additionally, the differences in end-gas burn rate as the fraction of flame based heat release varies were also attributed to differences in the work transferred from end-gas expansion during autoignition, which influenced the end-gas temperature time history [141]. Lastly, the lower ϕ' cases are achieved by increasing the intake pressure, hence the end-gas reactivity stratification is expected to be decrease based on the findings from Chapter IV.

Table 5.4: Experimental conditions for the ϕ' sweep at constant load and constant spark advance.

Parameter	*Case1*	*Case 2*	*Case 3*	*Case 4*
Engine speed [RPM]	2000			
Fuel injected [mg/cycle/cyl]	15			
Intake temperature [°C]	45			
Fuel injection pressure [bar]	110			
Spark timing [°aTDC]	-40.5			
Start of injection [°aTDC]	-330			
Intake valve opening / closing timing [°aTDC]	-265 / -161			
Fuel-to-air equivalence ratio, ϕ [-]	1.01			
Intake pressure [kPa]	120	110	97	84
Fuel-to-charge equivalence ratio, ϕ' [-]	0.55	0.59	0.65	0.70
Autoignition timing, θ_{AI} [°aTDC]	7.2	7.5	7.5	7.6
Combustion phasing, θ_{50} [°aTDC]	10.2	10.3	9.9	9.3
Exhaust valve closing [°aTDC]	182	186	194	208
Exhaust valve closing [°aTDC]	286	290	298	312
Internal EGR mass fraction [-]	0.32	0.29	0.24	0.17
External EGR mass fraction [-]	0.12	0.11	0.11	0.12

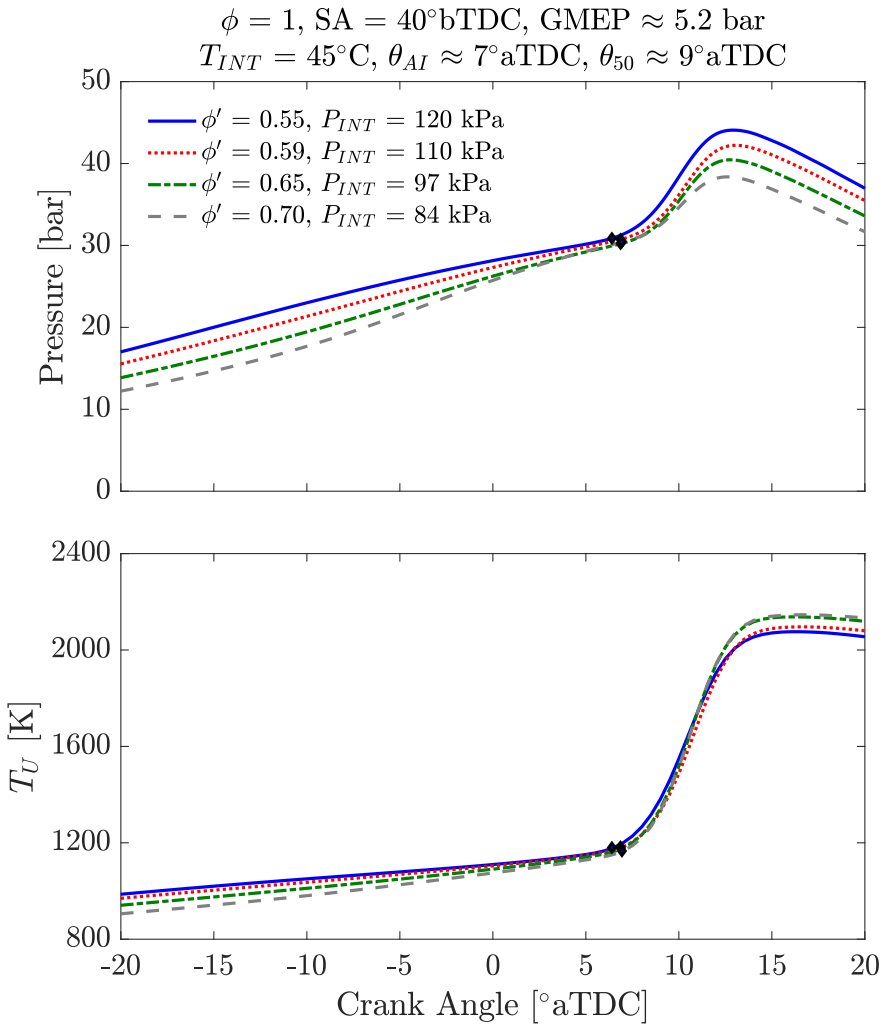

Figure 5.9: Cylinder pressure variation (top) and unburned gas temperature (bottom) as a function of ϕ' at similar estimated end-gas energy at the onset of autoignition. Intake pressure, engine speed, intake temperature and autoignition phasing were all held constant.

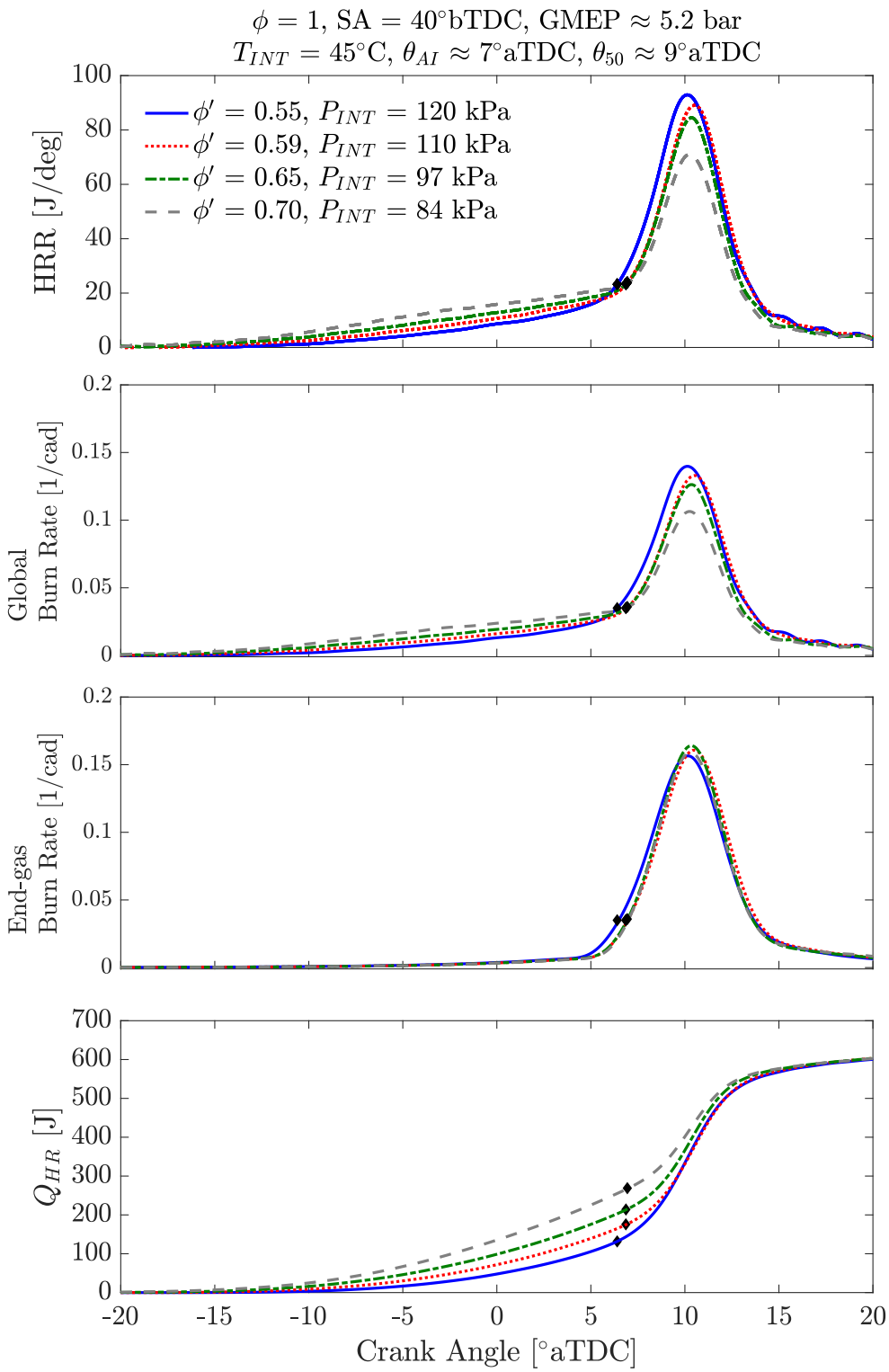

Figure 5.10: From top to bottom: Effect of ϕ' on gross heat release rate, global burn rate, end-gas burn rate and cumulative heat release at constant load and spark timing. Engine speed, intake temperature and autoignition phasing were all held constant.

5.3.2 Experiments at Constant Mass Fraction Burned at the Onset of Autoignition

A set of conditions were investigated to complement the study in Section 5.3.2 by fixing the mass fraction burned at the onset of autoignition for increasing ϕ' cases. Similarly, the fuel mass injected was fixed at 15 mg per cycle per cylinder which corresponded to a GMEP of approximately 5.2 bar. Intake pressure was varied from 120 kPa to 81 kPa which led to an increase in ϕ' from 0.55 to 0.77. The mixture was kept at stoichiometry and EGR dilution was achieved using a combination of internal and external EGR. The temperature of the charge at IVC was adjusted by varying the ratio of internal to external EGR. Spark timing and IVC temperature were adjusted to match both the mass fraction burned at the onset of autoignition and the autoignition phasing. The details of the experimental approach can be found in Table 5.5.

Figure 5.11 shows heat release analysis results. When spark timing and IVC temperature are adjusted so that the mass fraction burned by the flame is matched, then the peak end-gas burn rates exhibit an increasing trend with increasing ϕ'. In order to match the mass fraction burned at the onset of autoignition, the lower ϕ' cases are ignited earlier to compensate for the slower burn of the higher dilution mixtures. Since the total fuel mass injected and the mass fraction burned at the onset of autoignition is similar between the cases, the heat release profiles follow a similar trend to the global burn rate profiles. The increasing trend in the peak heat release profile is attributed to the faster end-gas burn rates driven by the lower EGR dilution levels. Comparing the results from this section to those at constant intake pressure from Section 5.2.2, one can see that the increase in end-gas autoignition rate with ϕ' is much more pronounced when the intake pressure is maintained constant as opposed to in the constant load cases. Based on the findings in Chapter IV it is believed that for the constant load cases, the increased dilution (i.e. lower ϕ') and higher pressure have opposing effects on the end-gas autoignition rates.

Table 5.5: Experimental conditions for the ϕ' sweep at constant load and constant mass fraction burned at the onset of autoignition.

Parameter	*Case1*	*Case 2*	*Case 3*
Engine speed [RPM]		2000	
Fuel injected [mg/cycle/cyl]		15	
Intake temperature [°C]		44	
Start of injection [°aTDC]		-330	
Intake valve opening / closing timing [°aTDC]		-265 / -161	
Fuel-to-air equivalence ratio, ϕ [-]		1.00	
Spark timing [°bTDC]	41	35	30
Intake pressure [bar]	1.20	0.97	0.80
Exhaust pressure [bar]	1.31	1.16	1.12
Fuel-to-charge equivalence ratio, ϕ' [-]	0.56	0.65	0.77
Autoignition timing [°aTDC]	7.0	7.7	7.5
Combustion phasing, θ_{50} [°aTDC]	9.8	10.2	9.8
Exhaust valve closing [°aTDC]	183	192	201
Exhaust valve closing [°aTDC]	287	296	305
Internal EGR mass fraction [-]	0.31	0.26	0.21
External EGR mass fraction [-]	0.13	0.09	0.03

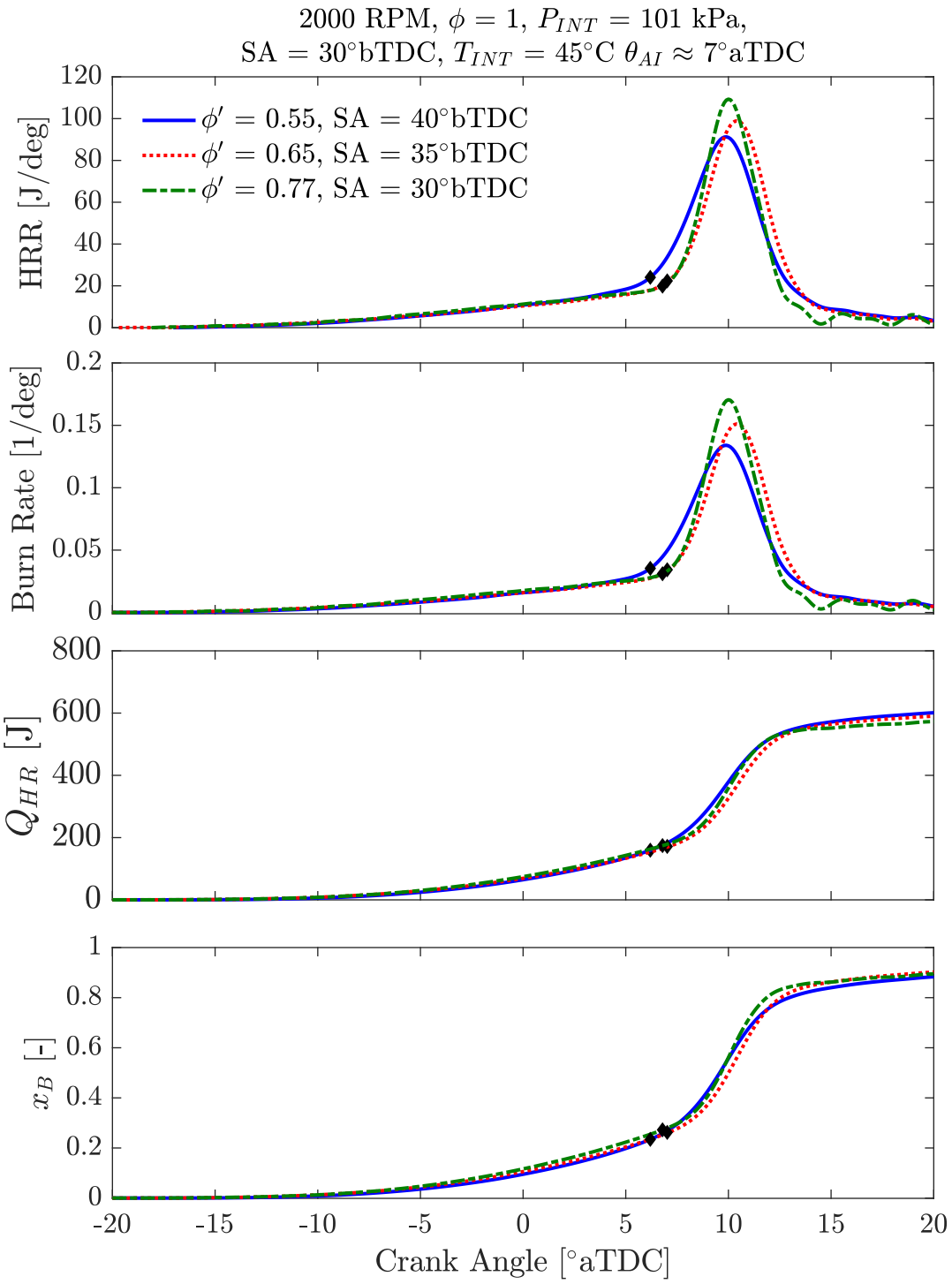

Figure 5.11: From top to bottom: Effect of ϕ' on gross heat release rate, global burn rate, end-gas burn rate and cumulative heat release at stiochiometric conditions and similar mass fraction burned at the onset of autoignition. Engine speed, intake temperature and autoignition phasing were held constant for all conditions.

5.4 Summary

An experimental approach was designed to investigate the effect of fuel-to-charge equivalence ratio (ϕ') on stoichiometric SACI burn rates. First, ϕ' sweeps were performed at constant intake pressure by allowing the total fuel mass injected per cycle to vary and then ϕ' sweeps were performed at constant fuel energy input by allowing the intake pressure to vary. Changes in fuel to charge equivalence ratio were achieved solely by varying the EGR dilution levels from 23% to 55%. For each set of experiments, spark timing was initially kept constant and the temperature of the charge was varied so that autoignition occured close to 7°aTDC. Then spark timing and unburned charge temperature were both varied so that the mass fraction burned at the onset of autoignition ($\approx$ 7°aTDC) was maintained constant.

Increasing the fuel-to-charge equivalence ratio at unthrottled conditions and constant spark advance required a decrease in unburned gas temperature of up to 60 K at spark timing in order to match autoignition phasing. Higher ϕ' cases exhibited faster flame burn rates, which was explained by the increasing trend in estimated laminar flame speeds due to higher burned gas temperatures. The higher flame burn rates of higher ϕ' mixtures resulted in a higher mass fraction of fuel burned at the onset of autoignition; however, the end-gas absolute energy at the onset of autoignition increased due to the increase in the total energy content of the mixtures. Excessive peak heat release rates were observed at the highest ϕ' conditions due to faster autoignition rates and higher end-gas energy at the onset of autoignition. The ϕ' investigation was extended at intake pressures between 0.8 and 1.5 bar and the increasing trends in peak autoignition rate rates, end-gas energy at autoignition and peak heat release rate with ϕ' were found to be consistent for all intake pressures. When spark advance and unburned charge temperature were adjusted to match the mass fraction burned at the onset of autoignition, similar trends were observed but the increase in end-gas energy and autoignion burn rate with ϕ' was found to be even more pronounced. An increase in ϕ' from 0.58 to 0.71 led to an increase in the peak autoignition rates by approximately 70%. This difference compared to the constant

spark advance results was attributed to the changes in the mass fraction burned at the onset of autoignition, which is consistent with previous published work [60] for cases at constant composition. It was also shown that if the mass fraction burned at the onset of autoignition increases sufficiently, it is possible to offset the higher autoignition rates of higher ϕ' mixtures and maintain a constant peak heat release rate.

The fuel-to-charge equivalence ratio effects at constant load were found to be similar trendwise to those at constant pressure. At constant autoignition phasing and mass fraction burned at the onset of autoignition, higher ϕ' cases exhibited higher peak heat release rates due to faster autoignition rates. However, the increase in the autoignition rate with ϕ' was observed to be much lower than the results at constant intake pressure. Since fuel mass injected was maintained constant, low ϕ' mixtures were associated with higher intake pressures and vice versa. Based on the findings in Chapter IV, it is believed that for the constant load cases the pressure effect on end-gas autoignition rate is likely being counteracted by the EGR dilution effect.

CHAPTER VI

Understanding the End-Gas Autoignition Rates under Boosted SACI Conditions

This chapter uses computational tools to further investigate the changes in end-gas autoignition rates observed under boosted SACI conditions. Experimental studies presented in Chapter IV showed that for mixtures with the same composition, when combustion phasing and mass fraction burned at the onset of autoignition are held constant, the peak end-gas burn rate increases approximately proportionally with intake pressure. Higher pressure conditions are expected to increase the mixture reactivity due to a reduction in the mean free path between the species, however, the experimental results indicated that higher pressure mixtures were also cooler in order to match combustion phasing. Constant volume ignition delay computations with a detailed kinetic mechanism representing gasoline suggested that the effect of the higher pressure on the mean reactivity of the unburned gas is likely being offset by the reduction in the temperature at the onset of autoignition. Changes in the pre-ignition reactivity stratification or the evolution of the mixture reactivity post-ignition could be possible reasons for the end-gas autoignition rate trends observed. The main source of this increase in autoignition rate with higher boost pressure is therefore unclear. The role of thermal and compositional stratification and the resulting reactivity stratification are investigated in this chapter to better understand the physical processes leading to the experimental findings. The effect of charge preheating method on the evolution of the reactivity stratification and the resulting

heat release rate is also investigated.

6.1 KIVA-CFMZ Model for Open Cycle SACI Simulations

6.1.1 KIVA-CFMZ Model Description

The work presented in this chapter exercises a detailed SACI model previously developed at the University of Michigan, the Coherent Flamelet Multi-Zone model (KIVA-CFMZ). The KIVA-CFMZ model was initially developed by Martz [57] for closed cycle SACI simulations of air dilute mixtures and subsequently extended by Middleton [82] to account for open cycle breathing, the presence of EGR and direct fuel injection and evaporation during NVO. A transport equation was added to account for the non-uniform EGR dilution in the cylinder as internal residual gas is being retained from the previous cycle. The fuel injection model uses the high-pressure swirl model of Chryssakis and Assanis [142], which has been previously validated and showed good agreement with experimental optical engine studies using planar laser-induced fluorescence (PLIF) measurements [143]. The CFMZ model has been built into the 3-D CFD framework KIVA-3V [144], which uses a Reynolds Averaged Navier Stokes solver for fluid dynamics calculations. Turbulent reaction front propagation is modeled using the Coherent Flamelet model [145, 146], coupled with detailed chemistry calculations for the end-gas and product zones using the multi-zone approach presented by Babajimopoulos et al. [147]. The standard k-epsilon model is used for flow turbulence modeling, while the laminar flame speed and thickness are estimated using correlations developed from simulations of steady, premixed laminar reaction fronts of relevant SACI conditions by Middleton et al. [79]. Standard KIVA-3V wall functions and the log-law of the wall approach are used to model heat losses to the cylinder liner, head, piston and valves.

The benefit of the multi-zone approach is that the computationally intensive chemical kinetics processes are solved for a small number of zones, while the fluid mechanical processes are still computed in a highly resolved grid in KIVA-3V. Computational time was further reduced by using multiple processors for the chemical kinetics calcu-

lations with a parallel computing approach adopted from Middleton [82]. The tens of thousands of computational cells are grouped into a small number of chemistry zones of similar thermodynamic state and reaction progress. According to the original Multi-Zone model formulation of Babajimopoulos et al. [147] at each computational time step the pressure in the combustion chamber is assumed to be uniform and the chemistry zones are sorted based on temperature and progress equivalence ratio (φ) defined as:

$$\varphi = \frac{2\mathrm{C}^{\#}_{-\mathrm{CO_2}} + \frac{1}{2}\mathrm{H}^{\#}_{\text{-}\mathrm{H_2O}} - z'\mathrm{C}^{\#}_{\text{-}\mathrm{CO_2}}}{\mathrm{O}^{\#}_{\text{-}\mathrm{CO_2}\text{-}\mathrm{H_2O}} - z'\mathrm{C}^{\#}_{\text{-}\mathrm{CO_2}}} \tag{6.1}$$

where $\mathrm{C}^{\#}_{-\mathrm{CO_2}}$, $\mathrm{H}^{\#}_{\text{-}\mathrm{H_2O}}$ and $\mathrm{O}^{\#}_{\text{-}\mathrm{CO_2}\text{-}\mathrm{H_2O}}$ are the number of C, H and O atoms present in a cell without counting the contributions from complete combustion products (CO_2 and H_2O), as indicated by the subscipts used. The z' term is given by the ratio of z/x and refers to the ratio of oxygen to carbon atoms in the fuel. For non-oxygenated fuels as in this case, z' is equal to zero.

The original multi-zone model was formulated for HCCI mixtures which are typically ultra lean ($0.1< \phi <0.4$). However, the current work investigates globally stoichiometric mixtures diluted with EGR, which means that the local fuel-to-air equivalence ratio can vary from lean to rich depending on the level of stratification induced by the direct injection of the fuel. This poses several problems in the definition of the reaction progress variable (φ) [148]. For unreacted mixtures, φ is the same as the fuel-to-oxygen equivalence ratio. The evolution of φ will be always less than 1 for lean mixtures and equal to 1 for stoichiometric mixtures. For rich mixtures, φ can take values greater than 1 up to infinity for pure fuel mixtures, which can lead to very large differences in φ for similar composition. To avoid generating an excessively large number of chemistry zones for rich cells with high levels of reaction progress, the progress variable, φ^*, which was initially defined in previous work [82] and is shown in Equation 6.2 below. The range of φ^* is 0 to 2 from pure air to pure fuel. Additionally, changes in EGR dilution for stoichiometric mixtures are not captured in the φ definition. To address those shortcomings in the zoning process,

the current work uses the temperature, the progress variable, φ^*, and the fraction of stoichiometric combustion products in the cell, X_{SCP} defined in Section 2.2.6.

$$\varphi^* = \begin{cases} \varphi & \text{if } \varphi \leq 1 \\ 2 - \frac{1}{\varphi} & \text{if } \varphi > 1 \end{cases} \tag{6.2}$$

The resolution in φ^* and X_{SCP} for grouping the chemistry zones in this work was 0.03 and 0.1, respectively. The temperature width of each zone used in this work follows the variable width approach presented by Middleton [82], where 5 K temperature widths are used from 900 K to 1200 K, where auto-ignition chemistry is very sensitive to temperature changes and coarser temperature bins are used for temperatures further away from those limits, as shown in Figure 6.1. Once the chemistry zones have been generated, the average temperature, pressure and composition is used to perform chemical kinetics calculation over the timestep using the CHEMKIN [149] solver. After the kinetics computations are complete, the new composition is remapped from the zone to the individual cells through variable *ch*, defined in Equation 6.3, which represents the number of C and H atoms in non-product species.

$$ch = 2\mathrm{C}^{\#}_{-\mathrm{CO_2}} + \frac{\mathrm{H}^{\#}_{-\mathrm{H_2O}}}{2} \tag{6.3}$$

$$m_m = \frac{ch_{cell}}{ch_{zone}} m_{m,zone} \tag{6.4}$$

For all species except CO_2, H_2O, O_2 and N_2, the new mass of species m is calculated using Equation 6.4. For CO_2, H_2O, O_2 and N_2, the new masses are calculated through atom balances in the cell to enforce that the overall cell mass remains invariant over the chemistry calculation, as well as ensuring atom conservation.

Additional details on the full KIVA-CFMZ model formulation can be found in the original work by Martz [57] and Middleton [82]. The model was initially validated [57] against lean SACI engine experiments from an optically accessible engine [151]. Trendwise agreement was shown between the predicted cylinder pressure and the

experimental engine. Additionally, the evolution of the reaction fronts predicted by the model were similar to those observed in the experimental chemiluminescence images of SACI combustion. Subsequently, the model was validated and showed good agreement to SACI experimental conditions using EGR dilution from a single cylinder NVO research engine at the University of Michigan [82]. The multi-zone approach has been previously validated under similar conditions to this study in the work of Babajimopoulos [152] and Kodavasal [131].

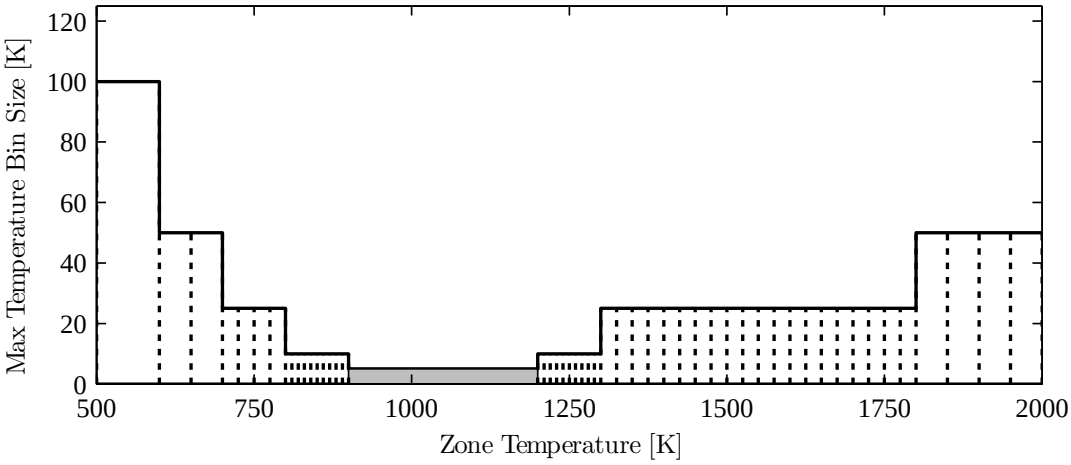

Figure 6.1: Variable sizing of temperature bins with high resolution (5 K) being used for temperatures between 900 K - 1200 K (solid grey) where autoignition chemistry is sensitive to temperature changes. Reproduced from [82].

6.1.2 Model Configuration

The KIVA-CFMZ open cycle simulations were performed using a 156,000 cell detailed 3-D mesh with moving valves and piston, corresponding to an engine geometry similar to that of the experimental engine described in Section 2.1.1. The details of the mesh geometry are described in Table 6.1 and two views of the mesh are presented in Figure 6.2. Both the experimental engine and mesh geometries feature the same bore length, centrally mounted spark plug, side-mounted fuel injector and pent-roof combustion chamber. The fuel injector is located between the two intake valves for both engines and both pistons feature an asymmetrical bowl for enhancing air-fuel mixing. The main difference between the computational and the experimental ge-

ometry is the longer stroke of the computational mesh (156.6 mm vs. 145.5 mm), which results in a small increase in the displacement volume (550 cm^3 vs. 500 cm^3) and compression ratio (12.4 vs. 11.25). Despite the small differences between the geometries, the use of the existing computational mesh was considered appropriate for the studies presented in this chapter, which attempt to gain further insight on the trendwise experimental behaviors observed in Chapter IV under similar operating conditions rather than validate absolute behavior.

The intake and exhaust temperatures were set based on the experimental measurements described in Section 4.3 on a case by case basis. The thermal boundary condition were set using 1-D full engine model predictions of the simulated engine [82]. The exact values used for the mesh thermal boundary are provided in Table 6.2. The dynamic pressure measurements at the runners of cylinder 1 were used as boundary conditions for the simulation. Figure 6.3 displays high speed measurements of cylinder 1 intake and exhaust runner pressures for a typical boosted SACI operating condition. The vertical lines indicate valve opening and closing times for the intake valves (left) and exhaust valves (right). The valve motion in the simulation was imposed based on the experimental NVO valve profiles. The intake composition was prescribed as a mixture of fresh air and external EGR based on the experimental measurements. External EGR was assumed to be composed of complete combustion products. The exhaust gas composition was imposed based on the measured equivalence ratio, assuming complete combustion products. The initial flow turbulence field was determined using a full motored engine cycle simulation. Simulations were initialized at 640° bTDC firing using an 8 species chemical mechanism with no reactions during NVO. The simulation was stopped immediately after IVC timing at 115° bTDC firing and restarted with the 312 species chemical mechanism of Mehl et al. [128,129] representing a surrogate for RD-387 gasoline, shown in Table 6.3. Figure 6.4 displays a schematic of the threshold and mechanism swap [150] technique, which was used to speed up the simulation by using an 8 species chemical mechanism during NVO and up until IVC.

Table 6.1: Mesh geometry

Parameter	*Value*
Displacement	550 cm^3
Bore	86.0 mm
Stroke	94.6 mm
Connecting Rod Length	156.5 mm
Compression Ratio	12.4:1
Cylinder head design	Pent-roof
Fuel Injection	Side mounted DI

Table 6.2: Mesh thermal boundary conditions

	Temperature [K]
Cylinder Wall	450
Piston Top	480
Head / Firedeck	450
Intake Valve	480
Exhaust Valve	650

Table 6.3: Gasoline surrogate composition

Surrogate	*Mass fraction* [-]
Iso-octane	0.54130
n-Heptane	0.1488
Toluene	0.2738
2-pentene	0.0361

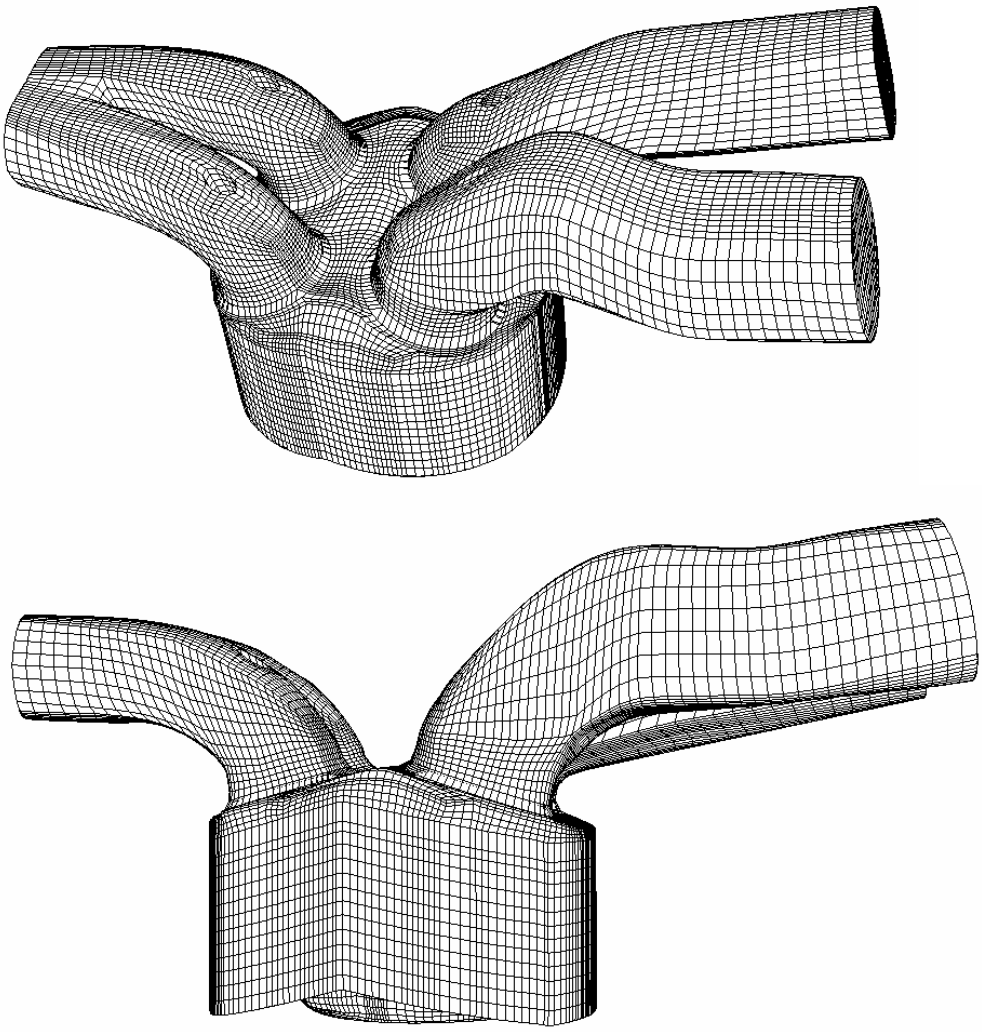

Figure 6.2: Computation mesh used in this work, containing 156,000 cells, based on the FFVA engine [14, 42, 153]. Exhaust ports shown on the left, intake ports on the right.

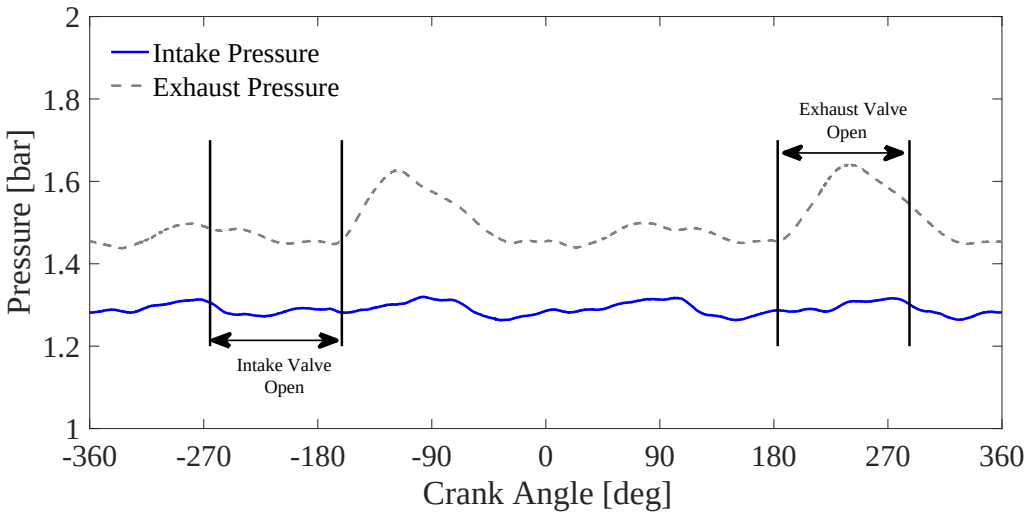

Figure 6.3: Example high speed pressure measurements of cylinder 1 intake and exhaust runners for a boosted SACI operating condition. The measurements are used as boundary conditions for the KIVA simulation. The vertical lines indicate valve opening and closing times for intake valve (left) and exhaust valves (right).

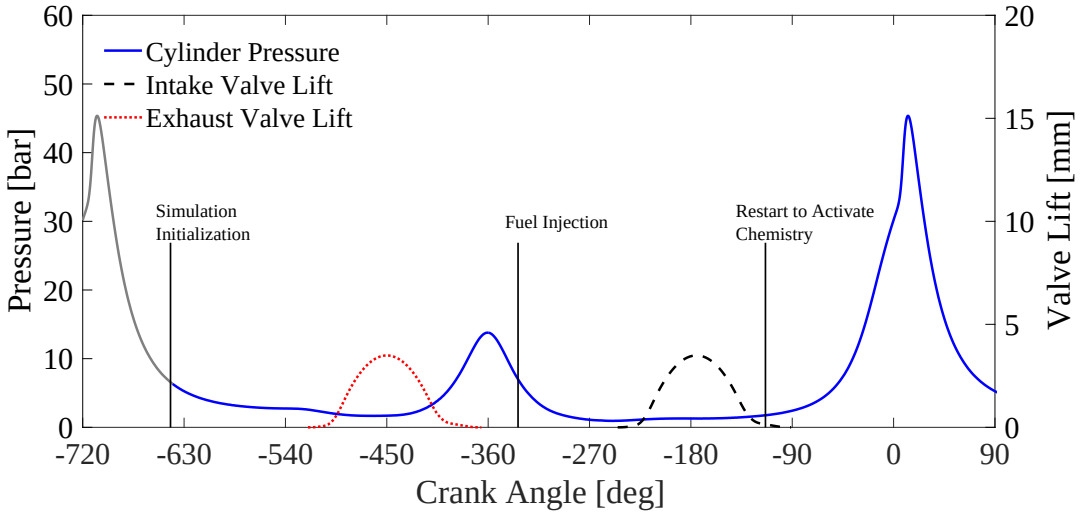

Figure 6.4: Schematic of simulation procedure for a typical boosted SACI case highlighting cylinder pressure and valve lift traces. Simulations are initialized at 640° bTDC firing using an 8 species chemical mechanism with no reactions to capture the effects of NVO on mixture preparation. The simulation is stopped immediately after IVC at 115° bTDC firing and restarted with the 312 species chemical mechanism of Mehl et al. [128, 129].

6.2 Comparison of Simulated and Experimental SACI trends

The detailed SACI model was exercised using input conditions from the experimental cases presented in Table 4.1, which correspond to intake pressures of 80 kPa, 100 kPa and 150 kPa, respectively. Due to the differences in the displacement volume and compression ratio between the experimental engine and the computational mesh, the simulation results were not expected to match exactly to the experimental pressure traces. The mixture composition for all the simulation results presented in this section was stoichiometric at a $\phi' = 0.49$, as opposed to the experimental conditions which were stoichiometric at a $\phi' = 0.55$. However, the composition of the simulation results still lie between the ϕ' levels where the boost pressure effects on end-gas autoignition were observed experimentally (i.e. $0.45 < \phi < 0.65$).

To match the composition, autoignition timing and mass fraction burned at the onset of autoignition for all the simulation cases, intake manifold temperature was increased by 15 K for the lower pressure case compared to the high pressure case. Additionally, spark timing had to be retarded by 12 CAD for the high pressure case compared to the lower pressure case. These changes had to be done to compensate for the higher flame burn rate predictions with higher pressure in the model compared to the experimental cases. However, the objective of this study was to understand the differences in end-gas autoignition rates with higher intake boost, so examining the discrepancies in the flame burn rates between the experimental and modeling results was beyond the scope of this study.

Figure 6.5 compares the trends in the cylinder pressure traces between the experiments and simulation for the boost sweep, while maintaining combustion phasing near 9° aTDC. While the end of compression pressures are slightly higher for the simulation cases due to the increase in compression ratio aforementioned, the difference in TDC pressure between the experiments and simulation is small ($\approx$ 3 bar) for all cases. More importantly the increasing pressure rise rate trend for higher boost conditions is captured well in the simulation results. Figures 6.7 and 6.8 display the trends in heat release rate and burn rate, respectively. When the mass frac-

tion burned at the onset of autoignition is matched, the simulation results exhibit a trendwise agreement in the peak heat release rate and burn rate with the experimental data. Specifically, for an increase in intake pressure from 80 kPa to 150 kPa, the simulation results depict an increase in peak heat release rate by approximately a factor of 4.4, while the peak burn rate is seen to approximately double for that same change in intake pressure. The temperature at IVC decreases by approximately 60 K with higher intake pressures and this drop in unburned gas temperature continues up to onset of autoignition, as seen in Figure 6.6. The trendwise agreement between the simulation and experimental cases gives confidence that the model can be used as an additional tool to understand the changes in the autoignition behavior observed experimentally. The pre-ignition reactivity stratification and its evolution from early in the compression until TDC is investigated in the following sections to better understand the sources of the changes in the autoignition behavior.

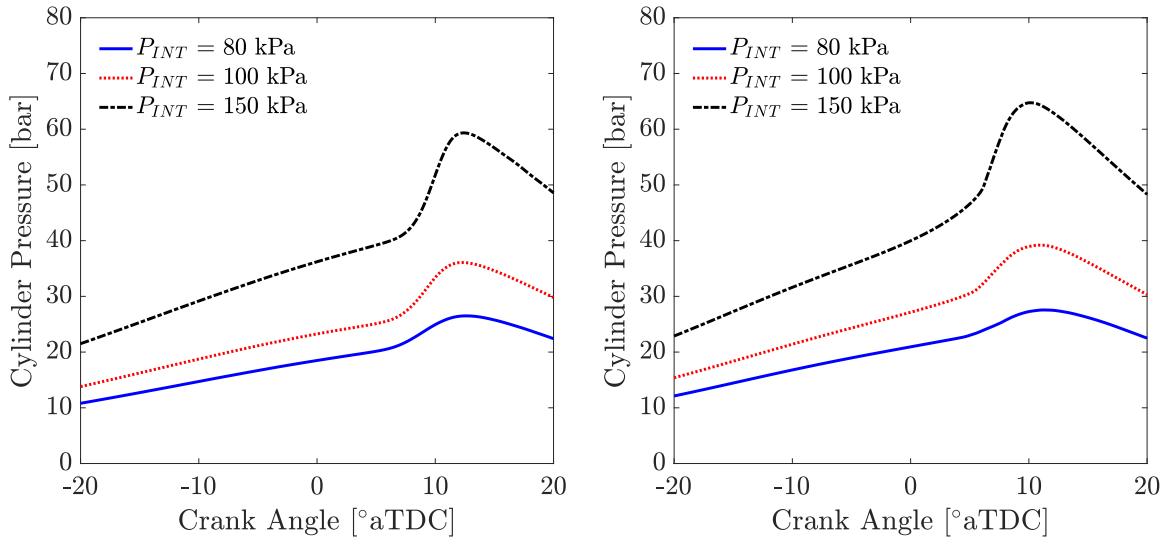

(a) Experimental results **(b)** Simulation results

Figure 6.5: Comparison of cylinder pressure results between (a) experimental cases and (b) simulation results.

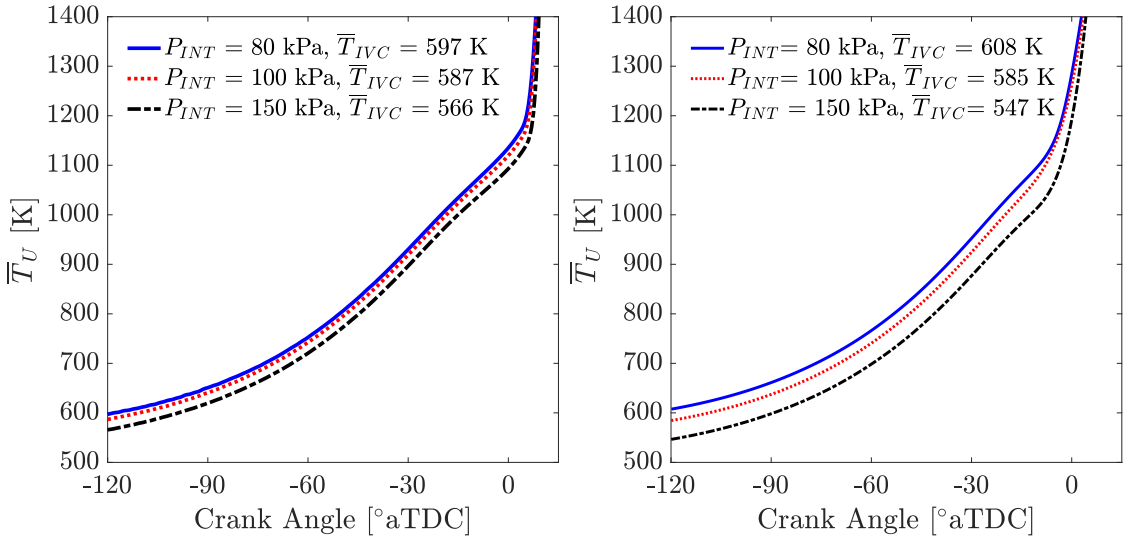

(a) Experimental results **(b)** Simulation results

Figure 6.6: Comparison of mass averaged unburned gas temperature trends during compression between (a) experimental and (b) KIVA-CFMZ simulation results.

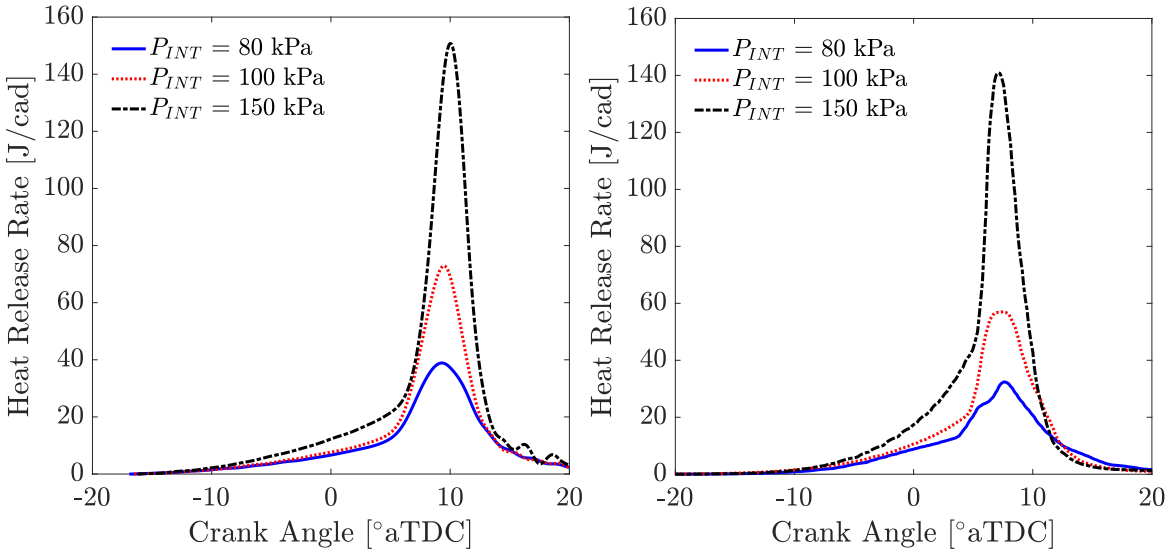

(a) Experimental results **(b)** Simulation results

Figure 6.7: Comparison of heat release rate results between (a) experimental cases and (b) KIVA-CFMZ simulation results. The increasing trend in peak heat release rate is captured well in the simulation results.

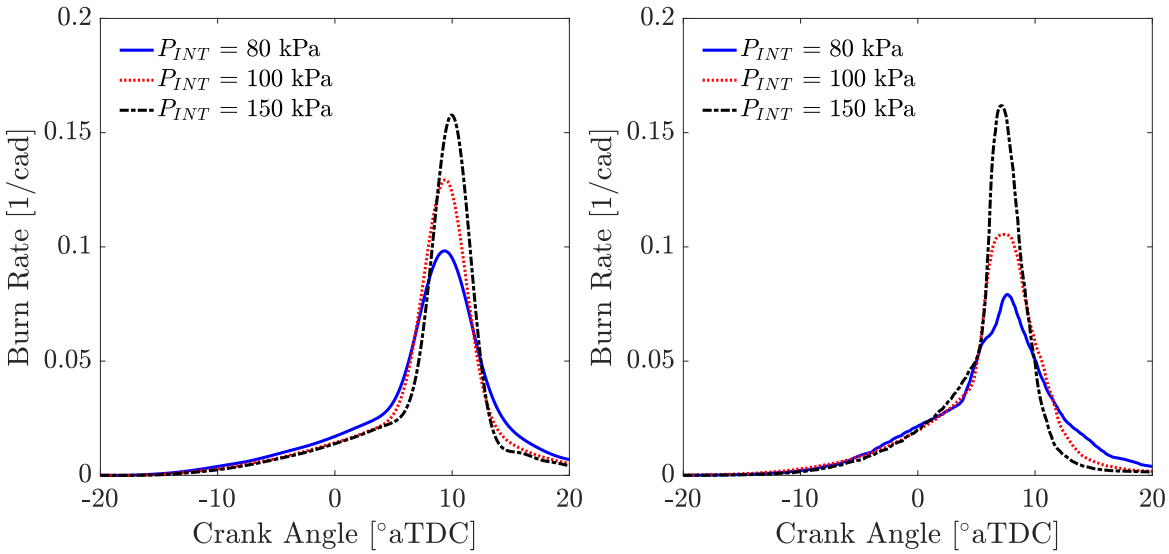

(a) Experimental results **(b)** Simulation results

Figure 6.8: Comparison of burn rate between (a) experimental cases and (b) KIVA-CFMZ simulation results.

6.3 Effect of Intake Boost on the End-Gas Reactivity Stratification

The pre-ignition charge reactivity from the simulation results is analyzed in more detail in this section to understand the mechanisms leading to the increase in end-autoignition rates at higher intake pressures. The reactivity stratification of the mixtures was initially evaluated by calculating the ignition delay at the onset of autoignition using the ignition delay correlation developed by He et. al [49] for the unburned zone of each computational cell at the onset of autoignition at 5° aTDC.

Figure 6.9 displays the normalized mass distributions of ignition delay for the three mixtures at increasing intake pressure. The higher pressure cases display a narrower reactivity stratification, with more mass concentrated at shorter ignition delay times. To understand the changes in reactivity stratification observed, the normalized mass distributions of temperature and non-product equivalence ratio for the unburned zones are analyzed just prior to autoignition at TDC. The thermal stratification in this work was quantified as two standard deviations (2σ) of the mass distribution in cell unburned zone temperature. The standard deviation was computed on a mass-weighted basis as shown in Equation 6.5 below. A similar approach was employed to assess compositional stratification using the non-product equivalence ratio, φ^*, of the unburned zone in each computational cell.

$$\sigma T = \sqrt{\frac{\sum_{i=1}^{N} n_i (T_i - \overline{T})^2}{\frac{N-1}{N} \sum_{i=1}^{N} n_i}} \tag{6.5}$$

where i is the subscript denoting a CFD cell, n represents cell mass, N represents the total number of CFD cells and T is the mass-weighted average temperature within the CFD domain.

Figure 6.10 displays the normalized mass distribution of unburned gas temperature at TDC. As expected, the higher pressure mixtures display a lower mass-averaged unburned gas temperature by approximately 80 K, however the thermal stratification

is narrower for higher pressure mixtures as $2\sigma T_U$ decreases from 127 K to 101 K. The narrower distribution of the high pressure case has a higher peak, since the area under all distributions should be equal to unity. The normalized mass distributions of non-product equivalence ratio, shown in Figure 6.11, display a similar decrease in $2\sigma\varphi^*$ as intake pressure increases.

To understand the pre-ignition reactivity stratification results discussed above, the evolution of the thermal and compositional stratification during the compression stroke was analyzed. Figure 6.12 shows the evolution of $2\sigma T_U$ and $2\sigma\varphi^*$ from early in the compression stroke until TDC. Higher pressure mixtures at constant intake temperature display consistently lower thermal stratification levels from early in the compression stroke until TDC. Additionally, all mixtures show a decrease in the thermal stratification up until 50 - 60° bTDC at which point $2\sigma T_U$ starts increasing again monotonically until TDC. This behavior can be attributed to the competition between mixing of fresh charge and residuals and higher heat transfer losses to the walls, as seen in other computational studies of HCCI combustion with high residual gas fractions [154]. Depending on the level of residual gas fraction and the wall temperature, mixing of residual gases and fresh charge may dominate early in the compression stroke creating a more homogeneous mixture, as seen in this set of simulation results. Late in the compression stroke the turbulence intensity level decreases [105], while the mixture temperature increases. As a result, the heat loss to the wall becomes more important in the development of the mixture's temperature stratification prior to autoignition. The importance of the heat transfer to the walls and the associated transport of cold gases from the cylinder wall toward the cylinder center has been also highlighted in previous work using quantitative tracer-based PLIF diagnostics in optically accessible engines [155–158].

Figure 6.13 displays the cumulative heat loss to the cylinder walls during compression until TDC on an absolute basis (top) and mass normalized basis (bottom). As expected, the absolute heat loss increases for the higher pressure cases, however the specific heat loss results display an opposite trend. Higher pressure mixtures reject less heat to the walls on a mass normalized basis, which agrees with the estimated

heat transfer loss trends using the experimental data and the Woschni heat transfer correlation presented in Section 3.5.2. The significance of the reduced normalized heat loss for the high pressure mixtures on the resulting thermal stratification is unclear from the above results, but is further investigated in Section 6.5.

In Figure 6.12, higher pressure mixtures exhibit lower compositional stratification early in the compression stroke. All cases show a monotonic decrease in $2\sigma\varphi^*$ as the piston moves towards TDC, since there is more mixing time between residual gases and fresh charge. Since the fuel injection event is during the NVO period and all mixtures are stoichiometric, it is reasonable that higher residual gas fraction cases result in a wider $2\sigma\varphi^*$ mass distribution at IVC timing. Under the conditions investigated the $2\sigma\varphi^*$ trend observed with pressure early in the compression stroke can be attributed to the changes in residual gas fraction between the cases.

Overall, the boost pressure sweep results using residual gas heating presented in this section show that higher pressure mixtures have narrower reactivity stratification at the onset of autoignition, which explains the increase in end-gas autoignition rate observed in both experiments and simulations. However, the relative importance of thermal and compositional stratification on the pre-ignition reactivity stratification is unclear. Additionally, the importance of thermal/compositional stratification early in the compression stroke on the reactivity stratification close to TDC is also unclear. The above questions motivated the simulations presented in Section 6.4 below, which compare boost pressure effects on end-gas autoignition rates using residual gas heating and intake manifold heating.

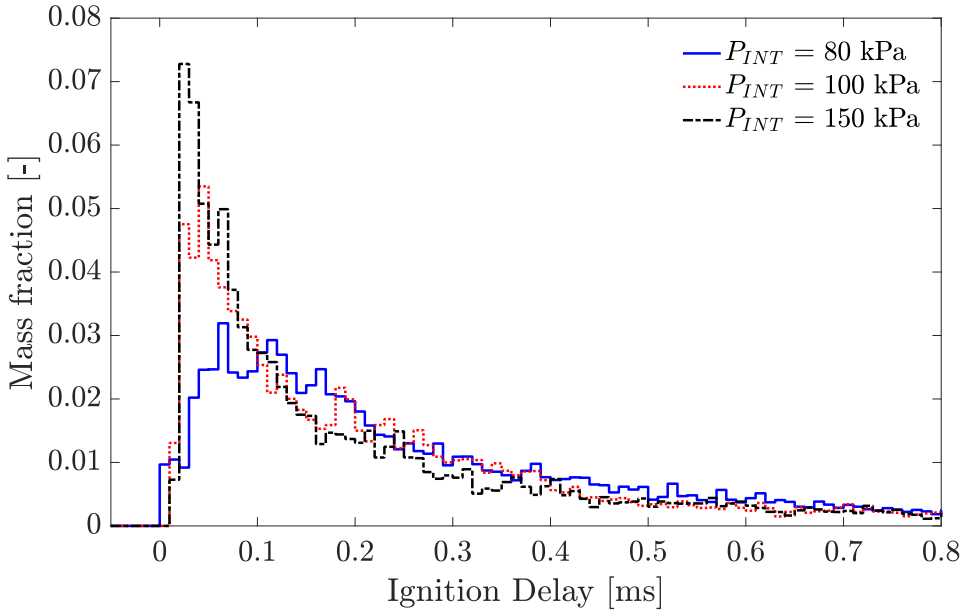

Figure 6.9: Ignition delay distributions at onset of autoignition (5° aTDC) for increasing intake pressure mixtures, with constant autoignition timing, composition and mass fraction burned at the onset of autoignition.

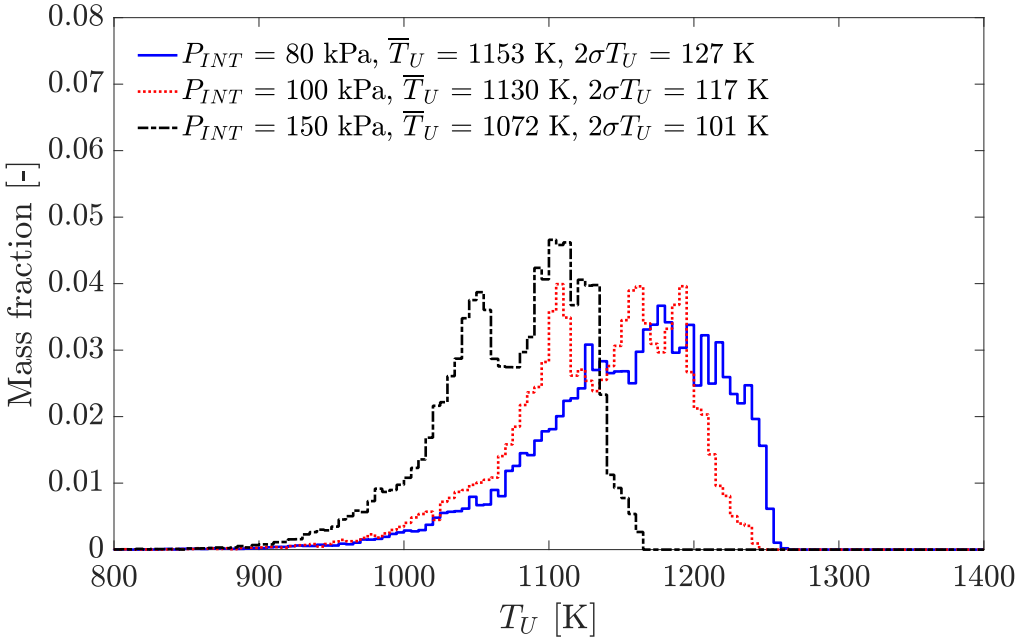

Figure 6.10: Pre-ignition unburned gas temperature distribution at TDC for increasing intake pressure mixtures at constant end-gas autoignition timing, composition and mass fraction burned at the onset of autoignition.

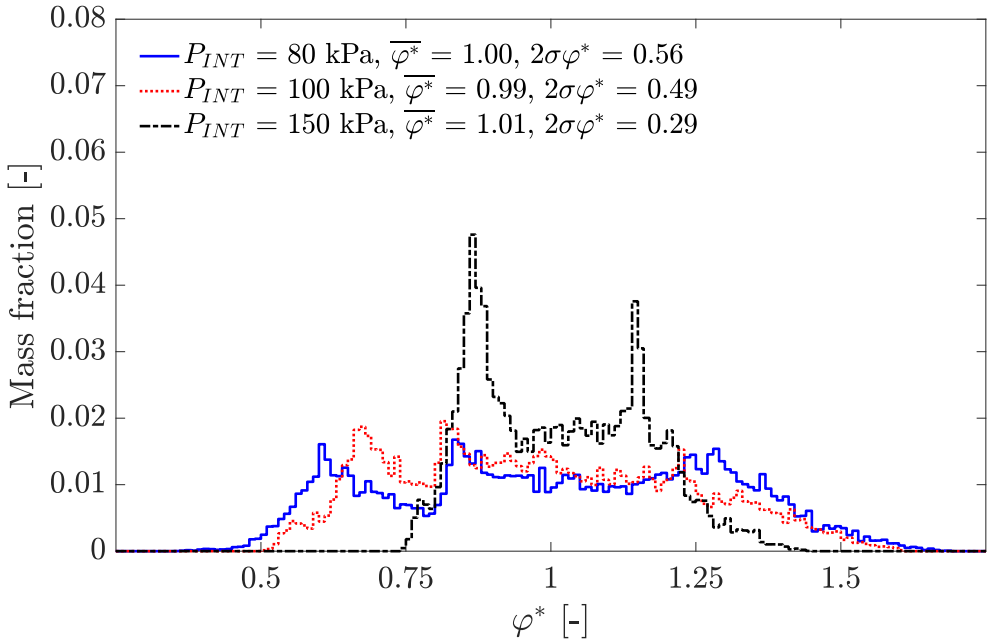

Figure 6.11: Pre-ignition non-product equivalence ratio distribution at TDC for increasing intake pressure mixtures at constant end-gas autoignition timing, composition and mass fraction burned at the onset of autoignition.

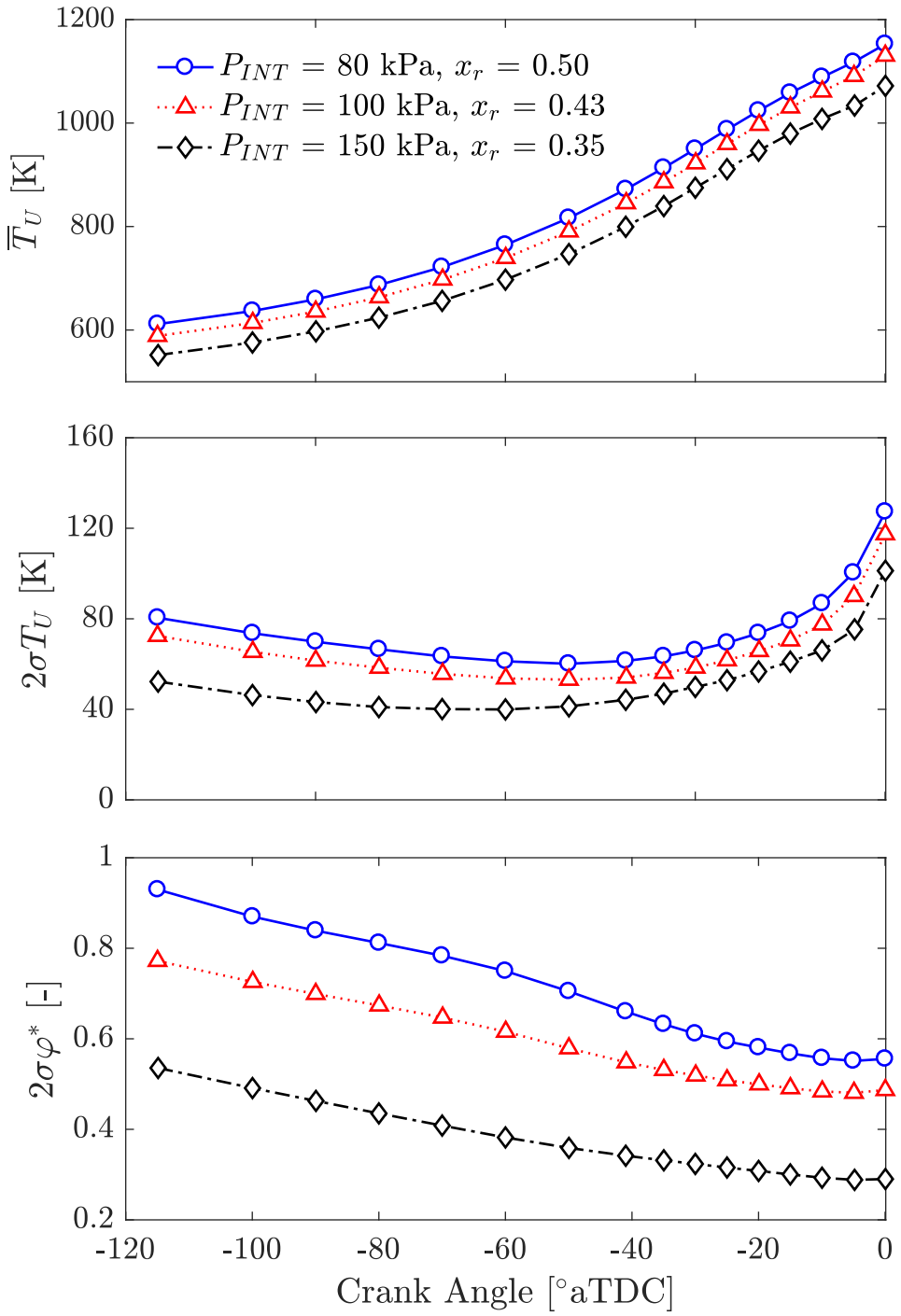

Figure 6.12: Evolution of mass averaged unburned gas temperature (top), unburned gas thermal stratification (middle) and non-product equivalence ratio stratification (bottom) during the compression stroke up to TDC for the intake pressure sweep using residual gas heating at same composition and end-gas autoignition timing.

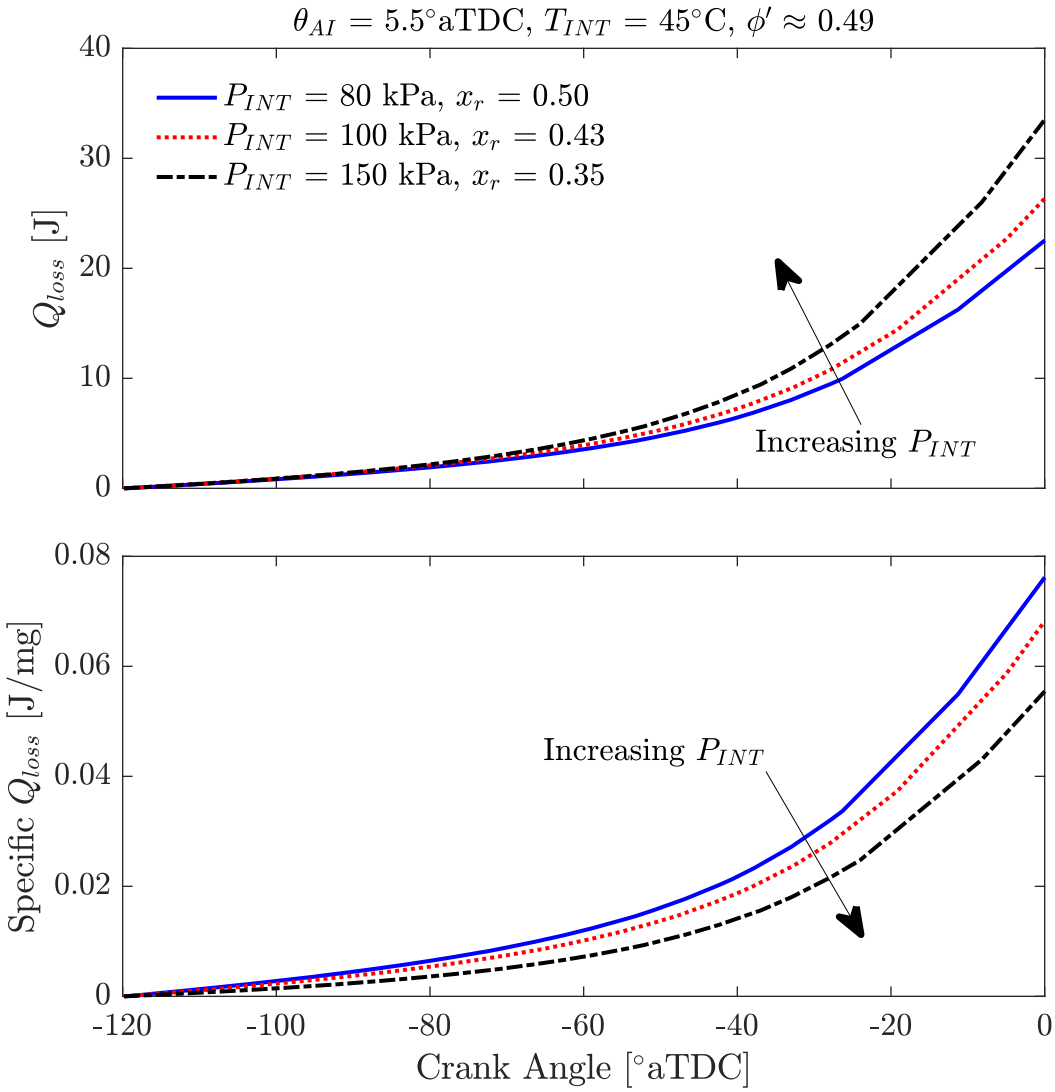

Figure 6.13: Cumulative heat loss through the cylinder walls during compression until combustion on an absolute basis (top) and mass normalized basis (bottom) for the intake pressure sweep using residual gas heating at constant composition and end-gas autoignition timing.

6.4 Comparison of Charge Preheating Methods on Reactivity Stratification and End-Gas Autoignition Rates under Boosted Conditions

Under the conditions investigated, charge preheating is required to ensure autoignition near TDC, which can be achieved by varying residual levels or modulating the intake manifold temperature. Experimental results presented in Section 4.6 showed that the increase in end-gas burn rates with higher intake pressure is similar irrespective of charge preheating method. The experimental results covered a limited boost range due to hardware limits associated with intake temperature heating. To better understand the underlying mechanisms that lead to the observed trend in end-gas autoignition rates, the CFD model was used to compare the effect of the charge preheating methods on reactivity stratification and end-gas autoignition rates under boosted, highly EGR-dilute, stoichiometric conditions.

Tables 6.4 and 6.5 outline the intake pressure sweep conditions investigated for residual gas heating and intake manifold heating, respectively. For the residual gas heating cases, intake temperature was maintained constant at 45° C and IVC temperature was achieved by varying the residual gas content through changes in EVO timing. Conversely, for the boost sweep using intake charge preheating, the residual gas fraction was maintained constant at 36% and changes in IVC temperature were achieved by modulating the intake temperature. For each case, spark timing and IVC temperature were varied to maintain a constant autoignition timing at approximately 5° aTDC and mass fraction burned at the onset of autoignition constant in order to remove the effect of those variables on the end-gas autoignition rate.

Figures 6.14, 6.15 and 6.16 display heat release rate curves, burn rate curves and mass fraction burned curves, respectively, for intake pressure sweeps comparing the two charge preheating methods. The heat release rate curves and burn rate curves are trendwise similar, however, as intake pressure is increased from 80 kPa to 150 kPa, intake charge preheating leads to a smaller increase in burn rate and heat release rate. The smaller increase in peak burn rate with intake charge preheating is observed due

to both a faster autoignition for the low pressure case (80 kPa) as well as a slower autoignition for the high pressure case (150 kPa) compared to the residual heating cases.

To better understand the underlying causes of the observed trends, the evolution of mean unburned gas temperature ($\overline{T}_U$), $2\sigma T_U$ and $2\sigma\varphi^*$ is analyzed. Figure 6.17 shows the evolution of $2\sigma T_U$ from early in the compression stroke until TDC for all six cases. An opposite trend in $2\sigma T_U$ at IVC timing can be observed when comparing the boost sweeps using residual gas heating as opposed to intake charge heating. While the increase in intake pressure leads to lower thermal stratification for the residual gas heating cases, the intake charge preheating cases exhibit an increase in thermal stratification with higher intake pressure. Unlike the residual gas heating cases, the intake charge preheating cases have same residual gas fraction and similar exhaust temperatures due to similar composition and combustion phasing. Consequently, the higher intake pressure cases require lower intake manifold temperature to achieve a lower mass averaged IVC temperature. This leads to a larger temperature difference between the residual gas and the charge in the intake manifold and hence a higher thermal stratification early in the compression stroke.

The variation in thermal stratification early in the compression stroke has negligible effect on the pre-ignition thermal stratification close to TDC, as $2\sigma T_U$ values converge for each intake pressure condition irrespective of charge preheating method. The most extreme change can be seen for the lowest pressure case, where $2\sigma T_U$ values at 115° bTDC are more than double for the residual gas heating case as opposed to intake charge preheating, but both cases reach a $2\sigma T_U$ value of 100 K at 5° bTDC. This observation agrees with the findings of direct numerical simulation studies in an engine like geometry by Schmitt and Boulouchos [137], which investigated the role of intake generated thermal stratification on the temperature distribution at TDC of the compression stroke. While their study was done at a much lower engine speed of 560 RPM without the use of residual gas heating, they concluded that thermal inhomogeneities at bottom dead center had nearly no impact on the temperature field close to TDC of compression. The wall temperature and the flow field were found

to be the main parameters controlling the evolution of the temperature distribution during compression.

Figure 6.18 displays the evolution of $2\sigma\varphi^*$ for all six mixtures from early in the compression stroke until TDC. The compositional stratification results for the intake preheating cases early in the compression stroke follow a similar trend to that of thermal stratification. Higher intake pressure mixtures exhibit higher $2\sigma\varphi^*$ values, however, the increase in compositional stratification is much smaller than the magnitude observed for the boost sweep using residual gas heating. The small changes in the compositional stratification early in the compression stroke can be attributed to the higher mixing rates of the high pressure cases, as residual gas fraction is maintained constant. Again, as the piston compresses the charge the in-cylinder fluid motion leads to less compositional inhomogeneity towards TDC, which is depicted by a decrease in $2\sigma\varphi^*$.

Even though thermal compositional and compositional stratification is different depending on charge preheating method, the mean unburned gas temperature evolution during compression shows minimal discrepancies at each intake pressure between the two charge preheating methods, as shown in Figure 6.19.

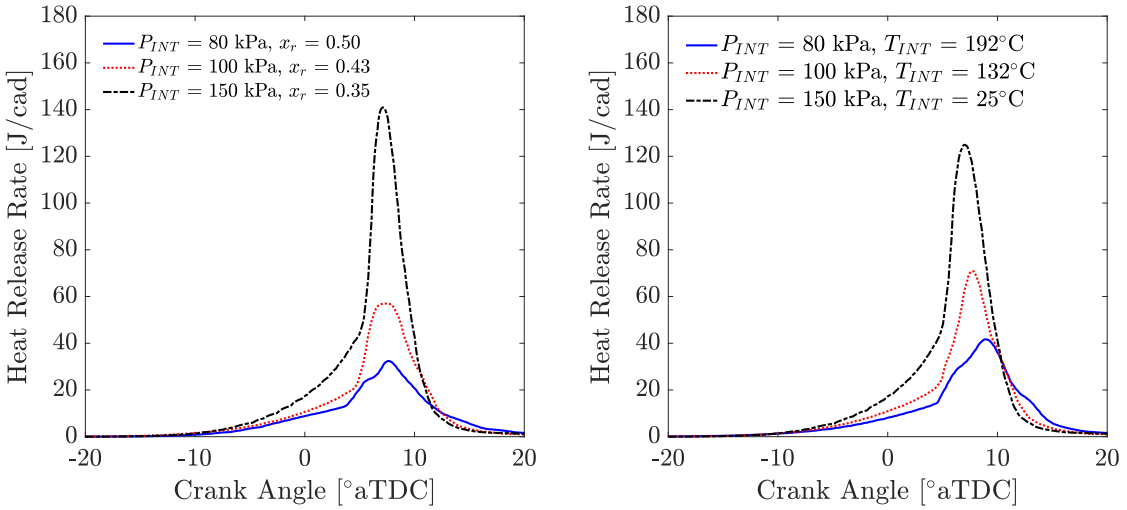

(a) Residual gas heating **(b)** Intake manifold heating

Figure 6.14: Comparison of KIVA-CFMZ heat release rate results for intake boost sweeps using (a) residual gas heating and (b) intake manifold heating at constant autoignition timing and mass fraction burned at the onset of autoignition.

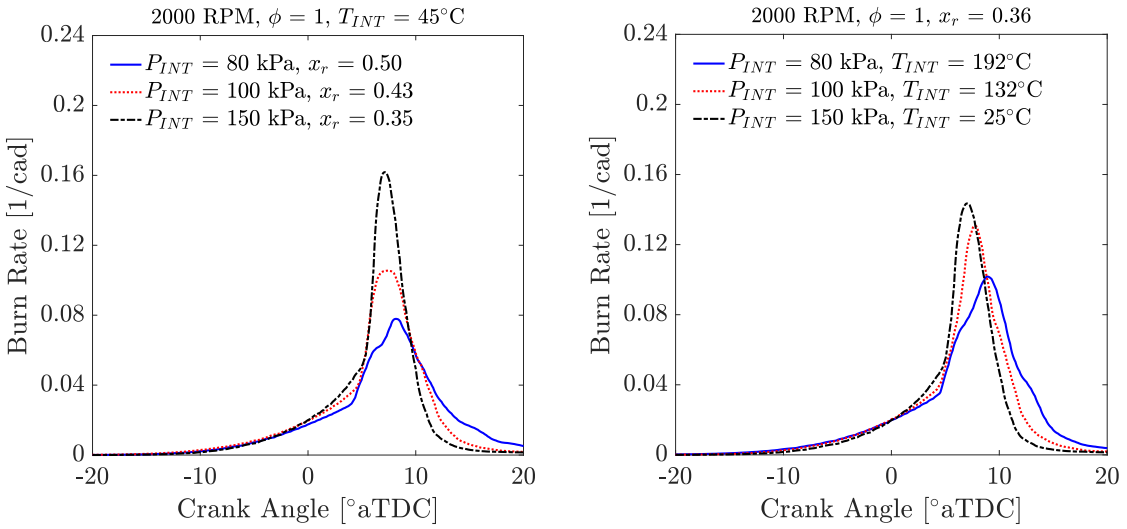

(a) Residual gas heating **(b)** Intake manifold heating

Figure 6.15: Comparison of KIVA-CFMZ burn rate results for intake boost sweeps using (a) residual gas heating and (b) intake manifold heating at constant autoignition timing and mass fraction burned at the onset of autoignition.

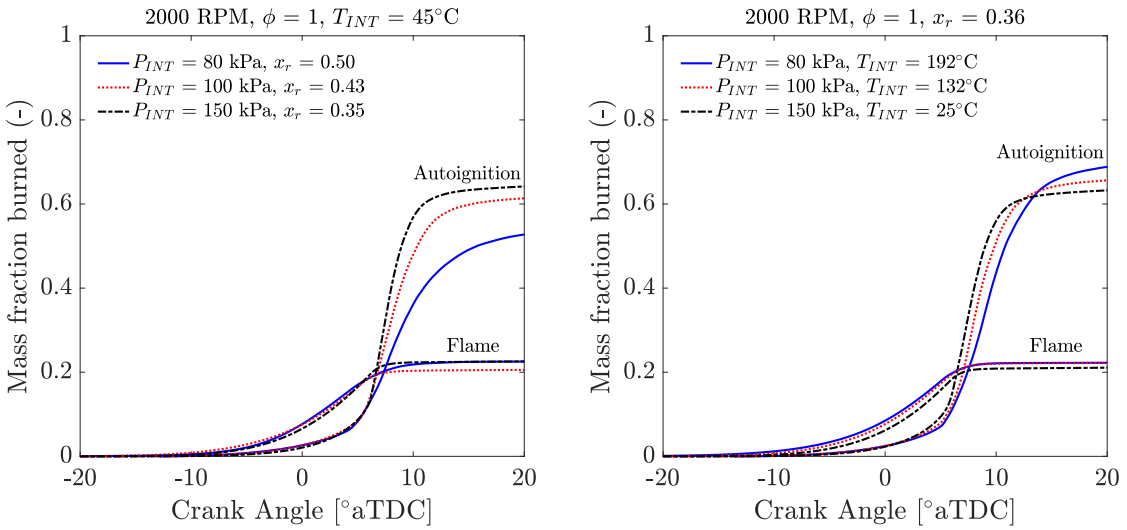

(a) Residual gas heating **(b)** Intake manifold heating

Figure 6.16: Comparison of KIVA-CFMZ flame and autoignition burned mass fraction results for intake boost sweeps using (a) residual gas heating and (b) intake manifold heating at constant autoignition timing and mass fraction burned at the onset of autoignition.

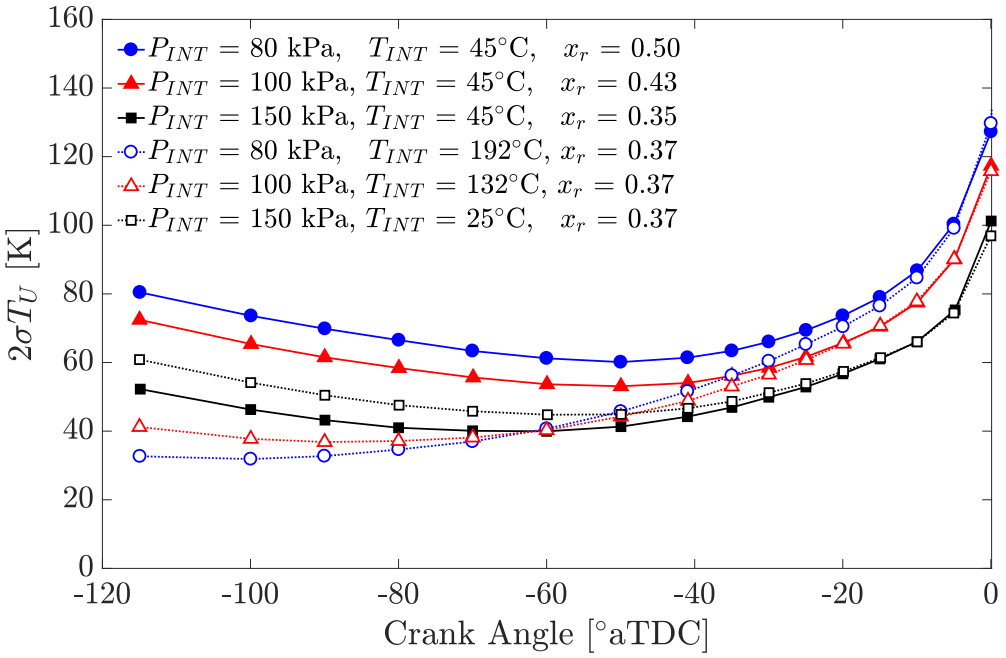

Figure 6.17: Comparison of charge preheating method on the evolution of thermal stratification ($2\sigma T_U$) for the intake pressure sweep at same composition, mass fraction burned at the onset of autoignition and end-gas autoignition timing.

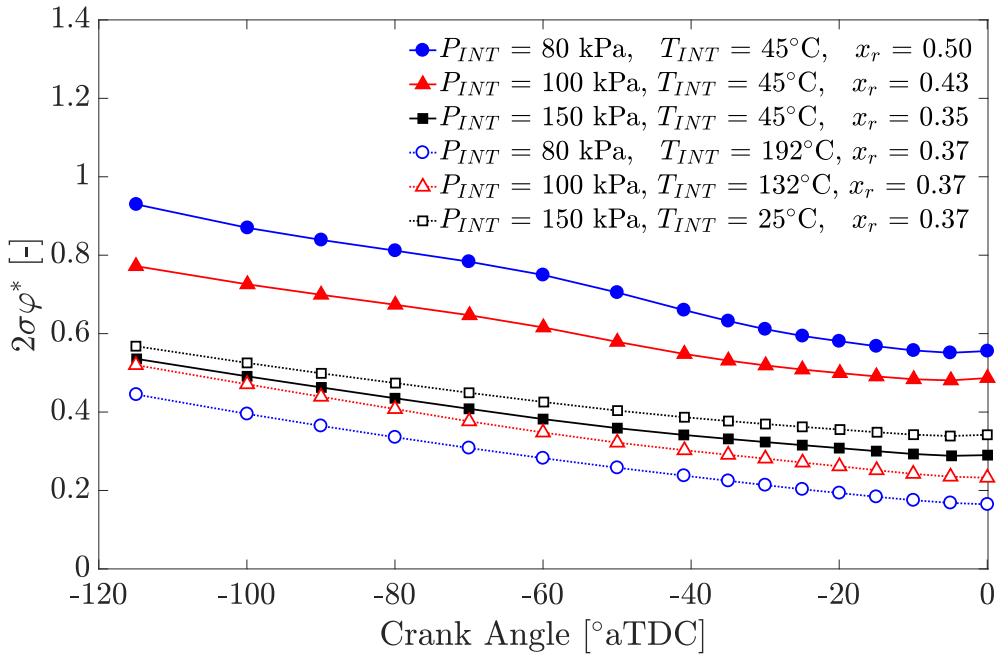

Figure 6.18: Comparison of charge preheating method on the evolution of compositional stratification ($2\sigma\varphi^*$) for the intake pressure sweep at same composition, mass fraction burned at the onset of autoignition and end-gas autoignition timing.

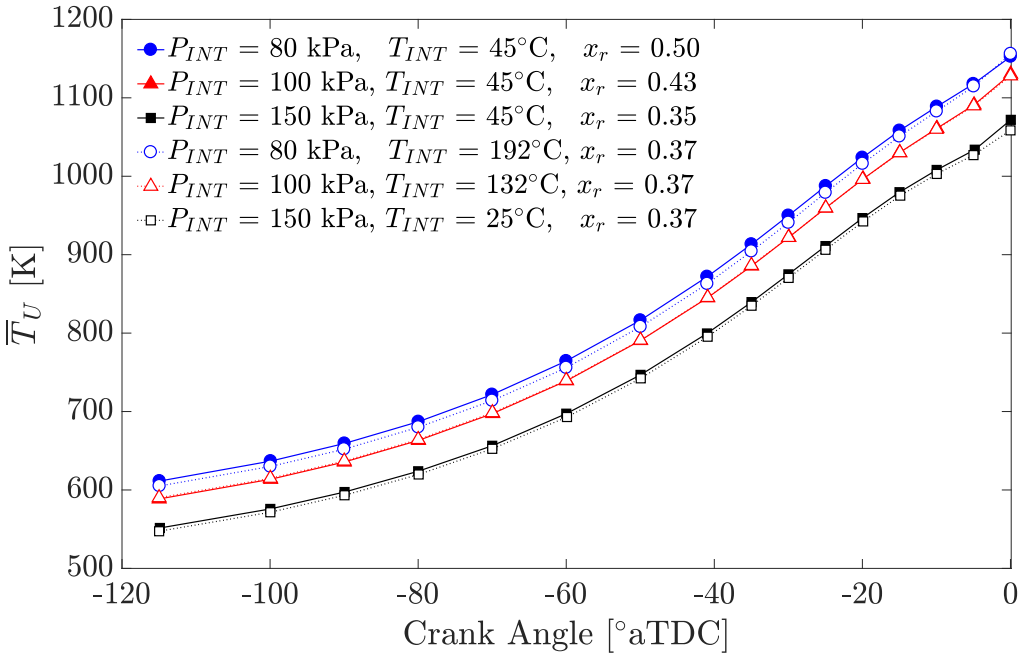

Figure 6.19: Comparison of charge preheating method on the evolution of mass averaged unburned gas temperature for the intake pressure sweep at same composition, mass fraction burned at the onset of autoignition and end-gas autoignition timing.

Table 6.4: Simulation input conditions for the boost sweep using residual gas heating at constant intake temperature, autoignition timing and composition.

Parameter	*Case1*	*Case 2*	*Case 3*
Engine Speed [RPM]		2000	
Intake Temperature [°C]		45	
Fuel Injection Pressure [bar]		100	
Intake Valve Opening/Closing Timing[1] [°aTDC]		-265/-161	
Start of Injection [°aTDC]		-330	
Autoignition timing [°aTDC]		5.5	
Fuel-to-air equivalence ratio, ϕ [-]	1.01	1.00	1.01
Fuel Mass Injected [mg/cycle/cyl]	9.4	12.3	19.9
Spark Timing [°bTDC]	48.5	32.5	28.5
Intake Pressure [kPa]	80	100	150
Fuel-to-charge equivalence ratio, ϕ' [-]	0.48	0.49	0.49
Exhaust Valve Opening Timing [°aTDC]	174	177	193
Exhaust Valve Closing Timing [°aTDC]	278	281	297
Internal EGR Mass fraction [-]	0.50	0.43	0.35
External EGR Mass fraction [-]	0.02	0.08	0.14

[1]All timings are referenced to combustion TDC. Valve timings are defined at 0.2 mm opening.

Table 6.5: Simulation inputs conditions for the boost sweep using intake manifold heating at similar residual gas fraction, autoignition timing and composition.

Parameter	*Case1*	*Case 2*	*Case 3*
Engine speed [RPM]		2000	
Fuel injection pressure [bar]		100	
Start of injection [°aTDC]		-330	
Intake valve opening/closing timing [°aTDC]		-265/-161	
Exhaust valve opening/closing timing [°aTDC]		193/297	
Fuel mass injected [mg/cycle/cyl]	9.4	12.3	19.9
Spark timing [°bTDC]	41	35	30
Intake pressure [kPa]	80	100	150
Intake temperature [°C]	192	132	25
Fuel-to-air equivalence ratio, ϕ [-]	0.99	1.01	1.01
Fuel-to-charge equivalence ratio, ϕ' [-]	0.48	0.48	0.48
Autoignition timing [°aTDC]	7.0	7.7	7.5
Combustion phasing, θ_{50} [°aTDC]	9.8	10.2	9.8
Internal EGR mass fraction [-]	0.36	0.37	0.36
External EGR mass fraction [-]	0.16	0.15	0.16

6.5 Comparison of Reactivity Stratification and End-Gas Autoignition Rates under Boosted Conditions for Diabatic and Adiabatic Conditions Late in the Compression Stroke

Additional KIVA simulations were performed to evaluate the importance of heat transfer induced thermal stratification late in the compression stroke on the changes in end-gas autoignition rates with boost pressure. Intake manifold pressures of 80 kPa and 150 kPa were investigated, while spark timing and IVC temperature were adjusted to match autoignition timing and mass fraction burned at the onset of autoigniton. The simulations were initialy run until 70° bTDC, where both high and low pressure mixtures displayed similar thermal stratification ($2\sigma T_U \approx 40$ K), as shown in Figure 6.20 (middle). At that timing, the simulations were run using both diabatic and adiabatic walls. The results from 70° bTDC until close to TDC are analyzed in this section. The details for the experimental inputs can be found in Table 6.6. The baseline simulation conditions were selected so that preignition compositional stratification at 5°bTDC is matched for both low and high pressure conditions. A decrease of 20 K in intake manifold temperature was used for the low pressure adiabatic case compared to the diabatic case, in order to match autoignition timing with the high pressure adiabatic case.

Figure 6.20 displays the evolution of mean unburned gas temperature, $2\sigma T_U$ and $2\sigma\varphi^*$ from 70°bTDC, where heat transfer to the walls was disabled for two cases, until 5°bTDC where the adiabatic cases started autoigniting. As expected, mean unburned gas temperature are lower for the higher pressure cases. Adiabatic cases increase linearly late in the compression stroke as opposed to the diabatic cases that show a decreasing temperature rise rate due to the effect of heat transfer loss. The $2\sigma T_U$ curves show an increase in thermal stratification for the diabatic cases, with the low pressure case having a larger $2\sigma T_U$ value near the end of compression, similarly to the results earlier in Section 6.4. On the other hand, $2\sigma T_U$ for the adiabatic cases decreases slightly after 70°bTDC until the onset of end-gas autoignition close to TDC, but are very similar between the low and high pressure cases suggesting that

the thermal stratification observed is primarily due to the heat transfer loss to the walls. The $2\sigma\varphi^*$ curves decrease for all cases after 70° bTDC and are very similar at the onset of autoignition for the diabatic cases.

Figure 6.21 compares the KIVA-CFMZ heat release rate curves, burn rates rates and mass fraction burned curves between diabatic and adiabatic cases under the same boost sweep. The peak heat release rates and peak burn rates for the adiabatic cases are much higher due to the advanced phasing and lower thermal stratification, effected by the absence of heat loss to the walls. Flame burn fractions at the onset of autoignition are matched for each set of cases (i.e. diabatic and adiabatic). However, the peak burn rates between the low and high pressure adiabatic cases are very similar, unlike the diabatic cases where the high pressure case depicts an increase of approximately 75%, from 0.09 1/cad to 0.16 1/cad. This finding supports the argument that the effect of higher pressure on the mean mixture reactivity is offset by the decrease in temperature, which is needed to match autoignition timing. Additionally, the higher pressure mixture leads to a greater pressure rise rate during combustion due to the higher energy content of the compared to the lower pressure mixture, however, the change in the post-autoignition pressure evolution has a minimal effect on the end-gas burn rate. The lower heat transfer induced thermal stratification is the primary reason for the large increase observed in the end-gas autoignition rates under the conditions investigated. The reduction in the pre-ignition thermal stratification at higher intake pressures is primarily due to the lower mass normalized heat transfer loss to the walls. This finding agrees with the modeling study by Shingne et al. [159], who concluded that under lean, highly EGR dilute HCCI conditions, the shorter burn durations at higher boost were primarily due to the lower thermal stratification.

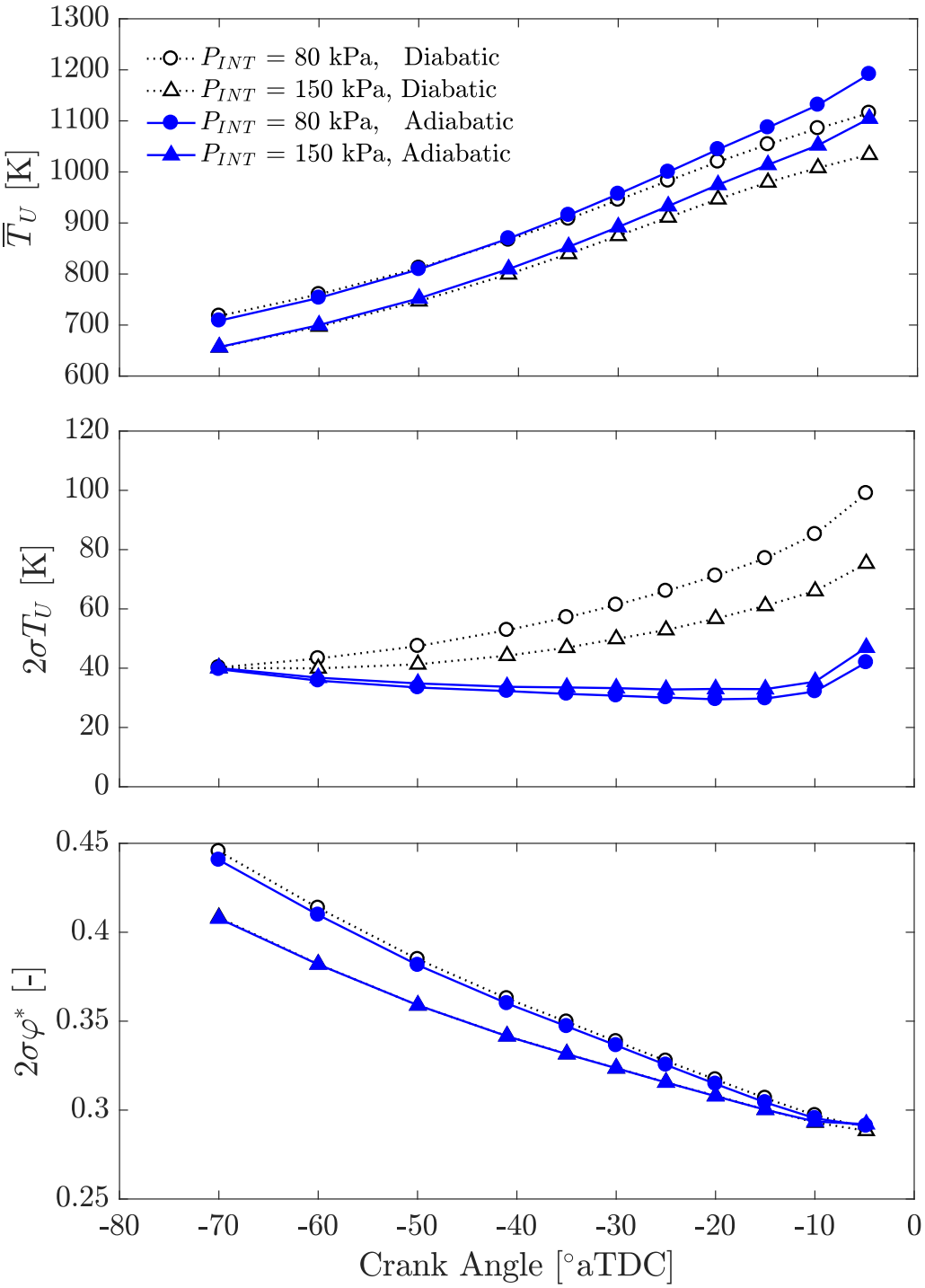

Figure 6.20: Boost pressure effect on mean unburned gas temperature (top), $2\sigma T_U$ (middle) and $2\sigma\varphi^*$ (bottom) for diabatic and adiabatic cases during the same intake boost sweep using intake manifold heating.

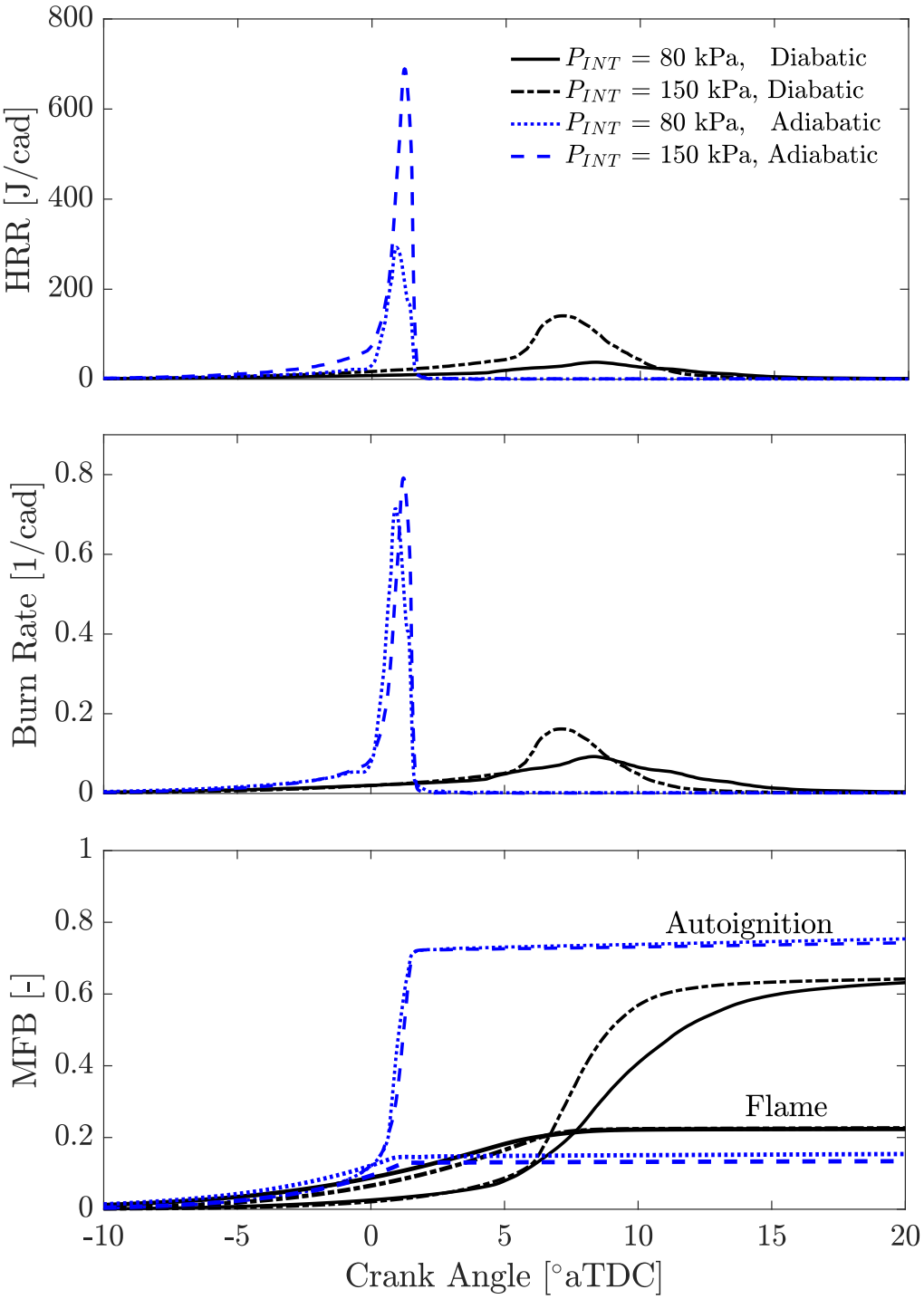

Figure 6.21: Boost pressure effect on heat release rates (top), burn rates (middle) and mass fractions burned (bottom) for diabatic and adiabatic cases using intake manifold heating.

Table 6.6: Simulation input conditions for the boost sweep with diabatic and adiabatic walls late in the compression stroke.

Parameter	*Case1*	*Case 2*	*Case 3*	*Case 4*
	Diabatic		Adiabatic	
Engine speed [RPM]	2000			
Fuel injection pressure [bar]	100			
Start of injection [°aTDC]	-330			
Intake valve opening/closing timing [°aTDC]	-265 / -161			
Exhaust valve opening/closing timing [°aTDC]	193 / 297			
Fuel mass injected [mg/cycle/cyl]	9.4	19.9	9.4	19.9
Spark timing [°bTDC]	38	28.5	38.5	28.5
Intake pressure [kPa]	80	150	80	150
Intake temperature [°C]	152	45	132	45
Fuel-to-air equivalence ratio, ϕ [-]	1.00	1.01	1.01	1.01
Fuel-to-charge equivalence ratio, ϕ' [-]	0.47	0.49	0.47	0.49
Internal EGR mass fraction [-]	0.39	0.35	0.39	0.35
External EGR mass fraction [-]	0.14	0.16	0.14	0.16

6.6 Summary

This chapter used the Coherent Flamelet Multi-Zone model (KIVA-CFMZ) to investigate the underlying mechanisms leading to changes in end-gas autoignition rate under boosted, highly EGR-dilute conditions. The analysis focused on the effect of intake pressure on the pre-ignition reactivity stratification as well as the evolution of thermal and compositional stratification from early in the compression stroke until TDC. The thermal and compositional stratification was evaluated using two standard deviations of the normalized mass distribution for unburned gas temperature ($2\sigma T_U$) and non-product equivalence ratio ($2\sigma\varphi^*$) of the unburned zone, respectively. Simulations were also used to understand the effect of charge preheating method (residual gas heating vs. intake manifold heating) in reactivity stratification and end-gas burn rates under boosted SACI conditions. Mixture composition, autoignition timing and mass fraction burned at the onset of autoignition were held constant for all comparisons between low and high pressure mixtures.

The detailed SACI model was initially configured based on experimental inputs presented in Chapter IV for intake pressures increasing from 80 kPa to 150 kPa using residual gas heating and constant intake temperature. Good trendwise agreement in global heat release rate, end-gas burn rate and unburned gas temperature was observed between experimental and simulation results, once autoignition timing as well as mass fraction burned at the onset of autoignition were matched. As intake pressure increased, mean charge temperature decreased by a similar amount irrespective of charge preheating method, in order to initiate autoignition at the same timing. For the residual gas heating cases, the decrease in IVC temperature was achieved by a reduction in residual gas fraction from 50% to 35%, while for the intake manifold heating cases intake manifold temperature had to be reduced from 192°C to 25°C.

For the intake pressure sweep using residual gas heating, a reduction in both thermal and compositional stratification was observed early in the compression stroke which carried on until the onset of autoignition close to TDC. The resulting decrease in pre-ignition reactivity stratification explained the increase in end-gas autoignition rate

at higher intake pressures. The decrease in thermal and compositional stratification early in the compression stroke was attributed to the reduction in residual gas fraction that was required as intake pressure was increased.

An opposite trend in thermal and compositional stratification was observed early in the compression stroke for the same intake pressure sweep using intake manifold heating. Early in the compression stroke, higher pressure mixtures exhibited an increase in both thermal and composition stratification, which was attributed to the reduction in intake manifold temperature. While compositional stratification levels reduced for mixtures as piston moved towards TDC, the trend in thermal stratification reversed late in the compression stroke, with higher pressures mixtures exhibit lower thermal stratification. Interestingly, the thermal stratification levels for both charge preheating methods were almost identical close to TDC, even though the $2\sigma T$ values were very different early in the compression stroke. The increase in end-gas burn rate with pressure was less pronounced using intake manifold heating at constant residual gas fraction, likely due to the increase in compositional stratification. Regardless of charge preheating method and stratification levels early in the compression stroke, higher pressure mixtures exhibited faster end-gas autoignition rates, which were primarily attributed to lower thermal stratification levels due to lower normalized heat transfer losses to the walls.

CHAPTER VII

Summary, Conclusions and Recommendations for Future Work

7.1 Summary and Conclusions

The work presented in this document used experimental and computational methods to investigate SACI combustion behavior under boosted, ultra-EGR dilute stoichiometric SACI conditions in an internal combustion engine employing negative valve overlap. The research work was motivated by the findings of previously published thermodynamic simulations [39], which suggested that the thermodynamic sweetspot for high efficiency, dilute, boosted engines lies at conditions potentially attainable using boosted SACI combustion. The studies presented in this document are the first attempt to experimentally investigate the boosted SACI combustion regime in an internal combustion engine at EGR dilution levels between 25% and 55%. The range of intake pressure and fuel-to-charge equivalence ratio studied, varied from 80 kPa to 150 kPa and approximately 0.45 to 0.75, respectively.

- In Chapter 3, the maximum pressure rise conditions in SACI were initially analyzed using energy balance equations for a closed thermodynamic system. Assuming that the maximum pressure rise rate timing is constant and that there is an orderly transition from flame propagation to autoignition, it was shown that the maximum pressure rise rate should be approximately proportional to the end-gas energy at the onset of autoignition ($Q_{EG,\,\theta_{AI}}$) and inversely propor-

tional to the end-gas autoignition characteristic duration ($\delta\theta_{AI}$). The limits in efficiency, load, stability and combustion phasing were then investigated experimentally under the boosted stoichiometric SACI combustion regime with high levels of EGR dilution ($0.45 < \phi' < 0.7$). The high load limit at 2000 RPM and 150 kPa intake pressure was reached at a GMEP $\approx$ 7.3 bar and a $\phi' = 0.57$ due to a convergence of the ringing and stability limits, typical of LTC engines. As intake pressure was increased, the ringing/stability limit shifted towards lower ϕ' mixtures (i.e. higher EGR dilution), creating a gap between the conventional spark-ignition dilution limit ($\approx$ 25 - 30% EGR) and the boosted SACI operating limits. Combustion phasing retard was demonstrated to be very effective at reducing maximum pressure rise rate levels primarily due to slower end-gas autoignition rates but also due to higher volume expansion rates. However, the late combustion phasing limit was constrained to approximately 14° aTDC, where the likelihood of partial burning cycles caused by the absence of end-gas autognition increased. This behavior was attributed to the lower charge temperature and the greater expansion cooling rates at retarded combustion phasings.

Gross fuel conversion efficiency improvements of approximately 3% absolute (8% relative) were demonstrated experimentally by using boosting to dilute the mixture from $\phi' = 0.75$ to $\phi' = 0.45$ at constant load. The increase in gross thermal efficiency was primarily attributed to the favorable thermodynamic properties of diluted mixtures during the expansion stroke. Estimated heat transfer losses were found to be approximately constant as EGR dilution was increased at constant load, due to the competing effects of lower expansion temperatures and higher pressure on heat transfer loss. An increase in load from 300 kPa to 700 kPa GMEP at constant composition ($\phi' = 0.55$) led to an efficiency improvement of approximately 4% absolute (10% relative), which was explained by an equivalent drop in the estimated heat transfer losses. While the operation and design of the valvetrain was not optimized in this work, a large variation in pumping work was observed due to the use of the exhaust cam tim-

ing for residual gas fraction control. Operating conditions that required lower residual gas fraction were achieved using late EVC/EVO timing, which led to recompression of the exhaust gases early in the exhaust stroke, thereby resulting in elevated pumping work. Asymmetric NVO operation also contributed to the higher pumping penalty observed.

An increase in engine speed at constant composition, intake pressure and spark advance necessitated higher unburned gas temperatures to match end-gas autoignition timing. Under the conditions investigated, the overall effect of engine speed on the SACI burn profile was negligible on a crank angle basis. On a time basis, maximum pressure rise rates scaled with engine speed, so lower engine speeds were found to be favorable for high load expansion in order to satisfy the ringing limit. Higher cyclic variability, defined by the standard deviation in θ_{50}, was observed at optimal combustion phasing when spark timing was advanced and unburned gas temperatures were lowered. Cyclic heat release analysis results revealed that the variability in θ_{50} was driven by a variability in autoignition timing (θ_{AI}), which in turn correlated extremely well with θ_{02}. These findings strongly suggested that the cyclic variability in combustion phasing is determined early in the early flame development rather than later due to variation in the end-gas state near autoignition timing.

- In Chapter 4, the effect of boost pressure on the SACI combustion process was investigated experimentally at constant engine speed, composition, spark advance and combustion phasing. An increase in intake pressure required a decrease in bulk gas temperature to match combustion phasing due to the effect of pressure on the mixture reactivity. Absolute heat release rates increased at higher intake pressures during both flame propagation and end-gas autoignition. As intake pressure was increased, initial flame burn rates were similar, leading to a similar mass fraction burned at the onset of end-gas autoignition. However, end-gas autoignition rates increased approximately proportionally with pressure. An increase in intake pressure by approximately a factor of 2 led to

an increase in peak heat release rate, maximum pressure rise rate and ringing intensity by approximately a factor of 4. Approximately half of this increase was attributed to the higher end-gas energy content and the other half was attributed to the increase in end-gas burn rate. The aforementioned relationship between intake pressure and end-gas autoignition rate was demonstrated experimentally for a range of mixture compositions ($0.45 < \phi' < 0.63$) and spark timings (30 - 40° bTDC), as long as those were kept constant during the intake pressure sweep. The intake pressure sweep comparison between residual gas heating and intake charge heating showed a similar increase in end-gas burn rate with pressure, suggesting that the changes in residual gas fraction and the associated effects in temperature and/or compositional stratification were not responsible for the changes in end-gas autoignition rates observed. Constant volume ignition delay predictions using a detailed 312 species chemical mechanism representing a surrogate for RD-387 gasoline showed that the average ignition delay at the onset of the estimated end-gas autoignition timing is similar (≈ 0.8 ms) for all experimental cases during the intake pressure sweep, due to the competing effects of higher pressure and lower temperature on ignition delay. Under the conditions investigated, no visible low temperature heat release was observed and the experimental P - T_U trajectories did not cross the NTC region on constant volume ignition delay prediction.

- In Chapter 5, the impact of fuel-to-charge equivalence ratio on the tradeoff between flame and end-gas autoignition heat release rate was studied experimentally at both constant intake pressures and constant load. Under all conditions investigated, end-gas autoignition timing was targeted at approximately 7°aTDC. Experiments at constant intake pressure and spark advance showed that as ϕ' is increased, lower unburned gas temperatures are needed to match autoignition timing. Higher ϕ' cases exhibited faster initial flame burn rates, which was attributed to the increasing trend in estimated laminar flame speed due to a larger temperature difference between burned and unburned gas tem-

perature estimates. At constant intake pressure and constant mass fraction burned at the onset of autoignition, end-gas autoignition rates increased significantly at higher ϕ' conditions. Increasing the mass fraction burned at the onset of autoignition by advancing the spark timing and lowering T_U was shown to be effective, to some extent, at reducing the peak heat release rates. The ϕ' investigation was extended at intake pressures between 0.8 and 1.5 bar and the increasing trends in peak autoignition rate rates, end-gas energy at autoignition and peak heat release rate with ϕ' were found to be consistent for all intake pressures. For a constant spark timing and end-gas autoignition timing, the mass fraction burned at the onset of autoignition correlated linearly with ϕ', regardless of intake pressure. Changes in SACI burn rates at constant load were trendwise similar to the results at constant pressure, albeit less pronounced. This was thought to be caused by the effect of pressure on the end-gas reactivity stratification at the onset of autoignition, which was further investigated in Chapter 6.

- In Chapter 6, a previously developed CFD model capable of capturing HCCI, SI, and SACI combustion modes, KIVA-CFMZ (KIVA Coherent Flamelet Multi-Zone), was exercised to understand the effect of intake pressure on the end-gas autoignition rate using a mesh that closely matched the experimental hardware. The analysis focused on the effect of intake pressure on the pre-ignition reactivity stratification as well as the evolution of thermal and compositional stratification from early in the compression stroke until TDC. Mixture composition, end-gas autoignition timing and mass fraction burned at the onset of autoignition were held constant for all simulations. Good trendwise agreement in cylinder pressure, unburned gas temperature, global heat release rate and end-gas autoignition rate was observed between experimental and simulation results for an intake pressure sweep from 80 kPa to 150 kPa.

  Opposite trends in compositional/thermal stratification were observed between charge preheating methods early in the compression stroke. Under the con-

ditions investigated, increasing the residual gas fraction or lowering the intake temperature led to higher thermal/compositional stratification early in the compression stroke. While compositional stratification trends early in the compression stroke continued towards TDC of combustion, TDC thermal stratification levels were not affected by the states early in the compression stroke. It was shown that the reduced specific heat transfer losses at higher intake pressure were mostly responsible for the lower pre-ignition thermal stratification, which in turn was the primary reason for the increase in end-gas burn rate observed.

7.2 Recommendations for Future Work

The work presented in this thesis used metal engine experiments and computational tools to investigate SACI combustion under boosted, ultra-EGR dilute conditions in an negative valve overlap engine. Valuable findings were presented under previously unexplored P - T_U - ϕ' conditions, however, several questions and directions for future work arise from this thesis.

Future efforts to alleviate the high pressure rise rates observed at high loads in SACI should focus on ways to reduce the end-gas energy at the onset of autoignition, limit the end-gas autoignition rate and extend the late combustion phasing limit. With that in mind, stratified mixtures, ignition at multiple sites, advanced ignition systems and reformed fuels would be areas worth investigating under boosted SACI conditions as a way to enhance the ignition and initial flame development processes. Additionally, the introduction of a high reactivity gradient in the end-gas through fuel stratification or water injection is another area worth exploring. Future studies should focus on understanding the impact of NTC behavior on SACI burn rates under highly EGR dilute conditions and its potential use as a high load enabler. Previously published experimental work [97] under boosted HCCI conditions has shown that intermediate temperature heat release due to NTC behavior of gasoline can extend the late combustion phasing limit of HCCI combustion, by increasing the bulk gas temperature despite the higher expansion cooling rates at late combustion phasings. Appropriate selection of compression ratio and intake boost level can be used to target gasoline NTC behavior at the ringing limits presented in this work. Additionally, changes in compression ratio would vary the residence time at TDC as well as the volume expansion rates and thus cooling rates, which could be also used as a way to manipulate end-gas autoignition rates.

The high load limit investigation in this work was partly constrained by the maximum intake pressure achievable (i.e. 150 kPa) with the hardware configuration. Extrapolating from the ringing limits presented in this work, it is expected that higher loads could be achieved with higher boost levels albeit at lower ϕ' mixtures. Lower

burned gas temperatures associated with lower ϕ' mixtures are expected to lead to poor flame initiation/propagation but these limits are currently unknown. Future work should try to extend the high load limits using higher levels of boost as well as investigate the flammability limits under those pressure, temperature and dilution conditions for representative fuels.

From a practical engine system standpoint, the use of boosting for dilution can offer brake thermal efficiency improvements as long as pumping and/or frictional losses associated with the generation of boost do not overcome the efficiency gains from dilution. Additionally, the use of exhaust cam phasing for residual gas fraction control over a range of load conditions can lead to significant efficiency penalties, as shown in this work. Given the above, future work should investigate optimal boosting and valvetrain strategies based on the requirements in unburned gas temperature and residual gas fraction under boosted SACI conditions presented in this work.

In this work autoignition timing variability for relatively high ϕ' mixtures was shown to be determined early during the initial flame based heat release and strongly correlated with the mean mass fraction burned at the onset of autoignition. High variability in autoignition timing was frequently responsible for partial burning cycles due to the narrow combustion phasing range at high loads. It is thus important that future work focuses on fundamentally understanding the dominant causes of variability in the initial flame development under similar P - T_U - ϕ' conditions.

Lastly, it is unclear whether the application of the low pass ringing intensity metric is sufficient at preventing damage to the engine structure at high load, high ϕ' conditions. Future work should focus on understanding the differences, if any, in the end-gas autoignition mechanism between low dilution SI mixtures and high dilution SACI mixtures and the respective impact on engine durability.

BIBLIOGRAPHY

BIBLIOGRAPHY

[1] J. B. Heywood, *Internal Combustion Engine Fundamentals*. New York:: McGraw-Hill, 1988.

[2] T. Lake, J. Stokes, R. Murphy, R. Osborne, and A. Schamel, "Turbocharging Concepts for Downsized DI Gasoline Engines," *SAE Technical Paper 2004-01-0036*, 2004.

[3] B. Lecointe and G. Monnier, "Downsizing a Gasoline Engine Using Turbocharging with Direct Injection," *SAE Technical Paper 2003-01-0542*, 2003.

[4] D. Petitjean, L. Bernardini, C. Middlemass, and S. M. Shahed, "Advanced Gasoline Engine Turbocharging Technology for Fuel Economy Improvements," *SAE Technical Paper 2004-01-0988*, 2004.

[5] L. Koopmans, R. Ogink, and I. Denbratt, "Direct Gasoline Injection in the Negative Valve Overlap of a Homogeneous Charge Compression Ignition Engine," *SAE Technical Paper 2003-01-0542*, 2003.

[6] J. Szybist, E. Nafziger, and A. Weall, "Load Expansion of Stoichiometric HCCI Using Spark Assist and Hydraulic Valve Actuation," *SAE International Journal of Engines*, vol. 3, pp. 244–258, 2010.

[7] S. Curran, R. Hanson, R. Wagner, and R. D. Reitz, "Efficiency and Emissions Mapping of RCCI in a Light-Duty Diesel Engine," *SAE Technical Paper 2013-01-0289*, 2013.

[8] J. Heywood, D. MacKenzie, I. Akerlind, P. Bastani, I. Berry, K. Bhatt, A. Chao, E. Chow, V. Karplus, D. Keith, M. Khusid, E. Nishimura, and S. Zoepf, "On the Road toward 2050: Potential for Substantial Reductions in Light-Duty Vehicle Energy Use and Greenhouse Gas Emissions". Cambridge, Massachusetts: MIT Sloan Automotive Laboratory, 2015.

[9] Estimated U.S. Energy Consumption in 2017 [Online]. Available: https://flowcharts.llnl.gov/commodities/energy. [Accessed: 10-Oct-2018].

[10] M. Noguchi, Y. Tanaka, T. Tanaka, and Y. Takeuchi, "A Study on Gasoline Engine Combustion by Observation of Intermediate Reactive Products during Combustion," *SAE Technical Paper 790840*, 1979.

[11] S. Onishi, S. H. Jo, K. Shoda, P. D. Jo, and S. Kato, "Active Thermo-Atmosphere Combustion (ATAC) - A New Combustion Process for Internal Combustion Engines," *SAE Technical Paper 790501*, 1979.

[12] P. M. Najt and D. E. Foster, "Compression-Ignited Homogeneous Charge Combustion," *SAE Technical Paper 830264*, 1983.

[13] H. Zhao, J. Li, T. Ma, and N. Ladommatos, "Performance and analysis of a 4-stroke multi-cylinder gasoline engine with CAI combustion," *SAE Technical Paper 2002-01-0420*, 2002.

[14] L. M. Olesky, J. Vavra, D. Assanis, and A. Babajimopoulos, "Effects of Charge Preheating Methods on the Combustion Phasing Limitations of an HCCI Engine With Negative Valve Overlap," *Journal of Engineering for Gas Turbines and Power*, vol. 134, no. 11, p. 112801, 2012.

[15] A. Hultqvist, M. Christensen, B. Johansson, M. Richter, J. Nygren, J. Hult, and M. Aldjn, "The HCCI Combustion Process in a Single Cycle - Speed Fuel Tracer LIF and Chemiluminescence Imaging," *SAE Technical Paper 2002-01-0424*, 2002.

[16] N. Iida, "Combustion Analysis of Methanol-Fueled Active Thermo-Atmosphere Combustion (ATAC) Engine Using a Spectroscopic Observation," *SAE Technical Paper 940684*, 1994.

[17] C. K. Westbrook, "Chemical kinetics of hydrocarbon ignition in practical combustion systems," *Proceedings of the Combustion Institute*, vol. 28, no. 2, pp. 1563–1577, 2000.

[18] J. E. Dec, W. Hwang, and M. Sjöberg, "An Investigation of Thermal Stratification in HCCI Engines Using Chemiluminescence Imaging," *SAE Technical Paper 2006-01-1518*, 2006.

[19] M. Yao, Z. Zheng, and H. Liu, "Progress and recent trends in homogeneous charge compression ignition (HCCI) engines," *Progress in Energy and Combustion Science*, vol. 35, no. 5, pp. 398–437, 2009.

[20] J.-O. Olsson, P. Tunestål, B. Johansson, S. Fiveland, R. Agama, M. Willi, and D. Assanis, "Compression Ratio Influence on Maximum Load of a Natural Gas Fueled HCCI Engine," *SAE Technical Paper 2002-01-0111*, 2002.

[21] J. E. Dec and M. Sjöberg, "A Parametric Study of HCCI Combustion the Sources of Emissions at Low Loads and the Effects of GDI Fuel Injection," *SAE Technical Paper 2003-01-0752*, 2003.

[22] M. Sjöberg and J. E. Dec, "An investigation into lowest acceptable combustion temperatures for hydrocarbon fuels in HCCI engines," *Proceedings of the Combustion Institute*, vol. 30, pp. 2719–2726, 2005.

[23] A. Babajimopoulos, G. A. Lavoie, and D. N. Assanis, "On the Role of Top Dead Center Conditions in the Combustion Phasing of Homogeneous Charge Compression Ignition Engines," *Combustion Science and Technology*, vol. 179, pp. 2039–2063, 2007.

[24] J. Hyvönen, G. Haraldsson, and B. Johansson, "Operating Conditions Using Spark Assisted HCCI Combustion During Combustion Mode Transfer to SI in a Multi-Cylinder VCR-HCCI Engine," *SAE Technical Paper 2005-01-0109*, 2005.

[25] J. E. Dec, Y. Yang, and N. Dronniou, "Boosted HCCI - Controlling Pressure-Rise Rates for Performance Improvements using Partial Fuel Stratification with Conventional Gasoline," *SAE Int. J. Engines*, vol. 4, no. 1, pp. 1169–1189, 2011.

[26] J. E. Dec and Y. Yang, "Boosted HCCI for High Power without Engine Knock and with Ultra-Low NO_x Emissions - using Conventional Gasoline," *SAE Int. J. Engines*, 3(1):750–767, 2010.

[27] D. Assanis, P. M. Najt, J. E. Dec, J. A. Eng, T. N. Asmus, and F. Zhao, *Homogeneous charge compression ignition (HCCI) engines key research and development issues*. 2003.

[28] B. T. Zigler, P. E. Keros, K. B. Helleberg, M. Fatouraie, D. Assanis, and M. S. Wooldridge, "An experimental investigation of the sensitivity of the ignition and combustion properties of a single-cylinder research engine to spark-assisted HCCI," *International Journal of Engine Research*, vol. 12, pp. 353–375, 2011.

[29] H. Persson, B. Johansson, and A. Remón, "The Effect of Swirl on Spark Assisted Compression Ignition (SACI)," *SAE Technical Paper 2007-01-1856*, 2007.

[30] D. Assanis, S. W. Wagnon, and M. S. Wooldridge, "An experimental study of flame and autoignition interactions of iso-octane and air mixtures," *Combustion and Flame*, vol. 162, pp. 1214–1224, 2015.

[31] M. Fatouraie and M. Wooldridge, "Optical Investigation of the Effects of Ethanol/Gasoline Blends on Spark-Assisted HCCI," *Journal of Engineering for Gas Turbines and Power*, vol. 136, 2014.

[32] D. L. Reuss, T.-W. Kuo, G. Silvas, V. Natarajan, and V. Sick, "Experimental metrics for identifying origins of combustion variability during spark-assisted compression ignition," *International Journal of Engine Research*, vol. 9: 409-434, 2008.

[33] Z. Wang, X. He, J. X. Wang, S. Shuai, F. Xu, and D. Yang, "Combustion visualization and experimental study on spark induced compression ignition (SICI) in gasoline HCCI engines," *Energy Conversion and Management*, 51(5):908–917, 2010.

[34] G. A. Lavoie, J. Martz, M. Wooldridge, and D. Assanis, "A multi-mode combustion diagram for spark assisted compression ignition," *Combustion and Flame*, vol. 157, pp. 1106-1110, 2010.

[35] J. Dernotte, J. Dec, and C. Ji, "Investigation of the Sources of Combustion Noise in HCCI Engines," *SAE Int. J. Engines*, 7(2):730-761, 2014.

[36] Y. Yang, J. E. Dec, N. Dronniou, M. Sjöberg, and W. Cannella, "Partial Fuel Stratification to Control HCCI Heat Release Rates: Fuel Composition and Other Factors Affecting Pre-Ignition Reactions of Two-Stage Ignition Fuels," *SAE Int. J. Engines*, 4(1):1903–1920, 2011.

[37] J. E. Dec, Y. Yang, and N. Dronniou, "Improving Efficiency and Using E10 for Higher Loads in Boosted HCCI Engines," *SAE Int. J. Engines*, 5(3):1009-1032, 2012.

[38] G. Gentz, J. Dernotte, C. Ji, and J. Dec, "Spark Assist for CA50 Control and Improved Robustness in a Premixed LTGC Engine - Effects of Equivalence Ratio and Intake Boost," *SAE Technical Paper 2018-01-1252*, 2018.

[39] G. A. Lavoie, E. Ortiz-Soto, A. Babajimopoulos, J. B. Martz, and D. N. Assanis, "Thermodynamic sweet spot for high-efficiency, dilute, boosted gasoline engines," *International Journal of Engine Research*, vol. 14, pp. 260-278, 2012.

[40] J. A. Caton, "The thermodynamic characteristics of high efficiency, internal-combustion engines," *Energy Conversion and Management*, vol. 58, pp. 8493, 2012.

[41] M. L. Wissink, D. A. Splitter, A. B. Dempsey, S. J. Curran, B. C. Kaul, and J. P. Szybist, "An assessment of thermodynamic merits for current and potential future engine operating strategies," *International Journal of Engine Research*, 18. 155–169, 2017.

[42] L. M. Olesky, J. B. Martz, G. A. Lavoie, J. Vavra, D. N. Assanis, and A. Babajimopoulos, "The effects of spark timing, unburned gas temperature, and negative valve overlap on the rates of stoichiometric spark assisted compression ignition combustion," *Applied Energy*, vol. 105, pp. 407417, 2013.

[43] R. L. Evans, "Chapter 4 - Lean-Burn Spark-Ignited Internal Combustion Engines," Academic Press, 2008.

[44] A. J. Weall and J. P. Szybist, "The Effects of Fuel Characteristics on Stoichiometric Spark-Assisted HCCI," *Journal of Engineering for Gas Turbines and Power*, 134(7):072805-072805-9, 2012.

[45] L. Li, H. Xie, T. Chen, W. Yu, and H. Zhao, "Experimental Study on Spark Assisted Compression Ignition (SACI) Combustion with Positive Valve Overlap in a HCCI Gasoline Engine," *SAE Technical Paper 2012-01-1126*, 2012.

[46] H. Yun, N. Wermuth, and P. Najt, "Extending the High Load Operating Limit of a Naturally-Aspirated Gasoline HCCI Combustion Engine," *SAE Int. J. Engines*, 3(1):681-699, 2010.

[47] P. Shingne, M. Gerow, V. Triantopoulos, S. Bohac, and J. Martz, "A comparison of valving strategies appropriate for multimode combustion within a downsized boosted automotive engine-part I: High load operation within the spark ignition combustion regime," *Journal of Engineering for Gas Turbines and Power*, vol. 136. 2014.

[48] M. Gerow, P. Shingne, V. Triantopoulos, S. Bohac, and J. Martz, "A comparison of valving strategies appropriate for multimode combustion within a downsized boosted automotive engine-part II: Mid load operation within the SACI combustion regime," *Journal of Engineering for Gas Turbines and Power*, vol. 136. 2014.

[49] X. He, B. T. Zigler, S. M. Walton, M. S. Wooldridge, and A. Atreya, "A rapid compression facility study of OH time histories during iso-octane ignition," *Combustion and Flame*, vol. 145, pp. 552–570, 2006.

[50] G. Woschni, "A Universally Applicable Equation for the Instantaneous Heat Transfer Coefficient in the Internal Combustion Engine," *SAE Technical Paper 670931*, 1967.

[51] S. Chen and P. Flynn, "Development of a Single Cylinder Compression Ignition Research Engine," *SAE Technical Paper 650733*, 1965.

[52] Gamma Technologies - Engine and Vehicle simulation, gtisoft.com. [Online]. Available: http://gtisoft.com/. [Accessed: 10-Mar-2016].

[53] M. Weinrotter, E. Wintner, K. Iskra, T. Neger, J. Olofsson, H. Seyfried, M. Aldén, M. Lackner, F. Winter, A. Vressner, A. Hultqvist, and B. Johansson, "Optical Diagnostics of Laser-Induced and Spark Plug-Assisted HCCI Combustion," *SAE Technical Paper 2005-01-0129*, 2005.

[54] T. Urushihara, K. Yamaguchi, K. Yoshizawa, and T. Itoh, "A Study of a Gasoline-fueled Compression Ignition Engine - Expansion of HCCI Operation Range Using SI Combustion as a Trigger of Compression Ignition ," *SAE Technical Paper 2005-01-0180*, 2005.

[55] B. T. Zigler, P. E. Keros, K. B. Helleberg, M. Fatouraie, D. Assanis, and M. S. Wooldridge, "An experimental investigation of the sensitivity of the ignition and combustion properties of a single-cylinder research engine to spark-assisted HCCI," *International Journal of Engine Research*, vol. 12, pp. 353–375, 2011.

[56] L. Manofsky, J. Vavra, D. Assanis, and A. Babajimopoulos, "Bridging the Gap between HCCI and SI: Spark-Assisted Compression Ignition," *SAE Technical Paper 2011-01-1179*, 2011.

[57] J. B. Martz, "Simulation and Model Development for Auto-ignition and Reaction Front Propagation in Low-Temperature High-Pressure Lean-Burn Engines". Ph.D. Thesis, Department of Mechanical Engineering, University of Michigan, Ann Arbor, 2010.

[58] J. B. Martz, G. A. Lavoie, H. G. Im, R. J. Middleton, A. Babajimopoulos, and D. N. Assanis, "The propagation of a laminar reaction front during end-gas auto-ignition," *Combustion and Flame*, vol. 159, pp. 2077–2086, 2012.

[59] H. Yun, N. Wermuth, and P. Najt, "High Load HCCI Operation Using Different Valving Strategies in a Naturally-Aspirated Gasoline HCCI Engine," *SAE Int. J. Engines*, 4(1):1190-1201, 2011.

[60] R. J. Middleton, L. K. M. Olesky, G. A. Lavoie, M. S. Wooldridge, D. N. Assanis, and J. B. Martz, "The effect of spark timing and negative valve overlap on Spark Assisted Compression Ignition combustion heat release rate," *Proceedings of the Combustion Institute*, vol. 35, pp. 3117–3124, 2015.

[61] K. Siokos, R. Koli, R. Prucka, R. B. Llc, J. Schwanke, and J. Miersch, "Assessment of Cooled Low Pressure EGR in a Turbocharged Direct Injection Gasoline Engine," *SAE Int. J. Engines* 8(4):1535-1543, 2015

[62] J. Brettschneider, "Berechnung des luftverhältnisses lambda von luft-kraftstoffgemischen und des einflusses von messfehlern auf lambda," Bosch Technische Berichte, vol. 6, pp. 177186, 1979.

[63] E. A. Ortiz-Soto, G. A. Lavoie, J. B. Martz, M. S. Wooldridge, and D. N. Assanis, "Enhanced heat release analysis for advanced multi-mode combustion engine experiments," *Applied Energy*, vol. 136, pp. 465–479, 2014.

[64] D. L. Stivender, "Development of a Fuel-Based Mass Emission Measurement Procedure," *SAE Technical Paper 710604*, 1971.

[65] NIST-JANAF thermochemical tables. Available: http://kinetics.nist.gov/janaf/ [Accessed: 10-Jun-2014].

[66] Burcat A. Prof. Burcat's Thermodynamic Data. [Online] Available: http://garfield.chem.elte.hu/Burcat/burcat.html. [Accessed: 10-Jun-2014].

[67] R. G. Prucka, Z. Filipi, D. N. Assanis, D. M. Kramer, and G. L. Ohl, "An Evaluation of Residual Gas Fraction Measurement Techniques in a High Degree of Freedom Spark Ignition Engine," *SAE Technical Paper 2008-01-0094*, 2008.

[68] E. Ortiz-Soto, J. Vavra, and A. Babajimopoulos, "Assessment of Residual Mass Estimation Methods for Cylinder Pressure Heat Release Analysis of HCCI Engines With Negative Valve Overlap," *Journal of Engineering for Gas Turbines and Power*, vol. 134, no. 8, p. 82802, 2012.

[69] H. J. Yun and W. Mirsky, "Schlieren-Streak Measurements of Instantaneous Exhaust Gas Velocities from a Spark-Ignition Engine," *SAE Transactions*, vol. 83, pp. 3143–158, 1974.

[70] R. Fitzgerald, R. Steeper, J. Snyder, R. Hanson, and R. Hessel, "Determination of Cycle Temperatures and Residual Gas Fraction for HCCI Negative Valve Overlap Operation," *SAE Int. J. of Engines*, 3(1), 124 141, 2010.

[71] G. F. Hohenberg, "Advanced Approaches for Heat Transfer Calculations," *SAE Technical Paper 790825*, 1979.

[72] J. Chang, O. Güralp, Z. Filipi, D. Assanis, T.-w. Kuo, P. Najt, and R. Rask, "New Heat Transfer Correlation for an HCCI Engine Derived from Measurements of Instantaneous Surface Heat Flux," *SAE Technical Paper 2004-01-2996*, 2004.

[73] R. J. Tabaczynski, C. R. Ferguson, and K. Radhakrishnan, "A Turbulent Entrainment Model for Spark-Ignition Engine Combustion," *SAE Technical Paper 770647*, 1977.

[74] Y. G. Guezennec and W. Hamama, "Two-Zone Heat Release Analysis of Combustion Data and Calibration of Heat Transfer Correlation in an I. C. Engine," *SAE Technical Paper 1999-01-0218*, 1999.

[75] J. B. Heywood, J. M. Higgins, and P. A. Watts, "Development and Use of a Cycle Simulation to Predict SI Engine Efficiency and NO_x Emissions," *SAE Technical Paper 790291*, 1979.

[76] A. E. Catania, D. Misul, A. Mittica, and E. Spessa, "A Refined Two-Zone Heat Release Model for Combustion Analysis in SI Engines.," *JSME Int. J. Ser. B* 46(1): 75-85, 2003.

[77] H. Persson, a. Hultqvist, B. Johansson, and a. Remon, "Investigation of the Early Flame Development in Spark Assisted HCCI Combustion Using High Speed Chemiluminescense Imaging," *SAE Technical Paper 2007-01-0212*, 2007.

[78] J. B. Martz, R. J. Middleton, G. A. Lavoie, A. Babajimopoulos, and D. N. Assanis, "A computational study and correlation of premixed isooctane-air laminar reaction front properties under spark ignited and spark assisted compression ignition engine conditions," *Combustion and Flame*, vol. 158, no. 6, pp. 1089–1096, 2011.

[79] R. J. Middleton, J. B. Martz, G. A. Lavoie, A. Babajimopoulos, and D. N. Assanis, "A computational study and correlation of premixed isooctane air laminar reaction fronts diluted with EGR," *Combustion and Flame*, 159(10), pp. 3146–3157, 2012.

[80] C. Lund and C. Westbrook, "HCT, Time Dependent 1-D Gas Hydrodynamics, Chemical Kinetics, Chemical Transport," May 2001.

[81] V. K. Temel and J. Sterniak, "Characterization of SACI Combustion for Use in Model Based Controls," *SAE Technical Paper 2014-01-1289*, 2014.

[82] R. J. Middleton, "Simulation of Spark Assisted Compression Ignition Combustion Under EGR Dilute Engine Operating Conditions". Ph.D. Thesis, Department of Mechanical Engineering, University of Michigan, Ann Arbor, 2014.

[83] A. K. Sen, G. Litak, K. D. Edwards, C. E. A. Finney, C. S. Daw, and R. M. Wagner, "Characteristics of cyclic heat release variability in the transition from spark ignition to HCCI in a gasoline engine," *Applied Energy*, vol. 88, no. 5, pp. 1649–1655, 2011.

[84] E. Hellström, A. G. Stefanopoulou, J. Vavra, A. Babajimopoulos, D. N. Assanis, L. Jiang, and H. Yilmaz, "Understanding the dynamic evolution of cyclic variability at the operating limits of HCCI engines with negative valve overlap," *SAE Int. J. Engines*, 5(3):995–1008, 2012.

[85] M. M. Andreae, W. K. Cheng, and T. Kenney, "On HCCI Engine Knock," *SAE Technical Paper 2007-01-1858*, 2007.

[86] J. A. Eng, "Characterization of Pressure Waves in HCCI Combustion," *SAE Technical Paper 2002-01-2859*, 2002.

[87] M. Sjoberg and J. E. Dec, "Ethanol Autoignition Characteristics and HCCI Performance for Wide Ranges of Engine Speed, Load and Boost," *SAE Int. J. Engines*, 3(1):84-106, 2010.

[88] C. Wildman, R. J. Scaringe, and W. Cheng, "On the Maximum Pressure Rise Rate in Boosted HCCI Operation," *SAE Technical Paper 2009-01-2727*, 2009.

[89] L. M. Olesky, J. B. Martz, G. A. Lavoie, J. Vavra, D. N. Assanis, and A. Babajimopoulos, "The effects of spark timing, unburned gas temperature, and negative valve overlap on the rates of stoichiometric spark assisted compression ignition combustion," *Applied Energy*, 105. 407–417, 2013.

[90] N. Milovanovic, R. Chen, and J. Turner, "Influence of the variable valve timing strategy on the control of a homogeneous charge compression (HCCI) engine," *SAE Technical Paper 2004-01-1899*, 2004.

[91] J. Allen and D. Law, "Variable Valve Actuated Controlled Auto-Ignition: Speed Load Maps and Strategic Regimes of Operation," *SAE Technical Paper 2002-01-0422*, 2002.

[92] K. Hiraya, K. Hasegawa, T. Urushihara, A. Iiyama, and T. Itoh, "A Study on Gasoline Fueled Compression Ignition Engine A Trial of Operation Region Expansion ," *SAE Technical Paper 2002-01-0416*, 2002.

[93] L. Koopmans and I. Denbratt, "A four-stroke camless engine, operated in homogeneous charge compression ignition mode with commercial gasoline," *SAE Technical Paper 2001-01-3610*, 2001.

[94] A. Babajimopoulos, D. N. Assanis, and S. B. Fiveland, "An Approach for Modeling the Effects of Gas Exchange Processes on HCCI Combustion and its Application in Evaluating Variable Valve Timing Control Strategies," *SAE Technical Paper 2002-01-2829*, 2002.

[95] B. J. Lawler, "A Methodology for Assessing Thermal Stratification in an HCCI Engine and Understanding the Impact of Engine Design and Operating Conditions". Ph.D. Thesis, Department of Mechanical Engineering, University of Michigan, Ann Arbor, 2013.

[96] S. Klinkert, "An Experimental Investigation of the Maximum Load Limit of Boosted HCCI Combustion in a Gasoline Engine with Negative Valve Overlap". Ph.D. Thesis, Department of Mechanical Engineering, University of Michigan, Ann Arbor, 2014.

[97] J. E. Dec and Y. Yang, "Boosted HCCI for High Power without Engine Knock and with Ultra-Low NO_x Emissions - using Conventional Gasoline," *SAE Int. J. Engines*, 3(1):750-767, 2010.

[98] M. Mehl, W. Pitz, M. Sarathy, Y. Yang, and J. Dec, "Detailed kinetic modeling of conventional gasoline at highly boosted conditions and the associated intermediate temperature heat release," *SAE Technical Paper 2012-01-1109*, 2012.

[99] L. M. Hagen, L. Manofsky Olesky, S. V. Bohac, G. Lavoie, and D. Assanis, "Effects of a Low Octane Gasoline Blended Fuel on NVO Enabled HCCI Load Limit, Combustion Phasing and Burn Duration," *ASME 2012 Internal Combustion Engine Division Fall Technical Conference*, 2012.

[100] G. Lavoie, R. Middleton, J. Martz, S. Makkapati, and E. Curtis, "Characteristic Time Analysis of SI Knock with Retarded Combustion Phasing in Boosted Engines," *SAE Technical Paper 2017-01-0667*, 2017.

[101] T. Alger, J. Gingrich, B. Mangold, and C. Roberts, "A Continuous Discharge Ignition System for EGR Limit Extension in SI Engines," *SAE Int. J. Engines*, 4(1):677-692, 2011.

[102] N. Dronniou, and J. E. Dec, "Investigating the Development of Thermal Stratification from the Near-Wall Regions to the Bulk-Gas in an HCCI Engine with Planar Imaging Thermometry," *SAE Int. J. Engines*, 5(3):1046-1074, 2012.

[103] J. R. Theis, A. B. Getsoian, and C. K. Lambert, "The Development of Low Temperature Three-Way Catalysts for High Efficiency Gasoline Engines of the Future: Part II," *SAE Technical Paper 2018-01-0939*, 2018.

[104] K. N. C. Bray, "Studies of the Turbulent Burning Velocity," *Proceedings: Mathematical and Physical Sciences*, vol. 431, no. 1882, pp. 315–335, 1990.

[105] M. J. Hall and F. V. Bracco, "A Study of Velocities and Turbulence Intensities Measured in Firing and Motored Engines," *SAE Transactions*, vol. 96, pp. 414–441, 1987.

[106] H. Persson, B. Johansson, and A. Remón, "The Effect of Swirl on Spark Assisted Compression Ignition (SACI)," *SAE Technical Paper 2007-01-1856*, 2007.

[107] J. P. Szybist, R. R. Steeper, D. Splitter, V. B. Kalaskar, J. Pihl, and C. Daw, "Negative Valve Overlap Reforming Chemistry in Low-Oxygen Environments," *SAE Int. J. Engines*, 7(1):418-433, 2014.

[108] T. Alger and B. Mangold, "Dedicated EGR : A New Concept in High Efficiency Engines," *SAE Int. J. Engines*, 2(1):620-631, 2009.

[109] T. Han, G. Lavoie, M. Wooldridge, and A. Boehman, "Effect of Syngas (H2/CO) on SI Engine Knock under Boosted EGR and Lean Conditions," *SAE Int. J. Engines*, 10(3):959-969, 2017.

[110] J. A. Topinka, M. D. Gerty, J. B. Heywood, and J. C. Keck, "Knock behavior of a lean-burn, H2 and CO enhanced, SI gasoline engine concept," *SAE Technical Paper 2004-01-0975*, 2004.

[111] S. Jade, J. Larimore, E. Hellstrom, A. G. Stefanopoulou, and L. Jiang, "Controlled Load and Speed Transitions in a Multicylinder Recompression HCCI Engine," *IEEE Transactions on Control Systems Technology*, vol. 23, no. 3, pp. 868–881, May 2015.

[112] J. P. Szybist, K. D. Edwards, M. Foster, K. Confer, and W. Moore, "Characterization of Engine Control Authority on HCCI Combustion as the High Load Limit is Approached," *SAE Int. J. Engines*, 6(1):553-568, 2013.

[113] L. K. M. Olesky, R. J. Middleton, G. A. Lavoie, M. S. Wooldridge, and J. B. Martz, "On the Sensitivity of Low Temperature Combustion to Spark Assist near Flame Limit Conditions," *Fuel*, vol. 158, pp. 11–22, 2015.

[114] Y. Yang, J. E. Dec, N. Dronniou, M. Sjöberg, and W. Cannella, "Partial Fuel Stratification to Control HCCI Heat Release Rates: Fuel Composition and Other Factors Affecting Pre-Ignition Reactions of Two-Stage Ignition Fuels," *SAE Int. J. Engines*, 4(1):1903-1920, 2011.

[115] Y. Yang, J. E. Dec, N. Dronniou, and M. Sjöberg, "Tailoring HCCI heat-release rates with partial fuel stratification: Comparison of two-stage and single-stage-ignition fuels," *Proceedings of the Combustion Institute*, vol. 33, pp. 3047–3055, 2011.

[116] W. Bandel, G. K. Fraidl, P. E. Kapus, H. Sikinger, and C. N. Cowland, "The Turbocharged GDI Engine: Boosted Synergies for High Fuel Economy Plus Ultra-low Emission," *SAE Technical Paper 2006-01-1266*, 2006.

[117] Y. S. Jo, R. Lewis, L. Bromberg, and J. B. Heywood, "Performance Maps of Turbocharged SI Engines with Gasoline-Ethanol Blends: Torque, Efficiency, Compression Ratio, Knock Limits, and Octane," *SAE Technical Paper 2014-01-1206*, 2014.

[118] H. Xie, L. Li, T. Chen, W. Yu, X. Wang, and H. Zhao, "Study on Spark Assisted Compression Ignition (SACI) Combustion with Positive Valve Overlap at Medium-High Load," *Applied Energy*, 101. 622–633, 2013.

[119] G. Kalghatgi and R. Stone, "Fuel requirements of spark ignition engines," *Proceedings of the Institution of Mechanical Engineers, Part D: Journal of Automobile Engineering*, vol. 232, pp. 22–35, 2018.

[120] E. P. Kasseris and J. B. Heywood, "Comparative Analysis of Automotive Powertrain Choices for the Next 25 Years," *SAE Technical Paper 2007-01-1605*, 2007.

[121] G. Mittal and C.-J. Sung, "A Rapid Compression Machine For Chemical Kinetics Studies at Elevated Pressures and Temperatures," *Combustion Science and Technology*, vol. 179, pp. 497–530, 2007.

[122] G. Mittal and C.-J. Sung, "Homogeneous charge compression ignition of binary fuel blends," *Combustion and Flame*, 155, 431–439, 2008.

[123] K. Fieweger, R. Blumenthal, and G. Adomeit, "Shock-tube investigations on the self-ignition of hydrocarbon-air mixtures at high pressures," *Symposium (International) on Combustion*, 25. 1579–1585, 1994.

[124] K. Fieweger, R. Blumenthal, and G. Adomeit, "Self-ignition of S.I. engine model fuels: A shock tube investigation at high pressure," *Combustion and Flame*, 109. 599–619, 1997.

[125] B. M. Gauthier, D. F. Davidson, and R. K. Hanson, "Shock tube determination of ignition delay times in full-blend and surrogate fuel mixtures," *Combustion and Flame*, vol. 139, pp. 300–311, 2004.

[126] J. P. Szybist, S. W. Wagnon, D. Splitter, W. J. Pitz, and M. Mehl, "The Reduced Effectiveness of EGR to Mitigate Knock at High Loads in Boosted SI Engines," *SAE Int. J. Engines*, 10(5):2305-2318, 2017.

[127] H. J. Curran, P. Gaffuri, W. J. Pitz, and C. K. Westbrook, "A comprehensive modeling study of hydrogen oxidation," *Int. J. Chem. Kinet.*, vol. 36, pp. 603–622, 2004.

[128] M. Mehl, W. J. Pitz, C. K. Westbrook, and H. J. Curran, "Kinetic modeling of gasoline surrogate components and mixtures under engine conditions," *Proceedings of the Combustion Institute*, vol. 33, pp. 193–200, 2011.

[129] M. Mehl, J. Y. Chen, W. J. Pitz, S. M. Sarathy, and C. K. Westbrook, "An approach for formulating surrogates for gasoline with application toward a reduced surrogate mechanism for CFD engine modeling," *Energy and Fuels*, vol. 25, pp. 5215–5223, 2011.

[130] D. A. Rothamer, J. A. Snyder, R. K. Hanson, R. R. Steeper, and R. P. Fitzgerald, "Simultaneous imaging of exhaust gas residuals and temperature during HCCI combustion," *Proceedings of the Combustion Institute*, vol. 32, pp. 2869–2876, 2009.

[131] J. Kodavasal, "Effect of Charge Preparation Strategy on HCCI Combustion". Ph.D. Thesis, Department of Mechanical Engineering, University of Michigan, Ann Arbor, 2013.

[132] J. Kodavasal, G. A. Lavoie, D. N. Assanis, and J. B. Martz, "The effects of thermal and compositional stratification on the ignition and duration of homogeneous charge compression ignition combustion," *Combustion and Flame*, vol. 162, pp. 451–461, 2015.

[133] B. Lawler, S. Mamalis, S. Joshi, J. Lacey, O. Guralp, P. Najt, and Z. Filipi, "Understanding the effect of operating conditions on thermal stratification and heat release in a homogeneous charge compression ignition engine," *Applied Thermal Engineering*, vol. 112, pp. 392–402, 2017.

[134] A. Kakuho, M. Nagamine, Y. Amenomori, T. Urushihara, and T. Itoh, "In-Cylinder Temperature Distribution HCCI Combustion in Thermal Fluid Sciences 2006," *SAE Technical Paper 2006-01-1202*, 2006.

[135] P. S. Shingne, "Thermodynamic Modeling of HCCI Combustion with Recompression and Direct Injection". Ph.D. Thesis, Department of Mechanical Engineering, University of Michigan, Ann Arbor, 2015.

[136] R. E. Herold, "Optical Investigation of the Effects of Stratification on Homogeneous Compression Ignition Combustion". Ph.D. Thesis, Department of Mechanical Engineering, University of Wisconsin-Madison, 2008.

[137] M. Schmitt and K. Boulouchos, "Role of the intake generated thermal stratification on the temperature distribution at top dead center of the compression stroke," *International Journal of Engine Research*, 17(8):836–845, 2016.

[138] J. Krasselt, D. Foster, J. Ghandhi, R. Herold, D. Reuss, and P. Najt, "Investigations into the Effects of Thermal and Compositional Stratification on HCCI Combustion Part I : Metal Engine Results," *SAE Int. J. Engines*, 2(1):1034-1053, 2009.

[139] C. Mounaïm-Rousselle, L. Landry, F. Halter, and F. Foucher, "Experimental characteristics of turbulent premixed flame in a boosted Spark-Ignition engine," *Proceedings of the Combustion Institute*, 34(2): 2941–2949, 2013.

[140] J. E. Dec, M. Sjöberg, and W. Hwang, "Isolating the Effects of EGR on HCCI Heat Release Rates and NO_x Emissions," *SAE Int. J. Engines*, 2(2):58-70, 2010.

[141] J. Martz, R. Middleton, and G. Lavoie, "Understanding End-gas Auto-Ignition Rates during SACI Combustion," *Publication in preparation.*

[142] C. Chryssakis and D. N. Assanis, "A Unified Fuel Spray Breakup Model For Internal Combustion Engine Applications," *Atomization and Sprays*, 18(5): 375–426, 2008.

[143] C. A. Chryssakis, D. N. Assanis, J.-k. Lee, and K. Nishida, "Fuel Spray Simulation of High-Pressure Swirl-Injector for DISI Engines and Comparison with Laser Diagnostic Measurements," in *SAE Technical Paper 2003-01-0007*, 2003.

[144] A. A. Amsden, "KIVA-3V: A Block-Structured KIVA Program for Engines with Vertical or Canted Valves," United States: N. p., 1997.

[145] C. Meneveau and T. Poinsot, "Stretching and quenching of flamelets in premixed turbulent combustion," *Combustion and Flame*, vol. 86, pp. 311–332, 1991.

[146] T. A. Baritaud, J. M. Duglos, and A. Fusco, "Modeling turbulent combustion and pollutant formation in stratified charge SI engines," *Symposium (International) on Combustion*, vol. 26, pp. 2627–2635, 1996.

[147] A. Babajimopoulos, D. N. Assanis, D. L. Flowers, S. M. Aceves, and R. P. Hessel, "A fully coupled computational fluid dynamics and multi-zone model with detailed chemical kinetics for the simulation of premixed charge compression ignition engines," *International Journal of Engine Research*, vol. 6, no. 5, pp. 497–512, 2005.

[148] J. Kodavasal, S. H. Keum, and A. Babajimopoulos, "An extended multi-zone combustion model for PCI simulation," *Combustion Theory and Modelling*, vol. 15, no. 6, pp. 893–910, 2011.

[149] R. J. Kee, F. M. Rupley, and J. a. Miller, *Chemkin-II: A Fortran chemical kinetics package for the analysis of gas-phase chemical kinetics*. United States: N. p., 1989.

[150] R. J. Middleton and J. B. Martz, "An efficient model of gas exchange for multi-cycle CFD simulations with detailed chemistry," *Publication in preparation.*

[151] B. T. Zigler, "An Experimental Investigation of the Ignition Properties of Low Temperature Combustion in an Optical Engine". Ph.D. Thesis, Department of Mechanical Engineering, University of Michigan, Ann Arbor, 2008.

[152] A. Babajimopoulos, "Development of Sequential and Fully Integrated CFD / Multi-Zone Models with Detailed Chemical Kinetics for the Simulation of HCCI Engines". Ph.D. Thesis, Department of Mechanical Engineering, University of Michigan, Ann Arbor, 2005.

[153] L. M. Olesky, G. A. Lavoie, D. N. Assanis, M. S. Wooldridge, and J. B. Martz, "The effects of diluent composition on the rates of HCCI and spark assisted compression ignition combustion," *Applied Energy*, vol. 124, pp. 186–198, 2014.

[154] A. Sofianopoulos, M. R. Boldaji, B. Lawler, S. Mamalis, and S. Brook, "Analysis of Thermal Stratification Effects in HCCI Engines Using Large Eddy Simulations and Detailed Chemical Kinetics," *SAE Technical Paper 2018-01-01*, 2018.

[155] J. Snyder, N. Dronniou, J. Dec, and R. Hanson, "PLIF Measurements of Thermal Stratification in an HCCI Engine under Fired Operation," *SAE Int. J. Engines*, 4(1):1669-1688, 2011.

[156] J. E. Dec, "Advanced compression-ignition engines - Understanding the in-cylinder processes," *Proceedings of the Combustion Institute*, vol. 32, pp. 2727–2742, 2009.

[157] N. Dronniou and J. Dec, "Investigating the Development of Thermal Stratification from the Near-Wall Regions to the Bulk-Gas in an HCCI Engine with Planar Imaging Thermometry," *SAE Int. J. Engines*, 5(3):1046-1074, 2012.

[158] S. A. Kaiser, M. Schild, and C. Schulz, "Thermal stratification in an internal combustion engine due to wall heat transfer measured by laser-induced fluorescence," *Proceedings of the Combustion Institute*, 34(2): 2911–2919, 2013.

[159] P. S. Shingne, R. J. Middleton, C. Borgnakke and J. B. Martz, "The effects of boost pressure on stratification and burn duration of gasoline homogeneous charge compression ignition combustion," *International Journal of Engine Research*, 2018.